UNIVERSITY
OF SUSSEX

DOCTORAL THESIS

Searches for chargino and neutralino production in multileptonic final states using $\sqrt{s} = 13$ TeV proton-proton collisions with the ATLAS detector

A thesis submitted in fulfilment of the requirements
for the degree of Doctor of Philosophy

in the

Physics and Astronomy department
School of Mathematical and Physical Sciences
Experimental Particle Physics research group

Candidate:
Marco APARO

Supervisor:
Prof. Antonella DE SANTO

14th March 2023

I, Marco APARO, hereby declare that this thesis has not been and will not be, submitted in whole or in part to another university for the award of any other degree.

Brighton,
14th March 2023

Marco APARO

University of Sussex
Physics and Astronomy department
School of Mathematical and Physical Sciences
Experimental Particle Physics research group

DOCTORAL THESIS

Searches for chargino and neutralino production in multileptonic final states using $\sqrt{s} = 13$ TeV proton-proton collisions with the ATLAS detector

by Marco APARO

ABSTRACT

This thesis presents the work of the Candidate during his PhD on three analyses targeting the Electroweak Supersymmetry production of charginos and neutralinos decaying into multilptonic final states. Only electrons and muons are considered along with R-Parity-conserving decays. These analyses all use from $\sqrt{s} = 13$ TeV proton-proton collisions collected by the ATLAS experiment at the Large Hadron Collider in the 2015-2018 period for a total of $139\,\mathrm{fb}^{-1}$. Firstly, the analysis targeting final states with two leptons of the same electrical charge and intermediate W and Higgs on-shell bosons is presented. The results show no significant excess from the Standard Model predictions and new constraints on the masses of charginos and neutralinos are obtained for this model, significantly extending the known bounds from previous searches. Secondly, results of another analysis targeting intermediate states with on-shell WZ and Wh bosons and three-lepton final states are also presented. Once again, no significant deviation from the Standard Model prediction is observed and exclusion limits on the masses of charginos and neutralinos are set for these models. Finally, the statistical combination of these searches with those of other analyses targeting the same electroweak Supersymmetry production mechanism with different final states is also presented in this thesis. The final results show how such combination can be used to further improve the constraints on the masses of the charginos and neutralinos. Moreover, the details of a technical task concerning the characterisation of the performance of the Inner Detector Trigger tracking of electrons and muons in the ATLAS experiment through the usage of the Tag-and-Probe technique is also discussed. The final result show a significant improvement in the accuracy of the measured Trigger tracking efficiencies with respect to those obtained by means of the previously used procedure.

Contents

INTRODUCTION

Over the course of history, humankind has always strived to comprehend Nature and to predict the behaviour of natural phenomena. This pursuit has led to remarkable discoveries which have highlighted the fundamental composition of the known matter in the universe and the main forces which are responsible for the occurrence of the observed phenomena. Elementary particles have been found to be the fundamental building blocks of the known universe. Their interactions are described in the theoretical framework called the Standard Model (SM). The predictive power of the SM has been tested experimentally over the years, reaching unprecedented precision through the undeniable evidence collected at the Large Electron-Positron collider (LEP) and at the Large Hadron Collider (LHC), culminating with the discovery of the Higgs boson by the ATLAS and CMS experiments.

Despite its many experimental successes, the SM is still far from being considered an ultimate theory of Nature. Many limitations, based on the inability to explain several phenomena in the SM, imply the necessity of a wider theoretical framework which would extend the SM to also describe new physics phenomena. In this context, Supersymmetry (SUSY) offers a solution by introducing a fermion-boson correspondence. SUSY predicts the existence of new particles which to this day remain undiscovered. The predicted properties of SUSY lead to several phenomenological implications of physical interest. In particular, SUSY particles can be produced at the LHC by means of the SM strong and Electroweak (EWK) interactions. Due to existing constraints on the value of the masses of strongly-coupled SUSY particles, the EWK production of weakly-interacting sparticles can be considered a key mechanism to search for Beyond Standard Model (BSM) physics at the LHC.

The analyses outlined in this thesis all focus on the search for the EWK production of SUSY particles using the data from $\sqrt{s} = 13$ TeV proton-proton (p-p) collisions collected by the ATLAS experiment. The dataset used has been recorded between 2015 and 2018, and corresponds to a total integrated luminosity of 139 fb^{-1}. These searches represent the work that I have carried out and contributed to over the course of my PhD. This includes: the estimation of the performance of the Inner Detector (ID) Trigger, which allowed me to be qualified as an author of the ATLAS Collaboration; EWK SUSY searches focusing on final states with leptons, particularly those with two leptons of the same electrical charge and with three leptons; the statistical combination of analyses targeting analogous EWK SUSY production mechanisms.

The structure of this thesis is as follows. Chapter 1 presents an overview of the theoretical foundation onto which the SUSY models targeted by the searches described in this thesis are based. The phenomenological implications that these EWK SUSY models are expected to have at the LHC are also described, along with the state of these searches prior to the work outlined in this thesis. In Chapter 2 an overview of the ATLAS experiment at the LHC is provided. Particular focus is given to the description of the ATLAS Trigger system and the characterisation of the performance of the ID Trigger, to which I have personally contributed. In Chapter 3 the basic features of the procedure used to simulate events from a p-p collision in the ATLAS experiment are discussed, along with the techniques for reconstructing relevant object for physics analyses in ATLAS. Chapter 4 is devoted to the analysis addressing the search for the EWK production of charginos and neutrlinos decaying into a final state with two same-sign electrons or muons. I am the leading analyser for this search, and I have personally developed most of its aspects. In Chapter 5, an overview is given on another search for chargino and neutralino production, this time targeting three-lepton final states. During my PhD I also made significant contributions to this analysis, as described in this thesis. An important aspect of the EWK SUSY searches in ATLAS is the statistical combination of searches targeting the same production model but with different final states. Chapter 6 presents the procedure and the first results of such statistical combination of various EWK SUSY searches, including those described in the previous Chapter. Finally, conclusions and an outlook are given in Chapter 7.

Throughout this thesis, natural units ($c = \hbar = 1$) are employed.

THEORETICAL BACKGROUND 1

Over the past century continuous scientific advancements have brought humankind a step closer to formulating a theoretical model of Nature which could explain all physical phenomena. Furthermore, the progress in experimental techniques has led to outstanding discoveries that contribute to providing an increasingly deeper understanding of the elementary processes underlying the observed phenomena.

The SM is the theoretical framework that to date best describes the physics of elementary particles and their fundamental interactions. Despite its predictive power, which makes it one of the most successful theoretical constructs of all time, the SM still presents various limitations.

One of the best established, proposed theoretical extensions of the SM is SUSY. In SUSY new particle states are predicted through the introduction of a new symmetry linking fermions and bosons to one another. The production and decay of new heavy supersymmetric particles implies a series of phenomenological effects that may present themselves experimentally, e. g. in high-energy hadron colliders such as the LHC.

This thesis focuses on searches for supersymmetric particles at the LHC, using the ATLAS experiment. This Chapter outlines the theoretical foundation onto which the work presented in this thesis is based. Section 1.1 describes the key aspects of the SM. In Section 1.2, SUSY is introduced, focusing on the Minimal Supersymmetric Standard Model (MSSM). Finally, Section 1.3 provides an overview of the most relevant phenomenology of EWK SUSY processes and the experimental searches targeting them which are currently being carried out at the LHC.

1.1 The Standard Model

The SM is a gauge theory describing the behaviour of the known elementary particles and their interactions via the *strong*, *weak* and *electromagnetic* forces [1]. The fourth known fundamental interaction, *gravity*, is not included in the SM[1]. The electromagnetic force is described by Max-

[1] Gravitational effects are described by *general relativity* [2]. A viable formulation of a quantum theory of gravity is still being developed.

well's equations. Weak interactions are responsible for processes such as the β decay, whilst the strong force relates to the interaction of nuclei.

The SM is developed within the framework of Quantum Field Theory (QFT), in which particles and their interactions are represented in terms of fields and their quantisation [3]. The particle content of the SM is shown in Figure 1.1.

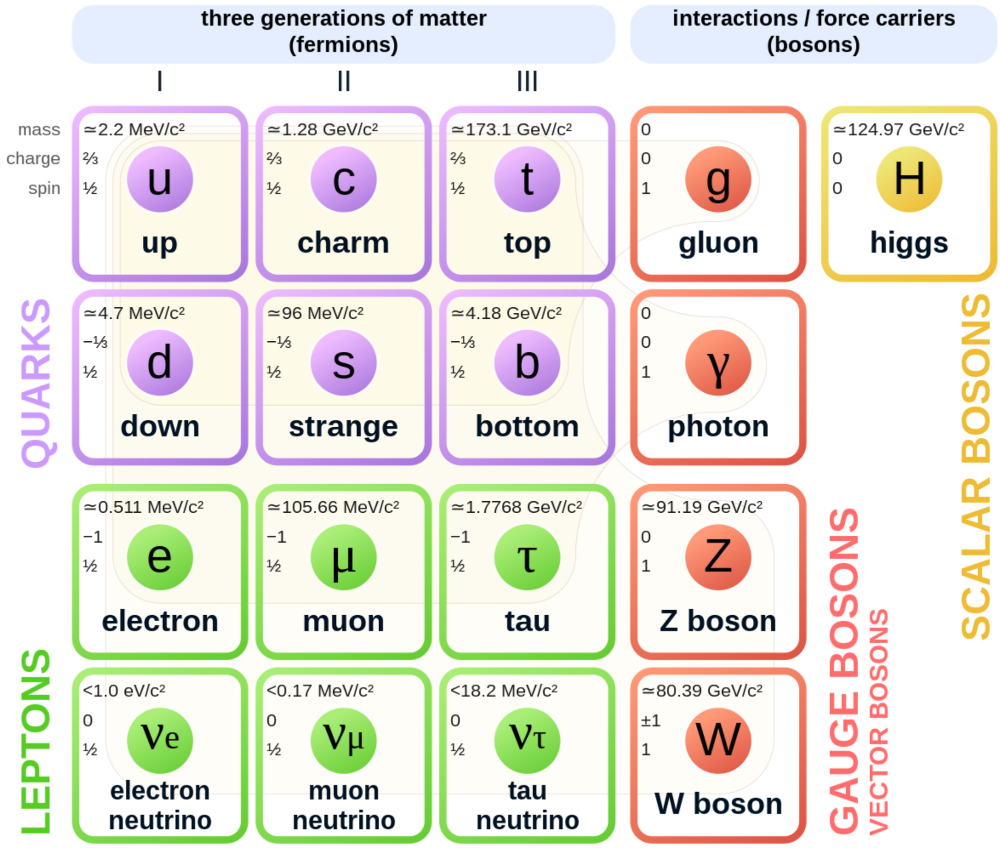

Figure 1.1: Elementary particle content of the SM. The quarks (u, d, s, c, b, t) are shown in purple, leptons (e, μ, τ, ν_e, ν_μ, ν_τ) in green, gauge bosons (g, γ, Z, W) in red and the Higgs boson (H) in yellow. The mass, the electric charge and the spin of each particle is also displayed [4]. The values of the masses show in this Figure may correspond to the most their recent measurements. Up-to-date measured values of the mass of the particles in the SM can be found in Reference [5].

A first distinction can be made between *bosons* and *fermions*. Fermions are the basic constituents of the known matter in the universe and include all spin-1/2 particles which are further sub-categorised into *quarks* and *leptons*. The *Dirac equation* describes the behaviour of fermions and predicts the existence of an *antiparticle* for each fermion in the SM. Antiparticles have opposite electric charge compared to their corresponding particle, but have the same spin and mass. Matter particles in the SM are also characterised by their *chirality*, a quantum number that generalises the concept of *helicity*, i. e. the projection of the spin of the particle along its direction of motion. Particles can be *left-handed* or *right-handed*, according to their chirality. Both leptons and quarks are arranged in a family structure based on three different *generations*, as shown in Figure 1.1. Only charged fermions can interact electromagnetically, whereas all fermions are sensitive to the weak interaction, since they carry a *weak isospin*. Quarks are the only fermions which are subject to the strong force.

For leptons, each generation identifies a distinct *flavour*. In particular, the charged leptons are the *electron*, e, the *muon*, μ, and the *tau*, τ. Each charged lepton is associated with the corresponding, electrically-neutral *neutrino* of the same flavour. The three lepton generations are characterised by three quantum numbers, called *lepton numbers* (L_e, L_μ, L_τ). Each lepton number is separately conserved in SM processes and is +1 for leptons, -1 for the corresponding anti-leptons, and zero otherwise.

The six different flavours of quarks (Figure 1.1) are also grouped into three distinct generations, as in the lepton case. Quarks carry an electric charge, a weak isospin and, additionally, a *colour charge*, whose three possible values are conventionally labelled *red*, *green* and *blue*. The colour charge makes quarks sensitive to the strong interaction. Quarks aggregate to form composite colourless particle states, called *hadrons*. Hadrons formed by three quarks are called *baryons* (e. g. protons, p, and neutrons, n), whereas those composed by a quark-antiquark pair are referred to as *mesons* (e. g. pions, π, and kaons, K). Each of the three generations of quarks is composed by an *up-type* and a *down-type* quark. Up-type quarks (*up*, u, *charm*, c, and *top*, t) have +2/3 electric charge, whereas down-type quarks (*down*, d, *strange*, s, and *bottom*, b) have -1/3 electric charge. Finally, quarks also carry a *baryon number*, B, which is +1/3 for quarks, -1/3 for anti-quarks, and zero otherwise. For all processes in the SM, the baryon number is conserved.

Both *vector* and *scalar bosons* are present in the SM. Vector bosons are spin-1 particles which act as mediators of the fundamental interactions between particles. The photon, γ, is the massless mediator of the electromagnetic force and only interacts with electrically charged particles. The 8 massless gluons, g, are responsible for the strong interaction between quarks and themselves carry the colour charge. The $W^\pm$ and Z bosons are, respectively, the charged and electrically neutral mediators of the weak interaction. Processes mediated by the W boson are referred to as *charged currents*, whilst those which involve the interchange of a Z boson are called *neutral currents*. Finally, the scalar, spin-0 *Higgs* boson completes the picture of the particle content of the SM. It is associated with the mechanism through which is possible to generate the masses of all particles in the SM, discussed in Section 1.1.4.

1.1.1 Quantum Electrodynamics

In the QFT formalism of the SM, the properties of each quantised field at any given point of the spacetime are described by means of the *Lagrangian*, $\mathcal{L}$, and its equation of motion, the *Euler-Lagrange equation* [3]. A fundamental aspect of the SM is the one-to-one correspondence between physical interactions and *gauge symmetries*. These are transformations of the fields that are based on a specific *symmetry group* and which leave the Lagrangian invariant.

The properties of electrically charged particles and their electromagnetic interaction are described by Quantum Electrodynamics (QED) [6], whose basic formulation starts from considering the Lagrangian for a free massless fermion:

$$\mathcal{L}(x) = \overline{\psi}(x)\left(i\gamma^\mu\partial_\mu\right)\psi(x). \tag{1.1}$$

In Equation 1.1 x is the four-vector of space-time coordinates and γ^μ are the four Dirac matrices, $\psi(x)$ is the four-component *Dirac spinor* describing a fermion field and $\overline{\psi}(x)$ is its Dirac adjoint. The Lagrangian in Equation 1.1 is symmetric under *global* $U(1)$ Abelian gauge transformations:

$$\psi(x) \xrightarrow{U(1)} \psi'(x) = e^{i\theta}\psi(x), \tag{1.2}$$

with θ being the generator of the $U(1)$ transformation. The *gauge principle* requires the Lagrangian to be invariant under *local* gauge transformations, which in this case is realised by allowing the generator of the $U(1)$ group to depend on space-time coordinates, i. e. $\theta = \theta(x)$. As a consequence, to preserve the symmetry, it is necessary to introduce a spin-1 vector field $A_\mu(x)$, such that:

$$A_\mu(x) \xrightarrow{U(1)} A'_\mu(x) = A_\mu(x) - \frac{1}{e}\partial_\mu\theta \tag{1.3}$$

as well as a *covariant derivative* D_μ:

$$D_\mu \doteq \partial_\mu + ieA_\mu(x). \tag{1.4}$$

It is then possible to obtain a Lagrangian symmetric for local $U(1)$ gauge transformation by simply making the $\partial_\mu \to D_\mu$ substitution in Equation 1.1. For completeness, a gauge-invariant kinetic term for the newly introduced vector field $A_\mu(x)$ must be included in the Lagrangian. This is obtained by considering the tensor $F_{\mu\nu} = \partial_\mu A_\nu - \partial_\nu A_\mu$. With this addition, the QED Lagrangian takes its final form:

$$\begin{aligned}\mathcal{L}_{\text{QED}}(x) &= \overline{\psi}(x)\left(i\gamma^\mu D_\mu\right)\psi(x) - \frac{1}{4}F^{\mu\nu}F_{\mu\nu} \\ &= \overline{\psi}(x)\left(i\gamma^\mu \partial_\mu\right)\psi(x) - \frac{1}{4}F^{\mu\nu}F_{\mu\nu} - e\overline{\psi}(x)\gamma^\mu\psi(x)A_\mu(x).\end{aligned} \tag{1.5}$$

The first term in Equation 1.5 is the same free-fermion Lagrangian as in Equation 1.1, whilst the second term represents the kinetic term for the field $A_\mu(x)$. If $A_\mu(x)$ is interpreted as the field of the photon γ, Maxwell's equations follow directly from solving the equations of motions of its kinetic term. The third term in Equation 1.5 represents the *interaction* between the photon and the fermion fields. Hence, the parameter e, called the *coupling*, represents the strength of such interaction and it is related to the electric charge of the fermion. Using a perturbation theory approach and considering the quantisation of the fields, it is possible to deduce from the interaction term a set of rules, known as *Feynman rules* [7], to extract the probability amplitude and, consequently, the cross-section of any possible interaction process between charged fermions and photons. For this purpose, a powerful tool is provided by the so-called *Feynman diagrams*, which are graphical representation of the process in question [1].

The presence of higher-order QED contributions modifies the strength of the electromagnetic interaction between photons and charged fermions in a manner which depends on the transferred momentum, q^2, as a consequence of the *renormalisability* of QED [3]. This is reflected in a so-called *running coupling* in QED, $\alpha_{\text{QED}}(q^2) = e^2(q^2)/4\pi$, which increases with higher q^2 scales. For small q^2 values, corresponding to large distances from the electrical charge producing the interaction, α_{QED} becomes constant at a value of approximately $1/137$. The measurements of the α_{QED} [8, 9], with their unprecedented precision (up to twelve significant figures) and which have been found to agree with its predicted value, represents one of the most successful theoretical predictions of all time.

1.1.2 Quantum Chromodynamics

The theory for strong interactions incorporated in the SM, called Quantum Chromodynamics (QCD), is formulated by using an analogous prescription to the one adopted for QED. Given the three-fold degrees of freedom of the colour charge, the QCD formulation is based on a local, non-Abelian $SU(3)$ gauge transformation:

$$\Psi(x) \xrightarrow{SU(3)} \Psi'(x) = U_C(x)\Psi(x), \quad \text{with} \quad U_C \doteq \exp\left\{ i\frac{\lambda^a}{2}\theta_a(x) \right\}, \tag{1.6}$$

where Ψ are three-vector in the colour space, with each element being a different Dirac spinor, and $\lambda^a/2$ are the eight generators of the $SU(3)$ group, with λ^a $(a = 1,...,8)$ being the Gell-Mann matrices. The local gauge invariance is once again guaranteed through the introduction of a covariant derivative and eight spin-1 vector fields, corresponding to the eight coloured gluons. This allows to derive interaction terms between fermion and gluon fields with coupling g_S.

As a consequence of the non-Abelian nature of the $SU(3)$ symmetry, the expansion of the gluon kinetic term leads to the presence of gluon-gluon self-interacting terms and, therefore, of Feynman diagrams with vertices in which three or four gluons converge. This leads to the most fundamental difference between QED and QCD, which is reflected in the dependence on q^2 of the strong coupling, $\alpha_S(q^2) = g_S^2(q^2)/4\pi$. As opposed to α_{QED}, the strong coupling, α_S, becomes progressively weaker as the energy of the interaction increases, a phenomenon referred to as *asymptotic freedom*. On the other hand, for progressively lower momentum transfers the strength of the interaction becomes so high that coloured particles can only aggregate with each other forming colourless hadrons in the process called *confinement*.

1.1.3 Electroweak unification

The properties of the weak interaction can be deduced in a similar fashion as the one followed for QED and QCD. However, additional phenomenological observations such as the long β-decay lifetimes and the maximal violation of Parity (P) and Charge Conjugation (C) symmetries must also be taken into account in the Lagrangian formulation of the weak interaction. In particular, the P and C violations arise from charged current interactions connecting left-handed fermion pairs differing by one unit of electric charge. Therefore, the SM formulation of the weak interaction is based on the inclusion of left-handed $SU(2)$ fermion doublets and right-handed $U(1)$ fermion singlets:

$$\begin{pmatrix} \nu_\ell \\ \ell^- \end{pmatrix}_L, \; (\nu_\ell)_R, \; (\ell^-)_R, \; \begin{pmatrix} q_u \\ q_d \end{pmatrix}_L, \; (q_u)_R, \; (q_d)_R. \tag{1.7}$$

With a formalism analogous to QED all Dirac spinors transform under $U(1)$ local gauge symmetries. The generator of such $U(1)$ local gauge symmetry is the *weak hypercharge*, Y, which is related to the electric charge of fermions, Q, and to the third component of the weak isospin, T_3, (Section 1.1) through the *Gell-Mann–Nishijima formula* [10, 11]:

$$Y = 2\left(Q - T_3\right). \tag{1.8}$$

On the other hand, only left-handed doublets can transform under $SU(2)$ local gauge symmetries:

$$\Psi_L(x) \xrightarrow{SU(2)} \Psi'_L(x) = U_L(x)\Psi_L(x) \quad \text{with} \quad U_L \doteq \exp\left\{ i\frac{\sigma^i}{2}\theta_i(x) \right\}, \tag{1.9}$$

where Ψ_L are general left-handed spinor doublets and σ^i are the three Pauli matrices. Through this process, four spin-1, vector fields are introduced: W^i_μ, for $i = 1,2,3$, from the $SU(2)$ symmetry and B_μ from the $U(1)$ symmetry. Hence, the couplings g and g' are associated with the W^i_μ and B_μ fields, respectively.

In the Glashow-Weinberg-Salam (GWS) model [12, 13, 14], weak and electromagnetic interactions are incorporated in a single theoretical framework (*EWK unification*). The fields of the W^+ and W^- bosons are obtained from linear combinations of W^1_μ and W^2_μ. Concurrently, the neutral current vector fields W^3_μ and B_μ mix together through the *Weinberg mixing angle*, θ_W, to form the photon (A_μ) and the Z boson (Z_μ) fields. The electroweak unification also connects the g and g' couplings to the QED coupling, e, through the relation:

$$g \sin\theta_W = g' \cos\theta_W = e. \tag{1.10}$$

Once the couplings of the EWK model are chosen to reproduce the electromagnetic couplings, the couplings of the Z boson to all the fermions is also completely specified. Unlike the photon, the Z boson couples differently to left- and right-handed fermions.

Having formulated the EWK unification and QCD, the overall symmetry group of the SM is $SU(3)_C \otimes SU(2)_L \otimes U(1)_Y$, where the subscripts Y, L, and C represent the weak hypercharge, left-handed chirality, and the colour charge, respectively.

1.1.4 Brout-Englert-Higgs mechanism

The SM theory constructed thus far does not allow for the presence of massive bosons or fermions. Indeed, explicit terms in the SM Lagrangian for the mass of the bosonic fields, of the form $-\frac{1}{2}m_B^2 B_\mu B^\mu$, would break the gauge invariance. On the other hand, explicit terms for the mass of fermionic fields, of the form $-m_f\overline{\psi}\psi$, would violate the $SU(2)_L \otimes U(1)_Y$ symmetry because they couple together the left- and right-handed components of a fermion [1]. Therefore, in order to explain the masses of fermions and boson in the SM, a *Spontaneous Symmetry Breaking* (SSB) mechanism must be considered. A solution in this context is offered by the Brout-Englert-Higgs (BEH) mechanism, sometimes also referred to as the Higgs-Kibble mechanism [15, 16, 17]. It provides a way to spontaneously break the local gauge electroweak $SU(2)_L \otimes U(1)_Y$ symmetry, thus generating particle masses in the SM. It implies considering the following terms in the SM Lagrangian with an additional complex scalar field, $\phi(x)$:

$$\mathcal{L}_S = \left(D_\mu\phi\right)^\dagger \left(D^\mu\phi\right) - V\left(\phi\right), \tag{1.11}$$

with

$$V(\phi) = \frac{1}{2}\mu^2\left(\phi^\dagger\phi\right) + \frac{1}{4}\lambda\left(\phi^\dagger\phi\right)^2. \tag{1.12}$$

The first term in Equation 1.11 represents the kinetic energy associated with the field ϕ and $V(\phi)$ is a scalar potential, with μ and λ being complex constants. In the most general case, D_μ is the covariant derivative of the $SU(2)_L$ gauge symmetry and ϕ is a $SU(2)_L$ doublet:

$$\phi \doteq \begin{pmatrix} \phi^+ \\ \phi^0 \end{pmatrix}. \tag{1.13}$$

If $\mu^2 < 0$ the ground state of the potential satisfies $(\phi^\dagger\phi) = -\mu^2/\lambda = v^2$ (representing an hypersphere in four dimensions), where the parameter v is the *EWK Vacuum Expectation Value* (VEV), which sets the so-called *EWK scale*. Moving from the metastable state with $(\phi^\dagger\phi) = 0$ to the VEV the $SU(2)_L \otimes U(1)_Y$ symmetry, which remains hidden in the Lagrangian of Equation 1.11, is spontaneously broken. Perturbations around the VEV which leave the potential level unchanged do not break the symmetry and correspond to the introduction of massless *Goldstone bosons* [18]. On the other hand, small fluctuations from the ground state of the form $v + H(x)$ spontaneously break the symmetry, and correspond to an additional scalar field, $H(x)$, which acquires the mass $m_H = \sqrt{2\lambda v^2}$. This field is the *Higgs boson*.

In the GWS model, which involves imposing a local gauge $SU(2)_L \otimes U(1)_Y$ invariance, the degrees of freedom corresponding to the massless scalar Goldstone bosons become the longitudinal polarisation[2] of the W and Z bosons. It can be shown that the “reabsorption” of the Goldstone bosons into the massive vector gauge bosons is achieved independently of the choice of the gauge transformation (e. g. the *unitary gauge*) [19]. Consequently, W and Z bosons acquire their mass through their interaction with the Higgs boson. Furthermore, the masses of the W and Z boson become related to each other and to the VEV through the Weinberg angle:

$$m_W = m_Z \cos\theta_W = \frac{gv}{2}. \tag{1.14}$$

Concurrently, it can be shown that the same Higgs field that generates the masses of the gauge bosons also gives mass to the fermions in the SM. This is achieved by considering additional terms in the Lagrangian with Yukawa-like interactions [13] in which the left- and right-handed components of the fermion fields are coupled to the scalar $SU(2)_L$ Higgs doublet (Equation 1.13). This procedure introduces a mixing between the flavour and mass eigenstates of the fermions, which are represented by the Cabibbo–Kobayashi–Maskawa (or CKM) matrix [20, 21] in the quark sector and the Pontecorvo–Maki–Nakagawa–Sakata (or PMNS) matrix [22, 23] in the lepton sector[3]. Thus, the Higgs boson couples to directly to all massive particles in the SM. Specifically, couplings to gauge bosons are proportional to their mass squared, whilst couplings to fermions are linear with respect to the fermion masses. Similarly to the W and Z boson case, couplings of the Higgs boson with itself – i. e. vertices of Feynman diagrams with three or four Higgs bosons – are also predicted.

[2] Massless vector bosons, such as gluons or photons, only have two transverse polarisations.

[3] Through the PMNS matrix it is possible to explain the phenomenon known as *neutrino oscillation* [24].

In 2012 the ATLAS and CMS experiments both reported the discovery of a new boson, whose properties are consistent with those of the expected Higgs boson. The measured mass of the Higgs boson is approximately 125 GeV [25, 26, 27].

1.1.5 Limitations of the Standard Model

Despite its many phenomenological successes, the SM presents various limitations. Hence, a theoretical extension is needed to explain observed and predicted phenomena which cannot be accounted for in the SM framework and are thus referred to as BSM phenomena. In this Section some of the limitations of the SM, which are relevant in the context of the searches described in this thesis, are outlined.

Hierarchy problem

The predictive power of a QFT for particle interaction is linked to its ability to predict finite values of the physics observables. In the SM, the predicted value of the mass of the Higgs boson, other than being related to the EWK VEV, receives quantum corrections from the virtual effects of every particle that couples, directly or indirectly, to the Higgs field. For instance, one-loop diagrams involving massive fermions, as shown in Figure 1.2, would result in a correction to the squared Higgs mass parameter of the form:

$$\Delta m_H^2 = -\frac{|\lambda_f|^2}{8\pi^2}\Lambda_{\mathrm{UV}}^2 + ..., \tag{1.15}$$

where λ_f is the coupling with f, Λ_{UV}^2 represents an ultra-violet cut-off, and the ellipses represent higher order terms in Λ_{UV}^2.

For progressively higher energy scales, e. g. when Λ_{UV}^2 approaches the Planck Mass scale, $M_P = (8\pi G_{\mathrm{Newton}})^{-1/2} = 2.4 \times 10^{18}$ GeV, these corrections become much greater than the measured mass of the Higgs boson. This problem, referred to as the *hierarchy problem* [28], indirectly affects the entire mass spectrum of the SM particles, since all masses are generated through the interaction with the Higgs field.

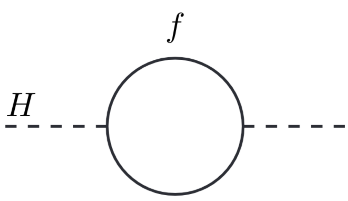

Figure 1.2: One-loop quantum corrections to the m_H^2 parameter due to the coupling of the Higgs boson with a massive fermion, f. [28]

Such divergences in the SM cannot be avoided by taking into account a dedicated fine-tuning of the parameters involved. However, a complete cancellation of the divergent terms can occur e. g. if a specific organising principle in the theory was to be considered. Since such situation does not present itself in the SM, a BSM extension is required.

Grand unification

Taking into account the running of the couplings of the SM gauge interactions with respect to the energy scale (Sections 1.1.1 and 1.1.2), several hypotheses and speculations have been formulated concerning the possible unification of the three fundamental interactions – electromagnetic, weak and strong – as manifestations of a single interaction. Such models are called Grand Unification Theories (GUTs) [29] and can occur only if there exist an energy scale at which the strengths of the three couplings converge into a single value. Such occurrence cannot be realised in the SM, as shown in Figure 1.3. Since the parameters of the SM do not allow the coupling constants of the three fundamental interactions to simultaneously meet at any energy scale, a grand unification is only possible in a BSM theory.

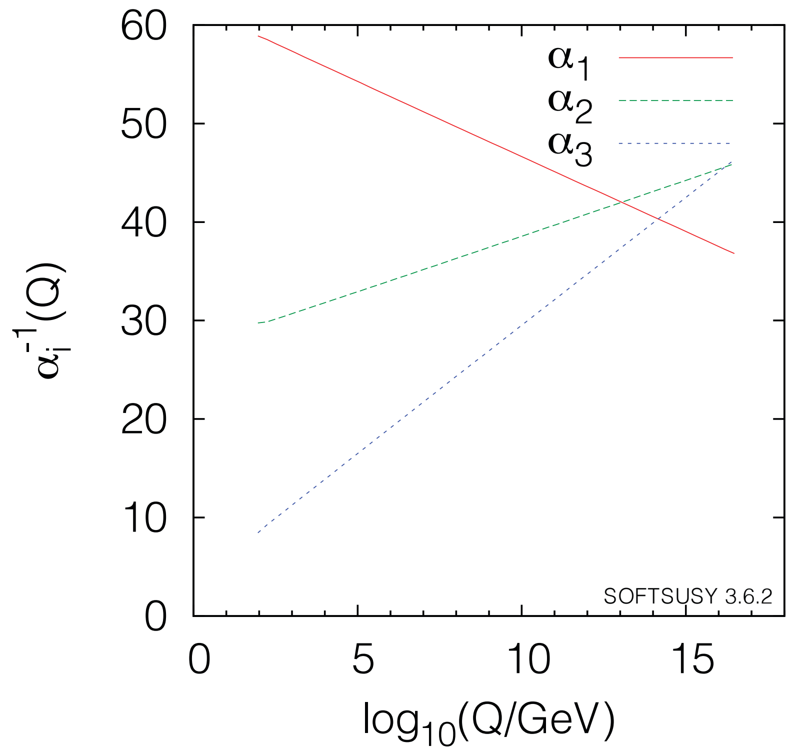

Figure 1.3: Running of the inverse gauge couplings, $\alpha^{-1}(Q)$, in the SM. α_1 corresponds to the $U(1)_Y$ gauge symmetry, α_2 to $SU(2)_L$, and α_3 to $SU(3)_C$. [5]

Dark Matter

Several observations have provided evidence for the existence in the universe of Dark Matter (DM), which takes its name from the fact that it can interact gravitationally but not through any other force. A historical motivation for the existence of DM comes from the observation of the rotational curves of spiral galaxies,as shown in Figure 1.4.

Considering only the “conventional”, baryonic matter in a galaxy, the orbital velocity of visible stars and gases should decrease with increasing radial distances from the centre of the galaxy. However, experimental observations show the opposite behaviour, which can only be explained if a considerable amount of invisible matter is also taken into account.

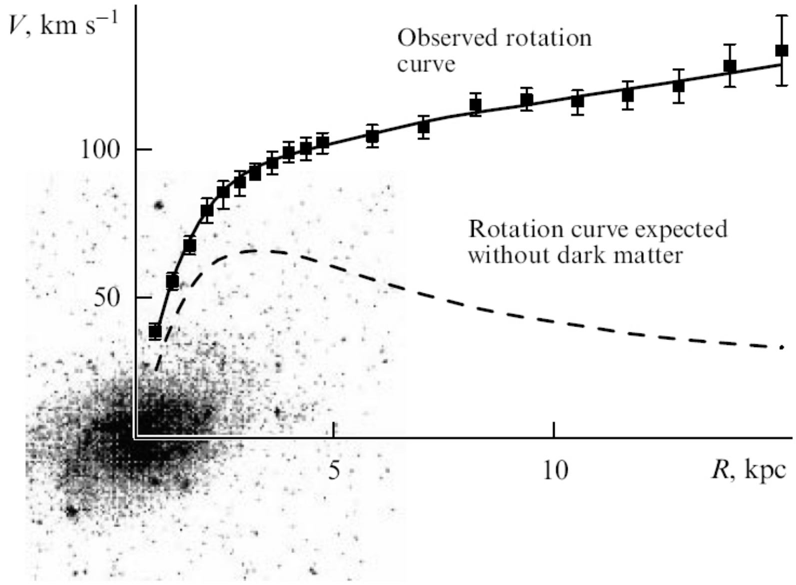

Figure 1.4: Decomposition of the rotation curve of the M 33 galaxy suggesting the DM dominance in the region inside the optical radius. [30]

The best current evidence for DM comes from the studies of the Bullet Cluster [31]. In this system of two galaxy clusters that have collided, the average position of the interacting visible matter has been found to be displaced with respect to the overall gravitational matter, which is estimated through gravitational lensing effects [32]. This is explained only if most of the matter in the clusters is collision-less, consistently with the existence of DM.

Through cosmological measurements [33] it was possible to estimate that DM constitutes approximately 85% of the matter in the universe. None of the particles and their interactions predicted in the SM can explain such DM composition in the universe.

1.2 Supersymmetry

SUSY is one of the most accredited and best studied extensions of the SM that have been proposed in the theoretical particle physics community. In SUSY a correspondence between all bosons and fermions is introduced by taking into account an operator, $\hat{Q}$, so that:

$$\hat{Q}\left|\text{Fermion}\right\rangle = \left|\text{Boson}\right\rangle, \qquad \hat{Q}\left|\text{Boson}\right\rangle = \left|\text{Fermion}\right\rangle. \tag{1.16}$$

SUSY offers a direct solution to the hierarchy problem (Section 1.1.5). A scalar, massive particle S would contribute to the determination of the Higgs mass through loops such as the one shown in Figure 1.5.

The loop in Figure 1.5 corresponds to a correction to Δm_H^2 of the form:

$$\Delta m_H^2 = \frac{\lambda_S}{16\pi^2}\Lambda_{\mathrm{UV}}^2 + \dots, \tag{1.17}$$

where λ_S is the coupling of S with the Higgs boson. If every fermion of the SM is accompanied by two complex scalars so that $\lambda_S = |\lambda_f|^2$, then the corrections of Equations 1.15 and 1.17

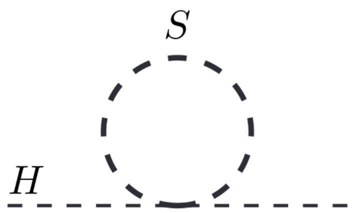

Figure 1.5: One-loop quantum corrections to the m_H^2 parameter due to the coupling of the Higgs boson with a massive scalar, S. [28]

mutually cancel, thus removing from the theory the dangerous divergences that cause the hierarchy problem. The organising principle that would lead to identities, such as $\lambda_S = |\lambda_f|^2$, can only stem from the occurrence of a *symmetry* relating fermions to bosons and vice versa. This symmetry is what is commonly referred to as *Supersymmetry*.

Equation 1.16 implies that the operator $\hat{Q}$ and its hermitian conjugate $\hat{Q}^\dagger$ are fermionic operators which carry spin 1/2. Moreover, $\hat{Q}$ and $\hat{Q}^\dagger$ must satisfy the anticommutation relation $\{\hat{Q}, \hat{Q}^\dagger\} \propto \hat{P}^\mu$, where $\hat{P}^\mu$ is the four-momentum generator of spacetime translations [28]. Single-particle states of SUSY theory thus fall into irreducible representations of the SUSY algebra, called *supermultiplets*. Each supermultiplet contains both bosons and fermions, which are called *superpartners*, such that the bosonic and fermionic degrees of freedom are the same.

Since both $\hat{Q}$ and $\hat{Q}^\dagger$ commute with the squared-mass operator, $-\hat{P}^2$, all particles belonging to the same supermultiplet are bound to have the same mass. Moreover, given that $\hat{Q}$ and $\hat{Q}^\dagger$ commute with the generators of the gauge transformations as well, particles in the same supermultiplet must also have the same quantum numbers, i. e. electric charges, weak isospins and color degrees of freedom [28].

1.2.1 The SUSY formalism

There are different possible ways to build a supermultiplet from SM particles and their superpartners. The simplest are:

- *chiral* or *matter* or *scalar* supermultiplet, containing a two-component Weyl fermion – which is either left- or right-handed – and a complex scalar field; this category is populated by all SM fermions, depending on their helicity, and their scalar superpartners generally called *sparticles*, e. g. *squarks* and *sleptons* are the scalar superpartners of quarks and leptons, respectively. The “s” in the naming convention indicates that these superpartners are scalar particles;

- *gauge* or *vector* or *real* supermultiplet, containing a combination of spin-1 SM gauge bosons and their spin-1/2 fermionic superparters which must share the same gauge transformation properties. The naming convention used to indicate the superpartners of vector bosons implies the addition of the suffix “ino” after the particle name, so that superpartners of SM gauge bosons are called *gauginos*, e. g. Wino and gluino.

Both sparticles and gauginos are commonly indicated with the same symbol as their SM counterpart capped with a tilde (e. g. $\widetilde{\ell}_L$ and $\widetilde{q}_L$ are the superpartners of a left-handed lepton and quark, respectively).

It follows that, with this distinction, the Higgs boson and its superpartner, the *higgsino*, must belong to a chiral supermultiplet. In order to avoid gauge anomalies that would make SUSY an inconsistent QFT, at least two separate Higgs supermultiplets with weak hypercharge $Y = +1/2$ and $Y = -1/2$, respectively, must be considered [28]. Only the $Y = +1/2$ Higgs chiral supermultiplet, H_u, has the Yukawa couplings necessary to give mass to up-type quarks, whereas the $Y = -1/2$ Higgs chiral supermultiplet, H_d, has the Yukawa couplings necessary to give mass to down-type quarks and charged leptons.

The simplest possible supersymmetric model, describing a free chiral supermultiplet, is represented by the massless, non-interacting *Wess-Zumino model* [34], with the following Lagrangian:

$$\mathcal{L}_{\text{free}} = -\partial^{\mu}\phi^{*i}\partial_{\mu}\phi_i + \psi^{\dagger i}\overline{\sigma}^{\mu}\partial_{\mu}\psi_i + F^{*i}F_i, \tag{1.18}$$

where: ψ is a left-handed two-component Weyl fermion; ϕ is its complex scalar superpartner; F is a complex scalar auxiliary field; $\sigma^{\mu} = (\sigma^0, \vec{\sigma})$ with σ^0 being the 2×2 identity and $\vec{\sigma}$ the three Pauli matrices; the index i runs over all gauge and flavour degrees of freedom. The last term in Equation 1.18 guarantees the on-shell and off-shell closing of the SUSY algebra [28].

A common procedure to formulate an interacting SUSY theory for chiral supermultiplets is to consider the most general set of renormalisable interactions which are still consistent with SUSY. It can be shown that these can be all expressed in terms of a single scalar holomorphic function of the scalar fields ϕ, called the *superpotential*, W:

$$W = \frac{1}{2}M^{ij}\phi_i\phi_j + \frac{1}{6}y^{ijk}\phi_i\phi_j\phi_k, \tag{1.19}$$

where M^{ij} is a mass matrix for the fermion fields and y^{ijk} is a Yukawa coupling between the scalar ϕ_k and two fermions ψ_i and ψ_j. The introduction of the superpotential allows to remove the dependency of the auxiliary fields, by considering their equation of motion $F_i = -W_i^*$. The interacting SUSY theory for chiral supermultiplets can then be expressed by considering the free Lagrangian in Equation 1.18 and then adding interacting terms which depend on the superpotential, namely $\mathcal{L}_{\text{chiral}} = \mathcal{L}_{\text{free}} + \mathcal{L}^{\text{int}}_{\text{chiral}}(W, \phi_i, \psi_i)$.

Similarly, the SUSY Lagrangian for gauge supermultiplets can be constructed following an analogous procedure:

$$\mathcal{L}_{\text{gauge}} = -\frac{1}{4}F^a_{\mu\nu}F^{\mu\nu}_a + i\lambda^{\dagger}_a\overline{\sigma}^{\mu}\nabla_{\mu}\lambda^a + \frac{1}{2}D^aD_a. \tag{1.20}$$

Here, the first term represents the kinetic term of the gauge boson field A^a_{μ}, λ^a is the two-component Weyl fermion of the gaugino, ∇_{μ} is the gauge-covariant derivative[4], and the index a runs over the adjoint representation of the gauge group. Once again, a term depending on the real bosonic auxiliary field D^a is added to ensure the off-shell consistency of the theory [28].

[4] Here, in order to indicate the gauge-covariant derivative, the ∇_{μ} is used instead of the previously-adopted D_{μ} notation to avoid confusion with the auxiliary field D^a.

As in the $\mathcal{L}_{\text{chiral}}$ case, the equation of motion of D^a removes the explicit dependency of the auxiliary fields from $\mathcal{L}_{\text{gauge}}$ by means of purely algebraic expressions of the scalar fields ϕ_i and the generators of the gauge group.

Finally, a fully-interacting renormalisable SUSY theory is obtained by considering the sum $\mathcal{L}_{\text{SUSY}} = \mathcal{L}_{\text{chiral}} + \mathcal{L}_{\text{gauge}}$. As a consequence, the interactions and masses of all particles are fully determined by considering their gauge transformation properties and the superpotential. Many supersymmetric models, called *supergravity* models, are also extended to include gravity, thus resulting in a non-renormalizable[5] QFT.

Soft SUSY breaking

As stated in the introduction of this Section, the fundamental properties of SUSY impose that SM particles and their superpartners must have the same mass. However, if that holds true then these additional particles would have already been discovered at the energies that are currently experimentally accessible. This implies that SUSY must be a *broken symmetry*. Since an unbroken SUSY is needed to achieve the cancellation required to solve the hierarchy problem (Equations 1.15 and 1.17), there must be a VEV chosen by nature that breaks SUSY, i. e. a SSB mechanism must be taken into account. Although there is currently no general consensus about the source for the SSB of SUSY, in order to still provide a solution to the hierarchy problem even in the presence of SUSY breaking, then the relationships between dimensionless couplings (i. e. λ_f and λ_S) that hold in an unbroken supersymmetric theory must be maintained. Therefore, it is necessary to consider a *"soft" SSB mechanism* for SUSY. This implies that the effective SUSY Lagrangian should be of the form $\mathcal{L}_{\text{SUSY}} + \mathcal{L}_{\text{soft}}$, where $\mathcal{L}_{\text{soft}}$ represents the explicit SUSY breaking Lagrangian term, which contains only mass terms and couplings with positive mass dimension. The largest mass scale at which the soft SSB can occur is $m_{\text{soft}} \simeq 1$ TeV [28]. This determines the estimated order of magnitude of the mass-splitting between the known SM particles and their superpartners. Regardless of the origin of the SSB, any $\mathcal{L}_{\text{soft}}$ term would dramatically increase the number of free parameters in the theory. However, it is believed that a fully-understood origin of SUSY breaking would act as an organizing principle in the theory reducing its degrees of freedom [35]. This topic is further discussed in Section 1.2.2.

1.2.2 The Minimal Supersymmetric Standard Model

The MSSM is the minimal supersymmetric extension of the SM in the sense that it predicts the smallest number of new particle states and new interactions consistent with phenomenology [28, 35]. This is realised by considering the chiral an gauge supermultiplets listed in Table 1.1.

[5] Non-renormalizable interactions can usually be neglected for most phenomenological purposes, since they must be proportional to powers of E/M_P, since gravitational effects start to become relevant at the Planck scale. Hence, at EWK energy scales (i. e. < 1 TeV) these contributions are expected to be small.

Table 1.1: Supermultiplets in the MSSM. The chiral supermultiplets for quarks and leptons are considered for all the three families. Hence the symbol "u" refers to u, d, t, "d" to d, s, b, "ν" to ν_e, ν_μ, ν_τ, and "ℓ" to e, μ, τ. [28]

Names and symbols		spin-0	spin-1/2	spin-1
Squarks, quarks	Q	$\left(\widetilde{u}_L, \widetilde{d}_L\right)$	$\left(u_L, d_L\right)$	-
	$\overline{u}$	$\widetilde{u}_R$	$\widetilde{u}_R$	-
	$\overline{d}$	$\widetilde{d}_R$	$\widetilde{d}_R$	-
Sleptons, leptons	L	$\left(\widetilde{\nu}_L, \widetilde{\ell}_L\right)$	$\left(\nu_L, \ell_L\right)$	-
	$\overline{\ell}$	$\widetilde{\ell}_R$	$\widetilde{\ell}_R$	-
Higgs, Higgsinos	H_u	$\left(H_u^+, H_u^0\right)$	$\left(\widetilde{H}_u^+, \widetilde{H}_u^0\right)$	-
	H_d	$\left(H_d^0, H_d^-\right)$	$\left(\widetilde{H}_d^0, \widetilde{H}_d^-\right)$	-
Gluinos, gluons		-	$\widetilde{g}$	g
Winos, W boson		-	$\widetilde{W}^\pm$, $\widetilde{W}^0$	$W^\pm$, W^0
Bino, B boson		-	$\widetilde{B}$	B

The gauge group of the MSSM is fixed to be the same as the one of the SM, which implies that the couplings of gauge interactions between SM particles and their superpartners have the same form as those predicted in the SM. Since the top quark, the bottom quark and the tau lepton are the heaviest fermions of the SM, the the superpotential (Equation 1.19) in the MSSM can be approximated with:

$$\begin{aligned} W_{\text{MSSM}} \simeq &+ y_t\left(\overline{t}tH_u^0 - \overline{t}bH_u^+\right) - y_b\left(\overline{b}tH_d^- - \overline{b}bH_d^0\right) \\ &- y_\tau\left(\overline{\tau}\nu_\tau H_d^- - \overline{\tau}\tau H_d^0\right) + \mu\left(H_u^+H_d^- - H_u^0H_d^0\right), \end{aligned} \tag{1.21}$$

where, μ is the Higgs mass parameter of the MSSM. Following the procedure outlined in Section 1.2.1, in order to complete the picture of the MSSM, it is necessary to consider a $\mathcal{L}_{\text{soft}}$ through which is possible to explain both the EWK and SUSY SSB:

$$\begin{aligned} \mathcal{L}_{\text{soft}}^{\text{MSSM}} = &-\frac{1}{2}\left(M_3\widetilde{g}\widetilde{g} + M_2\widetilde{W}\widetilde{W} + M_1\widetilde{B}\widetilde{B} + \text{h.c.}\right) \\ &-\left(\widetilde{\overline{u}}\mathbf{a_u}\widetilde{Q}H_u - \widetilde{\overline{d}}\mathbf{a_d}\widetilde{Q}H_d - \widetilde{\overline{\ell}}\mathbf{a}_\ell\widetilde{L}H_d + \text{h.c.}\right) \\ &-\widetilde{Q}^\dagger\mathbf{m_Q^2}\widetilde{Q} - \widetilde{L}^\dagger\mathbf{m_L^2}\widetilde{L} - \widetilde{\overline{u}}^\dagger\mathbf{m_{\overline{u}}^2}\widetilde{\overline{u}} - \widetilde{\overline{d}}^\dagger\mathbf{m_{\overline{d}}^2}\widetilde{\overline{d}} - \widetilde{\overline{\ell}}^\dagger\mathbf{m}_{\overline{\ell}}^{\mathbf{2}}\widetilde{\overline{\ell}} \\ &-m_{H_u}^2H_u^\dagger H_u - m_{H_d}^2H_d^\dagger H_d - \left(bH_uH_d + \text{h.c.}\right), \end{aligned} \tag{1.22}$$

where: $M_{1,2,3}$ are the gaugino mass parameters, $\mathbf{a}$ are the sfermion-higgsino tri-linear coupling matrices, $\mathbf{m^2}$ are the sfermion mass matrices, m_{H_u} and m_{H_d} are the higgsino mass parameters, and b is the higgsino bi-linear coupling. In order for $\mathcal{L}_{\text{soft}}^{\text{MSSM}}$ to satisfy the soft SSB condition, the value of all of these parameter must be of the order of $\sim m_{\text{soft}}$.

The Lagrangian with soft SUSY breaking introduces in the MSSM 105 new parameters with no counterpart in the SM and which cannot be rotated away by a redefinition of phases and supermultiplets [28, 35]. This implies a tremendous degree of arbitrariness of the theory. However, phenomenological constraints in the variability of such parameters can be imposed by suppressing CP-violating interactions, flavour-changing, lepton- and baryon- number non-conserving processes. Such conditions are realised by assuming the *soft SUSY breaking universality hypothesis*, in which squared-mass matrices are flavour-blind and mixing angles are rendered trivial in the tri-linear couplings, e. g.: $\mathbf{m_Q^2} = m_Q^2\mathbf{1}$, $\mathbf{a_u} = A_u\mathbf{y_u}$, $\mathrm{Im}\{M_{1,2,3}\} = \mathrm{Im}\{A_u\} = 0$, etc.

With this choice of parameters, as opposed to the SM (Figure 1.3), in the MSSM it is possible to achieve the unification of the SM gauge coupling, g_1, g_2 and g_3, as shown in Figure 1.6.

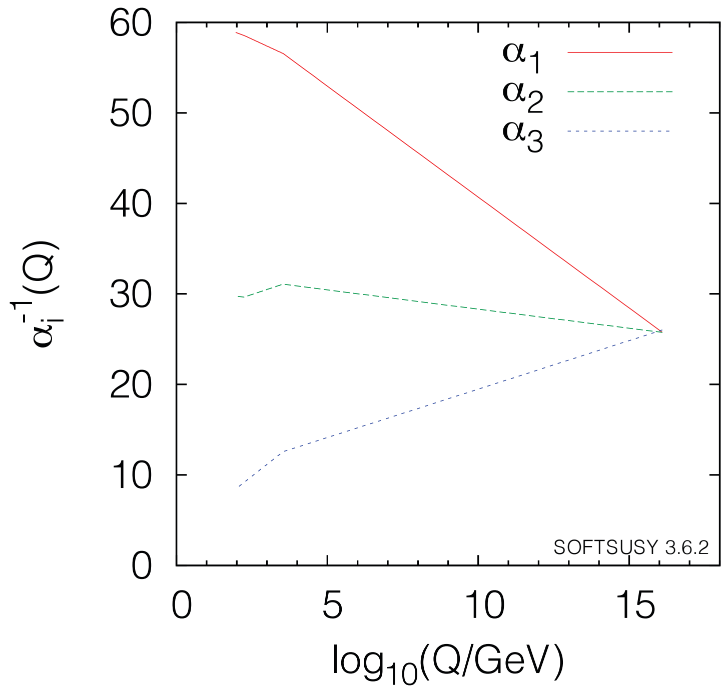

Figure 1.6: Running of the inverse gauge couplings, $\alpha^{-1}(Q)$, in the SM. α_1 corresponds to the $U(1)_Y$ gauge symmetry, α_2 to $SU(2)_L$, and α_3 to $SU(3)_C$. [5]

In particular, it can be shown that at the GUT scale:

$$\frac{M_1}{g_1^2} = \frac{M_2}{g_2^2} = \frac{M_3}{g_3^2} = \frac{m_{1/2}}{g_U^2}, \tag{1.23}$$

with $m_{1/2}$ being the *gaugino universal mass parameter*. Other consequences of the running of the gauge couplings include that fact that the $m^2_{H_u}$ parameter becomes negative near the EWK scale, destabilizing the $H_u = H_d = 0$ state, thus provoking the SSB of the EWK sector.

The SSB of SUSY, as in the EWK case, always implies the existence of a massless Goldstone boson, which in the MSSM case is a neutral Weyl fermion, called the *goldstino*, $\widetilde{G}$. However, it can be shown that none of the particles of the MSSM can produce the necessary conditions to provoke the SSB of SUSY. The soft breaking of SUSY must, therefore, occur in a *hidden sector*, which "communicates" with the visible sector of the chiral and gauge supermultiplets of the MSSM through dedicated mediators depending of the model taken into account. The proposed models for soft SUSY braking include: the *gauge-mediated* [36], the *extra-dimension-mediated* [37] and the *gravity-mediated* or *Planck-scale-mediated* (PMSB) SUSY breaking [38, 39]. In the latter, the nature of the invisible interactions is gravitational. In a supersymmetric theory of gravity, or *supergravity* (SUGRA), the spin-2 mediator, the graviton, has a fermionic spin-3/2 superpartner named *gravitino*. Once SUSY is spontaneously broken, the gravitino acquires mass by absorbing the degrees of freedom of the goldstino (*super-Higgs mechanism*) [28]. Hence, the $\mathcal{L}_{\text{soft}}^{\text{MSSM}}$ becomes fully determined by considering only the following free parameters at the M_P scale: the universal gaugino mass $m_{1/2}$, the universal scalar (sfermion) mass m_0, the universal tri-linear coupling A_0, and the Higgs mass parameter $b = B_0\mu$. This framework represents the bulk of phenomenological studies and searches for SUSY in collider experiments. It is sometimes referred to as *minimal Supergravity* (mSUGRA) or *constrained MSSM* (cMSSM).

The MSSM mass spectrum

The mass spectrum of the particles in the MSSM is obtained by fixing the four soft SUSY SSB parameters, discussed in the previous Section, and by considering the EWK symmetry breaking. Similarly to the SM, a mixing occurs between the flavour eigenstates of the particles that share similar quantum numbers to form other mass eigenstates.

Higgs bosons Starting from the two Higgs doublets of the MSSM, $H_u = (H_u^+, H_u^0)$ and $H_d = (H_d^0, H_d^-)$, it is possible to show that the stable minimum of the Higgs scalar potential can be reached setting $H_u^+ = 0$ and $H_d^- = 0$. This leads to the introduction of two VEVs, corresponding to the neutral components of the two Higgs doublets, namely $v_u = \left\langle H_u^0 \right\rangle_0$ and $v_d = \left\langle H_d^0 \right\rangle_0$. These are related to each other and to the gauge parameters of the SM through the relations $v_u^2 + v_d^2 = v^2 = 2m_Z^2/(g^2 + g'^2) \simeq (174\,\text{GeV})^2$ and $\tan\beta = v_u/v_d$. When the EWK symmetry is broken, out of the eight degrees of freedom of the two complex, scalar Higgs doublets, three give rise to Goldstone bosons, which, in turn, become the longitudinal polarisations of the massive $W^\pm$ and Z bosons. The remaining five form the mass eigenstates of five different Higgs bosons: two CP-even neutral scalars h and H^0, one CP-odd neutral scalar A^0, and two charged scalars $H^\pm$. By convention, h is the lightest Higgs boson. It presents many phenomenological affinities with the SM Higgs boson to which is, thus, identified [28]. Henceforth, the SM Higgs boson is indicated with the h symbol.

Charginos and neutralinos Due to the EWK symmetry breaking, higgsinos and gauginos have analogous quantum numbers. Hence, their flavour eigenstates are mixed to give rise to corresponding mass eigenstates. The neutral gauginos and higgsinos combine to form *neutralinos*, $\widetilde{\chi}_i^0$ $(i = 1,2,3,4)$, whereas charged gauginos and higgsinos combine to form *charginos*, $\widetilde{\chi}_j^\pm$ $(j = 1,2)$. The subscripts indicate the ascending order of the value of their masses, namely: $m_{\widetilde{\chi}_1^0} < m_{\widetilde{\chi}_2^0} < m_{\widetilde{\chi}_3^0} < m_{\widetilde{\chi}_4^0}$ and $m_{\widetilde{\chi}_1^\pm} < m_{\widetilde{\chi}_2^\pm}$. Considering the typically assumed soft SUSY breaking parameters, the flavour composition of charginos and neutralinos can become unbalanced towards a particular flavour. In particular, with the $M_1 \sim 0.5M_2 < |\mu|$ choice, their mass eigenstates are very nearly: a “Bino-like” $\widetilde{\chi}_1^0 \sim \widetilde{B}$, “Wino-like” and nearly mass-degenerate $\widetilde{\chi}_2^0 \sim \widetilde{W}^3$ and $\widetilde{\chi}_1^\pm \sim \widetilde{W}^\pm$, and “higgsino-like” $\widetilde{\chi}_3^0, \widetilde{\chi}_4^0 \sim |\mu| \sim (\widetilde{H}_u^0 \pm \widetilde{H}_d^0)/\sqrt{2}$.

Squarks and sleptons In general, the universality hypothesis of flavour-blind soft parameters prevents large mixing effects to occur in the squark and slepton sector. After the EWK SSB, these are expected to be all proportional to the m_0 parameter. However, because of their large Yukawa and tri-linear couplings, the third family of squarks and the sleptons mix to form the mass eigenstates $\widetilde{t}_i$, $\widetilde{b}_i$ and $\widetilde{\tau}_i$ ($i = 1,2$). In contrast the masses of the remaining sfermions of the same family are nearly degenerate.

A summary of the mass eigenstates of the MSSM is reported in Table 1.2.

Table 1.2: Gauge and mass eigenstates of the particles in the MSSM. [28]

Names	Spin	Gauge eigenstates	Mass eigenstates
Higgs bosons	0	H_u^0, H_d^0, H_u^+, H_u^-	h, H^0, A^0, $H^\pm$
squarks	0	$\widetilde{u}_L$, $\widetilde{u}_R$, $\widetilde{d}_L$, $\widetilde{d}_R$	(same)
		$\widetilde{c}_L$, $\widetilde{c}_R$, $\widetilde{s}_L$, $\widetilde{s}_R$	(same)
		$\widetilde{t}_L$, $\widetilde{t}_R$, $\widetilde{b}_L$, $\widetilde{b}_R$	$\widetilde{t}_1$, $\widetilde{t}_2$, $\widetilde{b}_1$, $\widetilde{b}_2$
sleptons	0	$\widetilde{e}_L$, $\widetilde{e}_R$, $\widetilde{\nu}_e$	(same)
		$\widetilde{\mu}_L$, $\widetilde{\mu}_R$, $\widetilde{\nu}_\mu$	(same)
		$\widetilde{\tau}_L$, $\widetilde{\tau}_R$, $\widetilde{\nu}_\tau$	$\widetilde{\tau}_1$, $\widetilde{\tau}_2$, $\widetilde{\nu}_\tau$
neutralinos	1/2	$\widetilde{B}$, $\widetilde{W}^3$, $\widetilde{H}_u^0$, $\widetilde{H}_d^0$	$\widetilde{\chi}_1^0$, $\widetilde{\chi}_2^0$, $\widetilde{\chi}_3^0$, $\widetilde{\chi}_4^0$
charginos	1/2	$\widetilde{W}^\pm$, $\widetilde{H}_u^+$, $\widetilde{H}_d^-$	$\widetilde{\chi}_1^\pm$, $\widetilde{\chi}_2^\pm$
gluinos	1/2	$\widetilde{g}$	(same)
goldstino (gravitino)	1/2 (3/2)	$\widetilde{G}$	(same)

Gluinos are a separate case compared to the remaining gauginos, since they form a color-octet of fermions and, therefore, cannot mix with any other particle in the MSSM. According to the majority of SUSY breaking model, the gluino mass parameter, M_3, is related to the other gaugino masses near the TeV scale, in a $M_3 : M_2 : M_1 \sim 6 : 2 : 1$ proportion. Hence, it is reasonable to suspect that the gluinos are considerably heavier than the neutralinos and charginos [28].

1.2.3 R-Parity

The general form of the superpotential (Equation 1.19) admits terms that explicitly violate the the total baryon number, B, and lepton number, L. In principle, there is no reason to build a SUSY theory which requires the absolute conservation of B and L. However, in order to be consistent with phenomenological observations, such as the search for proton decays [40], these can be required in the MSSM by imposing the conservation of the *R-Parity* [41], P_R, defined as:

$$P_R = (-1)^{3(B-L)+2s}, \tag{1.24}$$

where s is the spin of the particles. All SM particles and the Higgs bosons carry even R-parity ($P_R = +1$), whilst all the sparticles (squarks, sleptons, gauginos and higgsinos) have odd

R-parity ($P_R = -1$). The conservation of R-Parity implies that the B- and L-violating terms in the superpotential would be forbidden and, therefore, cancelled.

Other important phenomenological consequences follow from the requirement of the conservation of R-Parity:

- the *Lightest Supersymmetric Particle* (LSP), must be stable. If the LSP is electrically neutral, it interacts only weakly with ordinary matter, thus, providing an excellent candidate for the non-baryonic, cold DM. In mSUGRA and many other SUSY breaking models, such a particle is the $\tilde{\chi}_1^0$ or $\tilde{G}$;
- Each sparticle other than the LSP must eventually decay into a state with an odd number of LSPs, i. e. typically one;
- In collider experiments, sparticles can only be produced in even numbers, i. e. in pairs.

1.2.4 The MSSM phenomenology at hadron colliders

Many searches for SUSY are currently being carried out in hadron collider experiments. This Section outlines the main phenomenological implications of the MSSM, focusing on the types of experimental signatures that the production of SUSY particles generates in experiments such as ATLAS.

Production channels

Taking into account an R-Parity-conserving MSSM and assuming mSUGRA or a similar model to hold, at hadron colliders sparticles can be produced in pairs from hard scattering processes (Section 1.2.3). These can occur with either QCD or EWK strength. The main processes occurring as a result of a p-p collision via the strong interaction, collectively referred to as *strong SUSY*, are:

$$gg \to \tilde{g}\tilde{g}, \tilde{q}\tilde{q}^*, \quad gq \to \tilde{g}\tilde{q}, \quad q\bar{q} \to \tilde{g}\tilde{g}, \tilde{q}\tilde{q}^*, \quad qq \to \tilde{q}\tilde{q}^*. \tag{1.25}$$

On the other hand, production channels which involve EWK couplings, collectively called *EWK SUSY*, include:

$$q\bar{q} \to \tilde{\chi}_i^+\tilde{\chi}_j^-, \tilde{\chi}_i^0\tilde{\chi}_j^0, \quad q\bar{q}' \to \tilde{\chi}_i^\pm\tilde{\chi}_j^0, \tag{1.26}$$

$$q\bar{q} \to \tilde{\ell}_{L,R}^+\tilde{\ell}_{L,R}^-, \tilde{\nu}\tilde{\nu}^*, \quad q\bar{q}' \to \tilde{\ell}_L^\pm\tilde{\nu}^{(*)}, \tag{1.27}$$

where the subscripts i and j represent the mass indices of charginos and neutralinos. Regarding the slepton pair production (Equation 1.27), the superpartners of either the left- or right-handed charged leptons can be produced. On the other hand, sneutrinos are assumed to be mostly just the superpartners of left-handed neutrino, since the right-handed sneutrino masses are expected to be so heavy that the mixing with the left-handed sneutrinos is irrelevant at EWK energy scales [42]. The analyses described in this thesis (Chapters 4, 5, and 6) all take into account the direct EWK production of mostly Wino-like charginos and neutralinos, i. e. $pp \to \tilde{\chi}_1^{\pm}\tilde{\chi}_2^0$.

Estimated values of the production cross-section at $\sqrt{s} = 13$ TeV p-p collisions of the channels listed above are shown in Figure 1.7.

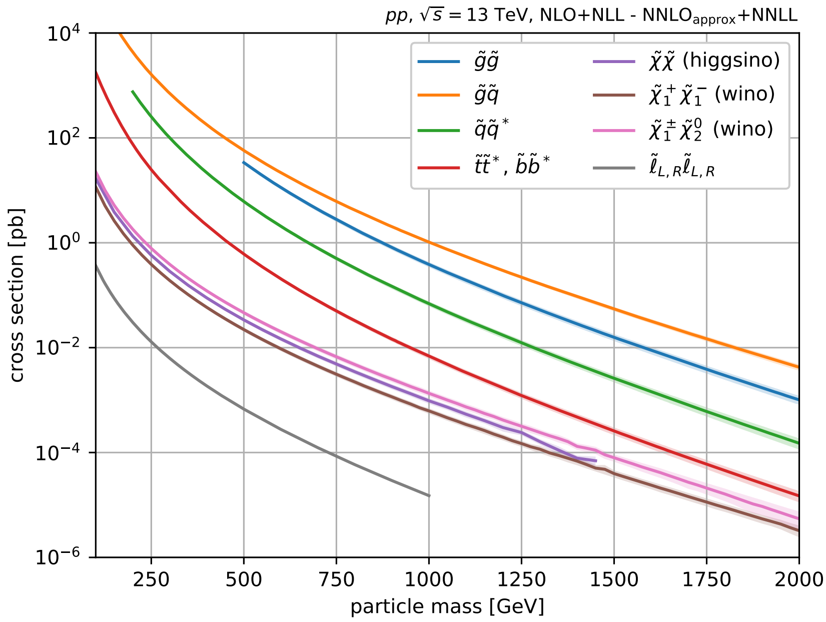

Figure 1.7: Typical cross-sections for the main SUSY production modes as a function of their masses in p-p collisions at $\sqrt{s} = 13$ TeV . [43]

In general, the production cross-sections increase with the centre-of-mass energy of the p-p collision and steeply fall with the increase of the mass of the sparticles produced. Strong production modes involving gluinos and squarks are dominant with respect to EWK SUSY productions. However, if very high gluino, stop and sbottom masses are considered (i. e. ~ 1 TeV) along with relatively light neutrinos and charginos (i. e. ~ 100 GeV), then the EWK production of the latter becomes the dominant SUSY production mechanism at hadron colliders.

Decay modes

The decay modes of the particles in the MSSM largely depend on the strength of their couplings and on the assumed mass hierarchy. Moreover, imposing the conservation of R-Parity restricts the possibilities in which SUSY particles can decay, e. g. to processes with vertices in Feynman diagrams which presents an outgoing sparticle for each incoming sparticle.

For what concerns neutralinos and charginos, since they are mixed states of gauginos and higgsinos and they couple to other particles via the EWK interaction, their decay can give rise to a large number of possibilities for the final state. Assuming that R-Parity is conserved, the dominant two-body decay modes are:

$$\tilde{\chi}_i^0 \to Z\tilde{\chi}_j^0,\, W^{\pm}\tilde{\chi}_j^{\mp},\, h\tilde{\chi}_j^0,\, \ell\tilde{\ell},\, \nu\tilde{\nu}, \tag{1.28}$$

$$\widetilde{\chi}_i^{\pm} \to W^{\pm}\widetilde{\chi}_j^0, Z\widetilde{\chi}_j^{\pm}, h\widetilde{\chi}_j^{\pm}, \ell\widetilde{\nu}, \nu\widetilde{\ell}, \tag{1.29}$$

where $j < i$. If sleptons are lighter than charginos and neutralinos, the decay of the latter to sleptons are favoured. Otherwise, decays to gauge and Higgs boson dominate. In this thesis, particular focus is given to the $\widetilde{\chi}_1^{\pm} \to W^{\pm}\widetilde{\chi}_1^0$ and $\widetilde{\chi}_2^0 \to Z\widetilde{\chi}_1^0, h\widetilde{\chi}_1^0$ decays, in which $\widetilde{\chi}_1^0$ is assumed to be the LSP.

Once the decays of charginos and neutralinos are known, those of sleptons can be deduced as well:

$$\widetilde{\ell}^{\pm} \to \ell^{\pm}\widetilde{\chi}_i^0, \widetilde{\nu}\widetilde{\chi}_i^{\pm}, \quad \widetilde{\nu} \to \nu\widetilde{\chi}_i^0, \ell^{\pm}\widetilde{\chi}_i^{\mp}. \tag{1.30}$$

For what concerns squarks, if kinematically allowed, the decay $\widetilde{q} \to q\widetilde{g}$ usually dominates, since it involves a vertex with a QCD coupling. A peculiar case is that involving the lightest stop, $\widetilde{t}_1$. Since in many mass hierarchy scenarios $\widetilde{t}_1$ is the lightest squark, its decay with QCD strength might not be kinematically allowed, so that EWK processes – e. g. $\widetilde{t}_1 \to t\widetilde{\chi}_1^0$ or $\widetilde{t}_1 \to b\widetilde{\chi}_1^{\pm}$ – become relevant. Finally, the only possibility for gluino decays is via the strong process $\widetilde{g} \to g\widetilde{q}$.

Simplified models

As stated previously, particular choices of MSSM free parameters, along with those related to the Higgs sector, characterise the possible production modes and decay channels of the various SUSY particles. Taking into account, for example, mSUGRA models with the soft SUSY breaking universality hypothesis and the conservation of R-Parity, it is possible to dramatically constrain the degree of arbitrariness of the theory. However, even in this case, in which the theory free parameters are m_0, $m_{1/2}$, $\tan\beta$, μ and A_0 (Section 1.2.2), the number degrees of freedom remains very high from a phenomenological point of view. Hence, experimental searches for SUSY become extremely challenging, due to the inability to design a search that would probe all the free parameters of the theory simultaneously.

For this reason, SUSY searches are often carried out by taking into accout *simplified models* [44, 45]. These correspond to specific choices of the values of the free parameters, which further constrain the variability of the SUSY model being tested, thus, enabling an experimental search to set bounds on a smaller set of parameters. The choice for the parameters values in simplified models usually leads to considering, for instance, determined flavour compositions of the gauginos, and/or to assumptions on decays with 100% Branching Ratio (BR) of certain intermediate states.

In this thesis, the simplified models taken into account consider that $\widetilde{\chi}_2^0$ and $\widetilde{\chi}_1^{\pm}$ are mostly Wino-like and mass-degenerate, whilst the LSP, $\widetilde{\chi}_1^0$, is almost purely Bino-like. 100% BR for the decays of these particles to W, Z and h are also considered, so that the overall cross-section for these processes is simply given by the direct Wino-like $\widetilde{\chi}_1^{\pm}\,\widetilde{\chi}_2^0$ production, reported with the pink line of Figure 1.7, and it is, thus, only dependent on $m_{\widetilde{\chi}_1^{\pm}/\widetilde{\chi}_2^0} \doteq m_{\widetilde{\chi}_1^{\pm}} = m_{\widetilde{\chi}_2^0}$. Further details on the studied simplified models are given in Sections 4.1, 5.1 and 6.1.

1.3 Electroweak SUSY searches

Several searches for SUSY, taking into account different production mechanisms and simplified models, are currently carried out by both the ATLAS and CMS Collaborations. The bulk of these searches targets the MSSM and R-Parity-conserving scenarios for what concerns both strong and EWK production scenarios.

At the time of writing, searches involving the strong production of gluinos have been carried out by the ATLAS [46] and CMS [47] experiments. Similarly, searches targeting the direct strong production of the lightest stop quark have also been performed [48, 49, 50, 51]. A summary of the current (as of March 2021) 95% CL exclusion limits (see Section 4.5.1) for strong SUSY models concerning the gluino pair production obtained by the ATLAS experiment is shown in Figure 1.8 [52].

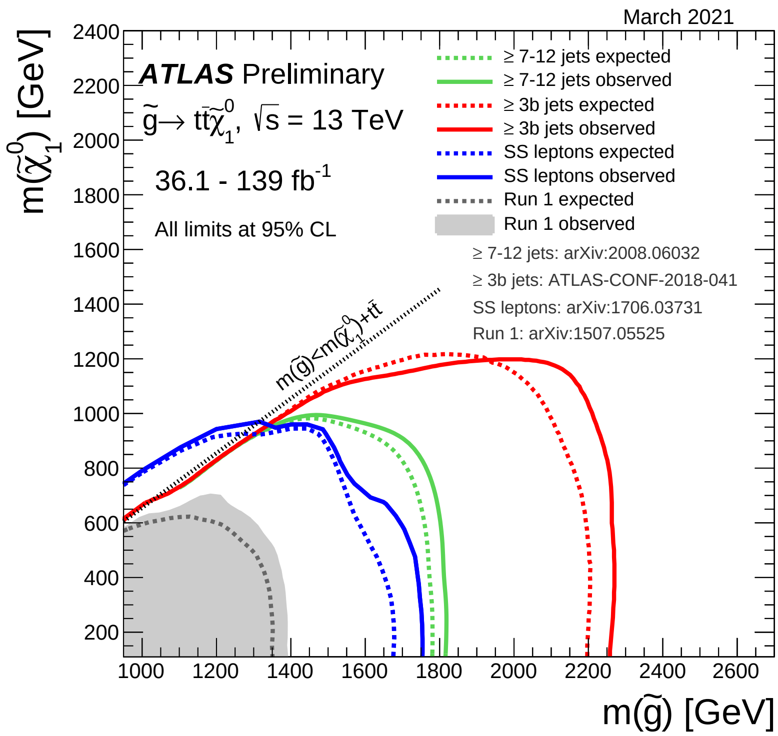

Figure 1.8: Observed and expected exclusion limits at 95% CL on $m_{\tilde{g}}$ and $m_{\tilde{\chi}_1^0}$ obtained with the ATLAS experiment as of March 2021. The dataset used corresponds to 36.1 fb^{-1} and 139 fb^{-1} data from $\sqrt{s}$ = 13 TeV p-p collisions collected with the ATLAS detector. [52]

Similarly, searches have also been conducted concerning EWK SUSY production mechanisms. In particular, both ATLAS and CMS have produced exclusion limits for the masses of electroweakly-produced sleptons [53, 54] and charginos/neutralinos [55, 56]. These searches show that in the vast majority of the simplified models involving strong SUSY production scenarios the masses of squarks and gluinos are excluded up to the ~ TeV scale, i. e. $m_{\tilde{t}_1}$ up to ~ 1.2 TeV and $m_{\tilde{g}}$ up to ~ 2.2 TeV (for massless LSPs).

On the other hand, the sensitivity of several EWK SUSY searches that have been carried out does not cover an equally significant portion of the phase-space compared to strong SUSY searches. As a consequence, the current bounds on electroweakly-produced sparticles, e. g. gauginos and sleptons, for several simplified models often do not exclude their masses beyond the TeV scale. Considering the very high existing constraints on the masses of strongly-coupled SUSY particles and the predicted SUSY production cross-section (Figure 1.7), the EWK productions of sparticles might be the dominant mechanism for producing SUSY at hadron colliders. This would increase the likelihood of discovering SUSY at experiments such as ATLAS and CMS. This represents a strong motivation for carrying out EWK SUSY searches at the LHC, such as those targeting $\tilde{\chi}_1^{\pm}\ \tilde{\chi}_1^0$ direct production. The various decay modes of the gauginos (Equations 1.28-1.29) and sleptons (Equations 1.30) lead to a wide variety of final states, including multileptonic final states. This allows to probe the available phase-space extensively, especially in scenarios where MSSM mass hierarchy predicts a small mass difference between the gauginos/sleptons ("compressed mass" scenarios).

1.3.1 $\tilde{\chi}_1^{\pm}\tilde{\chi}_2^0 \to Wh\tilde{\chi}_1^0\tilde{\chi}_1^0$ and $\tilde{\chi}_1^{\pm}\tilde{\chi}_2^0 \to WZ\tilde{\chi}_1^0\tilde{\chi}_1^0$ simplified models

The primary focus of this thesis is on the searches of the EWK production of $\tilde{\chi}_1^{\pm}$ and $\tilde{\chi}_2^0$, each decaying to a $\tilde{\chi}_1^0$ and a SM boson (gauge or Higgs bosons). In particular, the following R-Parity-conserving decays with 100% BR are considered: $\tilde{\chi}_1^{\pm} \to W^{\pm}\tilde{\chi}_1^0$, $\tilde{\chi}_2^0 \to Z\tilde{\chi}_1^0$ and $\tilde{\chi}_2^0 \to h\tilde{\chi}_1^0$. These simplified models are represented by the the diagrams in Figure 1.9.

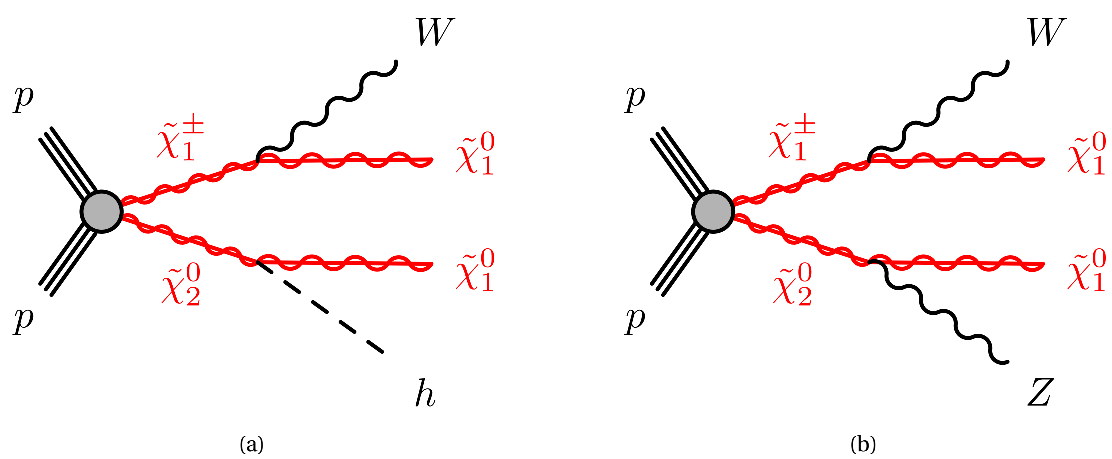

Figure 1.9: Diagram for the simplified model relative to the EWK production of $\tilde{\chi}_1^{\pm}\ \tilde{\chi}_2^0$ decaying to $\tilde{\chi}_1^0\ \tilde{\chi}_1^0$ and (a) W and Higgs bosons, and (b) W and Z bosons.

Models involving the production of W and Higgs bosons (Figure 1.9a) are here referred to as *Wh models*, whilst those with W and Z bosons (Figure 1.9b) are called *WZ models*. Leptonic final states arising from the decays of the W, Z and h bosons are taken into account. In particular, this thesis focuses on final states with either two light-leptons (electrons and/or muons) of the same electrical charge (same-sign), or three light-leptons. More details about these simplified models are given in Sections 4.1 and 5.1.

Earlier searches in the considered final states were carried out in the past by the ATLAS Collaboration. Prior to the work described in this thesis, the available limits on the masses of the charginos and neutralinos involved in these simplified models were the ones shown in Figures 1.10 [57] and 1.11 [58].

Seeing how less stringent these limits are compared to the bounds on the masses of strongly-produced SUSY particles (e. g. those reported in Figure 1.8), represents a compelling motivation for extending these results using the larger dataset from $\sqrt{s}$ = 13 TeV p-p collisions (i. e. 139 fb^{-1} data). These searches are described in Chapters 4, 5 and 6. The core of this thesis presents analyses from searches in which I have had a major or leading involvement, and which represent their state-of-the-art at the time of writing.

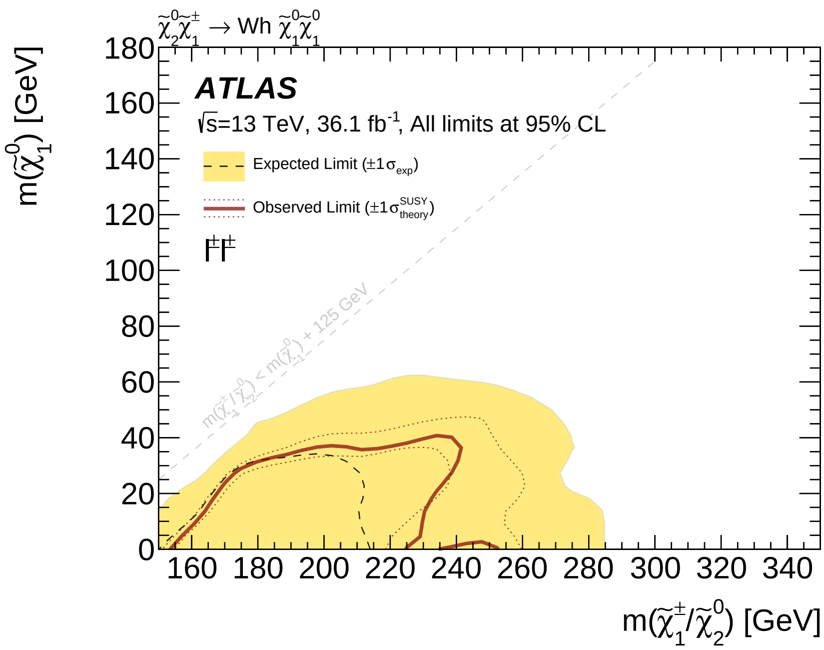

Figure 1.10: Observed (red solid line) and expected (dashed black line) exclusion limits at 95% CL on $m_{\tilde{\chi}_1^\pm,\tilde{\chi}_2^0}$ and $m_{\tilde{\chi}_1^0}$ for the Wh model with decays into a final state with two same-sign leptons using the dataset corresponding to 36.1 fb^{-1} data from $\sqrt{s}$ = 13 TeV p-p collisions collected with the ATLAS detector. The yellow band represents $\pm1\sigma$ total uncertainty on the expected result, whereas the dotted red lines represent $\pm1\sigma$ on the signal cross-section. [57]

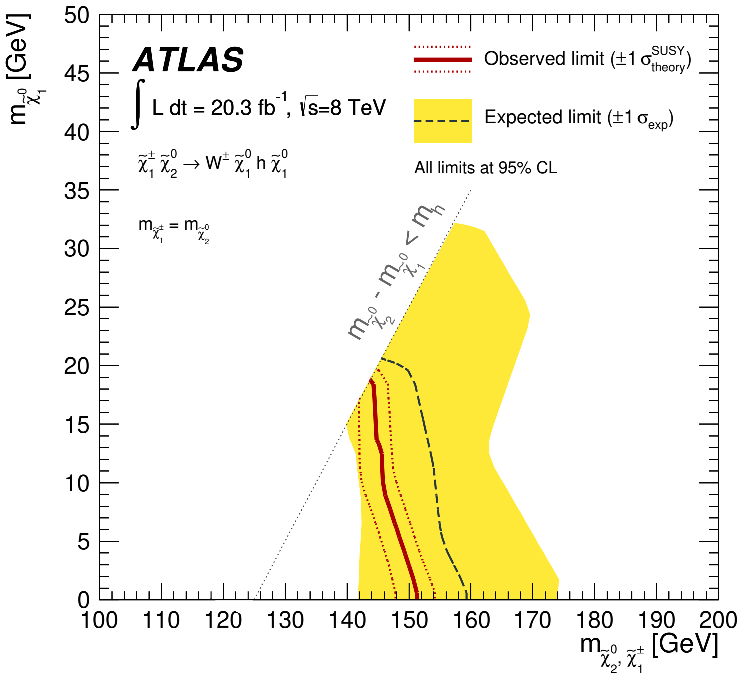

(a)

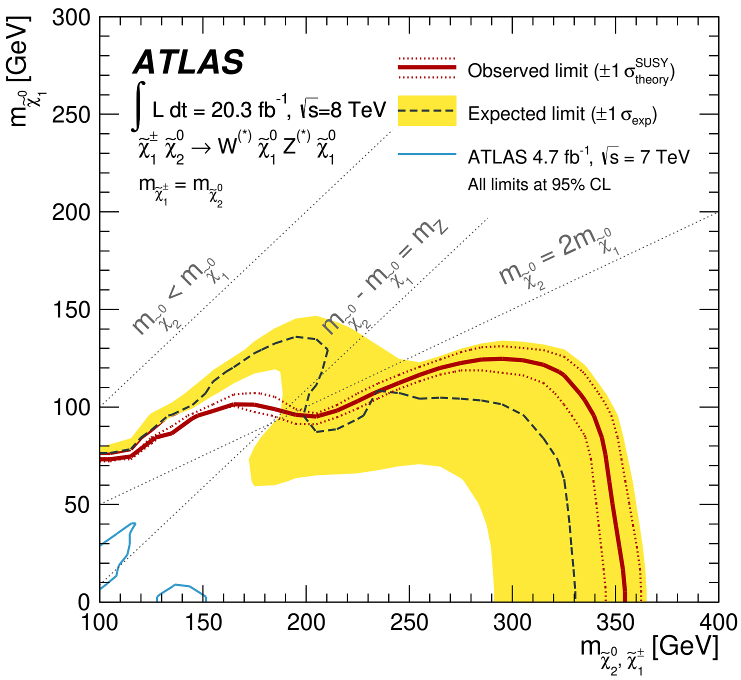

(b)

Figure 1.11: Observed (red solid line) and expected (dashed black line) exclusion limits at 95% CL on $m_{\tilde{\chi}_1^{\pm},\tilde{\chi}_2^0}$ and $m_{\tilde{\chi}_1^0}$ for the (a) Wh and (b) WZ model with decays into a final state with three leptons using the dataset corresponding to $20.3\,\mathrm{fb}^{-1}$ data from $\sqrt{s} = 8$ TeV p-p collisions collected with the ATLAS detector. The yellow band represents $\pm1\sigma$ total uncertainty on the expected result, whereas the dotted red lines represent $\pm1\sigma$ on the signal cross-section. [58]

The ATLAS experiment at the LHC

2

The pursuit of scientific advancement has often been a remarkable driving force for humankind to push the limits of technological advancement. To date, the LHC is arguably the most advanced experimental apparatus to explore the frontiers of high energy particle physics. This chapter is devoted to the description of the LHC and one of its main experiments, ATLAS (A Toroidal LHC ApparatuS), which was used to collect the data used in this thesis. Particular focus is given to the description of the ATLAS Inner Detector Trigger System and the measurement of its performance which has been the main objective of the "qualification task" that I have undertaken to become an author of the *ATLAS Collaboration*.

2.1 The Large Hadron Collider

The LHC [59] is the largest and most powerful circular particle collider ever built. It is installed at the European Organization for Nuclear Research (CERN) and it mainly consists of two underground rings, each with a 26.7 km circumference, located across the French-Swiss border near Geneva. The two rings are hosted in a pre-existing tunnel which lays between 50-175 m below the surface and which was originally built to house the LEP machine [60]. The LHC is designed to operate accelerating two counter-rotating beams of protons or, in special runs, heavy ions. The basic layout of the LHC is organised in octants, each containing alternate straight and arc sections. Each of the eight straight sections is approximatively 528 m long and allocates either a collision experiment or various utilities, e. g. beam injection, dumping, and cleaning. There are four beam crossings corresponding to the four main experiments: ATLAS [61] and CMS (Compact Muon Solenoid) [62] are general purpose experiments, and their vast physics program spans from SM measurements to BSM searches; LHCb (LHC beauty) [63] focuses on the study of the properties and the decays of the B-mesons, the investigation of CP violation, along with BSM searches in rare decays; ALICE (A Large Ion Collider Experiment) [64] is mainly dedicated to the study of the quark-gluon plasma state of matter via heavy-ion collisions.[1] The remaining four straight insertions are equipped with: collimation, Radio-Frequency (RF), and

[1] Other smaller experiments – TOTal cross section, Elastic scattering and diffraction dissociation Measurement at the LHC (TOTEM) [65], Monopole & Exotics Detector At the LHC (MoEDAL) [66] and LHC forward (LHCf) [67] – are located in correspondence of the existing, larger experiments and are dedicated to specialised research.

beam-abort systems. The 106.9 m long arcs of the LHC house the cryostats – operating at a temperature of 1.9 K – and the superconducting magnetic circuit, whose dipoles reach a nominal magnetic field of 8.33 T [59].

After being commissioned in 2010, the experiments at the LHC have collected data over two main periods, referred to as *Run 1* (2010-2012) and *Run 2* (2015-2018), respectively. Each Run was followed by two *Long Shutdown (LS)* periods – *LS1* (2012-2015) and *LS2* (2018-2022) – in which technical upgrades and general maintenance to the experimental apparatus were undertaken. Proton-proton collisions in Run 1 were collected initially at a centre-of-mass energy of 7 TeV , later increased to 8 TeV . Run 2 data were collected at 13 TeV . The amount of data collected in Run 1 and Run 2 will be mentioned hereafter in the text. At the time of writing this thesis, the commissioning of the upcoming *Run 3* (foreseen for 2022-2024) – which will see a progressive increase of the beam energies and intensities [68] – is ongoing.

2.1.1 The acceleration complex

In order to achieve the required energy for each beam, beam particles follow a specific acceleration procedure before being injected into the main LHC ring. Figure 2.1 shows a schematic representation of the CERN acceleration complex.

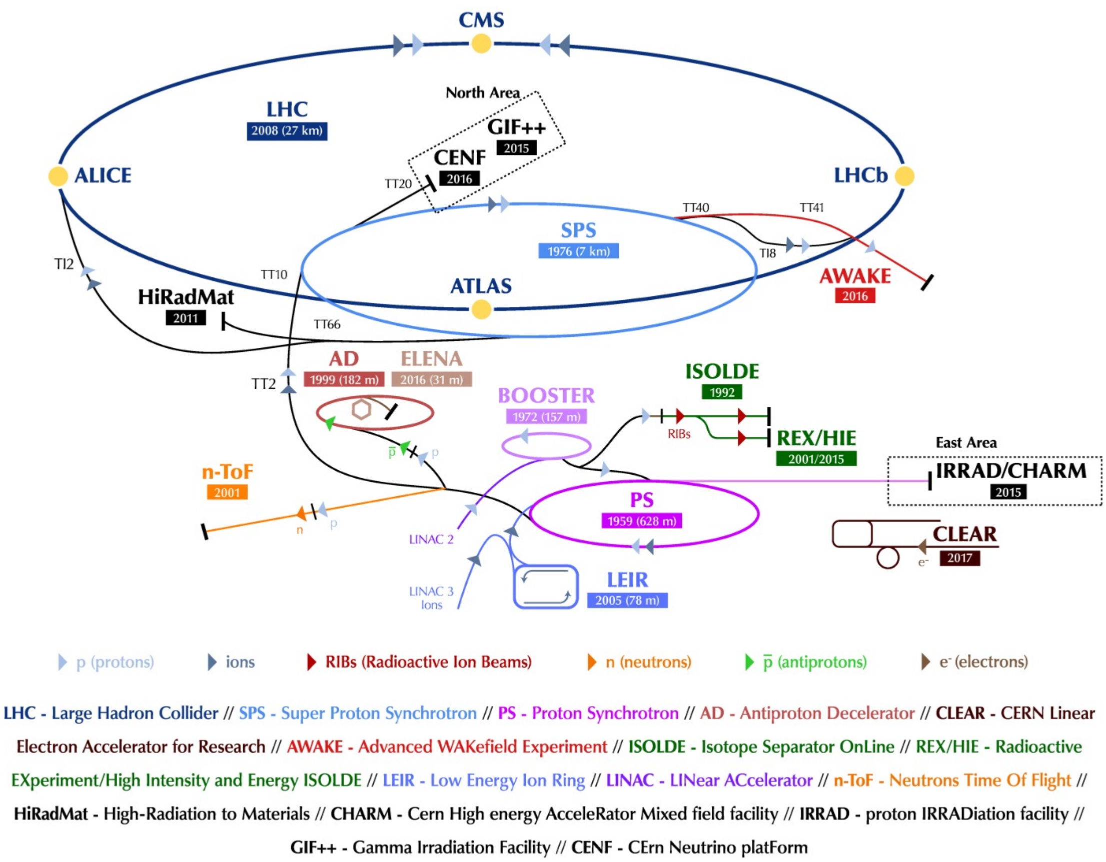

Figure 2.1: Schematic representation of the CERN acceleration complex. [69]

Protons, obtained from the ionisation of hydrogen atoms, are initially accelerated to 50 MeV through a linear RF acceleration system – Linear Accelerator 2 (LINAC2) – and then transferred to the Proton Synchrotron Booster (PSB) ring, where they are accumulated and accelerated to 1.4 GeV before being injected into the Proton Synchrotron ring. The latter accelerates the beam to 26 GeV and transfers them to the Super Proton Synchrotron (SPS), where the energy of 450 GeV is achieved. Finally, the bunches are injected in the two rings of the LHC, obtaining two counter-rotating beams each reaching the energy of 6.5 TeV , as of the end of Run 2.

2.1.2 The LHC parameters and performance

Due to the RF structure of the acceleration procedure, the two proton beams are organised in *bunches* with a nominal bunch-spacing of 25 ns [70].

The production rate $R(t)$ for a given process with cross-section σ can be quantified as:

$$R(t) = \sigma \cdot \mathscr{L}(t). \tag{2.1}$$

The quantity $\mathscr{L}(t)$ is the *instantaneous luminosity* which is time-dependent and it is related to the intensities of the beams through the following relation [71]:

$$\mathscr{L} = \frac{N_1 N_2 f}{4\pi\sigma_x\sigma_y}, \tag{2.2}$$

where N_1 and N_2 are the number of particles in beams 1 and 2, respectively, f is the beam revolution frequency, and the σ_x and σ_y are the horizontal and vertical widths of the two beams on the transverse plane. In order to get statistically significant physical measurements, especially of rare processes, it is essential to have high enough luminosity. However, many experimental limitations – beam-beam interactions, magnetic field oscillations, collective beam effects [59] – result in various luminosity instabilities. Furthermore, the instantaneous luminosity is intrinsically not constant over time due to the degradation of intensities and the emittance of the colliding beams. Integrating $\mathscr{L}(t)$ over one luminosity run of time duration, T_{run}, gives:

$$L = \int_0^{T_{\text{run}}} \mathscr{L}(t)\, dt, \tag{2.3}$$

where L is the *integrated luminosity*, also commonly used for quantifying the amount of data collected over a given period of time.

In the ATLAS experiment the luminosity is measured and monitored with the LUCID-2 Cherenkov detector [72, 73]. The highest instantaneous luminosity ever measured during Run 2 by the ATLAS experiment is 2×10^{34} cm^{-2} s^{-1} [70]. Figures 2.2a and 2.2b show the cumulative integrated luminosity collected by the ATLAS experiment during each year of Run 1 and Run 2, and overall in Run 2, respectively.

The measurement of observables in p-p collisions cans be affected by the presence of products of a collisions happening prior to the event of interest. Such effect is called *pile-up* and its occurrence is parametrised with the average number of proton-proton interactions per bunch-crossing, $\langle\mu\rangle$, for a given instantaneous luminosity $\mathscr{L}$, expressed as:

$$\langle\mu\rangle = \frac{\mathscr{L} \times \sigma_{\text{inel.}}}{N_{\text{bunch}} \times f} \tag{2.4}$$

where $\sigma_{\text{inel.}}$ is the total inelastic proton-proton cross-section and $N_{\text{bunch}} \times f$ is the average frequency of bunch crossing at the LHC.

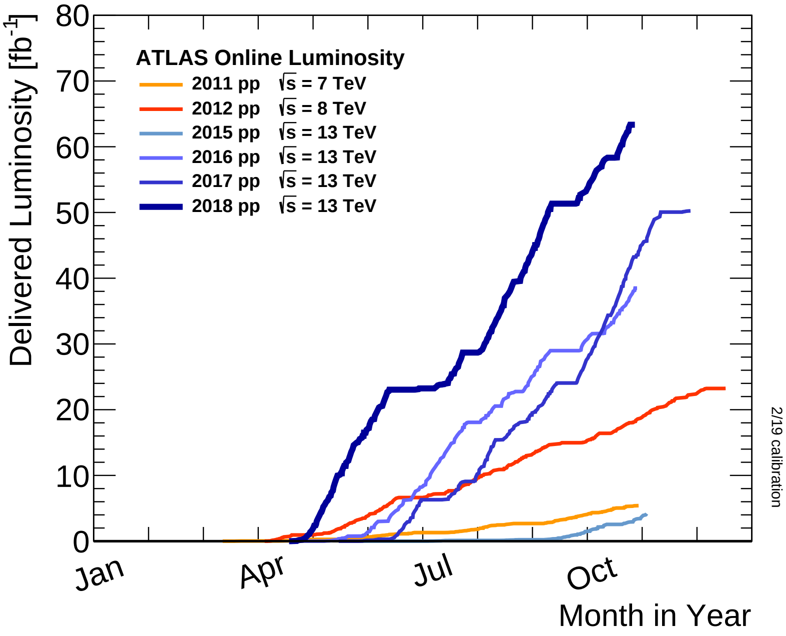

(a)

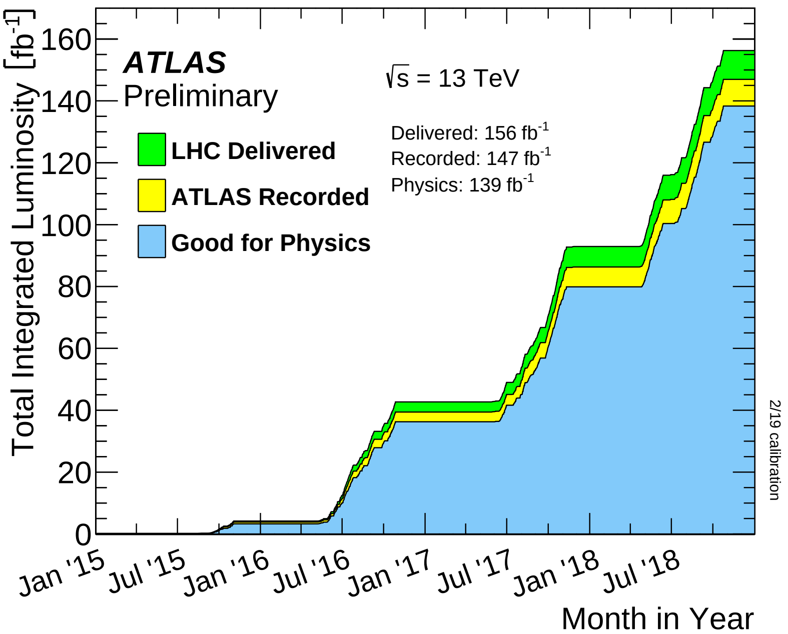

(b)

Figure 2.2: (a) Cumulative integrated luminosity delivered to the ATLAS experiment during the data taking years in Run 1 and Run 2, as measured by the LUCID2 detector. (b) Cumulative integrated luminosity versus time delivered by the LHC (green), recorded by ATLAS (yellow), and certified to be good quality data for physics analyses (blue) during Run 2. [74]

During the LHC Run 2 the ATLAS experiment has recorded a total of 139 fb^{-1} worth of data (Figure 2.2b). This impressively large dataset was collected over the Run 2 period at the cost of a considerably larger pile-up compared to the design value of $\langle\mu\rangle = 25$ [75]. Figure 2.3 shows the measured pile-up distributions for each of the four data-taking years of Run 2.

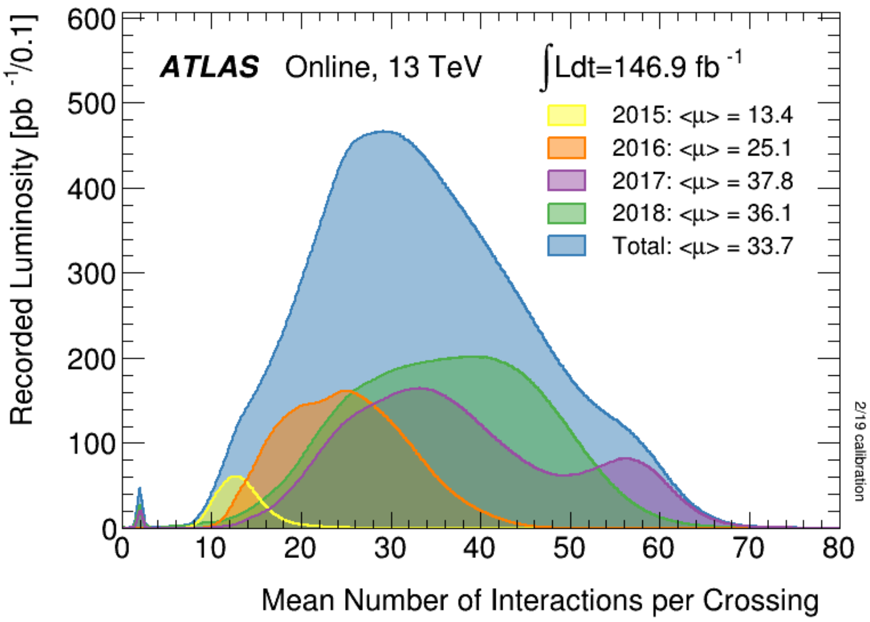

Figure 2.3: Distribution of the mean number of interactions per bunch crossing, $\langle\mu\rangle$, for the four years of data-taking in Run 2. [75]

Based on the change in the measured pile-up profile over the data-taking period of Run 2, shown in Figure 2.3, and the ability to simulate such conditions (as described in Chapter 3), the dataset used in this work is subdivided into three separate "campaigns": 2015+2016, 2017, and 2018 corresponding to a total integrated luminosity of 36.1 fb^{-1}, 44.3 fb^{-1}, and 58.5 fb^{-1}, respectively.

2.2 The ATLAS detector

ATLAS is a general purpose experiment which employs a variety of methods for the reconstruction and identification of different particles, and for the fast processing of collision data. The detector has a cylindrical geometry and it is 44 m in length and 25 m in diameter, resulting in a near 4π solid angle coverage around the nominal interaction point. A schematic representation of the detector and its main subcomponents, shown in Figure 2.4. Going from the innermost to the outermost part, one finds: the ID, the calorimeters, and the Muon Spectrometer (MS).

Each subdetector is positioned either in a coaxial geometry around the beam-pipe, in the so-called *barrel* region, or in "disks" at the two ends of the cylinder, referred to as *end-cap* regions.

The design of the ATLAS detector has been optimised to maximise the sensitivity for the purpose of discovering of the Higgs boson along with searching for new physics phenomena BSM, performing precision measurement of the SM, and searching for DM.

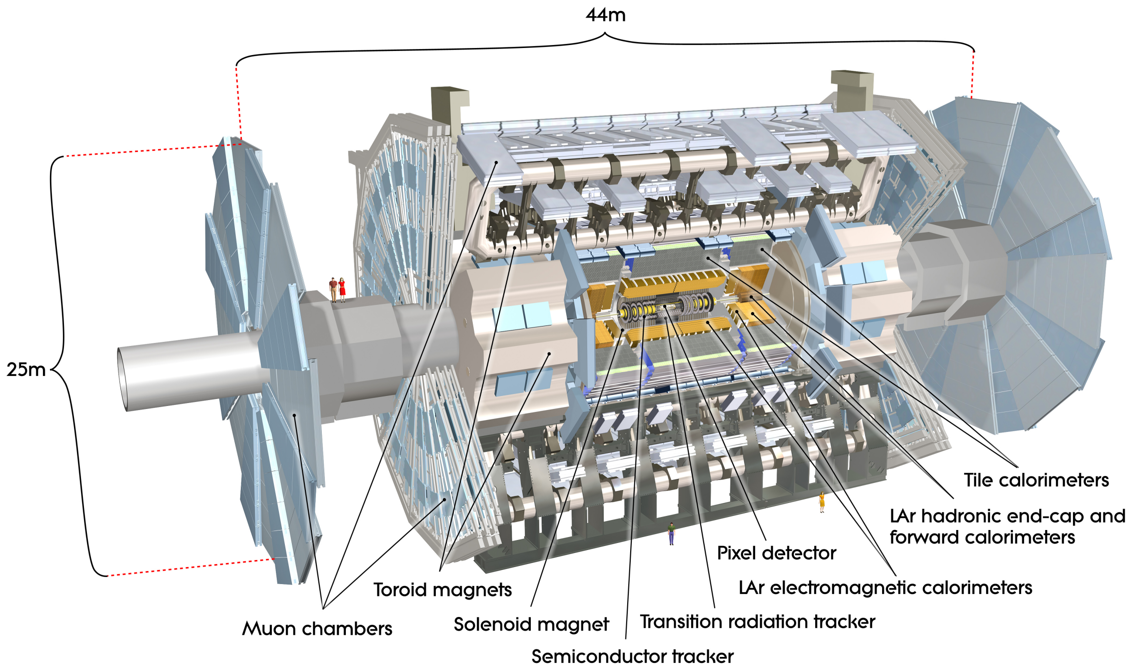

Figure 2.4: Schematic view of the ATLAS detector and its main subsystems. [61]

2.2.1 The ATLAS coordinate system and relevant quantities

A graphical representation of the right-handed coordinate system and nomenclature conventionally chosen to describe the ATLAS detector and the particles emerging from each p-p collision is shown in Figure 2.5.

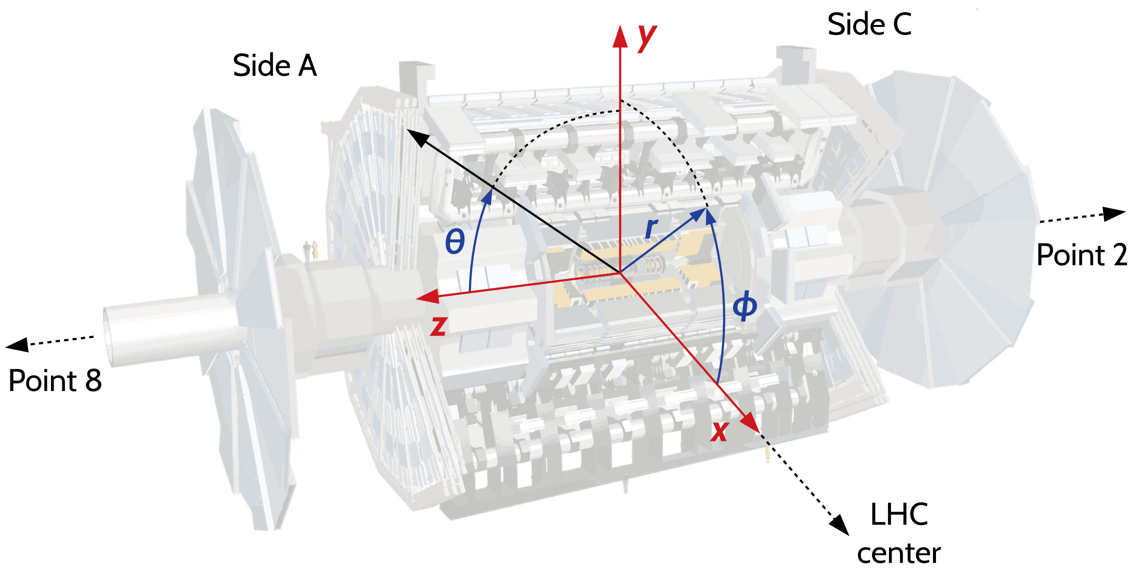

Figure 2.5: Representation of the ATLAS right-handed coordinate system. [76]

The origin is taken to coincide with the nominal interaction point. The beam direction defines the z-axis. The positive x-axis is defined to point towards the centre of the LHC ring, while the y-axis is directed upwards, thus completing a right-handed set of coordinates. The side of the detector with positive z is referred to as *Side A*, while that with negative z as *Side C*. The azimuthal angle ϕ is defined around the beam pipe, while the polar angle θ is measured from the positive z axis.

It is necessary for physics analyses to access the kinematic properties of the particles produced from each recorded p-p collision. The *transverse momentum* or p_{T} of such particles is measured by combining its components in the x-y or *transverse* plane:

$$p_{\mathrm{T}} = \sqrt{p_{\mathrm{x}}^2 + p_{\mathrm{y}}^2}. \tag{2.5}$$

Momentum conservation in the transverse plane implies a null vector sum of the $\vec{p}_{\mathrm{T}}$ of all the particles produced in a p-p collision. Since not all particles can be detected – especially those which do not interact via Electromagnetic (EM) or strong forces, most notably neutrinos – the *missing transverse momentum* can be defined as:

$$\vec{p}_{\mathrm{T}}^{\mathrm{miss}} = -\sum_{i \in \mathrm{visible}} \vec{p}_{\mathrm{T}}^{\,i}, \tag{2.6}$$

where the index i runs over all visible, or detected, particles. The magnitude $E_{\mathrm{T}}^{\mathrm{miss}} = \left|\vec{p}_{\mathrm{T}}^{\mathrm{miss}}\right|$ of the missing transverse momentum vector is called *missing transverse energy*, and it is used to quantify the amount of transverse energy associated with the invisible products of a p-p collision.

Another commonly used quantity is the *rapidity*, defined as:

$$y = \frac{1}{2}\ln\left(\frac{E + p_{\mathrm{z}}}{E - p_{\mathrm{z}}}\right), \tag{2.7}$$

where E and p_{z} are the particle energy and the longitudinal component of the momentum, respectively. The difference of the rapidities of two particles, Δy, is Lorentz-invariant. In the limit of ultra-relativistic particles ($E \gg m$), which is usually the case for the particles produced at the LHC, Equation 2.7 reduces to:

$$\eta = -\ln\left(\tan\frac{\theta}{2}\right), \tag{2.8}$$

commonly referred to as *pseudo-rapidity*.

Often, the angular separation between two reconstructed objects is expressed as:

$$\Delta R = \sqrt{(\Delta\phi)^2 + (\Delta\eta)^2}, \tag{2.9}$$

where $\Delta\phi$ and $\Delta\eta$ are the angular distances of the two particles in the transverse plane and in pseudo-rapidity, respectively.

2.2.2 The magnet system

The ATLAS magnet system (Figure 2.6) – 22 m in diameter and 26 m in length – generates a magnetic field which is used to deflect the trajectories of charged particle, thus, determining their charge and momentum from their curvature. The choices made for the magnetic field configuration have driven the design of the entire ATLAS detector [61].

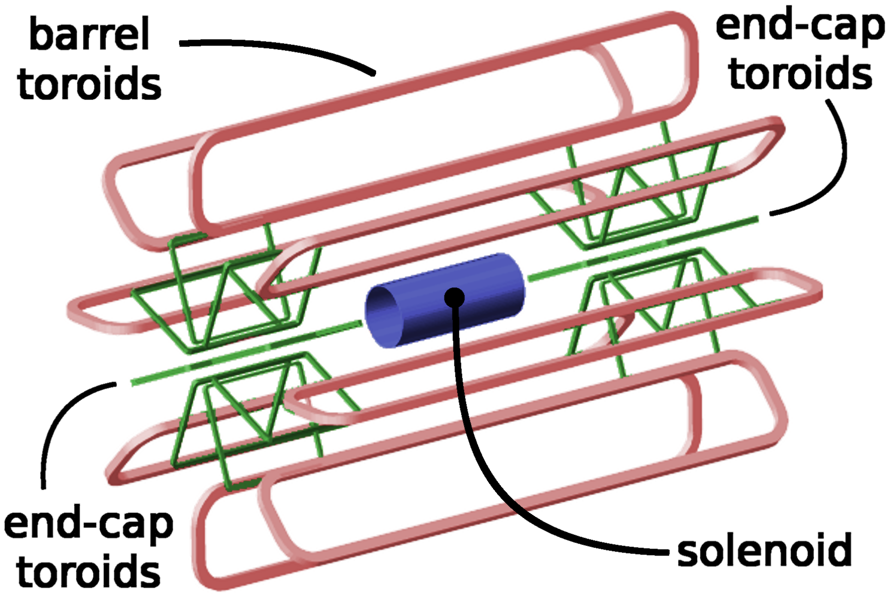

Figure 2.6: Schematic representation of the ATLAS magnet system. [77]

The magnet system layout comprises four main components: the superconducting *solenoid* and the superconducting *toroids* (one for the barrel and two for each end-cap). The solenoid presents a cylindrical geometry aligned with the beam pipe and surrounding the ID cavity. It produces an axial magnetic field of 2 T, which allows the tracks of charged particles detected by the ID to bend in the transverse plane. The three large toroids are arranged with an eightfold azimuthal symmetry around and outside the calorimeters. The barrel ($|\eta| < 1.4$) and end-caps ($|\eta| \in [1.6, 2.7]$) produce toroidal magnetic fields for the MS, of magnitude approximatively 0.5 T and 1 T, respectively.

2.2.3 The Inner Detector

The ID is the innermost component of the ATLAS experimental apparatus. Its function is to reconstruct the tracks and the vertices of the charge particles emerging from each p-p collision, by means of their curvature in the solenoidal magnetic field. The ID has a a total coverage of $|\eta| < 2.5$. It consists of three sub-components. Starting from the closest to the beam-pipe, one finds the silicon pixel detector, which in turn is surrounded by the SemiConductor Tracker (SCT). Finally, the third layer is that of the Transition Radiation Tracker (TRT). A sketch of the ID and its components is shown in Figure 2.7.

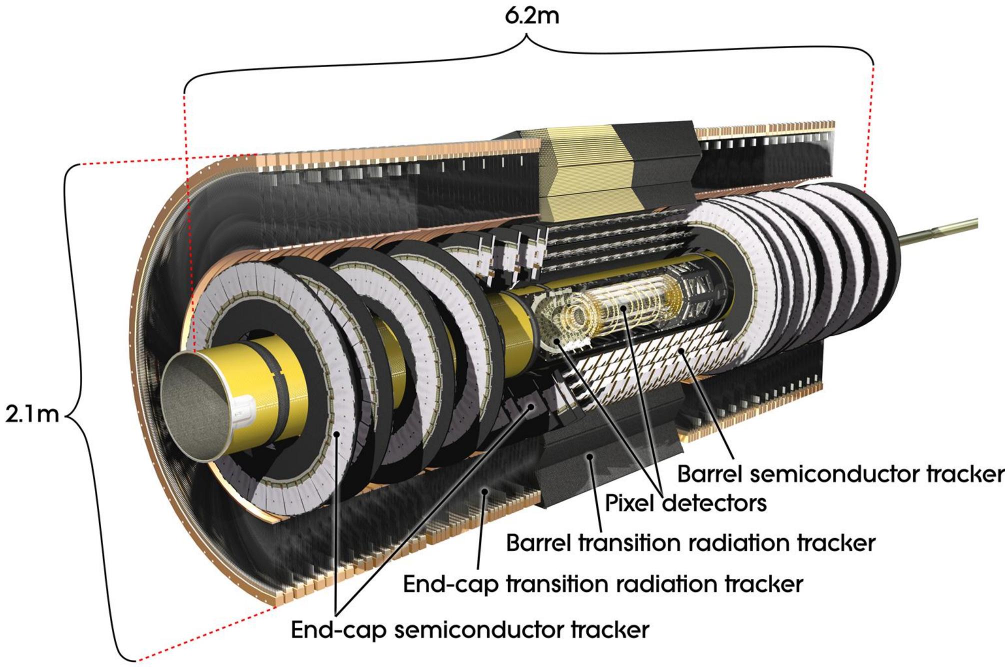

(a)

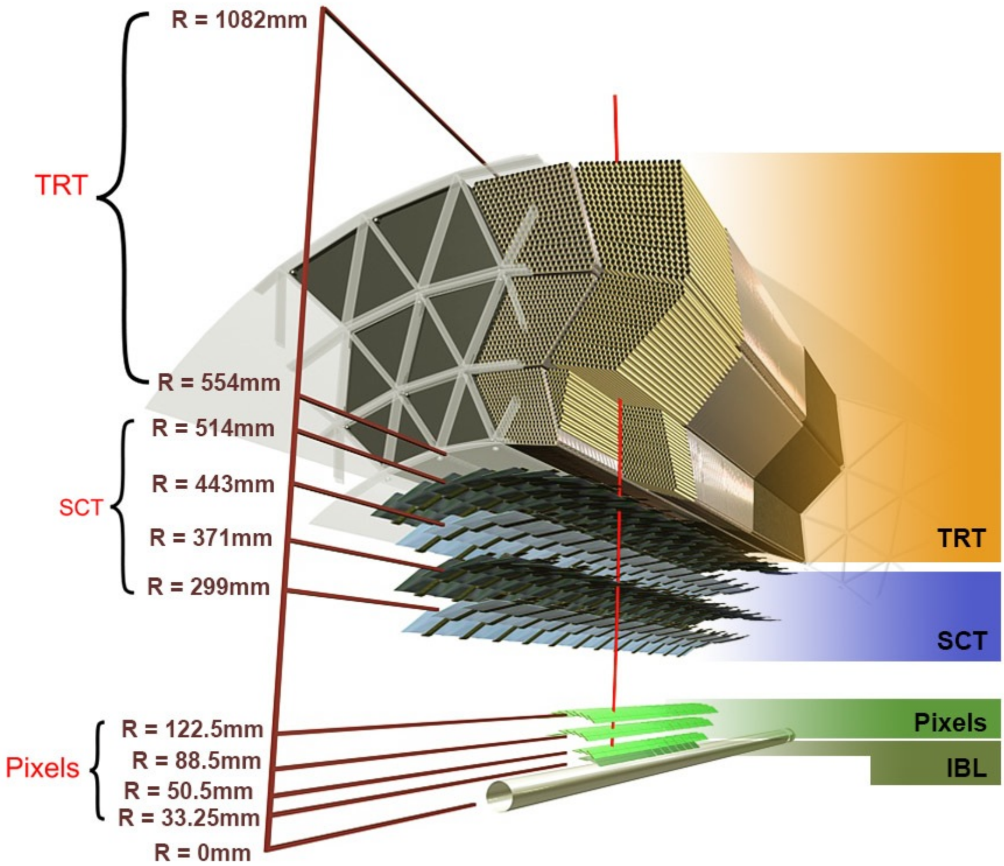

(b)

Figure 2.7: Schematic representations of (a) the ATLAS ID [61] and (b) its transverse cross-section showing the position of the barrel modules [78].

The Silicon Pixel Detector

The silicon pixel detector consists of three high-granularity barrel pixel layers surrounding the beam-pipe, and three forward and backward end-cap disks. Every silicon pixel sensor is identical and has a size of $50 \times 400\,\mu\text{m}^2$, resulting in an intrinsic resolution of $10\,\mu\text{m}$ (in $r - \phi$) and $115\,\mu\text{m}$ (in z for the barrel and r for the disks). This allows to achieve high tracking precision especially for the reconstruction of primary and secondary vertices. For the start of Run 2, a fourth innermost pixel layer, called Insertable B-Layer (IBL) [79], was added to further improve the vertex reconstruction performance, especially for what concerns the identification of heavy-flavour hadrons.

The Semiconductor Tracker

The ATLAS SCT has been designed to measure at least four space-points for each charge particle track. For this purpose, it comprises four double-sided layers of silicon strip sensors in the barrel, and nine double-sided disks in each end-cap, resulting in a total of 4088 modules covering an overall surface of $63\,\text{m}^2$. The silicon strips, arranged coaxially to the beam-pipe in the barrel and radially in the end-cap disks, are $80\,\mu\text{m}$ in width, enabling a maximum position resolution of $17\,\mu\text{m}$.

The Transition Radiation Tracker

The outermost sub-module of the ATLAS ID is the TRT. Unlike the pixel detector and the SCT, it consists of straw-tube gas detectors, which permit to extend the tracking up to $|\eta| = 2.0$. In the barrel region, the straws are parallel to the beam axis, whilst they are arranged radially in the end-cap wheels. With an intrinsic accuracy of $130\,\mu\text{m}$ per straw-tube, the TRT significantly improves the tracking especially for higher-momentum particles. Furthermore, the xenon-based gas mixture in the straw tubes enhances the capabilities for electrons identification, due to the production of transition-radiation photons whenever they cross each sensor.

2.2.4 The calorimetry system

The ATLAS calorimetry system consists of two different sub-detectors: the Electromagnetic Calorimeter (ECal) and the Hadronic Calorimeter (HCal). With a total coverage of $|\eta| < 4.9$, these calorimeters provide sufficient containment for the development of EM and hadronic showers, respectively, thus enabling the measurement of the energy of the particles entering them. Different technologies are used for the various components of the calorimetry system (Figure 2.8). The active material of the barrel of the ECal and all the end-caps is Liquid Argon (LAr), whereas a steel-sampling Tiles are used for the HCal barrel. In conjunction with the ID information, the fine granularity of the ECal provides a suitable precision for the identification and energy measurement of electrons and photons, whereas the coarser granularity of the rest of the calorimeter is sufficient to satisfy the physics requirements for jet reconstruction and $E_{\mathrm{T}}^{\mathrm{miss}}$ measurement.

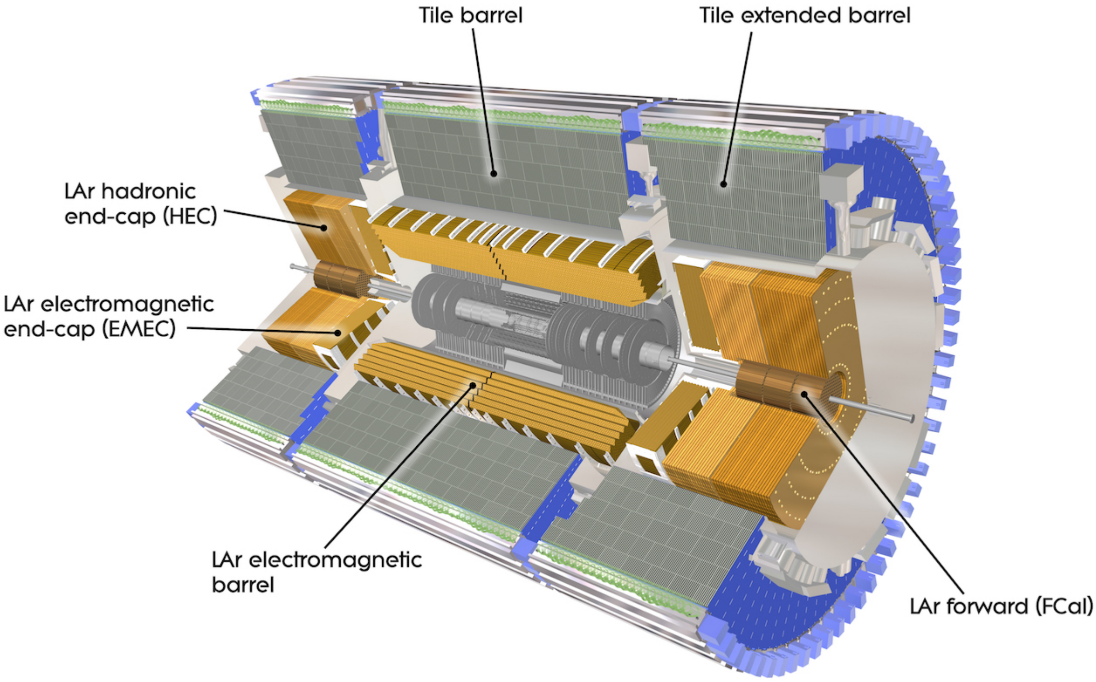

Figure 2.8: Schematic view of the ATLAS calorimetry system. [61]

The Electromagnetic Calorimeter

The ECal surrounds the solenoidal magnet and comprises the Electromagnetic Barrel (EMB) and the Electromagnetic End-Cap (EMEC) calorimeters, each housed in their own cryostat. They are both composed by layers of LAr as active material, piled-up with lead absorbers and positioned following an accordion geometry to maximise the η coverage. The thickness of the absorber plates has been optimised as a function of η to maximise the performance in energy resolution. The EMB calorimeter covers $|\eta| < 1.475$ and is further divided at $\eta = 0$ in two half-barrels, each with three layers in depth. The two EMEC calorimeters, on the other hand, are composed by two coaxial wheels, covering respectively $|\eta| \in [1.37, 2.5]$ and $|\eta| \in [2.5, 3.2]$. The total thickness of the ECal is > 2 radiation lengths (X_0) for the EMB and > 24 X_0 for the EMEC. In the region between the barrel and the end-cap cryostats $|\eta| \in [1.37, 1.52]$, here referred to as *crack region*, the energy resolution degrades significantly [61], despite it being equipped with wire scintillators to improve the performance of the ECal. Such region is therefore generally not used for photon identification or precision measurements with electrons. Finally, a pre-sampler detector, covering $|\eta| < 1.8$, is used to correct for the energy lost in the payload of the ID and the solenoid. It consists of an active LAr layer of thickness 1.1 cm (0.5 cm) in the barrel (end-cap) region.

The Hadronic Calorimeter

The Tile calorimeter is the barrel part of the HCal and it is placed outside and around the ECal. It covers $|\eta| < 1.0$, whilst two extra barrels extend its coverage in the region with $|\eta| \in [0.8, 1.7]$. It is a sampling calorimeters which employs steel absorbers and scintillating tiles as active material. It comprises three layers in depth, reaching an overall thickness of 9.7 interaction lengths (λ_0) at $\eta = 0$. The end-cap regions also house the LAr-based Hadronic End-Cap (HEC) calorimeters. Each are housed in cryostats and consist of 4 separate layers, for a total coverage of $|\eta| \in [1.5, 3.2]$. For the HEC copper plates are used as absorbers.

Additionally, the Forward Calorimeters (FCals) are placed in the forward η region ($|\eta| \in [3.1, 4.9]$), to further extend the HCal coverage. At each end-cap they are composed by three layers which employ LAr as an active medium. The first layer uses copper absorbers and it is optimised for EM measurements, whereas the other, outer layers are made of tungsten, which makes them more suitable to measure the energy produced via hadronic interactions.

2.2.5 The Muon Spectrometer

The MS is the outermost sub-system of the ATLAS detector. Its purpose is to reconstruct muon trajectories by means of their curvature in the magnetic field produced by the toroidal magnets, which the MS chambers are largely embedded into. The overall design of the toroids and the layout of the muon chambers are such that the magnetic field lines would be mostly orthogonal to the muon trajectories, whilst minimising the degradation of resolution due to multiple scattering.

Two different categories of muon chambers types can be identified in the ATLAS detector: precision-tracking and trigger chambers. The latter provide fast signal read-out that can be used to trigger the data acquisition of collision events containing muons, as discussed in Section 2.3.3, while the former provide a high-precision reconstruction of the coordinates on the muon hits. The precision-tracking chambers in the barrel are placed within and on top of the eight coils of the toroid barrel, providing a magnetic field in the range $|\eta| < 1.4$. On the other hand, the end-cap chambers are located in front of and behind the two end-cap toroid magnets, which are responsible for the track bending within $|\eta| \in [1.6, 2.7]$. In the so-called *transition region* ($|\eta| \in [1.4, 1.6]$) the magnetic deflection is provided by a combination of the fields in the barrel and end-cap toroids. A schematic representation of the general layout if the MS is shown in Figure 2.9.

Precision-tracking chambers

The main high-precision measurement of the muon tracks coordinates over almost the entire pseudo-rapidity range ($|\eta| < 2.7$) is provided by the Monitored Drift Tubes (MDTs) system. They consist of 1088 drift-tube gas-based detectors (with a diameter of 29.970 mm) which rely on the ionisation produced by the passing muon to produce electron avalanches, which are then

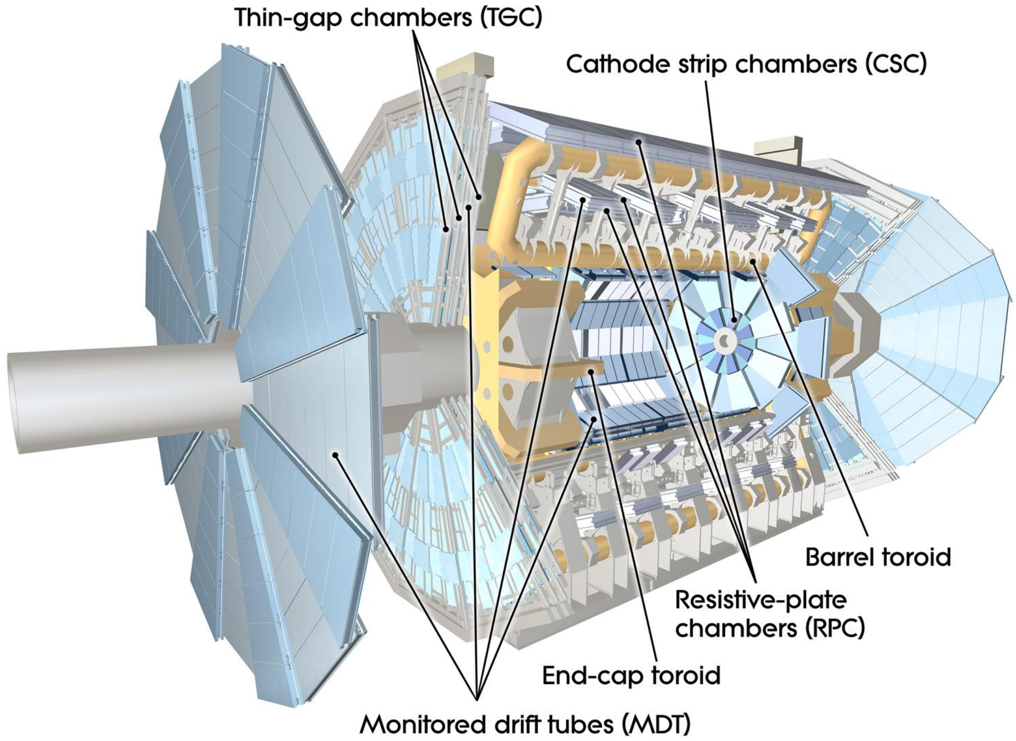

Figure 2.9: Schematic view of the ATLAS Muon Spectrometer. [61]

collected by anode wires, laying within each tube for their length. The spatial resolution that it is possible to achieve through the MDTs is 60-80 µm per tube. However, the maximum drift time from the wall to the wire is about 700 ns, which makes these detectors not suitable for fast tracking measurements.

At large pseudo-rapidities ($|\eta| \in [2, 2.7]$), in order to withstand the high particle rates and background conditions resulting from each p-p collision, in the innermost layer of MS end-caps, the MDTs are replaced by Cathode Strip Chambers (CSCs). These are essentially multi-wire proportional chambers with cathodes segmented into strips, thus achieving a higher granularity with respect to the MDTs. Although, depending on the muon track direction with respect to the magnetic field, the spatial resolution can vary between 60 µm and 5 mm, the maximum drift time achievable (of approximately 20 ns) is much faster compared to the MDTs.

Muon trigger chambers

Two additional kinds of muon detectors, in the range $|\eta| < 2.4$, are specifically designed for timing reconstruction and triggering purposes: the Resistive-Plate Chambers (RPCs) in the barrel and the Thin-Gap Chambers (TGCs) in the end-caps. They are also able to provide: bunch-crossing identification for each event; the measurement of the second coordinate of the muon tracks, orthogonal to that obtained via the precision-tracking chambers; a fast (<50 ns) muon p_{T} threshold discrimination above 6 GeV .

The RPCs consist of three planes of gaseous detectors with parallel electrode-plates replacing wires. Their coverage in the barrel is of $|\eta| < 1.05$. Although they have a coarser granularity compared to the MDTs in the barrel, their timing resolution can be up to 10 ns. Finally, the TGCs comprise three different planes for each end-cap, for a coverage of $|\eta| \in [1.05, 2.7]$. Their principle of operation is that of multi-wire proportional chambers – thus similar to the RPCs – with wire-to-cathode distance being smaller than the wire-to-wire distance. This and other technical characteristics make the TGCs more resilient against radiation damage compared to the RPCs, and therefore more suitable for the busier environment and conditions of the forward regions of the ATLAS detector.

2.3 The ATLAS Trigger and Data Acquisition system

A crucial role in the ATLAS experiment is played by the Trigger and Data Acquisition (TDAQ) system [80]. During Run 2 the LHC delivered collision events with a bunch-crossing rate of 40 MHz. Such a rate would be impossible to handle in terms of processing time and data storage. The TDAQ system is responsible for making real-time decisions on whether to record data from a given collision, trying to select events of interest to achieve the ATLAS physics goals. This has, therefore, a fundamental impact on the datasets used in physics analyses.

The Run 2 ATLAS TDAQ system consists of two separate components: a low latency, pipelined hardware-based Level-1 (L1) trigger followed by a software-based High-Level Trigger (HLT) for a more detailed event reconstruction. The L1 trigger processes events at the nominal 40 MHz bunch-crossing rate, accepting them at a rate below 100 kHz. These are then passed to the HLT which further reduces the rate to approximately 1.2 kHz for data recording to permanent storage [80]. A graphical representation of the ATLAS TDAQ architecture is shown in Figure 2.10.

2.3.1 The Level-1 Trigger

The L1 trigger uses a set of custom electronics to process and select events based on reduced granularity information from the calorimeters and the MS only. In particular, the L1 Calorimeter (L1Calo) [81] takes as inputs analogue signals from the calorimeters, which are then digitised, calibrated and sent to the Cluster Processor (CP) and the Jet/Energy-sum Processor (JEP). These identify electrons, photons, τ-leptons above a programmable p_{T} threshold and produce global sums total and missing transverse energy, respectively. The L1 Muon (L1Muon) [81] uses the hits from the RPCs and TGCs to determine the curvature of the muon tracks. The L1-Accept trigger decision is ultimately formed in the Central Trigger Processor (CTP), which interprets inputs from the L1Calo, the L1Muon Central Trigger Processor Interface (MUCTPI) and the L1 Topological (L1Topo) trigger [82]. In order to restrict the number of L1-Accept signals to be within the constraints of the detector read-out latency, the CTP is also responsible to apply *dead time*, to veto the number of two consecutive L1-Accepts (simple dead time) and more generally to restrict them for a given number of bunch-crossings (complex dead time) to prevent the detectors Front-End (FE) buffer electronics to overflow.

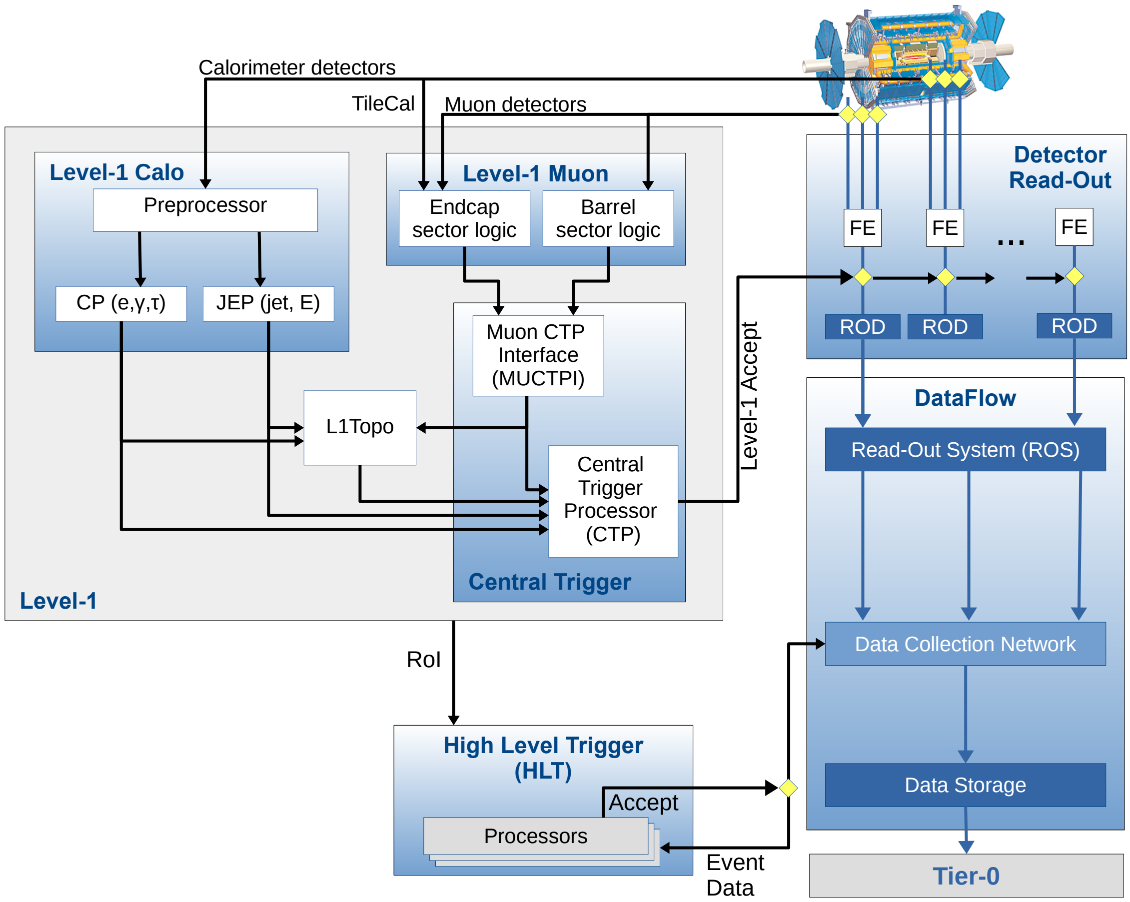

Figure 2.10: Schematic representation of the architecture of the ATLAS TDAQ system used in Run 2. [80]

Finally, the L1 triggers also identify Regions of Interest (RoIs) to reduce the amount of data transferred and later processed in the HLT.

2.3.2 The High-Level Trigger

The detector data read from the FE electronics are initially stored in custom on-detector, pipelined Read-Out Buffers (ROBs). On a L1-Accept signal, data are transferred to the HLT by means of the Read-Out Drivers (RODs).

The HLT consists of a farm of Central Processing Units (CPUs) which perform a more detailed event and object reconstruction by including the coarse-granularity information from the full detector through fast software-based algorithms. Each step in a sequence of such algorithms executes one or multiple feature extractions which request event-data fragments from within a RoI – using the L1 items as *seeds* – to ultimately form a trigger decision. In some cases, the HLT takes as input the full detector information, instead of just within each RoI, e. g. for the reconstruction of the missing transverse momentum. The ATLAS HLT algorithms are mostly based on the offline software `Athena` [83], which is in turn based on the data processing framework for high energy physics experiments `Gaudi` [84]. Once the HLT-Accept decision is made the event-data are transferred by the Read-Out System (ROS) to the local storage at the experimental site and exported to the *Tier-0* facility at the computing centre of CERN for the *offline reconstruction*. The physics output rate of the HLT during an ATLAS data-taking run has been on average 1.2 kHz with a transferring speed of about 1.2 GB/s [80].

2.3.3 Trigger chains, menu and streams

The events which are ultimately recorded are selected in *trigger chains*. Each chain consists of a L1 item and a series of HLT algorithms which aim to reconstruct physics objects by applying specific kinematic requirements, depending on the desired physics signature (leptons, photons, jets, missing transverse momentum, total energy and B-meson candidates). The naming convention for a trigger chain typically begins with `HLT` followed by the HLT kinematic requirements and, if applicable, the L1 item that seeded them. Examples of trigger chain names, which are employed in the work presented in this thesis, are: `HLT_2e12_lhloose_L12EM10VH` and `HLT_mu13_mu13_idperf_Zmumu`. The former requires the presence of two electrons with $p_{\mathrm{T}} \geq 12$ GeV, identified as electrons by the likelihood algorithm `lhloose` (Section 3.3.2), and seeded by the L1 item `L12EM10VH` with two clusters in the ECal of transverse energy greater than 10 GeV. The latter requires two muons of $p_{\mathrm{T}} \geq 13$ GeV, one of which passing the so-called `idperf` requirement, described in more details in Section 2.4.2.

At both L1 and HLT stages individually, *prescales* may be applied, to each specific chain to control the rate of accepted events. Specifically, for a positive integer prescale value of n, a probability of keeping an event of $1/n$ is applied, thus reducing the output rate of a given trigger chain. The list of trigger chains used in Run 2 for data-taking is referred to as the *trigger menu*. The main goal of the Run 2 trigger menu was to maintain un-prescaled single electron and muon chains for p_{T} thresholds around 25 GeV, thus ensuring the collection of the majority of events with leptonic decays of W and Z bosons, for the achievement of the ATLAS physics goals [80].

The trigger menu also defines to which *data stream* an event is written, depending on the trigger chains that had accepted it [80]. For Run 2, various data streams were defined: the *physics/main stream* contains events with data of interest for physics analyses; the *express stream*, with events reconstructed offline in real time for prompt monitoring and data quality checks; the *debug stream* stores events for which no trigger decision could be made, and need to be analysed and, possibly, recovered separately. Other supporting streams are used for technical tasks such as the *calibration*, *Trigger-Level Analysis* and *monitoring streams*.

2.4 The ATLAS Inner Detector trigger and its performance

This Section is dedicated to the detailed description of a specific component of the ATLAS HLT, namely the ID trigger. Particular focus is given to explain how the performance of the ID trigger is measured and monitored, especially, through the usage of the *Tag-and-Probe technique*.

The development of the Tag-and-Probe technique for the estimation of the ID trigger performance was the main objective of my authorship technical project, also called "qualification task", which allowed me to become an author of the ATLAS Collaboration. Over the course of my PhD, I have been responsible for the continuous development and maintenance of the software routines of this performance analysis for in the entire duration of my PhD.

The results of the ID trigger performance analysis which I performed using the full Run 2 dataset have been included in the publication by the ATLAS Collaboration indicated in Reference [85]. The Figures shown in the following Sections are extracted from that publication. I have contributed to the production of all of these results. In particular, I have personally obtained the results characterising the ID trigger performance analysis using the Tag-and-Probe technique (Section 2.4.3).

2.4.1 The ATLAS Inner Detector trigger

The ability of the TDAQ system to process information from the ID, especially for final states with electrons, muons, taus, and b-tagged jets, is a crucial requirement to achieve the ATLAS physics goals. The ID trigger is required to have a high performance for track reconstruction across the entire range of possible physics signatures, even under very harsh pile-up conditions. This is a challenging task given the extremely high track and hit occupancies in the ID arising from the large pile-up multiplicity (Section 2.1.2). During Run 2, thanks to the ID trigger, it was possible to achieve event rate reductions of approximately 50-100 for the electron and b-jet triggers, and 3-10 for muon and tau triggers [85].

As stated previously, the HLT is the first level at which the information from the ID are made available to the trigger. The ID tracking is performed in two consecutive stages: the *Fast Track Finder* (FTF) and the *precision tracking*. This enables the trigger to make a first, fast event rate reduction after which more precise and computationally demanding tracking algorithms can be executed.

The FTF stage is executed separately on the detector information retrieved within each RoI identified at L1. Here, initial track candidates are formed from triplets of space-points (*track seeds*) from the hits of the pixel and SCT modules, which are then processed by means of a fast track-finding and duplicate-removal algorithms. This provides an initial fast reconstruction of track candidates, which prioritises tracking efficiency (see Section 2.4.2) over the purity of the track selection and the precision of the measurement of the kinematic properties of the tracks.

The precision tracking uses the tracks identified in the FTF stage as inputs. Hence, by construction, the the precision tracking efficiency cannot exceed that of the FTF. The initial track candidates are processed with a version of the offline tracking algorithms, which also includes the information of the TRT, to improve the momentum measurements at larger radii. Then, high quality track fits with a global χ^2 fitter algorithm [85] are performed to improve the track p_{T} resolution and, therefore, the identification of the trigger tracks with respect to the offline reconstruction.

2.4.2 Inner Detector tracking performance

The performance of the ID trigger is evaluated with respect to the offline tracking (see Section 3.3.2), which is executed after the event is recorded. In particular, the ID trigger tracking efficiency is measured by considering in each event the fraction of the offline tracks that are are also matched to the tracks reconstructed in the FTF and precision tracking stages of the ID trigger. Having a high ID trigger tracking efficiency is of crucial importance to achieving the ATLAS physics goals given the significant triggered event rate reduction that can be achieved through the ID trigger, especially for what concerns physics signatures with electrons, muons and taus. If the ID track reconstruction in the HLT did not match the more precise offline track reconstruction, then such trigger decisions would be biased by track misreconstruction, and that would ultimately result in the rejection of events of interest.

In what will henceforth be referred to as the "standard" approach, the efficiency is determined by using a number of supporting triggers, called `idperf` chains. These are similar to the physics chains, but apply selections on the objects reconstructed in the MS and calorimeters only, without any quality requirements on the reconstructed ID tracks. This allows to estimate the tracking efficiency without introducing any biases on the ID track reconstruction itself. Examples of the trigger chains used in the tracking performance analysis are: `HLT_mu4_idperf` and `HLT_e5_lhtight_idperf`. The trigger tracks within a given RoI are matched to the selected offline tracks in that RoI if they lay within a cone of $\Delta R = 0.05$ around the offline track. The ID tracking efficiency is then measured, as a function of relevant kinematic quantities, from the fraction of offline tracks that are also matched to a trigger track in each RoI. Statistical uncertainties on the final efficiency are propagated from the Poisson errors on the number of trigger-matched and unmatched offline tracks.

A caveat of using `idperf` chains in the ID performance evaluation is that, in order to keep the event rate to manageable levels, large prescales are usually applied, ultimately resulting in statistically limited data samples. Moreover, since the trigger objects in `idperf` chains do include any ID tracking, the contribution from background processes (e. g. QCD jets for electrons) becomes significant. Therefore, stringent quality requirements (e.g. on the number of pixel and SCT hits, the number of "missed" silicon layers, etc.) must be applied to select offline tracks [85], to ensure to match the trigger tracks to actual offline objects. This further reduces the size of the sample used for the performance measurement, thus limiting the statistical precision of the efficiency measurement in certain regions of the phase-space.

The ATLAS ID tracking efficiencies for Run 2 are shown for muons in Figures 2.11-2.12, and for electrons in Figures 2.13-2.14.

The measured efficiencies for muons in the full Run 2 dataset exceed 99%, with a statistical precision which deteriorates for $p_{\mathrm{T}} > 100$ GeV (Figure 2.11b) and large impact parameters (Figure 2.12). The values of the muon ID trigger tracking efficiency for large p_{T} and impact parameters are not shown in Figures 2.11 and 2.12, due to the poor statistics in that region hampering the determination of the ID performance in that phase-space.

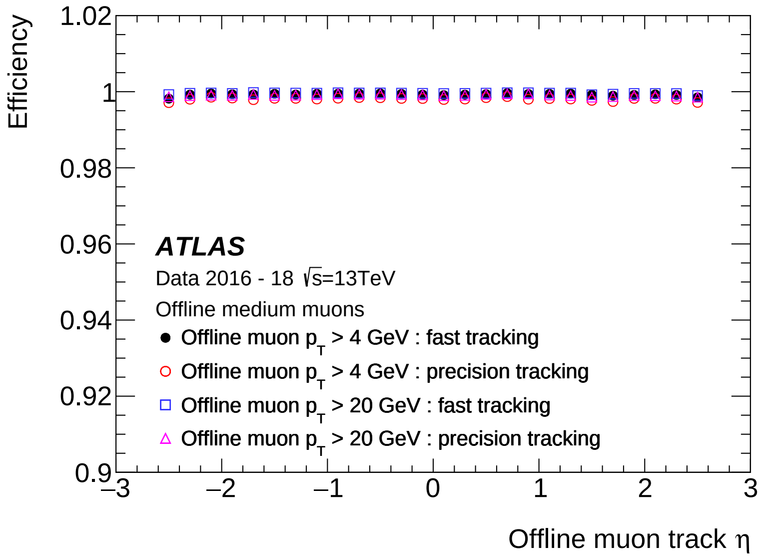

(a)

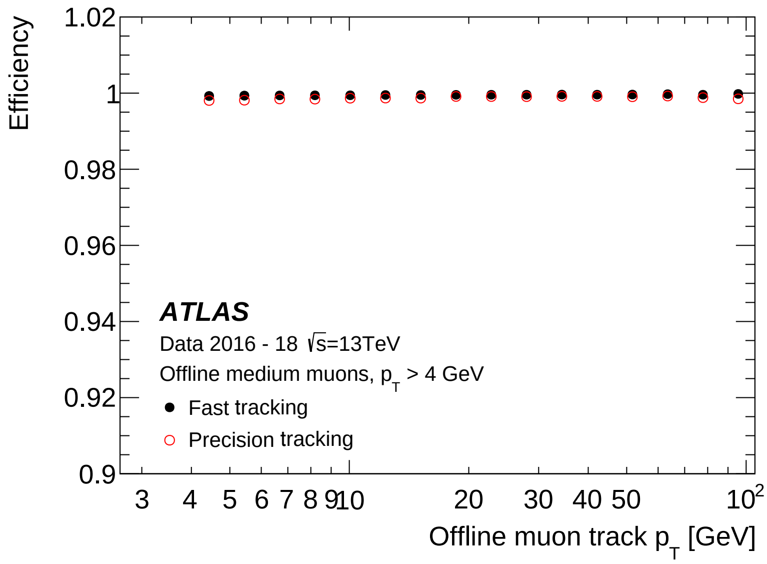

(b)

Figure 2.11: The ID tracking efficiency, estimated with the "standard" approach, described in the text, for muons selected by the 4 GeV and 20 GeV muon `idperf` chains, with respect to offline muon candidates with $p_{\mathrm{T}} > 4$ GeV and $p_{\mathrm{T}} > 20$ GeV. The efficiency is shown as a function of: (a) the offline-reconstructed muon η and (b) p_{T}. Efficiencies are shown for both FTF and precision tracking. The error bars represent the estimated statistical uncertainties. [85]

The electron tracking is affected by the energy radiated via bremsstrahlung, which is responsible for the occurrence of "kinks" in their tracks, corresponding to the emission of the radiated photon, which make the overall track fitting stage more challenging. Moreover, electron can loose a significant portion of their energy via bremsstrahlung. Hence, depending on how much energy has been radiated, the p_{T} of the electron measured from the curvature of the track in the ID may result smaller than the transverse energy, E_{T}, deposited in the corresponding ECal cluster, which instead accounts for the bremsstrahlung energy loss. Efficiencies are shown as a function of the offline electron transverse energy, E_{T} (Figure 2.13a) and the offline track p_{T} (Figure 2.14a). In the region with $E_{\mathrm{T}}/p_{\mathrm{T}} > 1$ of Figure 2.13b, which correspond to the region with small offline electron track p_T, bremsstrahlung effects dominate, resulting in a lower efficiency for the precision tracking, since i.e. the aforementioned occurrence of “kinks” in the track mostly affect the precision track fitting performed in this stage. On the other hand, the region with $E_T / p_T < 1$ is mostly populated by tracks which are mistakenly reconstructed with a p_T greater than the corresponding cluster E_T in the calorimeter. The offline track “migration” to higher p_T values can occur as a consequence of missing hits, especially in the innermost and outermost layers of the pixel and SCT sub-detectors [85]. Therefore, an additional cut of $E_T / p_T > 0.8$ is applied to the distributions in Figures 2.13 and 2.14, except for Figure 2.13b.

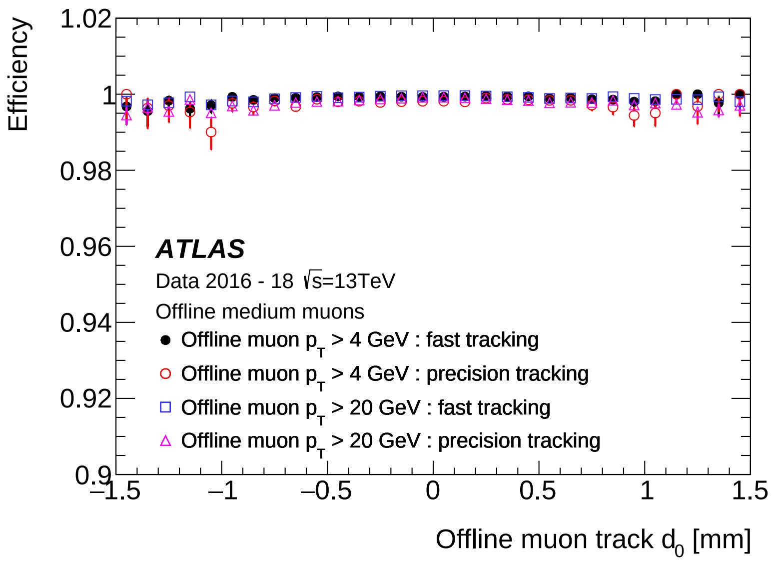

(a)

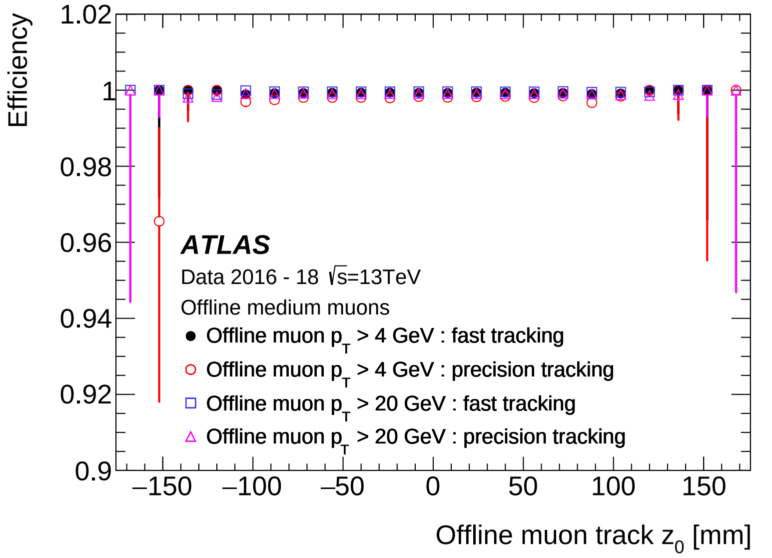

(b)

Figure 2.12: The ID tracking efficiency, estimated with the “standard” approach, described in the text, for muons selected by the 4 GeV and 20 GeV muon `idperf` chains, with respect to offline muon candidates with $p_T > 4$ GeV and $p_T > 20$ GeV. The efficiency is shown as a function of: (a) the offline-reconstructed muon transverse and (b) longitudinal impact parameter. Efficiencies are shown for both FTF and precision tracking. The error bars represent the estimated statistical uncertainties. [85]

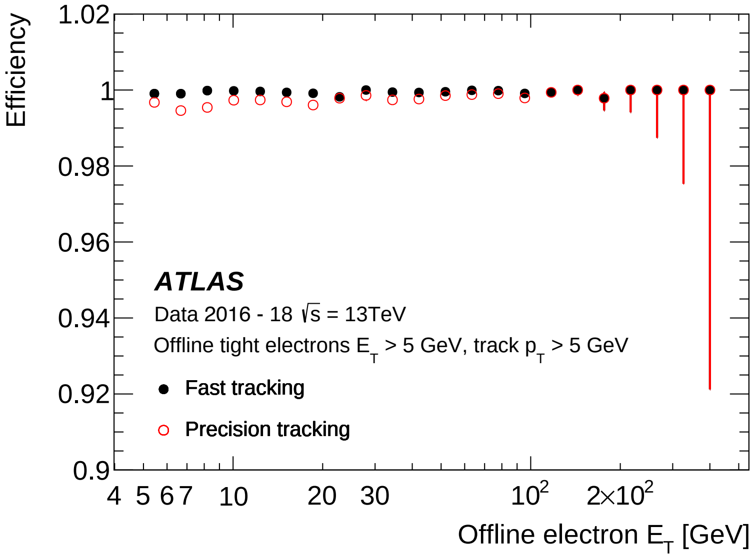

(a)

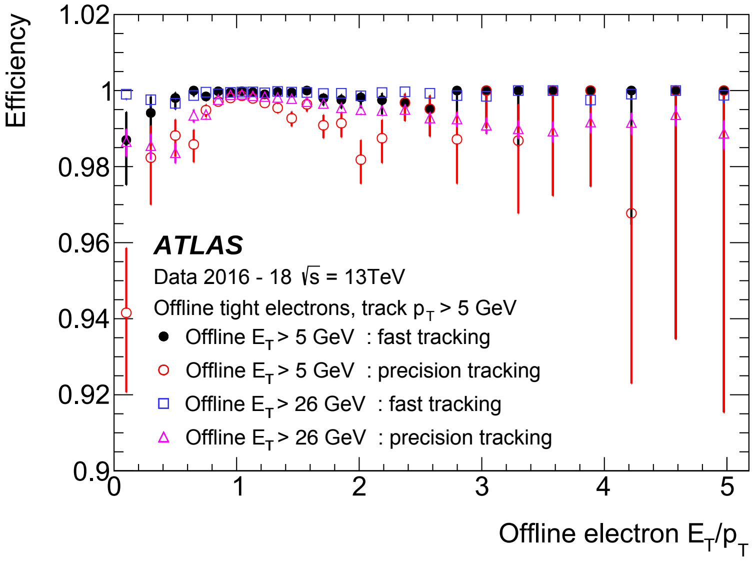

(b)

Figure 2.13: The ID tracking efficiency, estimated with the "standard" approach, described in the text, for electrons selected by the 5 GeV and 26 GeV electron `idperf` chains, with respect to offline electron candidates with the $E_T > 5$ GeV and $E_T > 26$ GeV. The efficiency is shown as a function of: (a) the offline-reconstructed electron E_T and (b) E_T / p_T. Efficiencies are shown for both FTF and precision tracking. The error bars represent the estimated statistical uncertainties. [85]

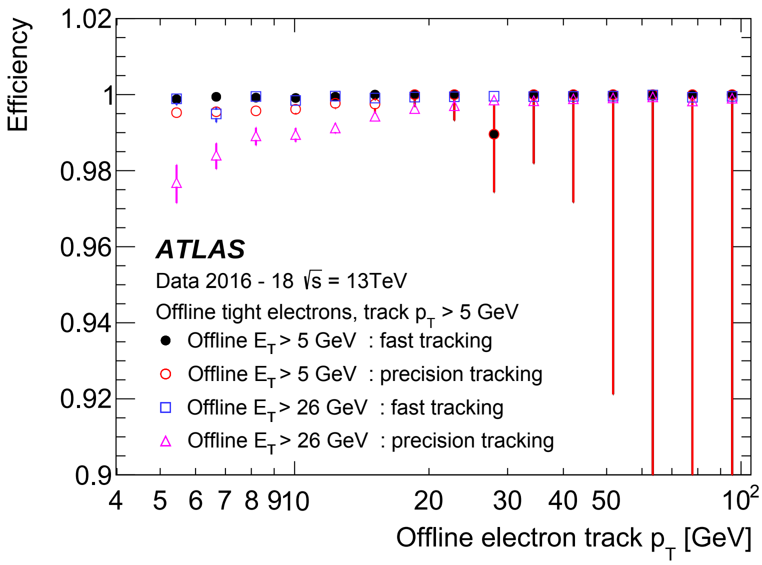

(a)

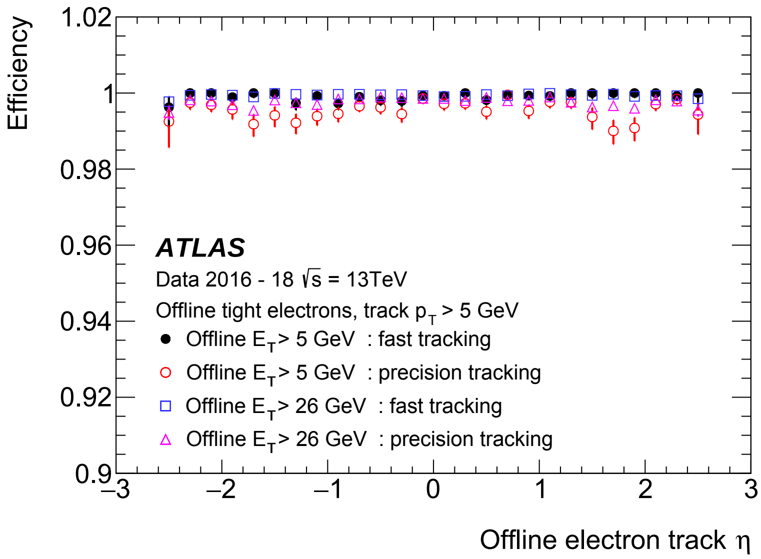

(b)

Figure 2.14: The ID tracking efficiency, estimated with the “standard” approach, described in the text, for electrons selected by the 5 GeV and 26 GeV electron `idperf` chains, with respect to offline electron candidates with the $E_T > 5$ GeV and $E_T > 26$ GeV. The efficiency is shown as a function of: (a) the offline-reconstructed electron track p_T and (b) η. Efficiencies are shown for both FTF and precision tracking. The error bars represent the estimated statistical uncertainties. [85]

2.4.3 Tag-and-Probe technique for Inner Detector tracking performance

The most relevant limitation of the “standard” approach described in Section 2.4.2, especially for what concerns electrons and muon signatures, is the limited statistical precision hampering the determination of the performance of the tracking in the ID trigger in certain regions of the phase-space. This is especially true in the case of electrons, in which the large error bars affect the measurement of the efficiency for most of the available statistics, particularly for $p_T > 40$ GeV, as shown in Figure 2.14a.

The main goal of the task that I have undertaken in order to qualify as an author of the ATLAS Collaboration was to develop and implement in the `Athena` software a method to improve the statistical precision with which the ID tracking performance is estimated. The adopted solution is based on an alternative approach which requires to use a sample of events that pass a di-lepton trigger selection and are consistent with the decay of a Z boson. This permits to use the *Tag-and-Probe technique*, which is commonly employed in high-energy physics experiments for performance measurements [86]. The di-lepton chains used here include `HLT_mu13_mu13_idperf_Zmumu` and `HLT_e26_lhtight_nod0_e15_etcut_L1EM7_Zee`. These chains select events with two same-flavour lepton (muon or electron) candidates which are consistent with the decay of a Z boson, i.e. the value of their invariant mass, $m_{\ell\ell}$ (see Section 4.2.4) lays in an interval of typically $40-50$ GeV around m_Z.

In the Tag-and-Probe analysis, each of these di-lepton trigger chains is split into two separate "legs", called the "Tag" and "Probe" legs, as shown in Figure 2.15.

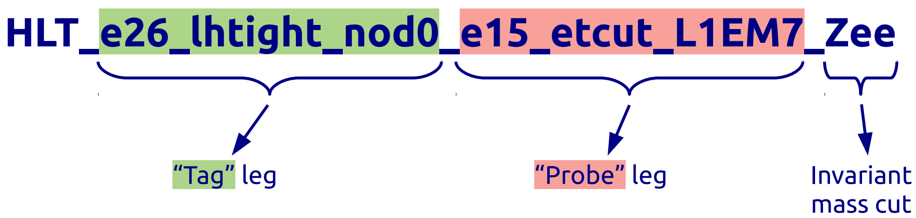

Figure 2.15: Structure of a di-lepton trigger chain used in the Tag-and-Probe analysis.

The "Tag" leg selects a muon (electron) candidate combining the MS (calorimeters) and ID information, whereas the "Probe" leg is itself an `idperf` chain and, therefore, selects a muon (electron) candidate solely on the MS (calorimeters) without using any ID information. For every triggered event, the two leptons must each be selected in different RoIs, i. e. the Tag RoI must belong to the Tag leg and the Probe RoI to the Probe leg. The ID tracking performance is then evaluated with respect to the lepton candidate in the Probe RoI, which guarantees an unbiased measurement of the ID trigger tracking efficiency. For each event, a Probe RoI is accepted only if it satisfies the so-called *Tag-and-Probe selection*: if the invariant mass of the pair of the offline-reconstructed lepton candidates in the Tag and Probe RoIs does not lay within a certain window around the Z boson mass (i. e. $m_{\mu\mu} \in [60, 120]$ GeV , and $m_{ee} \in [40, 180]$ GeV), the Probe RoI is discarded. The distributions of the invariant masses of the selected offline di-muon (di-electron) candidates are shown in Figure 2.16. Once the set of the Probe RoIs passing the Tag-and-Probe selection is defined, the performance analysis follows exactly the same procedure that is used in the "standard" approach, described in Section 2.4.2.

The presence of a fully-selecting Tag RoI in the requested trigger chains dramatically reduces the recorded event rate, resulting typically in the usage of either a much smaller prescale or no prescales whatsoever. This provides a significantly larger statistical sample for ID performance measurements compared to the "standard" approach. Furthermore, the Z mass requirement already at trigger-level, coupled with the additional Tag-and-Probe selection in the estimation of the ID trigger performance, guarantees the high purity of the chosen statistical sample. This ensures that the selected offline Probe candidates are in all likelihood actual

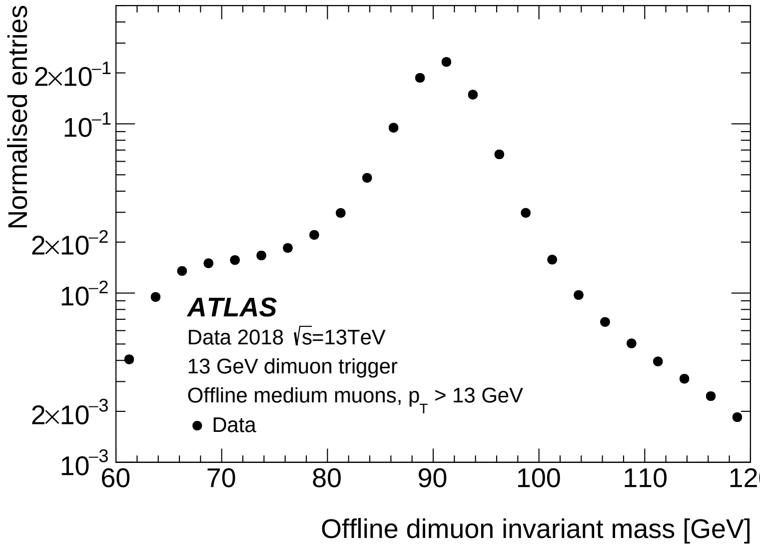

(a)

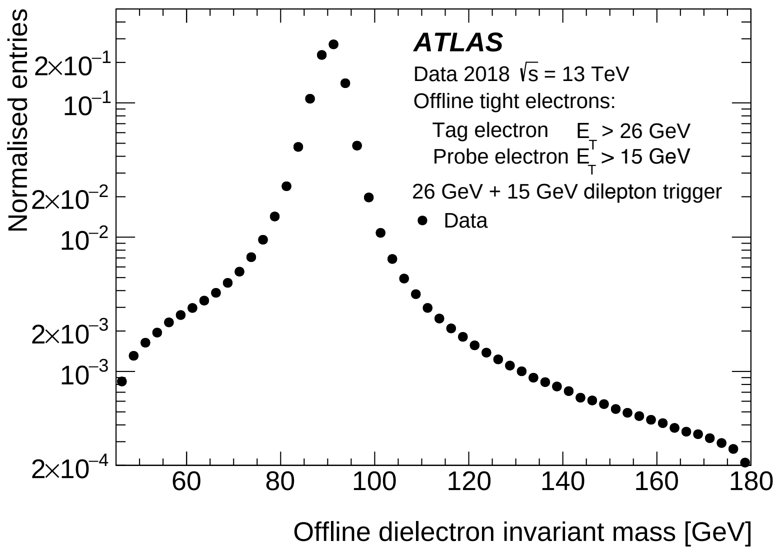

(b)

Figure 2.16: The offline (a) di-muon and (b) di-electron invariant mass from events passing the Tag-and-Probe analysis selection from the corresponding trigger chains. For the performance trigger chains, the RoIs used in the FTF and precision tracking are the same and, as such, the offline di-lepton candidates chosen for the analysis in both stages are identical. [85]

leptons and not other mis-identified objects (e. g. jets), thus also contributing to the good accuracy of the performance measurement.

The dataset used for this measurement is that collected by the ATLAS experiment in the 2018 data-taking period, when di-lepton trigger chains with `idperf` probe legs began to be included in the trigger menu. As it will be shown below, the Tag-and-Probe analysis performed in the 2018 dataset alone is sufficient to obtain a much greater statistical precision compared to the “standard” approach. As the ATLAS offline muon and electron reconstruction algorithms (see Section 3.3.2) have not changed dramatically over the course of Run 2, the 2018 dataset can be considered representative subset of the entire Run 2 statistics. The measured efficiencies with the Tag-and-Probe technique for muons and electrons are shown in Figures 2.17-2.18 and 2.19-2.20, respectively.

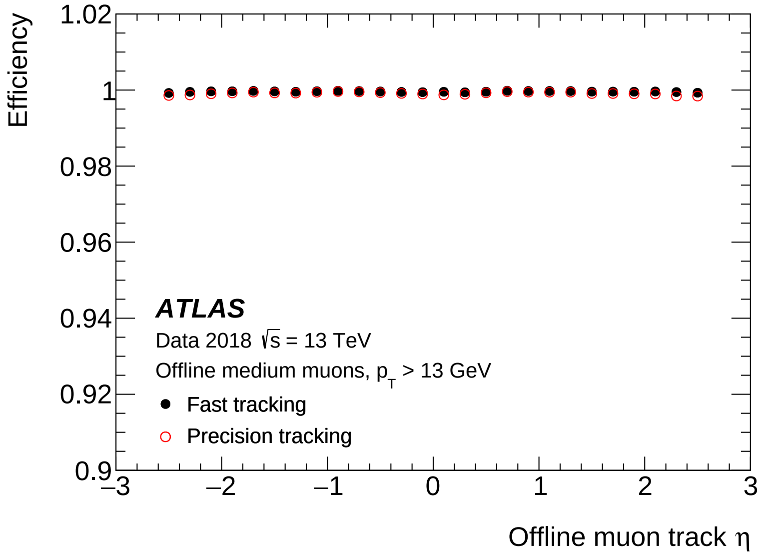

(a)

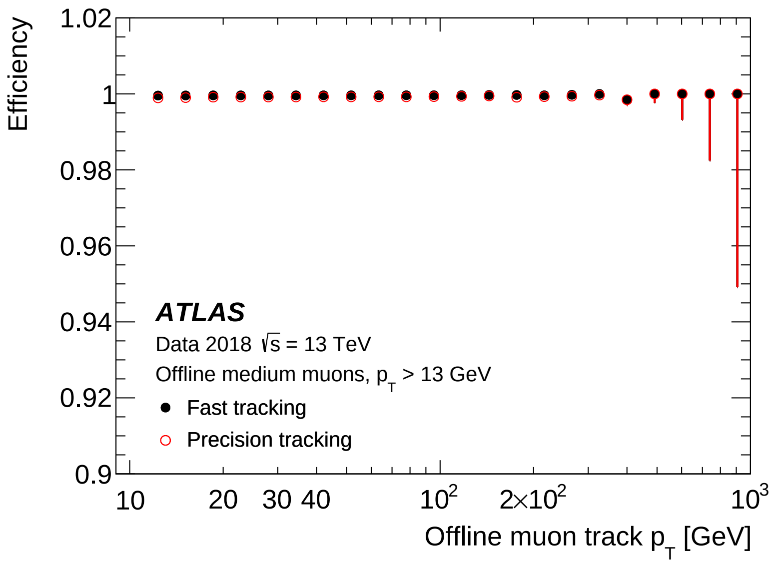

(b)

Figure 2.17: The ID tracking efficiency, estimated with the Tag-and-Probe technique, for muons selected by the di-muon chain, with respect to offline muon candidates with $p_T > 13$ GeV. The efficiency is shown as a function of: (a) the offline-reconstructed muon η and (b) p_T. Efficiencies are shown for both FTF and precision tracking. The error bars represent the estimated statistical uncertainties. [85]

From a one-to-one comparison with the full Run 2 ID trigger performance analysis using the “standard” approach (Figures 2.11-2.12 and 2.13-2.14), the results of the Tag-and-Probe analysis show a significantly reduced size of the error bars, thus the improvement of the statistical precision. This allows to study the features discussed in Section 2.4.2, such as the degradation of the efficiency for electrons due to bremsstrahlung, with much greater accuracy.

The tracking efficiencies for the muons for both FTF and precision tracking approach 100%. Furthermore, the smaller statistical uncertainties in the Tag-and-Probe approach extend the

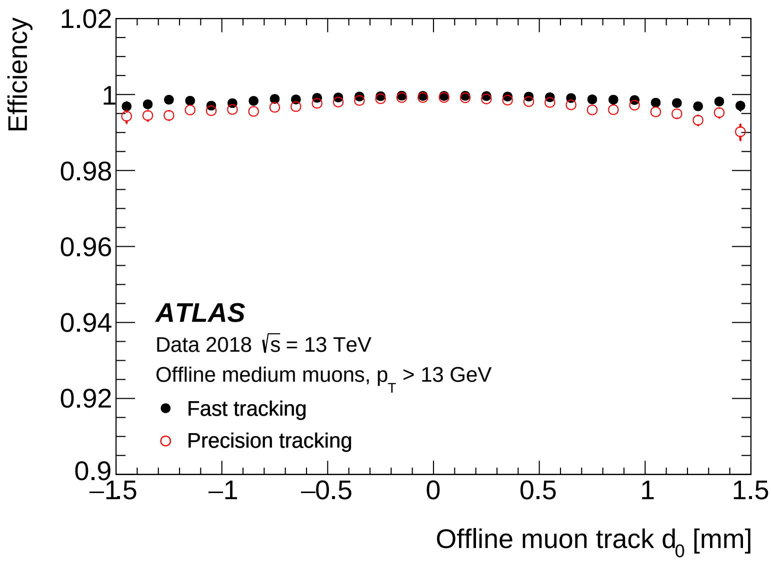

(a)

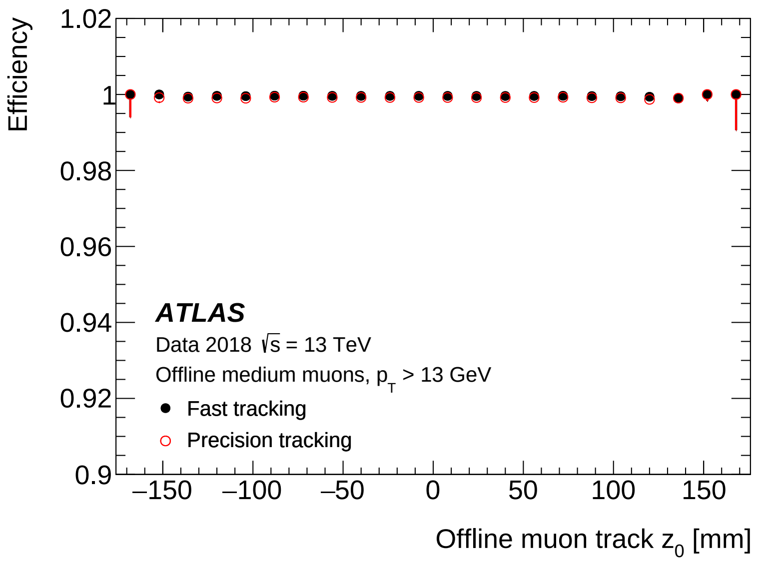

(b)

Figure 2.18: The ID tracking efficiency, estimated with the Tag-and-Probe technique, for muons selected by the di-muon chain, with respect to offline muon candidates with $p_T > 13$ GeV . The efficiency is shown as a function of: (a) the offline-reconstructed muon transverse and (d) longitudinal impact parameter. Efficiencies are shown for both FTF and precision tracking. The error bars represent the estimated statistical uncertainties. [85]

estimation of the efficiency up to a p_T of 1 TeV (Figure 2.17b), well beyond what is possible with the "standard" approach (Figure 2.11b).

For electrons, the statistical improvement is even greater compared to the muon case. This is mostly due to the significantly increased purity of the offline sample selection achievable through the Tag-and-Probe analysis compared to the "standard" approach, in which most of the available statistics does not satisfy the very stringent offline electron selection criteria and is therefore rejected. This enables to more precisely evaluate the impact of bremsstrahlung, which is responsible for the degradation of the efficiency in the precision tracking stage for high values of E_T / p_T (Figure 2.19b) and low offline electron track p_T (Figure 2.20a).

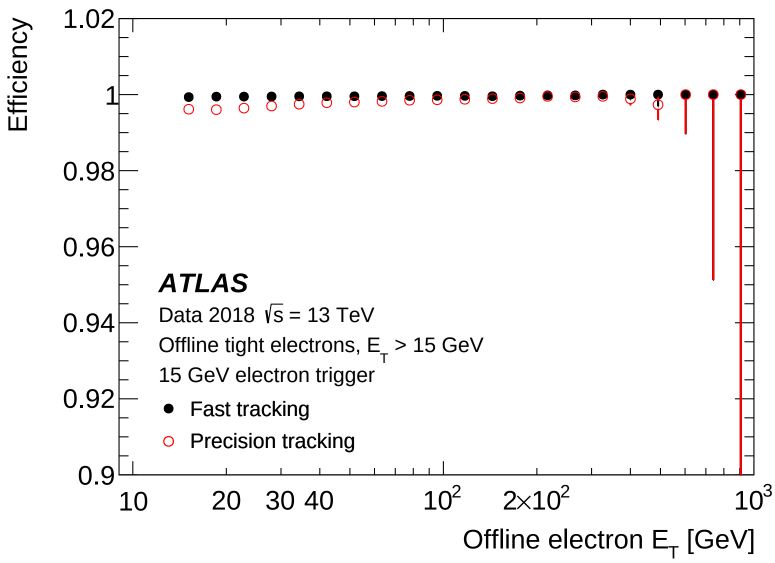

(a)

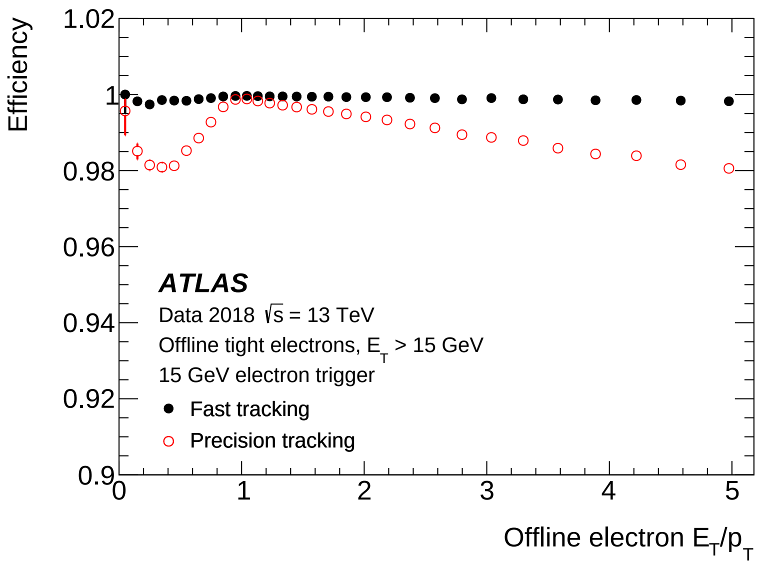

(b)

Figure 2.19: The ID tracking efficiency, estimated with the Tag-and-Probe technique, for electrons selected by the di-electron chain, with respect to offline electron candidates with the $E_{\mathrm{T}} > 15$ GeV. The efficiency is shown as a function of: (a) the offline-reconstructed electron E_{T} and (b) $E_{\mathrm{T}}/p_{\mathrm{T}}$. Efficiencies are shown for both FTF and precision tracking. The error bars represent the estimated statistical uncertainties. [85]

I started to work on the task outlined in this Section, at the end of Run 2. By that time, it was necessary to assess how the ID trigger had performed during the past data-taking period. For this reason I have contributed as well to the performance measurements following the "standard" approach, whose results have since then been published. Having demonstrated the feasibility of performing a similar analysis by using the Tag-and-Probe technique, and having shown the significant improvement in the statistical precision which can be attained through its usage, the results presented in this Section have also been included in the official performance paper of the ATLAS ID trigger [85].

For Run 3, which is set to begin in mid-2022, the Tag-and-Probe analyses are expected to

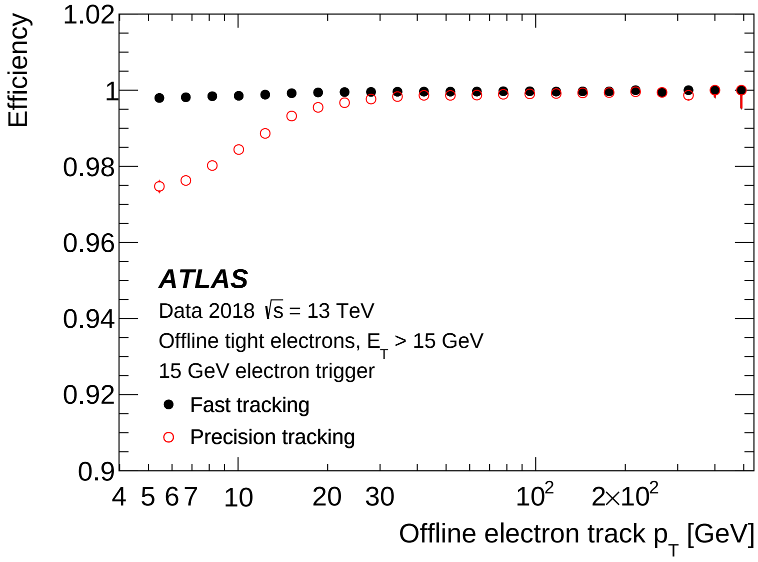

(a)

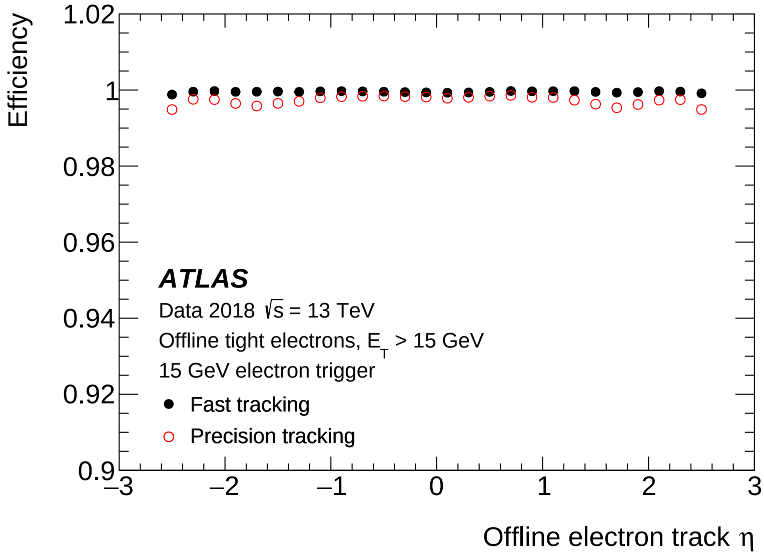

(b)

Figure 2.20: The ID tracking efficiency, estimated with the Tag-and-Probe technique, for electrons selected by the di-electron chain, with respect to offline electron candidates with the $E_T > 15$ GeV. The efficiency is shown as a function of: (a) the offline-reconstructed electron track p_T and (b) η. Efficiencies are shown for both FTF and precision tracking. The error bars represent the estimated statistical uncertainties. [85]

become a significant part of the standard validation and performance monitoring of the ID trigger. For this reason, over the course of my PhD I have continued to work in the development of the Tag-and-Probe software routine, contributing to migrate it to the newest releases of the official `Athena` software to be used in Run 3.

3 EVENT SIMULATION, RECONSTRUCTION AND OBJECTS DEFINITION

In order to properly carry out a physics analysis based on data collected with the ATLAS experiment, it is crucial to thoroughly understand the data recorded from each p-p collision, commonly referred to as an *event*. The usage of Monte Carlo (MC) techniques for the simulation of p-p collision events is of undeniable importance for this purpose. It is also necessary to interpret the detector-level information and the generated MC physics processes to identify and reconstruct the *physics objects* that make up an event.

In this Chapter, the features of the main MC generators used in the ATLAS experiment are introduced, followed by a description of the procedures employed to reconstruct and define the relevant physics objects in each event, which constitute the basic ingredients for performing the analyses described in the following Chapters of this thesis.

3.1 Structure of the proton and p-p interactions

The strong interaction nature of a p-p collision as well as the composed structure of the proton, make the understanding of the products of such interaction arduous compared to e. g. an e-e collision. A proton comprises three *valence quarks*, which determine the quantum numbers and the properties of the proton, together with a *sea* of gluons and virtual quark-antiquark pairs, all collectively referred to as *partons*. The partonic structure of the proton has been confirmed in Deep Inelastic Scattering (DIS) experiments [87], such as the ones carried out by the H1 [88] and ZEUS [89] Collaborations. In particular, the probability of finding a parton which carries a fraction x of the total momentum squared Q^2 transferred to the parent proton is described by the so called Parton Distribution Functions (PDFs). The latter have been measured in the aforementioned DIS experiments. Figure 3.1 shows such distributions measured by the ATLAS and H1 experiments [90].

A precise knowledge of the PDFs is crucial to understand the results of a p-p interaction. A typical collision event at p-p colliders is characterised by what is referred to as a *hard scattering* subprocess, where a large momentum transfer occurs between two partons, belonging respectively to each of the two incoming protons, and followed by a plethora of *soft* interactions, with progressively smaller momentum transfers involved. Given the asymptotically free nature of

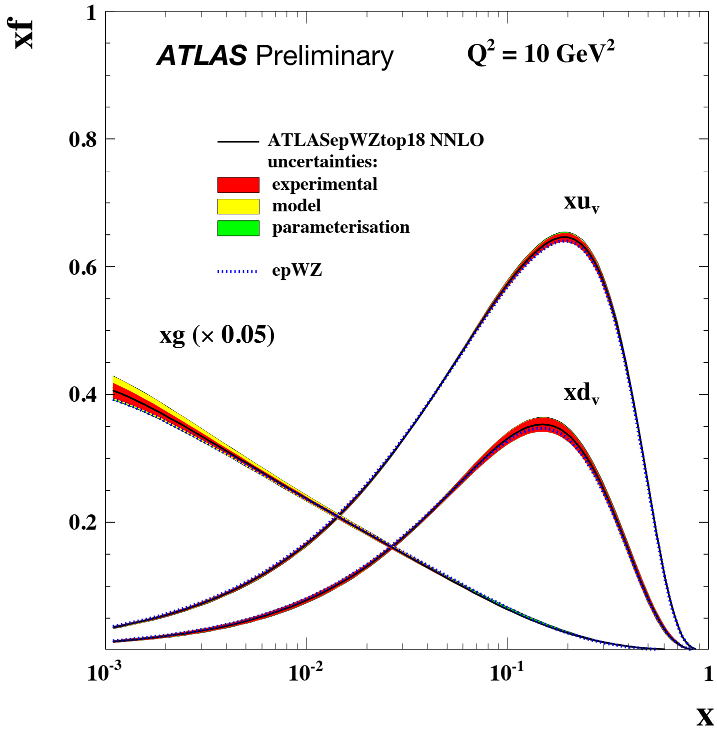

Figure 3.1: Proton PDFs measured with inclusive gauge boson and $t\bar{t}$ production data from the ATLAS experiment jointly with DIS data from the H1 experiment, at a scale of $Q^2 = 10\,\text{GeV}^2$. The xu_v and xd_v represent the PDF of valence up-quarks and down-quarks. The PDF for the gluons, xg, and the sea-quarks $xS = 2x(\bar{U} + \bar{D})$, are scaled down by a factor of 20. Experimental and modelling uncertainties are included. [90]

QCD, the hard scattering subprocess, $ab \to n$, can be described by perturbation theory, thus making it possible to compute the total p-p interaction cross-section [91] as:

$$\begin{aligned}\sigma_{p_1 p_2} &= \sum_{a,b} \int_0^1 \mathrm{d}x_a \mathrm{d}x_b \int f_a^{p_1}(x_a, \mu_F)\, f_b^{p_2}(x_b, \mu_F)\, \mathrm{d}\hat{\sigma}_{ab\to n}(\mu_F, \mu_R) \\ &= \sum_{a,b} \int_0^1 \mathrm{d}x_a \mathrm{d}x_b \int \mathrm{d}\Phi_n\, f_a^{p_1}(x_a, \mu_F)\, f_b^{p_2}(x_b, \mu_F) \times \frac{1}{2\hat{s}} \left|\mathcal{M}_{ab\to n}\right|^2 (\Phi_n; \mu_F, \mu_R),\end{aligned} \tag{3.1}$$

where: μ_F and μ_R are the *factorisation* and *renormalisation scales*, respectively, which regulate the occurrence of infrared and ultraviolet divergences of the theory; $f_{a(b)}^{p_{1(2)}}(x_{a(b)}, \mu_F)$ is the PDF, which depends on the momentum fraction x of the parton $a(b)$ with respect to its parent proton $(p_{1(2)})$, and on μ_F; $\hat{\sigma}_{ab\to n}$ represents the parton-level cross-section for the production of the final state n from the initial partons a and b, and depends on the momenta in the final-state phase-space Φ_n, as well as μ_F and μ_R. Moreover, the fully differential parton-level cross-section is given by the product of the corresponding *matrix element* squared $|\mathcal{M}_{ab\to n}|^2$, and the parton flux $1/(2\hat{s}) = 1/(2x_a x_b s)$, where s is the proton-proton collision centre-of-mass energy squared.

Events of physical interest studied at the LHC are usually the product of the primary hard scattering process. However, since the colliding protons are complex bound states of strongly-interacting partons, it is possible that more than one pair would interact. These multiple interactions, which usually involve lower momentum transfers compared to the hard scattering subprocess, are responsible for the presence of additional partons in the final state, which can contribute to any observable measurement related to the primary process of interest. Such part of the proton-proton collision event structure is commonly referred to as the *underlying event*.

Furthermore, given the properties of QCD, all the produced partons give rise to the so-called Parton Shower (PS), in which continuous interactions, i.e. $g \to gg$, $g \to q\overline{q}$ and $q \to qg$, generate an avalanche from the final state of the hard scattering. Moreover, given the progressively lower momentum transfers involved in the PS, these interactions are dominated by non-perturbative effects and their modelling must be assessed via phenomenological, stochastic algorithms.

As the collision event evolves to progressively lower transferred momentums, specifically at scales at the order of 1 GeV, referred to as the *hadronisation scale*, the QCD interaction between the generated partons becomes so strong that perturbation theory breaks down completely, resulting in a confined system of coloured partons in which clusters are formed to ultimately become colourless hadrons. An important feature of this process is that partons do not hadronise independently, but rather collectively in colour-connected systems of incoming and outgoing partons [92]. A sketch schematically illustrating the structure of a typical p-p interaction is reported in Figure 3.2.

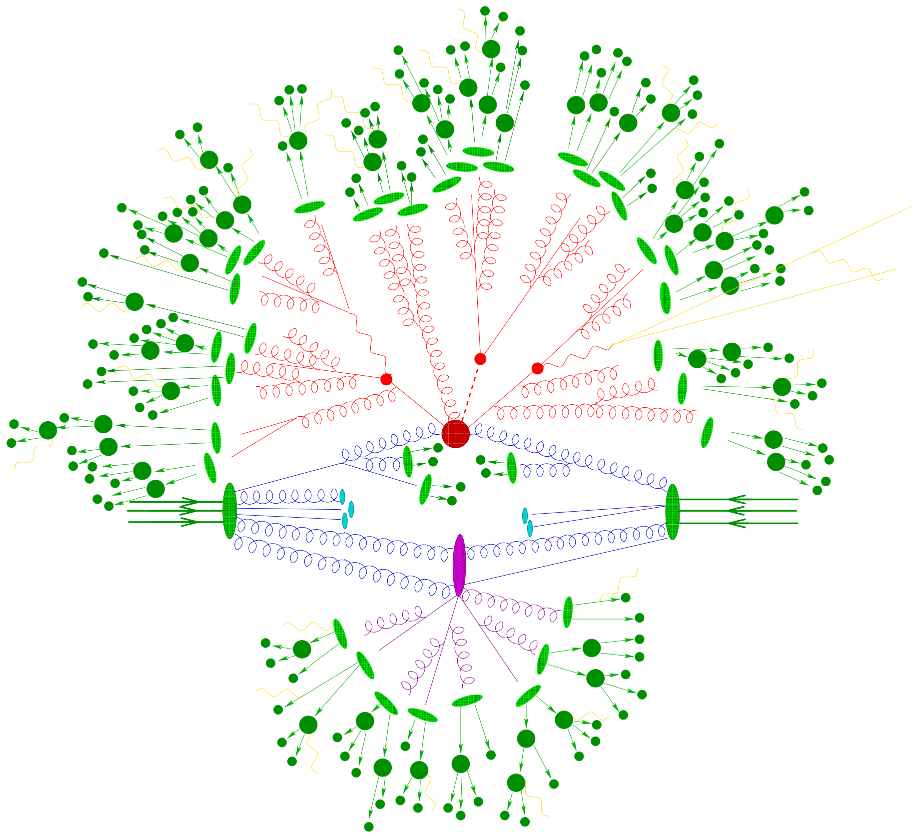

Figure 3.2: Sketch of a typical p-p collision. The red blob in the centre represents the hard scattering, surrounded by the PS interactions (see text). The purple blob indicates a secondary underlying event. Parton-to-hadron transitions are shown through light green blobs, dark green blobs indicate hadron decays, while yellow lines signal soft photon radiation. [93]

The PS evolution is largely dominated by the emission of additional partons, which are mostly soft and/or collinear with the outgoing partons. This results in structures where most of the energy is localised in collinear bundles of hadrons, called *jets*. The hadronisation mechanism preserves such jet structure, which can be observed experimentally [94]. Finally, some of the products of hadronisation and the hard scattering subprocess itself may be unstable particle resonances, which in turn might be long-lived enough to be experimentally accessible in the time-scales of particle physics detectors, thus contributing to the observed final state.

3.2 ATLAS event simulation

3.2.1 Event generation

The ATLAS experiment extensively employs general-purpose MC event generators in order to simulate p-p collisions at the LHC. The wide range of the simulated processes covers SM processes as well as BSM physics scenarios. The core of MC generators is the computation of the matrix-elements associated with the process of interest. The perturbative nature of the calculation allows to estimate them with fully automated tools, including a comprehensive list of Feynman diagrams relevant for the process in question. The Leading Order (LO) computation only takes into account tree-level diagrams and the corresponding phase-space parametrisations for these processes resulting in one, two or three particles from the hard scattering interaction [92]. The choice of μ_F and μ_R, and of the PDF, plays a crucial role in this context. The value of μ_F and μ_R usually varies from generator to generator. A typical example is the s-channel production of a resonance of mass M, in which $\mu_F = \mu_R = Q^2 = M^2$ is typically a suitable choice [92]. Regarding the PDF set, it is possible to choose any parametrisation that matches the accuracy of the cross-section calculation. All generators typically have access to a library of PDF sets contained in the `LHAPDF` interface [95]. Each generator uses a default PDF set, whilst the prediction of certain tunes of the parameters for the PS, hadronisation and underlying event may be addressed by changing the PDF set. A common choice for the default PDF sets of the MC samples used in this work is the `NNPDF` set [96].

In order to improve upon the LO prediction it is necessary to reach at least Next-to-Leading Order (NLO) accuracy. This is achieved by considering loop effects and radiative corrections, such as Initial State Radiation (ISR) and Final State Radiation (FSR) emissions of partons before and after the hard scattering. This process is not fully automated in multi-purpose generators and it is usually affected by the presence of divergences, which must cancel out between the various terms. In order to globally account for NLO effects, LO cross-sections can be in some cases multiplied by a flat correction factor, called the k-factor [92]. Moreover, for the purpose of minimising the statistical fluctuations of the simulation of a rare process, generators can be forced to feature certain decay modes requiring specific final states. In these circumstances, a *generator filter* is used to select the desired events, and a multiplicative *filter efficiency* correction factor is applied to reweight the cross-section of the process of interest, to account for the enhanced statistics. The algorithms for PS are typically formulated as an evolution in transferred momentum from the high scales of the hard process to the hadronisation scale. The properties of QCD allow to write the cross-section for the production of an additional parton in the final state, other than the particles produced in primary hard scattering process, by simply multiplying multiplying the tree-level cross-section by a certain splitting function. This allows to implement the PS in generators as iterative algorithms, called *Markov chains*, in which one parton is stochastically added to the final state at a time [92]. A consistent combination of tree-level matrix-elements containing multiple well-separated partons with each other and with the PS is usually achieved by using the *multi-jet merging algorithm* at LO, developed by Catani, Krauss, Kuhn and Webber (CKKW) [97]. In this procedure the second and higher emissions in the PS are corrected to the corresponding tree-level matrix-element at the price of introducing a technical *merging scale* above which the corrections are made [92]. For what concerns the hadronisation, the main implementations currently in use in event generators can be categorised in two separate classes: the *string* models, e.g. the *Lund* model [98], and the *cluster* models [99]. The Lund models "transform" partonic systems directly into hadrons through linear confinement models supported by lattice QCD calculations, whereas cluster models employ an intermediate stage with clusters of partons at typical mass scales of a few GeV . Finally, many of the most commonly used event generator have built-in components through which it is possible to simulate pile-up and the underlying event alongside the main hard scattering process. The effect of pile-up can be either simulated independently and than superimposed to the event of interest before the full reconstruction, or emulated on the basis of data collected during running as special "zero-bias" events [100].

Analogously to the Run 2 dataset, the MC samples used in the ATLAS experiment are divided into three separate "campaigns" to match the pile-up profile measured in each year of data-taking (Figure 2.3): `mc16a` for 2015 and 2016, `mc16d` for 2017, and `mc16e` for 2018.

3.2.2 Monte Carlo generators in ATLAS

This Section serves as an overview of the general purpose MC generators used in the ATLAS experiment and of their main characteristics.

HERWIG The `HERWIG7` [101] generator features an automated generation at LO precision with full spin correlation in the final state, also for a range of BSM scenarios. Its built-in functionalities allow to achieve NLO precision with PS matching. However, this is typically attained instead by interfacing `HERWIG7` with `PYTHYA`. It implements the cluster model [99] to simulate the hadronisation and it is able to model hard and soft multiple partonic interaction for the underlying event modelling.

PYTHIA `PYTHIA8` [102] is a general purpose MC framework. Although it implements an extensive list of hardcoded processes, it is usually interfaced to other matrix-element generators, e.g. `MadGraph` [103], to better simulate complex final state with high particle multiplicity. It features a good modelling of multiple parton interactions and it handles the processes associated with PS and the underlying event by ordering them from greater to lower values of the transferred momentums involved. The hadronisation modelling is based on the Lund string fragmentation algorithm [98].

SHERPA SHERPA [104] is a general purpose, all-inclusive event generator, which puts particular emphasis on the strict modularity of its physics packages. It features a complete matrix-element calculation with advanced phase-space integrations methods, including an infrastructure to allow the estimation of cross-sections with NLO accuracy. Its cornerstone is the implementation of the multi-jet merging scheme with the CKKW approach. SHERPA has a fully independent PS and hadronisation schemes, the latter of which is based on the cluster model.

MadGraph MadGraph5 [103] is a dedicated matrix-element and phase-space generator with LO accuracy in a wide range of physics models, including BSM scenarios, even for high particle multiplicity in the final state. It is possible to reach the NLO precision for cross-sections by means of the aMC@NLO extension [105]. It is usually interfaced with other generators, e. g.PYTHIA8, for PS and hadronisation simulation.

POWHEG POWHEG [106, 107] features an advanced matrix-element reweighting procedure, through which it is possible to achieve NLO precision. It implements a PS mechanism with parton emissions not ordered by hardness, which often result in a poor modelling for the colour structure. For its typical usage, it is commonly interfaced with PYTHIA8 or HERWIG7 generators for the simulation of PS and hadronisation.

EvtGen EvtGen [108] is an external package with a sophisticated simulation of hadronic decays, especially B-meson decays for precision studies of CP-violating phenomena. It is typically interfaced to PYTHIA8 or HERWIG7 simulations in order to improve the reliability of their hadronisation modelling.

3.2.3 ATLAS detector simulation and digitisation

The full simulation of the detector response is handled with the GEANT4 toolkit [109], which is fully integrated in the official software framework of the ATLAS Collaboration, Athena. Athena features an implementation of the full detector geometry and the material and utility services distribution. It is able simulate the interaction of the generated particles with each of the detector components of the ATLAS experiment, producing a pattern of all the energy deposits in the sensitive detector cells interested. The main drawback of such detailed simulations is the expensive use of CPU resources and the long computation time needed to simulate each event. About 90% of the computation power is spent just on the simulation of particle interactions with the calorimeters.

To reduce computation times without compromising on precision, the FastCaloSim package [110] was developed to provide a fast calorimeter simulation with a sufficiently good accuracy such that key features of reconstructed object properties can be reproduced and adequate, whilst still simplifying the simulation model. The FastCaloSim package has been implemented, along the full simulation of the ATLAS ID and MS from GEANT4, in the ATLFastII (AFII) simulation, which in general reduces the processing time compared to the full ATLAS simulation by a factor of ten. More details about the features and drawbacks of AFII can be found in [111]. The simulations of all SUSY processes taken into account in this thesis have been generated with the AFII prescription.

The final step for MC sample production, before the offline event reconstruction 3.3.2, is the so-called *digitisation*, in which the ATLAS detector discrete response is calculated in forms of digits from the hits in the sensitive detector volume generated in the previous step. The digits created are processed to emulate the output of the different RODs. In this way MC sample can have a format analogous to that of the recorded data, allowing both to be processed using exactly the same algorithms during the event reconstruction.

3.3 ATLAS event reconstruction

3.3.1 Event flow and data formats in ATLAS

The entire infrastructure for collecting, simulating and reconstructing data is also implemented in `Athena`. Such infrastructure is represented schematically in Figure 3.3 and consists of several steps, which correspond to specific data formats.

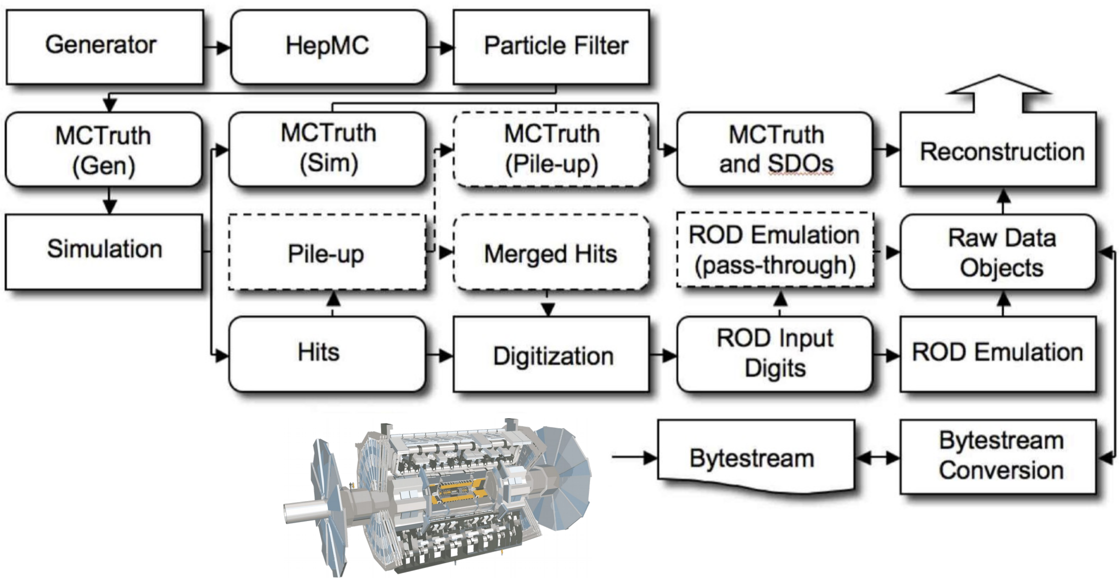

Figure 3.3: Schematic representation of the flow of data processing (starting from the bottom) and simulation (starting from the top-left) framework in the ATLAS experiment. The square-cornered boxes represent algorithms, while persistent data objects are placed in rounded boxes [112].

First, the event generators are used to produce the outgoing particles from LHC collisions in the `HepMC` format [113]. *Truth-level* information about the generated primary hard process is often retained through the entire data flow, thus making it available for dedicated studies during the final data-analysis stage. Next, through the detector simulation, HITS files are produced, which represent the energy deposits of particles in the sensitive detectors cells. These files are then processed via the digitisation, which, through the process described in

Section 3.2.3, converts byte-streams into C-files, called Raw Data Objects (RDOs) [112]. This is exactly the same format which is created after actual collision data (RAW format) are read and interpreted from the dedicated RODs. The final step of the ATLAS data-processing flow before the data analysis is the *reconstruction* (Section 3.3.2), in which times and voltages representing the detector response are reinterpreted into physics analysis objects. In this stage files are converted in the Analysis Objects Data (AOD) format [114] which is commonly used for physics analyses, along with its "lighter" version the Derived AOD (DAOD), by means of the `ROOT` interface [115].

3.3.2 Object reconstruction

In this Section a description of some of the dedicated reconstruction algorithms is given for the objects used in physics analyses. These include: electrons and photons, muons, hadronically-decaying taus, $E_{\mathrm{T}}^{\mathrm{miss}}$ and jets, also considering those originating from the heavy-flavour quarks.

Track and vertex reconstruction

The track reconstruction algorithms that are currently used in the ATLAS experiment [116] were firstly implemented in `Athena` for the commissioning of Run 1. Their design features an iterative track finding algorithm from the Pixel and SCT detectors, followed by an ambiguity solving stage and finally a high purity track fitting which also includes the information from the TRT [117]. The offline track reconstruction algorithm usually starts by collecting the hits from the trajectories of the charged particles travelling across the active material of the Silicon ID. Depending on the energy loss and the charge accumulated in the sensors, *clusters* are created from the group of pixels and strips in a given sensor which are affected by the passage of the charged particle. These clusters are then used to form three-dimensional representations, called *space-points*. A cluster in a Pixel layer would correspond to a single space-point, whereas two clusters in a SCT module – one for each side of the strip – are needed for creating a space-point.

Next, sets of three space-points are used to form *track seeds*, for which the impact parameter with respect to the centre of the interaction region is also estimated by assuming a perfect helical trajectory in a uniform magnetic field [117]. A combinatorial Kalman filter algorithm [118] is then used to build track candidates, which include additional space-points from the remaining layers of the Silicon detectors compatible with the preliminary particle trajectory. Due to the occurrence of instances related to e.g. shared clusters, track candidates can correspond to the same seed. Hence, the ambiguity solver stage becomes essential. It consists on assigning a *score* to each track candidate based on its properties (e.g. number of associated clusters, number of missed layers or *holes*, χ^2 value from the track fit, $\log(p_{\mathrm{T}})$ of the track, etc.).

Track candidates are then processed individually in a descending order of these scores, favouring higher scores. Moreover, candidates are rejected if they do not satisfy the following quality criteria: $p_{\mathrm{T}} > 400\,\mathrm{MeV}$, $|\eta| < 2.5$, ≥ 7 clusters in the Silicon layers, ≤ 1 shared Pixel cluster or ≤ 2 shared SCT clusters, ≤ 2 holes in the Silicon layers, and ≤ 1 hole in the Pixel layers [117]. Quality criteria are also required concerning the corresponding vertex candidates. The latter are identified if at least two track candidates are found to be originating from them. In particular, the *primary vertex* is defined as the one whose associated tracks give the highest sum of the squared transverse momenta, and it is linked to the hard scattering process.

Track candidates are rejected if their associated vertex does not satisfy the following criteria: $|d_0^{\mathrm{BL}}| < 2.0\,\mathrm{mm}$ and $|z_0^{\mathrm{BL}} \sin\theta| < 3.0\,\mathrm{mm}$, where d_0^{BL} is the transverse impact parameter with respect to the beam line, z_0^{BL} is the longitudinal impact parameter along the beam line, and θ is the polar angle of the track. In order to aid the ambiguity-solving stage, an artificial Neural Network (NN) for pixel clustering has been implemented for Run 2 [119]. Finally, a high-resolution, global-χ^2 track fit is performed for the candidates which survive the ambiguity-solving selection, also extending the tracks by including the information from the TRT [116].

Electrons and photons

As far as the ATLAS offline reconstruction is concerned, an electron is defined as an object consisting of a cluster built from the energy deposited in the ECal, which is matched to one (or more) ID tracks. The reconstruction can be made more challenging due to the fact that electrons interacting with the detector material may loose a considerable amount of their energy via bremsstrahlung, which can in turn be followed by an electron-positron pair production through the conversion of the radiated photon. The emitted particles are generally collimated with the original electron, resulting in a single energy cluster in the ECal. Moreover, these interactions may occur in the ID volume or even in the beam pipe, thus generating multiple ID tracks.

The ATLAS electron reconstruction algorithm starts by preparing the tracks and the clusters it will use, selecting the latter from energy deposits measured in topologically-connected ECal and HCal cells, called *topo-clusters*. These are identified if the measured energy is greater then a noise threshold, given by the electronic noise and the expected pile-up events. For Run 2, the original sliding-window algorithm [120], based on fixed-size clusters of calorimeter cells, has been replaced to use dynamic, variable-size clusters, called *superclusters* [121]. This improves the reconstruction by allowing to better recover the energy from bremsstrahlung photons or from electrons from photon conversions. The superclusters are then matched to ID tracks[1], which are in turn re-fitted accounting for bremsstrahlung, which may generate "kinks" in the trajectory of the original electron. This step employs a Gaussian Sum Filter (GSF) algorithm [122], which improves the original track parameter estimation. The reconstruction of photons follows a similar procedure to that of electrons for what concerning the algorithm based of the topo-clusters from the showers in the ECal. The main difference with respect to the electron case is that ECal clusters associated with a candidate photon are required not to match

[1] Tracks are considered matched to a cluster if they satisfy $|\Delta\eta| < 0.05$ and $-0.10 < q\cdot(\phi_{\mathrm{track}} - \phi_{\mathrm{cluster}}) < 0.05$, where $\Delta\eta$ is the measured pseudo-rapidity distance between the track and the cluster, q is the reconstructed charge of the track, ϕ_{track} and ϕ_{cluster} are the azimuthal angles of the track and the cluster, respectively [121].

any ID track. An ambiguity-solving procedure is applied to remove possible overlap between the reconstructed electrons and photons [121]. Electron and photon objects to be used for physics analyses are thus created after calibrating their energy.

Further quality criteria are applied on the *identification* of reconstructed electron objects, to better discriminate *real* or *prompt* electrons against the so-called *Fake/Non-Prompt* (FNP) electrons, i. e. objects originating from energy deposits of light-flavour hadronic jets and mis-reconstructed as electrons. The identification criteria are extracted with a Likelihood (LH) approach, which relies of relevant shower quantities as well as MC simulations of $Z \to ee$ and $J/\psi \to ee$ events [121]. Depending on the cut imposed on the LH discriminant and the corresponding efficiency for identifying prompt electrons, different Working Points (WPs) are defined: `Loose`, `Medium` and `Tight`. These correspond to efficiencies of 93%, 88% and 80%, respectively, for electrons with $E_{\mathrm{T}} = 40$ GeV [120]. Figure 3.4 shows the measured efficiencies for these WPs as functions of E_{T}. All WPs have fixed requirements of the tracking criteria. Specifically the `Medium` and `Tight` WPs both require a hit in the innermost pixel layer, to reduce the contamination from photon conversions. Additionally, a variation of the `Loose` WP – called `LooseAndBLayer` – is introduced by also requiring a hit in the IBL [120].

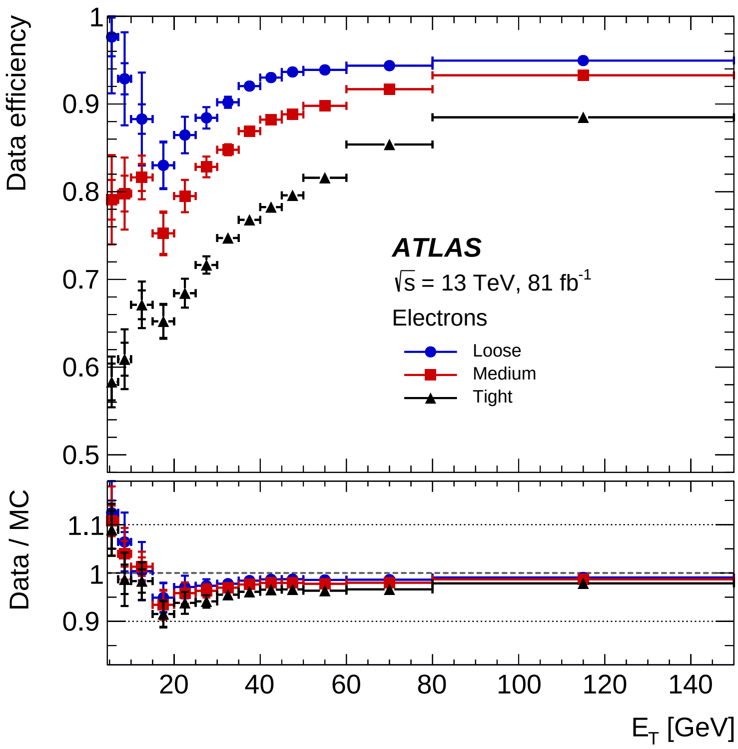

Figure 3.4: Efficiency for the LH-based identification of electrons measured in the data collected in 2015-2017, as a function of the electron E_{T}, for the three WPs: `Loose` (blue), `Medium` (red) and `Tight` (black). The lower panel shows the ratio between data and MC. Statistical and systematic uncertainties are considered [121].

A further suppression of the contamination from the FNP electrons, particularly those arising from the decay of heavy-flavour hadrons, is achieved by imposing quality requirements on the *isolation* of electrons. In ATLAS, electron isolation WPs are defined with a fixed cut of the energy deposited in a cone – usually of size $\Delta R = 0.2$ – around the reconstructed object and measured from both the calorimeters and the ID. The calorimeter-based isolation $E_{\mathrm{T}}^{\mathrm{cone20}}$ is extracted from the total calorimetric energy deposited within the cone subtracting the particle energy and accounting for leakage and pile-up effects, whereas the track-based isolation $p_{\mathrm{T}}^{\mathrm{varcone20}}$ is computed by summing the p_{T} of selected ID tracks within a the cone centred around the electron track. Since tracks from the decay of heavy-flavoured particles can be very close to the electron track, the track-based isolation uses a variable cone size, which shrinks for very energetic electrons. Electron isolation WPs can then be defined considering the cuts reported in Table 3.1). Figure 3.5 shows the measured isolation efficiency for the available WPs and for `Medium` identified electrons.

Table 3.1: Definition of the electron isolation WPs used in the analyses described here. The definition of other available WPs can be found in [121].

WP name	Calorimeter isolation	Track isolation
`Loose`	$E_{\mathrm{T}}^{\mathrm{cone20}} / p_{\mathrm{T}}^{e} < 0.20$	$p_{\mathrm{T}}^{\mathrm{varcone20}} / p_{\mathrm{T}}^{e} < 0.15$
`Tight`	$E_{\mathrm{T}}^{\mathrm{cone20}} / p_{\mathrm{T}}^{e} < 0.06$	$p_{\mathrm{T}}^{\mathrm{varcone20}} / p_{\mathrm{T}}^{e} < 0.06$

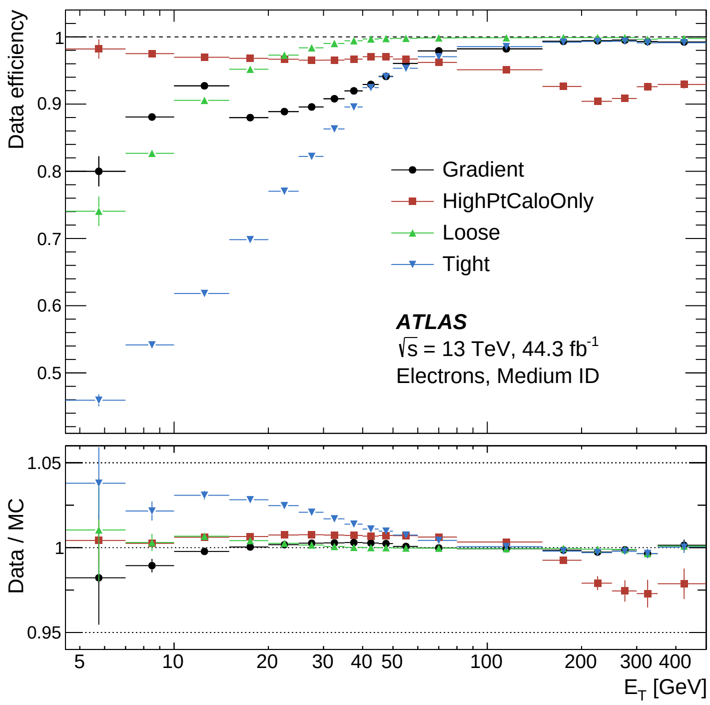

Figure 3.5: Efficiency of the different isolation WPs for electrons from inclusive $Z \to ee$ events measured in the data collected in 2017, as a function of the electron E_{T}. The electrons are required to fulfil the `Medium` selection from the LH-based electron identification. The lower panel shows the ratio of the efficiencies measured in data and in MC. Statistical and systematic uncertainties are considered [121].

Finally, the electric charge of the reconstructed electron is determined from the curvature of the associated ID track. The charge can be misidentified as a result of the calorimeter cluster being matched to the wrong track or from a mismeasurement of the curvature of the primary electron track, especially for high-p_{T} electrons, whose associated tracks tend to be straighter (Figure 3.6a). However, the most likely cause for the mis-reconstruction of the electron charge, can be traced back to bremsstrahlung emission and subsequent photon conversion to an electron–positron pair (Figure 3.6b).

The presence of additional electrons and positrons in close proximity can cause the track to be reconstructed from hits of primary and secondary electrons and positrons, which in turn can result in a reconstructed matched electron track with the opposite curvature compared to that of the primary electron. The probability for reconstructing these so-called *Charge-Flip* (CF) electrons increases significantly with the amount of detector material traversed, hence, it is higher for $|\eta| \gtrsim 2.0$. In the ATLAS offline reconstruction the presence of CF electrons can be reduced with an additional selection criterion based on the output discriminant of a Boosted Decisions Tree (BDT), trained using simulated single-electron samples and relying on a set of variables related to the electron cluster and track properties [120]. A selection requirement on the BDT output is chosen such as to achieve an efficiency in selecting the correct charge of 97.77% in $Z \to ee$ MC events for electrons satisfying the `Medium` or `Tight` identification with the `Tight` isolation requirement. Approximately 90% of the wrong-charge electrons with the same identification and isolation requirements are thus rejected [121]. This specific selection is available for the `Loose` WP of the ElectronChargeIDSelector (ECIDS) package [123].

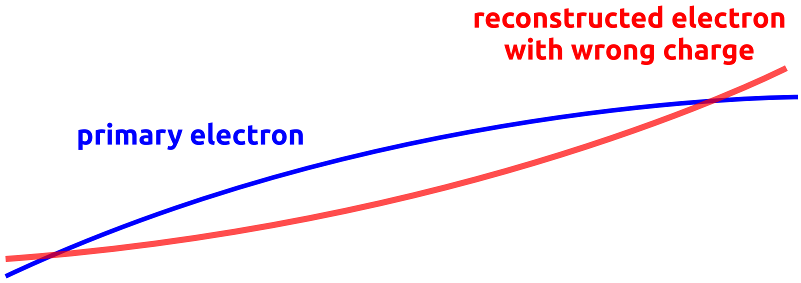

(a)

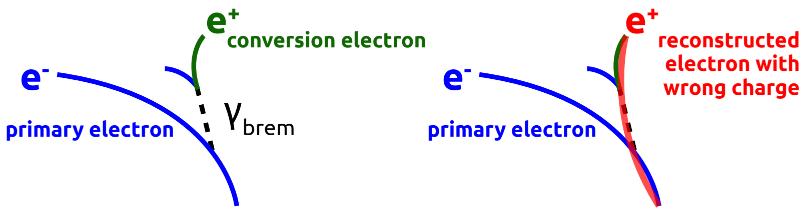

(b)

Figure 3.6: Schematic representation of the occurrence of the electron CF due to: (a) charge mis-reconstruction of high track p_{T} electrons, or (b) hard bremsstrahlung followed by photon conversion in the detector material.

Since photons have not been taken into account in any of the analyses included in this thesis, the description of their identification and isolation criteria is not discussed here. Further details can be found in [121].

Muons

In the ATLAS experiment the reconstruction of muon objects is based primarily on the matching of the track information from the MS and the ID. Specifically, the reconstruction starts from straight-line track candidates identified through a Hough transform [124] from hits in individual stations of the MS. These are then combined into muon track candidates by considering the measured impact parameter and a parabolic trajectory in the magnetic field. Finally, a global χ^2 track fit is performed including the information from the ID and the calorimeters into different types of muon reconstruction, depending on how such information is included [125]. Amongst these types, the *Combined muon* category is the one commonly used in physics analyses. It is obtained by performing a combined track fit within $|\eta| < 2.5$ on both the ID and MS hits, taking also into account the energy lost by the muon in the calorimeters, thus improving the measurement of the muon parameters.

Similarly to the electrons, WPs are introduced for the *muon identification*. The quantities used to define each muon identification WP are based on: the number of different hits in the ID layers and the MS stations, the global track fit parameters and variables useful to establish the degree of compatibility of the individual measurements in the two detector sub-systems. Each WP has a different efficiency in selecting prompt muons, but they are all designed to mainly reject FNP muons from in-flight decay of light hadrons, which usually present themselves with low-quality tracks. Amongst the main muon isolation WPs there are `Loose`, `Medium` and `Tight`, whose measured efficiency has been reported in Figure 3.7.

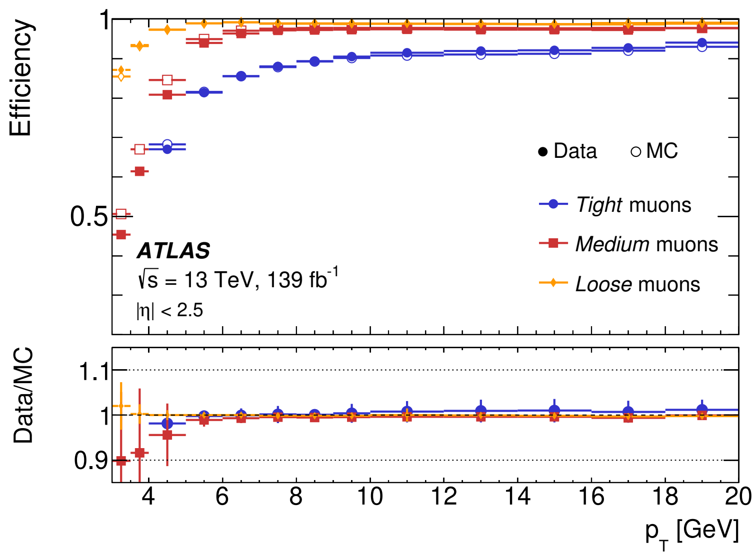

Figure 3.7: Efficiency for the reconstruction and identification of muons measured in with the full Run 2 dataset, as a function of the muon p_{T}, for the three WPs: `Loose` (yellow), `Medium` (red) and `Tight` (blue). The lower panel shows the ratio between data and MC. Statistical and systematic uncertainties are considered [125].

Muon isolation WPs are designed to further reject FNP muons from heavy-flavour hadron decays. Track-based, $p_{\mathrm{T}}^{\mathrm{varcone30}}$, and calorimeter-based isolation, $E_{\mathrm{T}}^{\mathrm{cone20}}$, variables, computed with the same procedure as that described in the electron case, are once again used to define these WPs [125]. The definition of some of the muon isolation WPs used in this work has been reported in Table 3.2. Combining selections on track-based and calorimeter-based isolations, such as in the `Loose` and `Tight` WPs, generally results in a better performance. However, since the track-based isolation is already largely independent of pile-up, thanks to the rejection of tracks from pile-up vertices or with large impact parameter with respect to the primary vertex, a higher isolation efficiency with an adequate purity can be achieved with the `TightTrackOnly` WP.

Table 3.2: Definition of the muon isolation WPs used in the analyses described here. The definition of other available WPs can be found in [125].

WP name	Calorimeter isolation	Track isolation
`Loose`	$E_{\mathrm{T}}^{\mathrm{cone20}} / p_{\mathrm{T}}^{\mu} < 0.3$	$p_{\mathrm{T}}^{\mathrm{varcone30}} / p_{\mathrm{T}}^{\mu} < 0.15$
`Tight`	$E_{\mathrm{T}}^{\mathrm{cone20}} / p_{\mathrm{T}}^{\mu} < 0.15$	$p_{\mathrm{T}}^{\mathrm{varcone30}} / p_{\mathrm{T}}^{\mu} < 0.04$
`TightTrackOnly`	-	$p_{\mathrm{T}}^{\mathrm{varcone30}} / p_{\mathrm{T}}^{\mu} < 0.06$

Jets and b-jets

The jet reconstruction is based on the lateral and longitudinal segmentation of the ECal and HCal, which allows a three-dimensional reconstruction of the hadronic showers. Similarly to the electron case, the inputs for the reconstruction are the topo-clusters. In order to account for the different response between hadronic and EM interaction, a local cluster weighting scheme [126] is applied to each topo-cluster. Clustering algorithms are then used to identify the bundles of the latter which represent the development of each hadronic jet. The *anti-*k_T algorithm [127] is a common choice to perform jet-clustering in the ATLAS experiment. It consists on an iterative procedure which bundles topo-clusters together mainly based on their distance. Another jet reconstruction scheme, called the *particle flow* algorithm [128], employs topo-clusters as well as ID tracks, in the attempt to reconstruct the development of the hadronic shower itself in the detector. Henceforth, jets reconstructed by means of the anti-k_{T} algorithm will referred to as *EMTopo* jets, whereas jets reconstructed through the particle flow algorithm will be called *PFlow* jets.

For the purpose of suppressing the impact of pile-up in the jet reconstruction the Jet Vertex Tagger (JVT) algorithm [129] is employed. It is based on a Multi-Variate Analysis (MVA) which aim to maintain the hard-scatterer jet efficiency as stable as possible as a function of the reconstructed number of vertices, using as inputs different track-based variables. Specific cuts on the output score of the JVT algorithm as well as optimised p_{T} and η ranges are used to define WPs, depending on the method used to reconstruct jets [130].

The ability to discriminate between a jet which originates from a b-hadron, referred to as a b*-jet*, against that coming from a light hadron, or *light jet*, is of crucial importance in many physics analyses both for SM precision measurements and for BSM searches. Dedicated b*-tagging* algorithms exploit the relatively long lifetime of b-hadrons, which can travel a few hundred µm in the ID before decaying, thus resulting in a secondary vertex displaced from the primary hard-scatter collision point. The ATLAS experiment makes use of dedicated b-tagging algorithms based on the measurements on the ID tracks, the interaction vertices and the properties of the reconstructed jets [131]. For this purpose only central jets, with $|\eta| < 2.5$, with at least two associated tracks are considered for b-tagging. In the analyses described in this thesis, two different b-tagging algorithms have been used: `MV2c10` [132] and `DL1r` [133]. The former is based on a BDT discriminant and it is the default choice for EMTopo jets, whereas the latter uses deep feed-forward NNs and it currently the recommended b-tagging algorithm for PFlow jets. For either of these algorithms a set of WPs are defined depending on the level of efficiency for selecting b-jets. These correspond to 60%, 70%, 77% and 85% efficiencies for jets with $p_{\mathrm{T}} \geq 20$ GeV, $|\eta| < 2.5$, and that pass the JVT criteria.

Taus

The reconstruction of hadronically-decaying taus in the ATLAS experiment starts from the identification of candidates from clusters in the HCal. Information from ID tracks are taken into account to form MVA discriminants to reject misidentified QCD jets and electrons. On the other hand, leptonically-decaying taus can be identified by the presence in the final state of electrons and muons, which are in turn reconstructed with the procedures described earlier in this Section. As the analyses described in this these do not target taus in the final state, further details about their reconstruction and identification are not reported here, but can be found in [134].

Missing transverse momentum

The reconstruction the missing transverse momentum is challenging because it involves all detector subsystems and requires the most complete and unambiguous representation of the hard interaction, whilst limiting the impact of pile-up. Two different terms contribute to the reconstruction of the final value of the $E_{\mathrm{T}}^{\mathrm{miss}}$ of each event: the *hard-event* signal comprised of the fully reconstructed and calibrated particles and jets, and the *soft-term* consisting of all reconstructed charged particle tracks associated with the primary vertex but not with any of the hard objects [135]. The computation of the $E_{\mathrm{T}}^{\mathrm{miss}}$ for each event then follows from Equation 2.6 of Section 2.2.1:

$$E_{\mathrm{T}}^{\mathrm{miss}} = \left| -\sum_{\substack{i\in\{\text{hard}\\ \text{objects}\}}} \vec{p}_{\mathrm{T}}^{\,i} - \sum_{\substack{j\in\{\text{soft}\\ \text{signals}\}}} \vec{p}_{\mathrm{T}}^{\,j} \right|. \tag{3.2}$$

The hard objects that enter the $E_{\mathrm{T}}^{\mathrm{miss}}$ calculation include electrons, muons, photons, hadronically-decaying taus and jets. They are required to be fully reconstructed and calibrated, without imposing any further requirements of their identification and isolation. On the other hand, all ID tracks entering the soft-term must satisfy reconstruction quality and kinematic selections: $p_{\mathrm{T}} > 400$ MeV, $|d_0| < 1.5$ mm and $|z_0 \sin\theta| < 1.5$ mm. Moreover, any overlap between these charged tracks and the remaining objects is ensured by requiring them to have sufficient angular separation from the latter: $\Delta R(\text{track}, e\text{-}/\gamma\,\text{cluster}) > 0.05$ and $\Delta R(\text{track}, \tau_{\text{had}}) > 0.2$.

3.3.3 Overlap removal

Given the procedures for the reconstructions described above, it is possible that overlaps may occur between two objects. Together with the double-counting of physics objects sharing similar features – i.e. an electron can be also identified as a photon or a jet – the main causes for overlap can be traced back to the energy leakage from the ECal to the HCal and semi-leptonic decays within jets. A specific *Overlap Removal* (OvR) procedure is employed to solve ambiguities between object in close vicinity to one another. The priority in which the order of the OvR is established depends on the specific requirements of each physics analysis. For the analyses described in this thesis, which target final states with electrons and muons in the final state the following procedure is used:

1. Electrons overlapping with muons within $\Delta R < 0.01$ are discarded, as they are likely constructed from the muon energy deposited in the calorimeter or FSR off the muon;
2. Non b-tagged jets close to an electron within $\Delta R < 0.2$ are rejected;
3. Jets with less than three tracks close a muon within $\Delta R < 0.4$ are also rejected;
4. Electrons or muons are discarded if they overlap with a jet within a p_{T}-dependent cone of size $\Delta R = \min\{0.4, A + B/p_{\mathrm{T}}(\ell)[\,\mathrm{GeV}\,]\}$, where A and B are analysis-specific parameters;
5. In some specific cases (see Section 4.2.1), the electron with the lowest p_{T} in electron pairs is rejected as it likely originates from radiation emitted from the other.

Analysis objects

The set of object definitions, including the choice of WPs when relevant, make up the pool of objects that is ultimately considered in a physics analysis, after passing the OvR selection discussed above. In particular, identification and isolation criteria for electrons and muons serve as an effective initial suppression of the contribution from FNP leptons which would otherwise affect the analysis.

Regarding electrons and muons, two levels of object definition are usually taken into consideration in an analysis: a lepton selection with looser criteria, called *baseline* selection, and a tighter definition, which identifies *signal* leptons from a subset of those passing the baseline criteria. Signal leptons are those used in the definitions of the search regions (Sections 4.2.5 and 5.2.4), whilst baseline leptons are used to perform background-related studies, especially concerning the data-driven estimation of the contribution of FNP leptons (Sections 4.3.5 and 5.3.2).

Depending on the targeted final state the optimal choices of object definition criteria is defined. Details of the final choice of the object definition for each of the analyses described in this thesis will be given in the corresponding Chapters (Sections 4.2.1 and 5.2.1).

Search for $\tilde{\chi}_1^{\pm}\,\tilde{\chi}_2^0$ decaying to same-sign lepton pairs via intermediate W and Higgs bosons

4

This Chapter presents the search for $\tilde{\chi}_1^{\pm}\,\tilde{\chi}_2^0$ production through their R-Parity-conserving decays to final states containing two light leptons (electrons o muons) of the same electrical charge ($\ell^{\pm}\ell^{\pm}$, with $\ell = e, \mu$), as well as $E_{\mathrm{T}}^{\mathrm{miss}}$ and possibly light jets. Intermediate states with W and Higgs (h) bosons are considered. The dataset taken into account is that collected during the full Run 2 with 139 fb^{-1}. A search targeting the same production model in the same final state was previously carried out in the ATLAS Collaboration using the early Run 2 dataset with 36.1 fb^{-1}. The analysis presented in this Chapter significantly extends and supersedes the one in Reference [57].

I am the leading analyser for this search. I have personally carried out the vast majority of the work for this analysis, including: development and maintenance of the analysis framework used to process and analyse MC and data samples; definition of the event selections based on cuts on relevant kinematic quantities to discriminate the targeted SUSY signal from the SM background processes; study of the composition of the SM background contributions and data-driven estimation of the relevant background processes; evaluation of detector-related and theoretical systematic uncertainties; statistical interpretation of the results.

The results of this analysis have been made public by the ATLAS Collaboration and can be found in Reference [136]. Unless specifically stated, all the plots, tables and results presented in this Chapter, including those taken from [136], have been personally produced by me.

4.1 Targeted SUSY scenario

The simplified model targeted with this search, referred to as the *Wh-SS model*, is represented in the diagram in Figure 4.1.

In the Wh-SS model, both $\tilde{\chi}_1^{\pm}$ and $\tilde{\chi}_2^0$ are assumed to be almost purely Wino-like, mass-degenerate ($m_{\tilde{\chi}_1^{\pm}/\tilde{\chi}_2^0} \doteq m_{\tilde{\chi}_1^{\pm}} = m_{\tilde{\chi}_2^0}$), and to decay with a 100% BR to a stable $\tilde{\chi}_1^0$ and SM W or h bosons (i. e. $\tilde{\chi}_1^{\pm} \to W^{\pm}\tilde{\chi}_1^0$ and $\tilde{\chi}_2^0 \to h\tilde{\chi}_1^0$). The two $\tilde{\chi}_1^0$ in the final state are in turn assumed to be

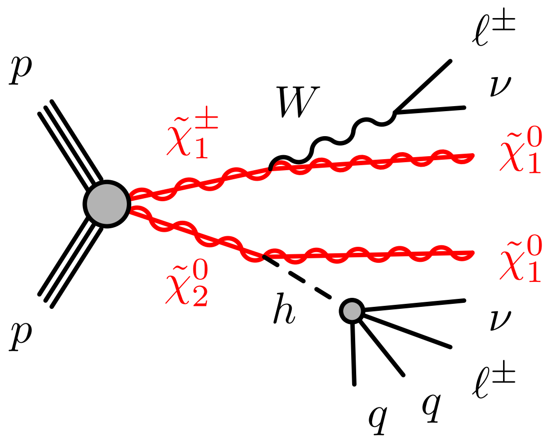

Figure 4.1: Diagram for the production mechanism of the Wh-SS model.

mostly Bino-like and also the LSPs. The same-sign lepton final state in this scenario arises from taking into account all possible decays of the SM Higgs boson, especially to W^+W^- or $\tau^+\tau^-$, which in turn decay leptonically.

The Wh-SS model is studied by considering a set of so-called *signal mass points* (constituting a *signal grid*), each requiring a specific choice for $m_{\tilde{\chi}_1^{\pm}/\tilde{\chi}_2^0}$ and $m_{\tilde{\chi}_1^0}$. Henceforth, the following notation will be used to indicate each mass point: Wh ($m_{\tilde{\chi}_1^{\pm}/\tilde{\chi}_2^0}$,$m_{\tilde{\chi}_1^0}$). For instance, the mass point with $m_{\tilde{\chi}_1^{\pm}/\tilde{\chi}_2^0} = 300$ GeV and $m_{\tilde{\chi}_1^0} = 100$ GeV will be referred to as Wh (300,100). Mass points in the signal grid (Figure 4.2) have been chosen to explore the kinematic properties of the Wh-SS model as a function of $m_{\tilde{\chi}_1^{\pm}/\tilde{\chi}_2^0}$ and $m_{\tilde{\chi}_1^0}$. An important parameter is the *mass-splitting* between the $\tilde{\chi}_1^{\pm}/\tilde{\chi}_2^0$ and $\tilde{\chi}_1^0$ masses, $\Delta m_{\mathrm{Sig}} = m_{\tilde{\chi}_1^{\pm}/\tilde{\chi}_2^0} - m_{\tilde{\chi}_1^0}$.

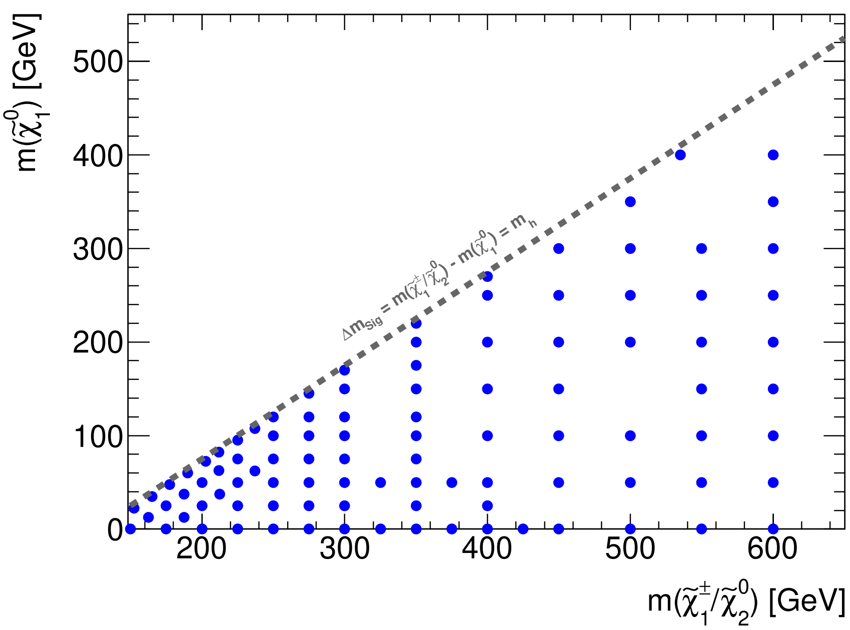

Figure 4.2: Signal grid used in the Wh-SS analysis.

To ensure the intermediate W and Higgs bosons to be on-shell, all mass points are required to be have Δm_{Sig} greater than the Higgs boson mass (i. e. $\Delta m_{\mathrm{Sig}} \geq m_h$), which represent the *kin-*

ematic limit of the Wh-SS model. The kinematics of the particles in the final state is strongly affected by the value of Δm_{Sig} considered. In particular, in the so-called “compressed” region, i. e. for $m_h \leq \Delta m_{\mathrm{Sig}} \lesssim 200$ GeV, lower p_{T} objects are observed. Here, small variations of Δm_{Sig} are expected to significantly change the kinematics of the final state, as they affect the energy and the momentum of the observed particles. For this reason, as shown in Figure 4.2, the “granularity” of the chosen signal grid increases moving closer to the kinematic limit.

MC samples for each mass point have been generated from LO matrix-elements using the `MadGraph` generator interfaced with `PYTHIA8` and `EvtGen` for the PS modelling. In order to increase the sensitivity of the search in the Wh-SS model, signal events are generated with at least two light leptons with truth-level $p_{\mathrm{T}} \geq 7$ GeV. Dedicated generator filter efficiencies are accounted for in the appropriate rescaling of the signal samples for the considered integrated luminosity.

4.2 Analysis strategy

4.2.1 Object definitions

The targeted final state in the Wh-SS analysis requires to reconstruct events with: electrons, muons, $E_{\mathrm{T}}^{\mathrm{miss}}$, and jets. The baseline collection of electrons and muons used in this analysis is composed by all reconstructed leptons passing the OvR procedure described in Section 3.3.3. Signal electrons and signal muons are selected from the baseline collection after imposing tighter criteria, especially for what concerns the lepton identification and isolation. The full list of cuts in the baseline and signal lepton definitions for the Wh-SS analysis have been reported in Table 4.1.

Table 4.1: Summary of the electron and muon selection criteria used in the Wh-SS analysis. Signal leptons criteria are applied on top of the baseline cuts.

	Baseline electrons	Baseline muons
Acceptance	$p_{\mathrm{T}} \geq 10$ GeV, $\lvert\eta\rvert < 2.47$	$p_{\mathrm{T}} \geq 10$ GeV, $\lvert\eta\rvert < 2.5$
Crack veto	$\lvert\eta\rvert \notin [1.37, 1.52]$	-
Identification WP	`LooseAndBLayer`	`Medium`
Impact parameter	$\lvert d_0/\sigma(d_0)\rvert < 5.0$, $\lvert z_0 \cdot \sin(\theta)\rvert < 0.5$ mm	$\lvert z_0 \cdot \sin(\theta)\rvert < 0.5$ mm
	Signal electrons	**Signal muons**
Acceptance	$\lvert\eta\rvert < 2.0$	-
Identification WP	`Medium`	-
Isolation WP	`Tight`	`TightTrackOnly`
Impact parameter	-	$\lvert d_0/\sigma(d_0)\rvert < 3.0$
`ECIDS`	97% efficiency WP	-

Specific requirements are applied to suppress the occurrence of CF electrons. Baseline electrons falling in the crack region of the ECal (see Section 2.2.4) are vetoed as well as signal electrons at forward pseudorapidities ($\lvert\eta\rvert \geq 2$). These cuts are effective since they remove events with electrons traversing a larger portion of the detector material, for which there is a higher probability for bremsstrahlung emission, thus with a more significant contribution from the CF background. The CF contribution is further suppressed by requiring all signal electrons to pass the selection of the `ECIDS` tool.

The definition of baseline jets, signal jets and signal b-jets has been reported in Table 4.2. Baseline jets are required to be PFlow jets. Signal jets must pass the baseline criteria and the JVT selection (Section 3.3.2). Finally, the b-jet collection comprises all central ($|\eta| < 2.5$) signal jets which pass the b-tagging criteria imposed using the `DL1r` tagger and its 70%-efficiency WP.

Table 4.2: Summary of the jet selection criteria used in the Wh-SS analysis.

Baseline jets	
Collection	PFlow
Acceptance	$p_{\mathrm{T}} \geq 20$ GeV , $|\eta| < 4.5$
Signal jets	
Acceptance	$p_{\mathrm{T}} \geq 20$ GeV , $|\eta| < 2.8$
JVT	`Tight` WP for $p_{\mathrm{T}} < 60$ GeV , $|\eta| < 2.4$
Signal b-jets	
Acceptance	$p_{\mathrm{T}} \geq 20$ GeV , $|\eta| < 2.5$
b-tagger	`DL1r`, 70% efficiency WP

Loose, Tight and Loose-Not-Tight lepton definitions

In the Wh-SS analysis, additional lepton definition categories, besides the baseline and signal collections, are used for the estimation of the SM background, which is further discussed in Section 4.3. These are:

- *Tight* lepton selection (indicated with T), which is usually the same as the signal lepton definition chosen for the analysis;
- *Loose* lepton selection (indicated with L), usually obtained from the tight lepton collection after loosening or removing completely the requirements of the lepton identification and/or isolation, thus propagating more FNP leptons into this sample;
- *Loose-Not-Tight* lepton selection (indicated with $\overline{T}$), complementary to the Tight selection and obtained from the leptons passing the Loose criteria but failing the Tight criteria, so that $L = T \cup \overline{T}$.

The cuts used to define the Tight and Loose collections are reported in Table 4.3. The Tight lepton collection has been chosen to be the the same as the signal lepton collection, since that is the main target of the Wh-SS analysis. The Loose collection includes leptons satisfying the baseline criteria and, in addition, $|d_0/\sigma(d_0)| < 3.0$ for muons, $|\eta| < 2.0$ and the `ECIDS` for electron, in order to match the acceptance of signal leptons. Consequently, the Loose-Not-Tight lepton collection is obtained from the signal/Tight leptons by requiring them to fail either the signal identification and/or isolation criteria, thus increasing the probability for a Loose-Not-Tight lepton to be FNP.

Table 4.3: Summary of the Tight and Loose selection criteria for electron and muon used in the Wh-SS analysis. The Loose-Not-Tight collection is obtained by requiring the leptons to pass the Loose criteria and to fail the Tight criteria.

	Tight electrons	Tight muons
Collection	Signal	Signal
	Loose electrons	**Loose muons**
Collection	Baseline	Baseline
Acceptance	$\|\eta\| < 2.0$	-
Impact parameter	-	$\|d_0/\sigma(d_0)\| < 3.0$
`ECIDS`	97% efficiency WP	-

4.2.2 Trigger selection

Data and MC events in the Wh-SS analysis are selected if they satisfy a trigger selection which is primarily based on the logical `OR` between di-lepton trigger chains. The requirement of passing the set of the di-lepton triggers, listed in Table 4.4, enhances the sensitivity of the search to final states with two light leptons (ee, $e\mu$, $\mu\mu$). Moreover, the di-lepton trigger chains chosen represent the set of available un-prescaled triggers with the lowest p_{T} thresholds for each year of the data-taking in Run 2.

Table 4.4: Summary of the di-lepton trigger chains used in the Wh-SS analysis.

Year	Flavour	Di-lepton trigger chains
2015	ee	`HLT_2e12_lhloose_L12EM10VH`
	$e\mu$	`HLT_e17_lhloose_mu14`
	$\mu\mu$	`HLT_mu18_mu8noL1`
2016	ee	`HLT_2e17_lhvloose_nod0`
	$e\mu$	`HLT_e17_lhloose_nod0_mu14`
	$\mu\mu$	`HLT_mu22_mu8noL1`
2017-2018	ee	`HLT_2e17_lhvloose_nod0_L12EM15VHI` || `HLT_2e24_lhvloose_nod0`
	$e\mu$	`HLT_e17_lhloose_nod0_mu14`
	$\mu\mu$	`HLT_mu22_mu8noL1`

Additionally, the following trigger chains, which select events based on their $E_{\mathrm{T}}^{\mathrm{miss}}$, have also been considered: `HLT_xe70` (for the 2015 dataset); `HLT_xe90/100/110_mht_L1XE50` (for 2016); `HLT_xe110_pufit_L1XE55` (for 2017); `HLT_xe110_pufit_xe70_L1XE50` (for 2018). The logical `OR` between the di-lepton triggers (Table 4.4) with these $E_{\mathrm{T}}^{\mathrm{miss}}$ trigger chains is applied only for events with $E_{\mathrm{T}}^{\mathrm{miss}} \geq 250$ GeV . This choice, in general, has been found to achieve approximately a 100% trigger efficiency for events with $E_{\mathrm{T}}^{\mathrm{miss}} \geq 250$ GeV , especially for analyses targeting a same-sign signature. In the Wh-SS analysis, a small contribution is expected from events with

$E_T^{miss} \geq 250\,\text{GeV}$ from the corresponding signals, and no significant change has been found compared to requesting events to pass the di-lepton trigger chains alone. However, since the Wh-SS search is part of an analysis group targeting other EWK SUSY searches with a same-sign signature and no disadvantage has been observed from using E_T^{miss} triggers as well, the trigger strategies have been harmonised.

4.2.3 Standard Model background processes

In the initial stages, the Wh-SS analysis has relied only on MC simulations for the SM background. In general, MC simulations for these SM events have been generated with NLO accuracy.

Considering the targeted same-sign lepton final state, SM backgrounds are grouped into two categories:

- *Irreducible backgrounds*: SM processes with two same-sign real/prompt leptons;
- *Reducible backgrounds*: SM processes which contribute to the final state by means of the presence of at least one FNP lepton or CF or electrons from photon conversion.

The following SM processes contributing to the targeted final state have been considered.

Di-boson (*VV*) The di-boson backgrounds refers to the SM production of two vector bosons, $V = W, Z$. MC samples are generated using SHERPA including effects deriving from off-shell production of gauge bosons and Higgs boson production contributions [137]. Only fully leptonic decays and, hence, final states are taken into account. Amongst these the $WZ \to \ell\ell\ell\nu$ process is the main source of SM background in the Wh-SS search (Section 4.3.1). Additionally, processes involving the production of leptonically-decaying vector boson pairs in association with two jets are considered. The most relevant process for the Wh-SS search which falls into this category is the production of a pair of same-sign W bosons, $W^{\pm}W^{\pm}$. To this process, which has been observed by the ATLAS [138] and CMS Collaborations [139], contribute production mechanisms which involve the radiation of W bosons off quarks and Vector Boson Scattering (VBS) scenarios. In what follows the di-boson backgrounds are generally categorised according to the number of light, charged leptons in the final state: $VV(1\ell)$, $VV(2\ell)$, $VV(3\ell)$, and $VV(4\ell)$.

Tri-boson (*VVV*) As in the di-boson production case, tri-boson MC samples are used to estimated the contribution from SM processes involving the production of three vector bosons, $V = W, Z$ [137]. They are once generated using SHERPA and take into account only leptonic decays of the W and Z bosons, e. g. $WWW \to 3\ell + 3\nu$.

$t\bar{t}$+V Another relevant source of background comes from the production of $t\bar{t}$ in association with a vector boson, $V = W, Z$ [140]. These events are generated with the aMC@NLO extension of MadGraph, interfaced with PYTHYA8 and EvtGen.

V+jets (W+jets, Z+jets) Single vector boson production in association with jets [141] is also considered as a SM background source. SHERPA is used to generate this processes in which only leptonic decays of the gauge boson are considered, i. e. $W^{\pm} \to \ell^{\pm}\nu$ and $Z \to \ell^{\pm}\ell^{\mp}$ with $\ell = e, \mu, \tau$. These processes contribute to a same-sign lepton final state because of the presence of FNP leptons or of CF events (from Z+jets).

$t\bar{t}$ Semi-leptonic and fully leptonic decays of the $t\bar{t}$ process [142] are also taken into account as a SM background source in the Wh-SS analysis. This background is simulated with MC samples generated with POWHEG interfaced with PYTHYA8 and EvtGen. The $t\bar{t}$ process contributes in phase-spaces with same-sign leptons via FNP leptons and CF.

Single-top Single-top production [143] in association with other quarks in the final state, is also considered. As for the $t\bar{t}$ production, MC samples are generated with POWHEG interfaced with PYTHYA8 and EvtGen. Finally, single-top is one of the sources of FNP leptons in the Wh-SS search.

SM processes including WZ (or $VV(3\ell)$), $W^{\pm}W^{\pm}$ (same-sign $VV(2\ell)$), $t\bar{t}+V$, $VV(4\ell)$ and VVV belong to the irreducible background category. On the other hand, $t\bar{t}$, W+jets, Z+jets, single-top, $VV(1\ell)$, and opposite-sign $VV(2\ell)$ are generally reducible backgrounds.

4.2.4 Discriminant variables used in the Wh-SS analysis

Different kinematic variables are used to achieve a discrimination between the considered SUSY signals and the SM backgrounds. The missing transverse momentum, $E_{\mathrm{T}}^{\mathrm{miss}}$, already defined in Equation 3.2 is one of such discriminants, since SUSY signals may yields a considerable amount of $E_{\mathrm{T}}^{\mathrm{miss}}$ from the undetected LSPs in the final state. The other variables used are described in what follows.

$E_{\mathrm{T}}^{\mathrm{miss}}$ significance The $E_{\mathrm{T}}^{\mathrm{miss}}$ significance, or Sig($E_{\mathrm{T}}^{\mathrm{miss}}$), measures the degree with which the reconstructed $E_{\mathrm{T}}^{\mathrm{miss}}$ in an event is consistent with the “real” transverse energy from undetected particles, and not with momentum resolution and particle identification effects [144]. As opposed to SUSY signal events, in which real $E_{\mathrm{T}}^{\mathrm{miss}}$ comes mainly from the LSPs, thus resulting in high Sig($E_{\mathrm{T}}^{\mathrm{miss}}$), many SM backgrounds have complex final states which may yield small Sig($E_{\mathrm{T}}^{\mathrm{miss}}$) values.

Invariant mass In a system with two or more object system it is possible to define the *invariant mass* as follows:

$$m_{\mathrm{INV}} = \sqrt{\left(\sum_i E_i\right)^2 - \left|\sum_i \vec{p}_i\right|^2} \tag{4.1}$$

where the index i runs over all the objects considered, whereas E_i and $\vec{p}_i$ are the energy and momentum of each object. In the Wh-SS analysis, invariant masses are used for di-lepton systems ($m_{\ell\ell}$), tri-lepton systems ($m_{\ell\ell\ell}$), and di-jet systems (m_{jj}), as follows:

$$m_{\ell\ell} = \sqrt{(E_{\ell_1} + E_{\ell_2})^2 - |\vec{p}_{\ell_1} + \vec{p}_{\ell_2}|^2}, \tag{4.2}$$

$$m_{\ell\ell\ell} = \sqrt{(E_{\ell_1} + E_{\ell_2} + E_{\ell_3})^2 - |\vec{p}_{\ell_1} + \vec{p}_{\ell_2} + \vec{p}_{\ell_3}|^2}, \tag{4.3}$$

$$m_{\mathrm{jj}} = \sqrt{\left(E_{jet_1} + E_{jet_2}\right)^2 - \left|\vec{p}_{jet_1} + \vec{p}_{jet_2}\right|^2}. \tag{4.4}$$

Transverse mass The transverse mass of a lepton ℓ and the $E_{\mathrm{T}}^{\mathrm{miss}}$ in the event is computed as:

$$m_{\mathrm{T}}\left(\ell, E_{\mathrm{T}}^{\mathrm{miss}}\right) = \sqrt{2 p_{\mathrm{T}}^{\ell} E_{\mathrm{T}}^{\mathrm{miss}} \left(1 - \cos\Delta\phi(\ell, E_{\mathrm{T}}^{\mathrm{miss}})\right)}, \tag{4.5}$$

where $\Delta\phi(\ell, E_{\mathrm{T}}^{\mathrm{miss}})$ is the azimuthal angular separation between the lepton and $E_{\mathrm{T}}^{\mathrm{miss}}$. For $W \to \ell\nu$ events, this variable has a peak at the end-point of its distribution, corresponding to $m_{\mathrm{T}} \sim m_W$ [145]. In SUSY events, in which $E_{\mathrm{T}}^{\mathrm{miss}}$ comes from the LSPs and the mother particle is usually much heavier than the W boson – e. g. $\tilde{\chi}_1^{\pm}$ – the distribution of m_{T} will spread to values greater than m_W – reflecting the presumably higher mass of the mother particle – thus making the threshold $m_{\mathrm{T}} > m_W$ is an effective cut for suppressing the SM background. In the Wh-SS analysis, an useful variable is obtained by taking the minimum of the m_{T} calculated with each of the two leptons, referred to as $m_{\mathrm{T}}^{\mathrm{min}}$:

$$m_{\mathrm{T}}^{\mathrm{min}} = \min\left\{m_{\mathrm{T}}\left(\ell_1, E_{\mathrm{T}}^{\mathrm{miss}}\right), m_{\mathrm{T}}\left(\ell_2, E_{\mathrm{T}}^{\mathrm{miss}}\right)\right\}. \tag{4.6}$$

Stransverse mass For events in which a pair of heavy mother particles each decay into a visible (e. g. leptons, jets) and an invisible system (thus contributing to the $E_{\mathrm{T}}^{\mathrm{miss}}$), the *stransverse mass*, m_{T2} [145], can be defined. In the case of the Wh-SS analysis, m_{T2} is computed from the two leptons and the $E_{\mathrm{T}}^{\mathrm{miss}}$ as follows:

$$m_{\mathrm{T2}} = \min_{q_{\mathrm{T}}}\left\{\max\left[m_{\mathrm{T}}\left(\ell_1, \vec{q}_{\mathrm{T}}\right), m_{\mathrm{T}}\left(\ell_2, \vec{p}_{\mathrm{T}}^{\mathrm{miss}} - \vec{q}_{\mathrm{T}}\right)\right]\right\}. \tag{4.7}$$

It can be shown that the distribution of m_{T2} has an end-point corresponding to the mass of one of the heavy mother particles. Therefore, for most SM backgrounds $m_{\mathrm{T2}} \lesssim m_W$ holds, as opposed to SUSY processes which, similarly to m_{T}, can spread to much higher values of m_{T2} due to the presence of the very heavy $\tilde{\chi}_1^{\pm}$ and $\tilde{\chi}_2^0$.

4.2.5 Wh-SS event selections

The event selection of the Wh-SS search is based on the so-called *cut-and-count* approach, which consists on designing regions enriched in events of the targeted SUSY models, called Signal Regions (SRs), by applying selection criteria, or "cuts", on relevant kinematic variables. The values of these cuts are chosen in a procedure referred to as *SR optimisation*, in which a value of a cut is chosen if it maximises the *expected significance* Z_{n} [146] with respect to the background contribution. Z_{n} is calculated with the ROOT toolkit taking into account the expected signal yields and the total background uncertainty, indicated with a flat envelope on the expected background fluctuation (e. g. 30%). A fundamental point followed in the definition of the different SRs in the optimisation procedures, is to make sure that the SRs are *orthogonal* to each other, which is to say that no kinematic overlap can exist between them. Before any other event selection is applied, events are requested to pass an initial *preselection* summarised in Table 4.5.

Table 4.5: Summary of the preselection cuts used in the Wh-SS analysis.

Variable	Preselection cut
n_{ℓ}^{BL}	$= 2$
$n_{\ell}^{\mathrm{Signal}}$	$= 2$
$p_{\mathrm{T}}^{\ell_1}$, $p_{\mathrm{T}}^{\ell_2}$ [GeV]	$\geq 25, 25$
Charge(ℓ_1,ℓ_2)	$++$ or $--$
n_{jets}	≥ 1
$n_{b\mathrm{-jets}}$	$= 0$
$E_{\mathrm{T}}^{\mathrm{miss}}$ [GeV]	≥ 50

In the preselection, events are required to have exactly two light, leptons (e or μ) of the same electric charge. This required must be true both at baseline ($n_{\ell}^{\mathrm{BL}} = 2$) and signal level ($n_{\ell}^{\mathrm{Signal}} = 2$) [1]. This helps to achieve good, initial background rejection, especially for what concerns the FNP contribution. The lower threshold for the p_{T} of both leptons has been set at 25 GeV to match that imposed in the di-lepton trigger used (Table 4.4). Events with any b-tagged jets are vetoed ($n_{b\mathrm{-jets}} = 0$) in order to suppress the top-related SM backgrounds (e. g. $t\bar{t}$ and $t\bar{t}+V$), whereas the $E_{\mathrm{T}}^{\mathrm{miss}} \geq 50$ GeV cut effectively rejects the background from Z+jets and Drell-Yan [147] processes. The Wh-SS search is carried out independently in the three *flavour channels*: $e^{\pm}e^{\pm}$, $e^{\pm}\mu^{\pm}$, $\mu^{\pm}\mu^{\pm}$. This has been done to exploit differences in the SM background composition (Section 4.3.1) and, therefore, to achieve higher sensitivity for the whole search when statistically combining the results of each orthogonal SR.

For the SR optimisation, four benchmark signal points have been chosen out of the available Wh-SS grid (Figure 4.2): Wh (177.5,47.5), Wh (202.5,72.5), Wh (300,100) and Wh (400,0). The first two lay at the edge of the kinematic limit $\Delta m_{\mathrm{Sig}} \gtrsim m_h$, whereas the other are used to

[1] An additional cut on the lepton multiplicity ($n_{\ell}^{\mathrm{Comb}} = 2$) has been imposed for leptons satisfying the the requirements listed in Table 6.2 and before passing the OvR, in order to guarantee the orthogonality with other analyses taking part in the EWK combination effort, which will be discussed in Chapter 6.

explore the signal significance for signals with progressively higher Δm_{Sig}, which are therefore expected to be characterised by higher p_{T} leptons and $E_{\mathrm{T}}^{\mathrm{miss}}$.

An effective tool to perform the SR optimisation is provided by the so-called "N-1 plots". An N-1 plot shows the distribution of a certain kinematic variable used in an event selection and obtained by applying all the desired cuts except for the one on the variable being plotted. Through this method it is possible to establish that, of the considered variables, the most powerful discrimination between signal and SM background is given by the m_{T2} (Equation 4.7). Figure 4.3 shows the m_{T2} distributions for each flavour combination at preselection.

Setting the lower threshold $m_{\mathrm{T2}} \geq 80$ GeV allows to suppress the main SM background contributions, especially from WZ, W+jets and $t\bar{t}$. Whilst this cut is very effective for achieving a higher Z_{n}, most of the signal statistics have low m_{T2} and would, especially for signals whose Δm_{Sig} is closer to the kinematic limit (Figure 4.3). The evident positive correlation (Figure 4.4) between m_{T2} and $m_{\mathrm{T}}^{\mathrm{min}}$ (see Section 4.2.4) is exploited to recover the sensitivity which would be otherwise lost if only high m_{T2} SRs were to be considered. This allows to define the two main SR categories of the Wh-SS search, here referred to as $\mathrm{SR}^{Wh}_{\text{high-}m_{\mathrm{T2}}}$ and $\mathrm{SR}^{Wh}_{\text{low-}m_{\mathrm{T2}}}$, as shown in Figure 4.4.

Furthermore, for low Δm_{Sig} signals and in events with $m_{\mathrm{T2}} < 80$ GeV it is possible to increase the Z_{n} by requiring $m_{\mathrm{T}}^{\mathrm{min}} \geq 100$ GeV, as shown in Figures 4.4 and 4.5. In both $\mathrm{SR}^{Wh}_{\text{high-}m_{\mathrm{T2}}}$ and $\mathrm{SR}^{Wh}_{\text{low-}m_{\mathrm{T2}}}$ it is possible to further suppress the SM background, especially the Z+jets processes in the $e^{\pm}e^{\pm}$ channel, by requiring a lower threshold on the $E_{\mathrm{T}}^{\mathrm{miss}}$ significance, as shown in Figure 4.6. This stems from the fact that, e. g. in the case of Z+jets, given the absence of neutrinos in the final state, no real $E_{\mathrm{T}}^{\mathrm{miss}}$ is expected and therefore low $E_{\mathrm{T}}^{\mathrm{miss}}$ significance, as opposed to the SUSY signals. The $\mathrm{SR}^{Wh}_{\text{high-}m_{\mathrm{T2}}}$ category is found to be the one with the highest sensitivity for the Wh-SS search. In order for this search to be simultaneously sensitive to different Δm_{Sig} signals, three independent bins are considered, each with increasing values of $E_{\mathrm{T}}^{\mathrm{miss}}$, as represented in Figure 4.7: $\mathrm{SR}^{Wh}_{\text{high-}m_{\mathrm{T2}}}$-1 targets low Δm_{Sig}, $\mathrm{SR}^{Wh}_{\text{high-}m_{\mathrm{T2}}}$-2 moderate Δm_{Sig} and $\mathrm{SR}^{Wh}_{\text{high-}m_{\mathrm{T2}}}$-3 high Δm_{Sig}.

Finally, in $\mathrm{SR}^{Wh}_{\text{high-}m_{\mathrm{T2}}}$ and $\mathrm{SR}^{Wh}_{\text{low-}m_{\mathrm{T2}}}$ the signal significance can be further increased by suppressing the contribution from the $W^{\pm}W^{\pm}$ background. As this process is expected to be accompanied by the presence of two relatively energetic and collimated light jets, the bulk of corresponding events are characterised by high di-jet invariant mass, m_{jj}. Therefore, the cut requiring $m_{\mathrm{jj}} < 350$ GeV is found to increase Z_{n}. In this case, m_{jj} is artificially set to zero for events with only one jet, to guarantee that they would fall into the SRs acceptance.

A summary of the definitions of the twelve orthogonal SRs – considering all the flavour and $E_{\mathrm{T}}^{\mathrm{miss}}$ bins – taken into consideration for the Wh-SS search is reported in Table 4.6.

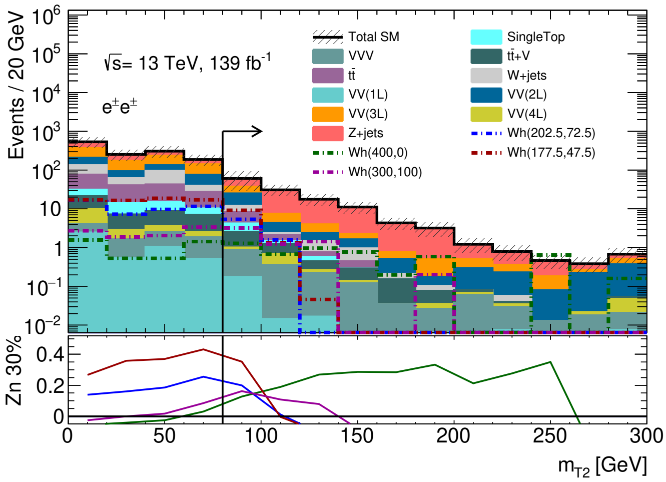

(a) $e^{\pm}e^{\pm}$ channel

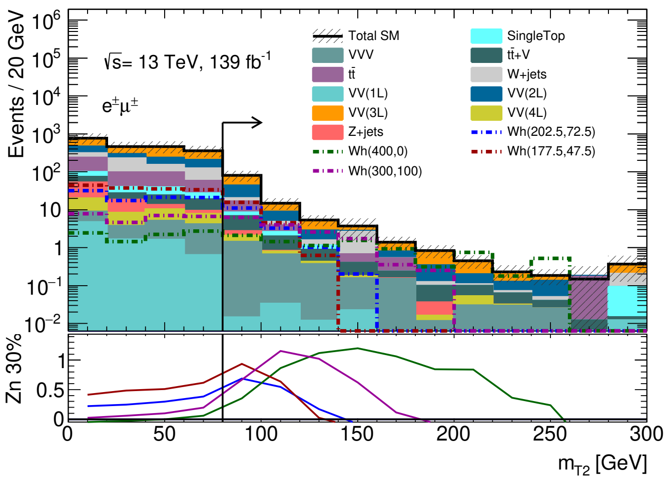

(b) $e^{\pm}\mu^{\pm}$ channel

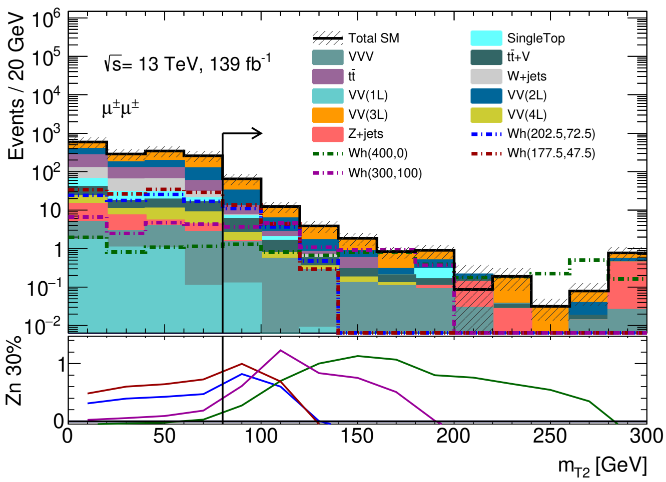

(c) $\mu^{\pm}\mu^{\pm}$ channel

Figure 4.3: N-1 plots showing the distributions of m_{T2} for events passing the preselection of the Wh-SS analysis (Table 4.5) and in the three flavour channels: (a) $e^{\pm}e^{\pm}$, (b) $e^{\pm}\mu^{\pm}$, and (c) $\mu^{\pm}\mu^{\pm}$. Contributions from MC are shown for the relevant SM background processes and four benchmark signal mass points: Wh (177.5,47.5), Wh (202.5,72.5), Wh (300,100) and Wh (400,0). Only statistical uncertainties from the MC backgrounds are shown. The lower panel shows the value of the sensitivity Z_n (calculated considering 30% as a total uncertainty on the background) as a function of the different choice of a lower cut threshold on m_{T2}, for the four signal mass points. The arrows show the cut that has been chosen, namely $m_{T2} \geq 80$ GeV .

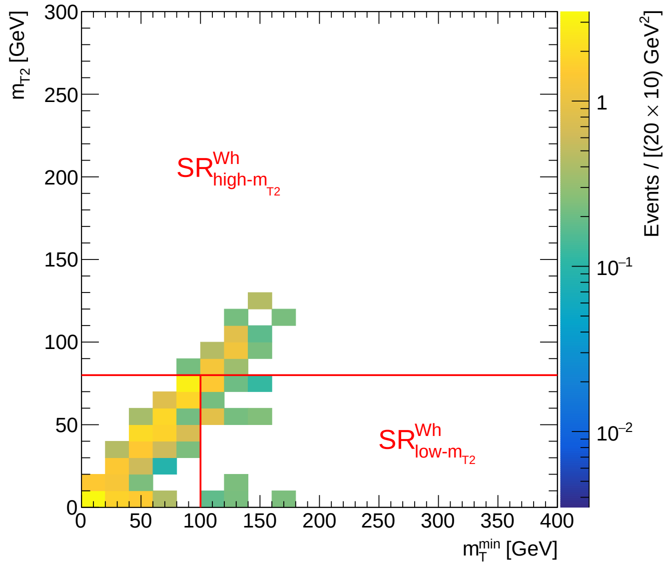

(a) Wh (202.5,72.5)

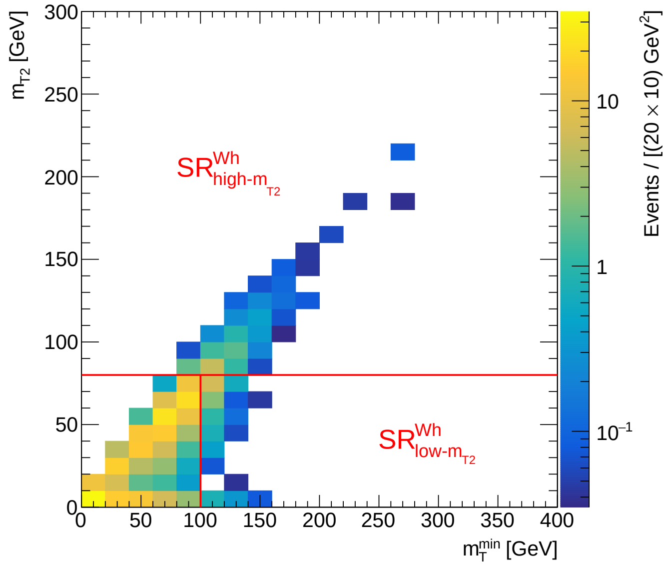

(b) WZ

Figure 4.4: Correlation between $m_{\mathrm{T}}^{\mathrm{min}}$ and m_{T2} for (a) Wh (202.5,72.5) and (b) SM WZ in the $e^{\pm}\mu^{\pm}$ channel of the Wh-SS preselection (Table 4.5). The red lines graphically show the cut chosen for the separation between $\mathrm{SR}^{Wh}_{\mathrm{high}\text{-}m_{\mathrm{T2}}}$ and $\mathrm{SR}^{Wh}_{\mathrm{low}\text{-}m_{\mathrm{T2}}}$.

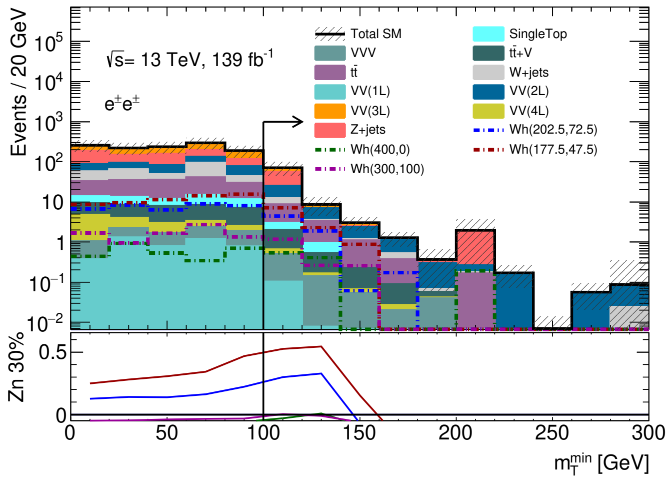

(a) $e^{\pm}e^{\pm}$ channel

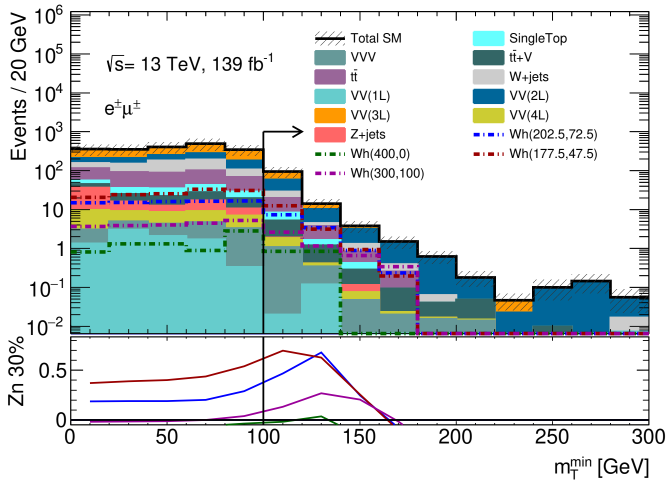

(b) $e^{\pm}\mu^{\pm}$ channel

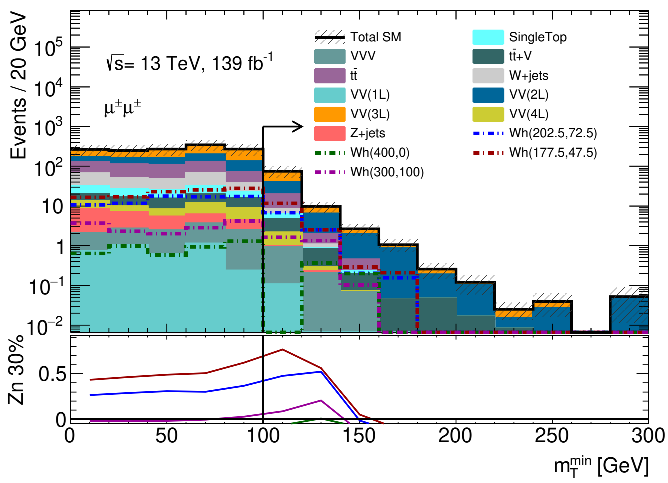

(c) $\mu^{\pm}\mu^{\pm}$ channel

Figure 4.5: N-1 plots showing the distributions of $m_{\mathrm{T}}^{\mathrm{min}}$ for events passing the preselection of the Wh-SS analysis (Table 4.5), $m_{\mathrm{T2}} < 80$ GeV , and in the three flavour channels: (a) $e^{\pm}e^{\pm}$, (b) $e^{\pm}\mu^{\pm}$, and (c) $\mu^{\pm}\mu^{\pm}$. Contributions from MC are shown for the relevant SM background processes and four benchmark signal mass points: Wh (177.5,47.5), Wh (202.5,72.5), Wh (300,100) and Wh (400,0). Only statistical uncertainties from the MC backgrounds are shown. The lower panel shows the value of the sensitivity Z_{n} (calculated considering 30% as a total uncertainty on the background) as a function of the different choice of a lower cut threshold on $m_{\mathrm{T}}^{\mathrm{min}}$, for the four signal mass points. The arrows show the cut that has been chosen, namely $m_{\mathrm{T}}^{\mathrm{min}} \geq 100$ GeV .

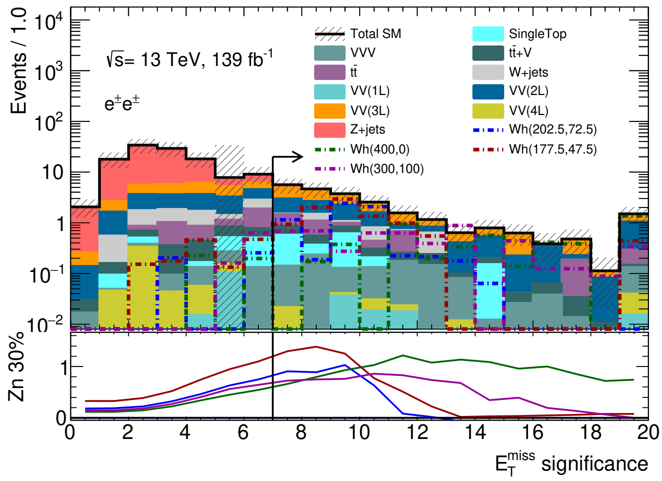

(a) $e^{\pm}e^{\pm}$ channel

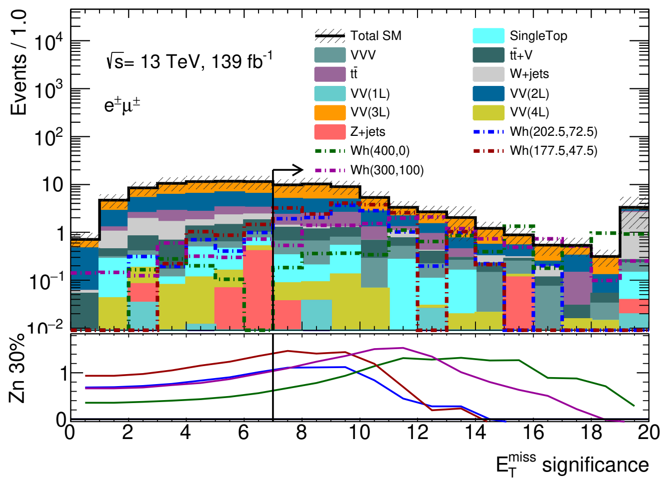

(b) $e^{\pm}\mu^{\pm}$ channel

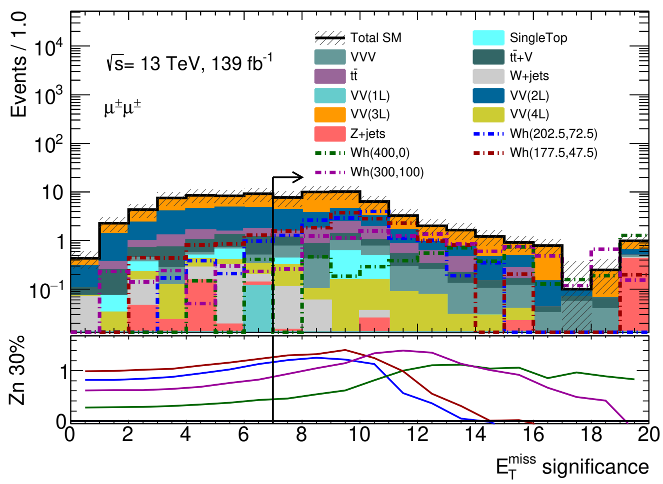

(c) $\mu^{\pm}\mu^{\pm}$ channel

Figure 4.6: N-1 plots showing the distributions of the E_T^{miss} significance for events passing the preselection of the Wh-SS analysis (Table 4.5), $m_{T2} \geq 80$ GeV, and in the three flavour channels: (a) $e^{\pm}e^{\pm}$, (b) $e^{\pm}\mu^{\pm}$, and (c) $\mu^{\pm}\mu^{\pm}$. Contributions from MC are shown for the relevant SM background processes and four benchmark signal mass points: Wh (177.5,47.5), Wh (202.5,72.5), Wh (300,100) and Wh (400,0). Only statistical uncertainties from the MC backgrounds are shown. The lower panel shows the value of the sensitivity Z_n (calculated considering 30% as a total uncertainty on the background) as a function of the different choice of a lower cut threshold on E_T^{miss} significance, for the four signal mass points. The arrows show the cut that has been chosen, namely Sig(E_T^{miss}) ≥ 7.

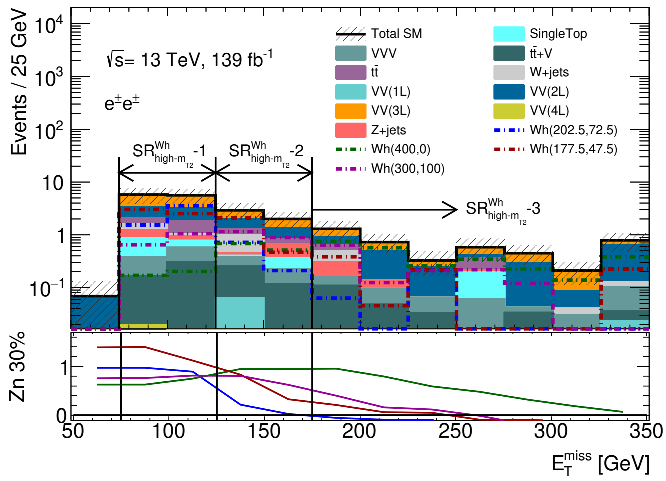

(a) $e^{\pm}e^{\pm}$ channel

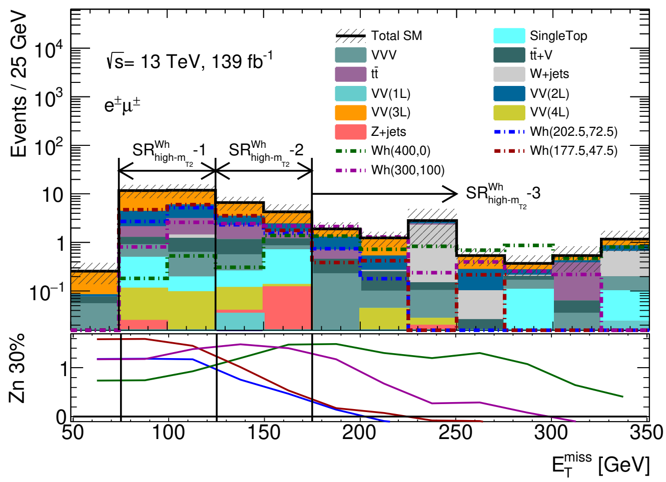

(b) $e^{\pm}\mu^{\pm}$ channel

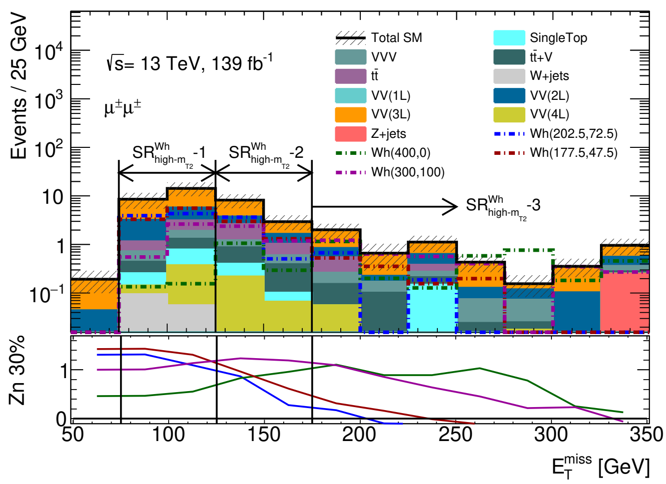

(c) $\mu^{\pm}\mu^{\pm}$ channel

Figure 4.7: N-1 plots showing the distributions of $E_{\mathrm{T}}^{\mathrm{miss}}$ for events passing the preselection of the Wh-SS analysis (Table 4.5), $m_{\mathrm{T2}} \geq 80$ GeV , Sig($E_{\mathrm{T}}^{\mathrm{miss}}$) ≥ 7 and in the three flavour channels: (a) $e^{\pm}e^{\pm}$, (b) $e^{\pm}\mu^{\pm}$, and (c) $\mu^{\pm}\mu^{\pm}$. The arrow indicate the choices for the three $E_{\mathrm{T}}^{\mathrm{miss}}$ bins chosen for $\mathrm{SR}^{Wh}_{\text{high-}m_{\mathrm{T2}}}$. Contributions from MC are shown for the relevant SM background processes and four benchmark signal mass points: Wh (177.5,47.5), Wh (202.5,72.5), Wh (300,100) and Wh (400,0). Only statistical uncertainties from the MC backgrounds are shown. The lower panel shows the value of the sensitivity Z_{n} (calculated considering 30% as a total uncertainty on the background) as a function of the different choice of a lower cut threshold on $E_{\mathrm{T}}^{\mathrm{miss}}$, for the four signal mass points.

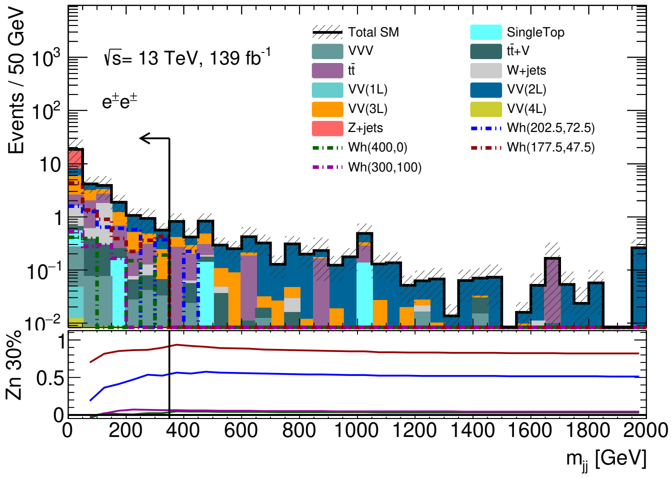

(a) $e^{\pm}e^{\pm}$ channel

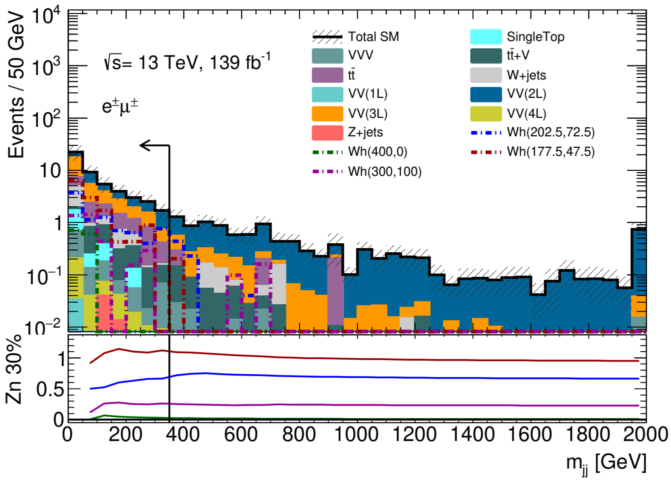

(b) $e^{\pm}\mu^{\pm}$ channel

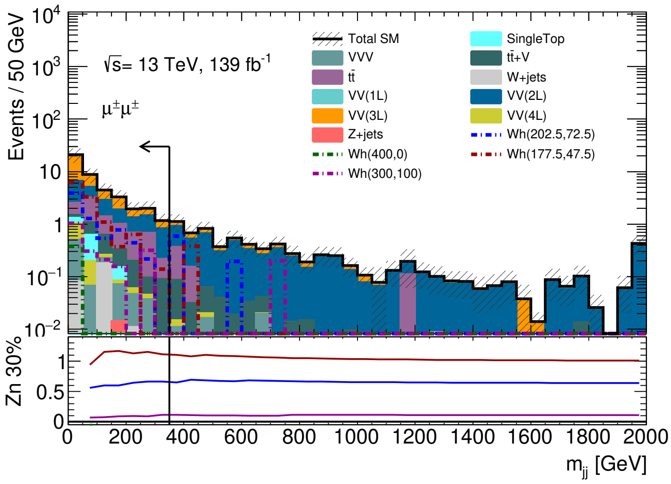

(c) $\mu^{\pm}\mu^{\pm}$ channel

Figure 4.8: N-1 plots showing the distributions of m_{jj} for events passing the selection of $\mathrm{SR}^{Wh}_{\text{low-}m_{\mathrm{T2}}}$. Contributions from MC are shown for the relevant SM background processes and four benchmark signal mass points: Wh (177.5,47.5), Wh (202.5,72.5), Wh (300,100) and Wh (400,0). Only statistical uncertainties from the MC backgrounds are shown. The lower panel shows the value of the sensitivity Z_{n} (calculated considering 30% as a total uncertainty on the background) as a function of the different choice of a upper cut threshold on m_{jj}, for the four signal mass points. The arrows show the cut that has been chosen, namely $m_{\mathrm{jj}} < 350$ GeV .

Table 4.6: Summary of the selection criteria for the SRs targeting the Wh-SS model. Every SR is split into three orthogonal flavour channels (ee, $e\mu$, $\mu\mu$) according to the flavour of the two leptons. $\mathrm{SR}^{Wh}_{\mathrm{high}\text{-}m_{\mathrm{T2}}}\text{-}i$ is further split in three $E_{\mathrm{T}}^{\mathrm{miss}}$ bins, indicated with the index $i = 1,2,3$. Preselection criteria (Table 4.5) are applied to all regions.

Selection requirements for the SRs targeting the Wh-SS model

Variable	$\mathrm{SR}^{Wh}_{\mathrm{high}\text{-}m_{\mathrm{T2}}}\text{-}i$			$\mathrm{SR}^{Wh}_{\mathrm{low}\text{-}m_{\mathrm{T2}}}$		
	$\text{-}ee$	$\text{-}e\mu$	$\text{-}\mu\mu$	$\text{-}ee$	$\text{-}e\mu$	$\text{-}\mu\mu$
Wh-SS preselection	Applied					
m_{T2} [GeV]	≥ 80			< 80		
$m_{\mathrm{T}}^{\mathrm{min}}$ [GeV]	-			≥ 100		
$E_{\mathrm{T}}^{\mathrm{miss}}$ significance	≥ 7			≥ 6		
m_{jj} [GeV]	< 350					
Flavour/charge	$e^{\pm}e^{\pm}$	$e^{\pm}\mu^{\pm}$	$\mu^{\pm}\mu^{\pm}$	$e^{\pm}e^{\pm}$	$e^{\pm}\mu^{\pm}$	$\mu^{\pm}\mu^{\pm}$
$E_{\mathrm{T}}^{\mathrm{miss}}$ [GeV]	$i = 1 : \in [75, 125]$ $i = 2 : \in [125, 175]$ $i = 3 : \geq 175$			≥ 50		

4.3 Standard Model background estimation

This section is devoted to the description of the procedure which has been followed to estimate the SM background contribution in the SRs. A precise estimation of SM background is of crucial importance for the search for BSM phenomena.

Detector and pile-up effects as well as a not precise prediction of the cross-sections may affect the modelling of the irreducible background processes from WZ and $W^{\pm}W^{\pm}$. Therefore, in the Wh-SS analysis, their estimation relies on MC simulation which are "corrected" by means of a semi-data-driven approach. Specifically, the predicted event yields from MC of the WZ and $W^{\pm}W^{\pm}$ processes are normalised to data in dedicated Control Regions (CRs), scaling them by a suitable Normalisation Factor (NF). The normalised contribution from each background is then validated in specific Validation Regions (VRs), which are designed to cover a phase space kinematically closer to the SRs then the corresponding CRs (Section 4.3.2). All CRs, VRs and SRs of the Wh-SS analysis are required to be orthogonal with respect to one another.

On the other hand, the modelling of reducible backgrounds with FNP or CF leptons is often not reliable in MC simulations, especially in the phase spaces targeted by SRs. Hence, dedicated data-driven techniques are used for their estimation, which are further described in Sections 4.3.3 and 4.3.5. For this purpose, a precise knowledge of the composition of the types of leptons contributing to each SM process is required (Section 4.3.1). VRs are once again used to validate the data-driven estimation of the FNP and CF backgrounds (Section 4.3.6).

The background estimation strategy used in the Wh-SS analysis is summarised in Table 4.7. The final estimation of each background source is achieved when performing the so-called *background-only fit*, which will be described in more details in Section 4.5.1. The fit takes as an input the number of events of the irreducible backgrounds from MC and the data-driven yields of the reducible backgrounds in every CRs, VRs and SRs.

Table 4.7: Overview of the background estimation techniques used to estimate the various SM background processes of the Wh-SS analysis. The “Other” category includes all remaining irreducible backgrounds (mainly from $VV(4\ell)$ and VVV).

Process	Estimation method
WZ, $W^{\pm}W^{\pm}$	MC, normalised in CR
FNP, CF	Data-driven
$t\bar{t}+V$, Other	MC

4.3.1 Standard Model background composition

In order to properly estimate the contribution of the reducible and irreducible sources SM backgrounds in the SRs of the Wh-SS analysis, it is necessary to assess the measure of their contribution – i. e. the relative yield of each background source in each region, hereafter referred to as their *background composition* – and how well they are modelled in MC.

As the distinction between background sources is based on the origin of the leptons in each event (Section 4.2.3), the background composition in each region of the Wh-SS search is studied from MC at truth-level by means of the `IFFTruthClassifier` tool of the ATLAS Collaboration. This tool takes as input the MC truth information of each lepton, including the decay chain that generated them, and classifies their origin according to the following categories, or “IFF classes”:

- *Prompt electron*, also called “Ele”;
- *Prompt muon*, also called “Mu”;
- *CF electron*, also called “CFEle”;
- *Photon conversion*, which includes electrons coming from the interaction of a photon with the detector material, and then undergoing e^+e^- pair production; if the photon is prompt or emitted as ISR this category is indicated as “PhConv”, whereas if it is emitted as FSR “FSRph”;
- *Electron from muon*, referring to those electrons arising either from the decay if a muon or from the conversion of a bremsstrahlung photon emitted off a muon; this category is here indicated as “EleMu”;
- *Tau decay*, including electrons and muons originating from the leptonic decay of a tau lepton and here indicated as “Tau”;
- *Heavy-Flavour* (HF) *lepton*, including all FNP leptons arising from the decay of a HF hadron; if the hadron is composed by at least a b quark the category is indicated as “BHad”, otherwise if it has c quarks “CHad”;

- *Light-Flavour* (LF) *lepton*, grouping all FNP leptons which originate from the misidentification of a light-jet as a lepton, and referred to as “LF”;
- *Unclassified leptons*, including all remaining leptons whose origin could not be determined likely due to missing informations in MC; two categories called “Unknown” or “Unkn”, and “KnownUnknown” or “KUnkn” are used.

The truth composition of the the two leptons at preselection has been studies for the main backgrounds by grouping each event based on the combination of IFF classes that each lepton falls into (Figure 4.9).

These studies show that: $t\bar{t}$ contributes in the SRs mainly as a CF and a FNP lepton background with HF leptons, depending on the flavour channel; Z+jets is the main source of CF background in the $e^{\pm}e^{\pm}$ channel, and also contributes as a FNP lepton background, mainly with LF electrons and HF muons; W+jets mainly enters the SRs as a FNP lepton background. Moreover, from these studies it is possible to determine that MC events passing the preselection have either two prompt leptons or one prompt lepton and the other from a different source (e. g. CF, HF, LF, etc.). The contribution from events with two FNP lepton or with a FNP lepton and a CF electron is statistically negligible, and so is the contribution from events with other sources, such as: EleMu, Tau, Unkn and KUnkn.

The truth lepton composition study presented here has allowed to further group the events passing the selection criteria of each SR of the Wh-SS search into different categories:

1. Events with two prompt leptons are classified as “Prompt”;
2. Events with at least a CF electron are classified as “ChargeFlip”;
3. Events with at least a HF lepton are classified as “FakeHF”;
4. Events with at least a LF lepton are classified as “FakeLF”;
5. Events with at least a lepton from photon conversion are classified as “PhotConv”;
6. Other types of events are not considered as their contribution is negligible.

Figure 4.10 shows the result of such MC event categorisation performed for the SM $VV(3\ell)$, $VV(2\ell)$, $t\bar{t}+V$, $t\bar{t}$, Z+jets and W+jets backgrounds in each SR.

Through this further event classification it is possible to show that in the $\mu^{\pm}\mu^{\pm}$ channel of every region only prompt or FakeHF events dominate, whereas the truth lepton composition is more articulate in the $e^{\pm}e^{\pm}$ and $e^{\pm}\mu^{\pm}$ channels. Such different background composition justifies the original choice of splitting the SRs into flavour channels. Additionally, the FNP muon contribution mainly arise from the HF source, whereas FNP electrons seem to have an equally significant contribution from both LF and HF. This is an essential point onto which the procedure to estimate the FNP lepton background (Section 4.3.5) is based.

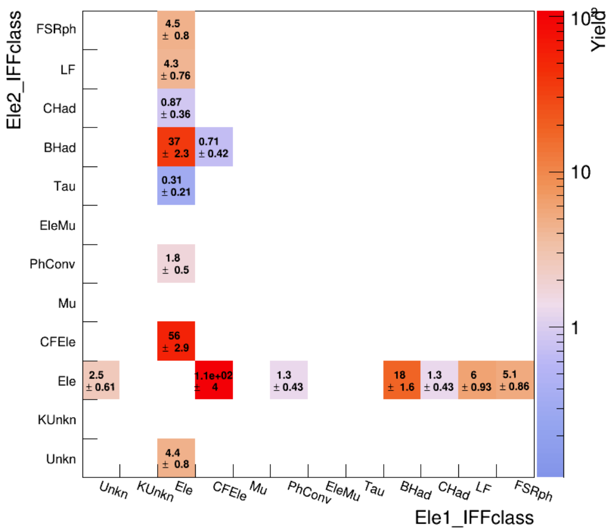

(a) $t\bar{t}$ - $e^{\pm}e^{\pm}$

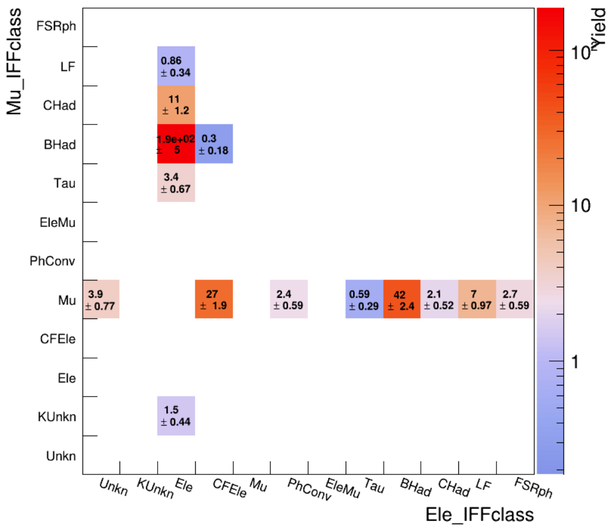

(b) $t\bar{t}$ - $e^{\pm}\mu^{\pm}$

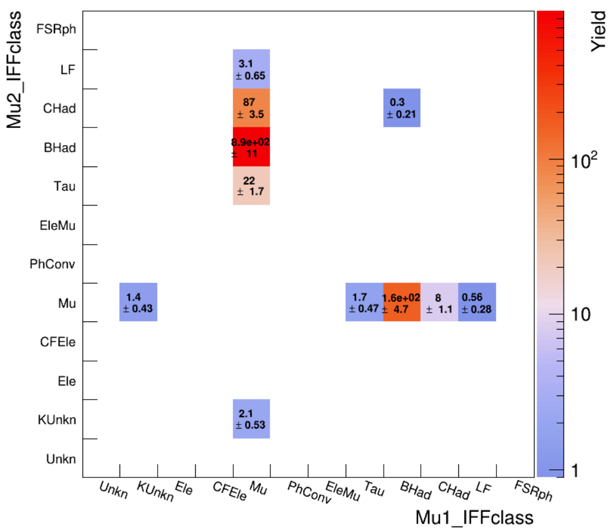

(c) $t\bar{t}$ - $\mu^{\pm}\mu^{\pm}$

Figure 4.9: Truth lepton composition at preselection (Table 4.5) for the $t\bar{t}$ processes. The two-dimensional plots represent: leading (highest p_T)-vs-subleading electron truth type in the $e^{\pm}e^{\pm}$ channel (left), electron-vs-muon truth type in the $e^{\pm}\mu^{\pm}$ channel (middle), and leading-vs-subleading muon truth type in the $\mu^{\pm}\mu^{\pm}$ channel (right).

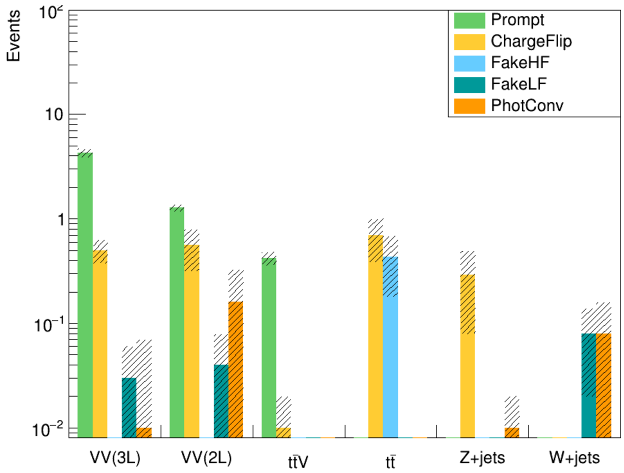

(a) $\mathrm{SR}^{Wh}_{\text{high-}m_{\mathrm{T2}}}$-1-$ee$

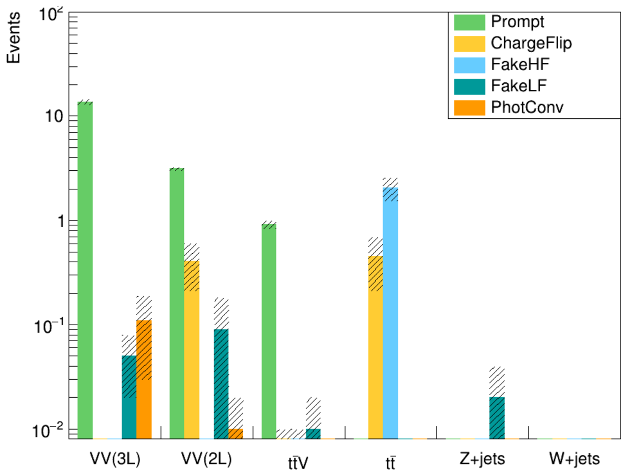

(b) $\mathrm{SR}^{Wh}_{\text{high-}m_{\mathrm{T2}}}$-1-$e\mu$

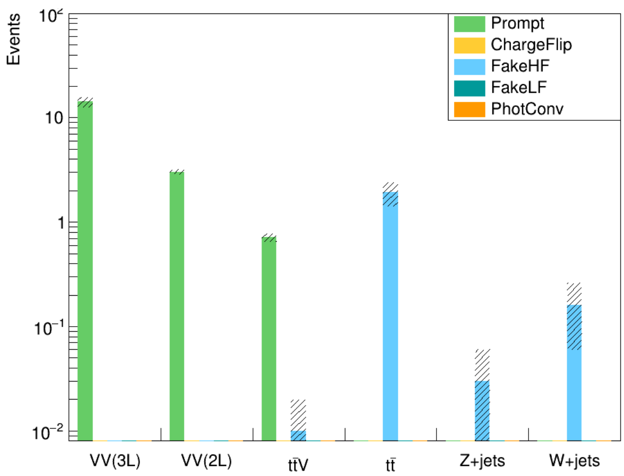

(c) $\mathrm{SR}^{Wh}_{\text{high-}m_{\mathrm{T2}}}$-1-$\mu\mu$

Figure 4.10: Bar charts showing the different sources of backgrounds based on the truth lepton composition of each event of the SM $VV(3\ell)$, $VV(2\ell)$, $t\bar{t}+V$, Z+jets and W+jets processes in each flavour channel of $\mathrm{SR}^{Wh}_{\text{high-}m_{\mathrm{T2}}}$-1. Statistical uncertainties from MC are shown.

The plots in Figure 4.10 also show that $VV(3\ell)$, or WZ, contributes almost exclusively as the main prompt lepton background, whereas $VV(2\ell)$ contributes either as a prompt lepton background, i.e. from its $W^{\pm}W^{\pm}$ component, or as a CF background arising from all SM di-boson processes resulting into two opposite-sign leptons. Finally, the contribution from photon conversion is largely negligible or compatible with zero within the statistical uncertainties, and is thus estimated exclusively from MC in the Wh-SS analysis.

4.3.2 Prompt lepton background estimation

WZ background estimation

In order to design a CR to estimate the SM WZ process it is necessary to understand the mechanism with which the fully leptonically-decaying WZ becomes a background for events with a same-sign lepton pair. This happens e.g. when one lepton from the Z decay fails the lepton definition criteria. Hence, the definition of this CR, called CRWZ^{Wh}, is based on an event selection similar to the Wh-SS preselection (Table 4.5), with the exception of the presence of a third lepton forming a Same-Flavour Opposite-Sign (SFOS) pair with one of the other two same-sign leptons (here referred to as ℓ_1^{Sig} and ℓ_2^{Sig}). Such lepton (referred to as ℓ^{BL}) is required to pass the baseline criteria whilst failing the signal criteria. Additional requirements are applied on the invariant mass of the SFOS lepton pairs (Equation 4.2), computed from ℓ^{BL} and either one of the signal leptons in the event, and called $m^{\mathrm{SFOS}}_{\ell^{\mathrm{Sig}}\ell^{\mathrm{BL}}}$. If more than one SFOS pair is found in the event , namely $n^{\mathrm{SFOS}}_{\ell^{\mathrm{Sig}}\ell^{\mathrm{BL}}} > 1$ (i.e. ℓ^{BL} forms a SFOS lepton pair with both ℓ_1^{Sig} and ℓ_2^{Sig}), the pair whose invariant mass is closer to the nominal m_Z is chosen for the computation of $m^{\mathrm{SFOS}}_{\ell^{\mathrm{Sig}}\ell^{\mathrm{BL}}}$. Then, $m^{\mathrm{SFOS}}_{\ell^{\mathrm{Sig}}\ell^{\mathrm{BL}}}$ is required to be compatible with the mass of the Z boson, namely $m^{\mathrm{SFOS}}_{\ell^{\mathrm{Sig}}\ell^{\mathrm{BL}}} \in [75, 105]$ GeV . This requirement increases the likelihood that ℓ^{BL} is a prompt lepton despite failing the signal selection criteria. In order to suppress background events from photon conversions, events are rejected if the invariant mass $m_{\ell\ell\ell}$ (Equation 4.3) of all three leptons in the event (ℓ^{BL}, ℓ_1^{Sig} and ℓ_2^{Sig}) is compatible with m_Z, i.e. $m_{\ell\ell\ell} \notin [80, 100]$ GeV . Finally, events passing the CRWZ^{Wh} selections are also required to satisfy $\mathrm{Sig}(E_{\mathrm{T}}^{\mathrm{miss}}) < 6$.

The definition of the VR for the WZ background, VRWZ^{Wh}, follows an analogous selection compared to CRWZ^{Wh}, with the only exception that events are required to satisfy $\mathrm{Sig}(E_{\mathrm{T}}^{\mathrm{miss}}) \geq 6$ to VRWZ^{Wh}. This makes the phase-space targeted by VRWZ^{Wh} closer to that of the SRs compared to CRWZ^{Wh}, whilst keeping CRWZ^{Wh} and VRWZ^{Wh} mutually orthogonal. A summary of the selection criteria used for CRWZ^{Wh} and VRWZ^{Wh} is given in Table 4.8.

With these event selections, the purity of the WZ background reaches more than 90% in both CRWZ^{Wh} and VRWZ^{Wh}, with a very small contamination from the SUSY signals (< 1%). The distributions of key variables in both regions before the background-only fit are shown in Figure 4.11. Prior to the application of any NF to the WZ prediction from MC, a satisfactory agreement between data and the total SM background is found in both CRWZ^{Wh} and VRWZ^{Wh}.

Table 4.8: Summary of the selection criteria for the CR and the VR for the SM WZ background in the Wh-SS search.

Variable	$\text{CR}WZ^{Wh}$	$\text{VR}WZ^{Wh}$
n_{ℓ}^{BL}	$= 3$	
n_{ℓ}^{Signal}	$= 2$	
$p_{\text{T}}^{\ell_1^{\text{Sig}}}$, $p_{\text{T}}^{\ell_2^{\text{Sig}}}$, $p_{\text{T}}^{\ell^{\text{BL}}}$ [GeV]	$> 25, 25, 10$	
Charge(ℓ_1^{Sig},ℓ_2^{Sig})	$++$ or $--$	
n_{jets}	≥ 1	
$n_{b-\text{jets}}$	$= 0$	
$E_{\text{T}}^{\text{miss}}$ [GeV]	≥ 50	
$n_{\ell^{\text{Sig}}\ell^{\text{BL}}}^{\text{SFOS}}$	≥ 1	
$m_{\ell^{\text{Sig}}\ell^{\text{BL}}}^{\text{SFOS}}$ [GeV]	$\in [75, 105]$	
$m_{\ell\ell\ell}$ [GeV]	$\notin [80, 100]$	
$E_{\text{T}}^{\text{miss}}$ significance	< 6	≥ 6

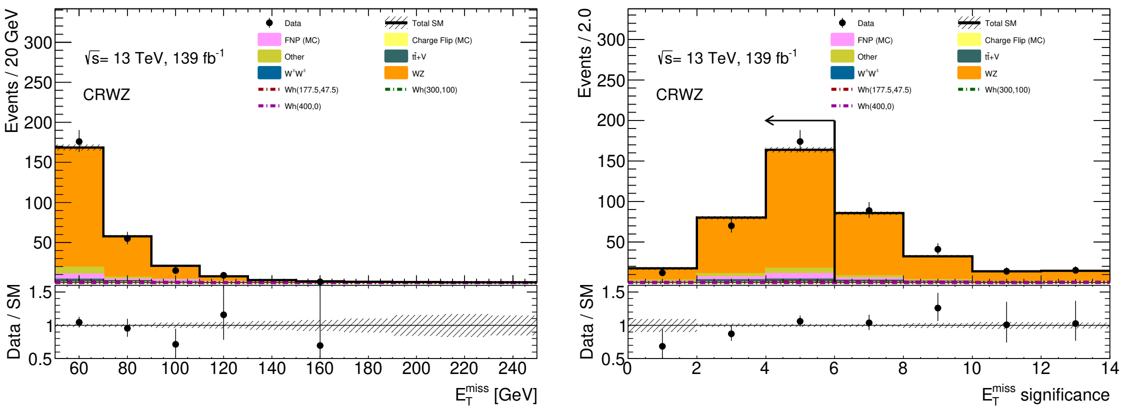

(a) $\text{CR}WZ^{Wh}$ – before background-only fit

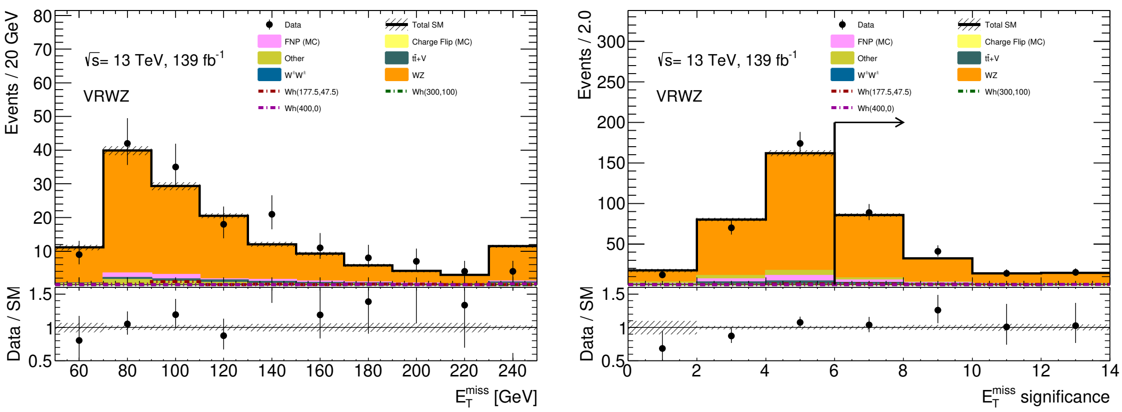

(b) $\text{VR}WZ^{Wh}$ – before background-only fit

Figure 4.11: Distributions of $E_{\text{T}}^{\text{miss}}$ (left) and $E_{\text{T}}^{\text{miss}}$ significance (right) for events passing the $\text{CR}WZ^{Wh}$ (top) and $\text{VR}WZ^{Wh}$ (bottom) of the Wh-SS analysis (Table 4.8) before the background-only fit. Contributions from MC are shown for the relevant SM background processes. The lower panel shows the ratio between data and SM background. Only statistical uncertainties from the MC predictions are shown.

$W^{\pm}W^{\pm}$ background estimation

In order to define a CR which is pure enough in the $W^{\pm}W^{\pm}$ contribution and at the same time orthogonal to the SRs, the preselection of the Wh-SS search (Table 4.5) is considered. Given that the SM $W^{\pm}W^{\pm}$ process occurs in association with jets in the final state (Section 4.2.3), only events with at least two jets ($n_{\text{jets}} \geq 2$) are requested. Moreover, the invariant mass of the leading and sub-leading di-jet system, m_{jj} (Equation 4.4) is required to satisfy $m_{\text{jj}} \geq 350$ GeV . This cut enhances the relative contribution of $W^{\pm}W^{\pm}$ in the CR, whilst guaranteeing the orthogonality with respect to the SRs. The purity of $W^{\pm}W^{\pm}$ in its CR is further increased by requiring the p_{T} of both leading and sub-leading jets to be at least 75 GeV . In the $e^{\pm}e^{\pm}$ flavour channel, the contribution from CF is suppressed by requiring the invariant mass of the di-electron system not to be compatible with the mass of the Z boson ($|m_{ee} - m_{\text{Z}}| \geq 15$ GeV). Finally, events are also required to satisfy $\text{Sig}(E_{\text{T}}^{\text{miss}}) < 6$.

Similarly to the WZ background case, the definition of the VR for $W^{\pm}W^{\pm}$ is obtained by taking the same event selections of the corresponding CR and inverting the $E_{\text{T}}^{\text{miss}}$ significance cut, i. e. $\text{Sig}(E_{\text{T}}^{\text{miss}}) \geq 6$. A summary of the selections used for this CR and VR, called CRWW^{Wh} and VRWW^{Wh}, is reported in Table 4.9.

Table 4.9: Summary of the selection criteria for the CR and the VR for the SM $W^{\pm}W^{\pm}$ background in the Wh-SS search. Preselection criteria (Table 4.5) are applied to both regions.

Variable	CRWW^{Wh}	VRWW^{Wh}
Wh-SS preselection	Applied	
n_{jets}	≥ 2	
m_{jj} [GeV]	≥ 350	
$p_{\text{T}}^{j_1}$, $p_{\text{T}}^{j_2}$ [GeV]	$\geq 75, 75$	
$\lvert m_{ee} - m_{\text{Z}}\rvert$ [GeV]	≥ 15 ($e^{\pm}e^{\pm}$ only)	
$E_{\text{T}}^{\text{miss}}$ significance	< 6	≥ 6

The distributions of key variables in CRWW^{Wh} and VRWW^{Wh} comparing data and MC background predictions before the background-only fit are shown in Figure 4.12.

The results show local over-fluctuations of data with respect to the SM background (e. g. for $p_{\text{T}}^{j_2} \simeq 110$ GeV in Figure 4.12a), and, more importantly, a systematic underestimation of the total SM background prediction from MC with respect to data in both CRWW^{Wh} and VRWW^{Wh}. This discrepancy has been found to be consistent with the recent measurement of the fiducial cross-section of the $W^{\pm}W^{\pm}$ process by the ATLAS Collaboration [138]. This measurement, which uses the 2015-2016 dataset, showed that in the SHERPA generator there is an underestimation of the $W^{\pm}W^{\pm}$ fiducial cross-section compared to data. Whilst measuring the total fiducial cross-section, it has also been assessed that, in order to match the observed data, MC events of the EWK $W^{\pm}W^{\pm}$ process generated with SHERPA must be scaled up by a measured value of $1.44^{+0.26}_{-0.24}$ (stat.) $^{+0.28}_{-0.22}$ (syst.), which is here referred to as a K-*factor*. The same distributions showed in Figure 4.12 obtained after multiplying the number of MC events from $W^{\pm}W^{\pm}$ by this K-factor are shown in Figure 4.13b.

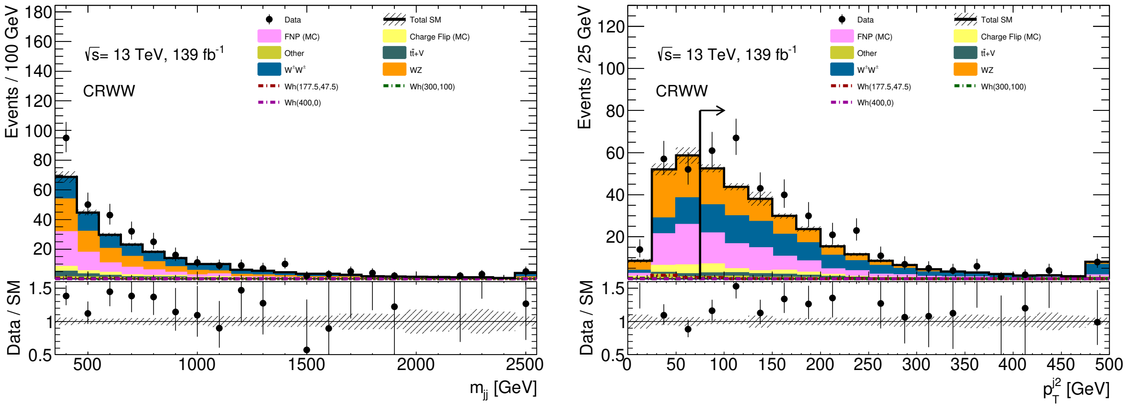

(a) CRWW^{Wh} – before background-only fit

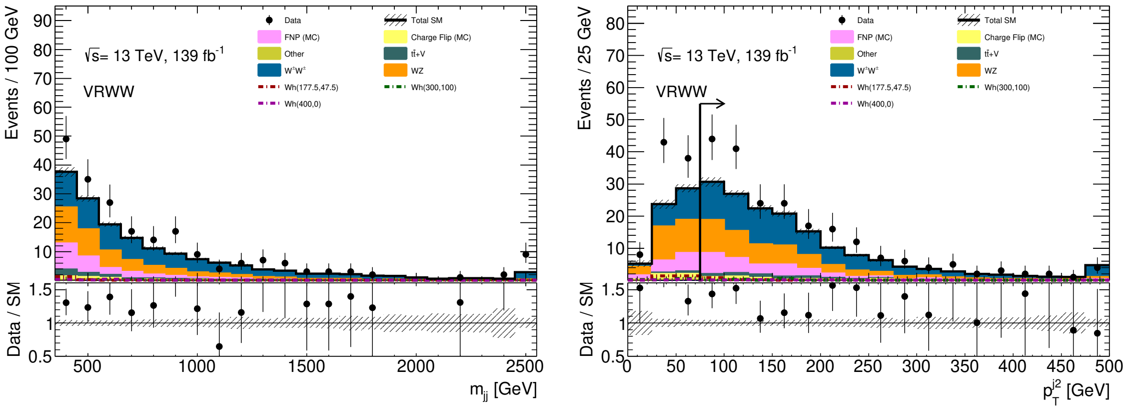

(b) VRWW^{Wh} – before background-only fit

Figure 4.12: Distributions of m_{jj} (left) and the second-leading jet p_{T} (right) for events passing the CRWW^{Wh} (top) and VRWW^{Wh} (bottom) of the Wh-SS analysis (Table 4.9) before the background-only fit. Contributions from MC are shown for the relevant SM background processes. The lower panel shows the ratio between data and SM background. Only statistical uncertainties from the MC backgrounds are shown.

After the application of the K-factor, results show in general a satisfactory agreement between data and SM background in both CRWW^{Wh} and VRWW^{Wh} within the statistical uncertainties. Therefore, henceforth and also when performing the background-only fit, the contribution of $W^{\pm}W^{\pm}$ events in every region of the Wh-SS analysis is multiplied by this K-factor.

Through the event selections of Table 4.9, it is possible to achieve a purity of the $W^{\pm}W^{\pm}$ background in CRWW^{Wh} of about 45%, with non-negligible contributions from the WZ and FNP backgrounds. The contamination of the SUSY signals of the Wh-SS model in both CRWW^{Wh} and VRWW^{Wh} is found to be small, i. e. less than 3%.

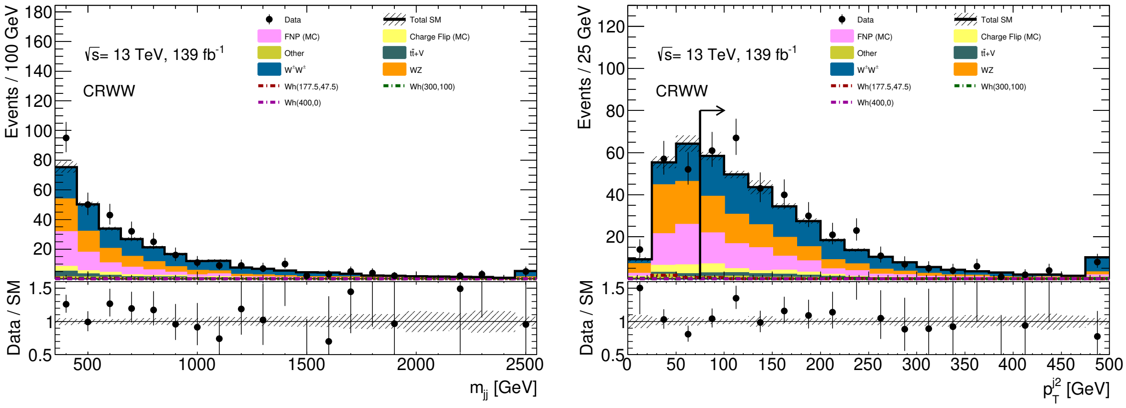

(a) CRWW^{Wh} – before background-only fit – with K-factor

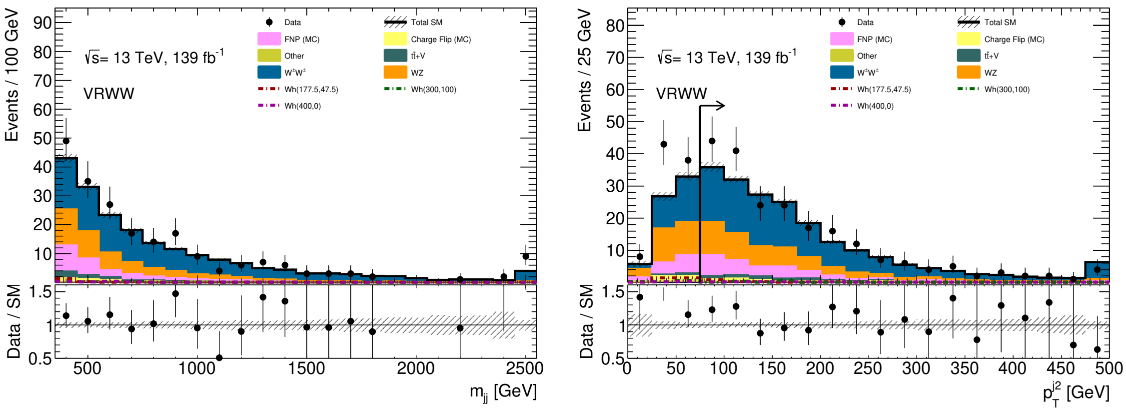

(b) VRWW^{Wh} – before background-only fit – with K-factor

Figure 4.13: Distributions of m_{jj} (left) and the second-leading jet p_{T} (right) for events passing the CRWW^{Wh} (top) and VRWW^{Wh} (bottom) of the Wh-SS analysis (Table 4.9) before the background-only fit. Contributions from MC are shown for the relevant SM background processes. The MC $W^{\pm}W^{\pm}$ contribution has been scaled by the corresponding K-factor (see text). The lower panel shows the ratio between data and SM background. Only statistical uncertainties from the MC backgrounds are shown.

4.3.3 Data-driven estimation of the Charge-Flip background

The data-driven estimation of the CF background in a region with two same-sign leptons is based on the idea to correlate CF events with same-sign leptons to opposite-sign leptons events by means of a *CF rate*, ϵ, which represents the probability for a lepton to be reconstructed with the wrong electrical charge (“flipped” charge). The probability for a lepton not to have undergone CF is given by $(1-\epsilon)$. Taking into account the CF rates of the two leptons in the event, ϵ_1 and ϵ_2, it is possible to define:

$$\begin{cases} p_{1\mathrm{CF}} = \epsilon_1(1-\epsilon_2) + (1-\epsilon_1)\epsilon_2 & \text{(4.8.a)} \\ p_{0/2\mathrm{CF}} = (1-\epsilon_1)(1-\epsilon_2) + \epsilon_1\epsilon_2 & \text{(4.8.b)} \end{cases}$$

where, $p_{1\mathrm{CF}}$ is the probability that one lepton of the di-lepton system has undergone CF, whereas $p_{0/2\mathrm{CF}}$ is the probability that either both or none of the leptons have undergone CF. From this:

$$\begin{pmatrix} N_{\mathrm{OS}} \\ N_{\mathrm{SS}} \end{pmatrix} = \begin{pmatrix} p_{0/2\mathrm{CF}} & p_{1\mathrm{CF}} \\ p_{1\mathrm{CF}} & p_{0/2\mathrm{CF}} \end{pmatrix} \begin{pmatrix} N_{\mathrm{OS}}^{\mathrm{R}} \\ N_{\mathrm{SS}}^{\mathrm{R}} \end{pmatrix} \tag{4.9}$$

where N_{OS} (N_{SS}) is the number of opposite-sign (same-sign) events in the considered di-lepton region and the superscript "R" stands for "real" and indicates events with the true lepton charges. The terms extracted from Equation 4.9 can, then, be re-written as follows:

$$\begin{cases} N_{\mathrm{OS}}^{\overline{\mathrm{CF}}} = p_{0/2\mathrm{CF}}\ N_{\mathrm{OS}}^{\mathrm{R}} & \text{(4.10.a)} \\ N_{\mathrm{OS}}^{\mathrm{CF}} = p_{1\mathrm{CF}}\ N_{\mathrm{SS}}^{\mathrm{R}} & \text{(4.10.b)} \\ N_{\mathrm{SS}}^{\overline{\mathrm{CF}}} = p_{0/2\mathrm{CF}}\ N_{\mathrm{SS}}^{\mathrm{R}} & \text{(4.10.c)} \\ N_{\mathrm{SS}}^{\mathrm{CF}} = p_{1\mathrm{CF}}\ N_{\mathrm{OS}}^{\mathrm{R}} & \text{(4.10.d)} \end{cases}$$

Here the superscript "$\overline{\mathrm{CF}}$" indicates events where two or no CFs have occurred, whereas the superscript "CF" indicates events where only one CF has occurred. For example, $N_{\mathrm{OS}}^{\overline{\mathrm{CF}}}$ are events reconstructed with an opposite-sign lepton pair, in which either the two leptons have the real charges or both the original charges have been switched through the occurrence of CFs. On the other hand, $N_{\mathrm{SS}}^{\mathrm{CF}}$ are events which are reconstructed with two same-sign leptons due to the CF of one of the leptons in an originally opposite-sign pair. $N_{\mathrm{SS}}^{\mathrm{CF}}$ is therefore the quantity that one wishes to estimated with the data-driven procedure here described. Given that the real lepton charges are not known, a measurement of $N_{\mathrm{SS}}^{\mathrm{CF}}$ can be obtained by combining Equations 4.10.a and 4.10.d:

$$N_{\mathrm{SS}}^{\mathrm{CF}} = \frac{p_{1\mathrm{CF}}}{p_{0/2\mathrm{CF}}}\ N_{\mathrm{OS}}^{\overline{\mathrm{CF}}}. \tag{4.11}$$

It is then possible to consider the following approximation: $N_{\mathrm{OS}}^{\overline{\mathrm{CF}}} \simeq N_{\mathrm{OS}}$. This follows from the fact that in data the contribution from the CF in events reconstructed with two opposite-sign leptons is generally negligible compared to same-sign events. Hence:

$$N_{\mathrm{SS}}^{\mathrm{CF}} = \frac{p_{1\mathrm{CF}}}{p_{0/2\mathrm{CF}}}\ N_{\mathrm{OS}} = w_{\mathrm{CF}}\ N_{\mathrm{OS}}. \tag{4.12}$$

Equation 4.12 represents basic formulation for the data-driven estimation of CF events in a same-sign region, used in the Wh-SS analysis. In practice, the procedure involves considering the data in a region with the same event selection as the targeted region (e. g. a SR), but with an opposite-sign lepton pair instead of same-sign (thus, achieving the orthogonality), and then re-weighting the number of data observed by a factor, here referred to as the *CF weight*, whose definition follows from Equations 4.8 and 4.12:

$$w_{\mathrm{CF}} = \frac{\epsilon_1(1-\epsilon_2) + (1-\epsilon_1)\epsilon_2}{(1-\epsilon_1)(1-\epsilon_2) + \epsilon_1\epsilon_2}. \tag{4.13}$$

In general, w_{CF} is a function of the CF rates of the two leptons, namely $w_{\mathrm{CF}} = w_{\mathrm{CF}}(\epsilon_1, \epsilon_2)$. Finally, given that the occurrence of the CF background arising from the mis-reconstruction of the muon charge is expected to be negligible, henceforth the $\epsilon_\mu = 0$ assumption is made.

Electron Charge-Flip rate measurement

In the Wh-SS analysis, the electron CF rates are measured as a function of the electron p_{T} and $|\eta|$ in MC and then multiplied by dedicated Scale Factors (SFs), called $\mathrm{SF}_{\mathrm{CF}}$, to correct any mis-modelling in MC to the observed data:

$$\epsilon^{\text{Data}}(i) = \epsilon^{\text{MC}}(i) \times \text{SF}_{\text{CF}}(i), \tag{4.14}$$

where the discrete index i indicates each p_{T} and $|\eta|$ bin. The values of SF_{CF} are extracted from data selected in a region with an enriched contribution from events with a real opposite-sign lepton pair, i. e. $Z \to ee$ events. The CF rate is then obtained from the fraction of same-sign and opposite-sign events observed, and the measurement of SF_{CF} is then obtained from the ratio of the CF rate in data with respect tot that from MC. More details about the measurement of these SFs can be found in Reference [121]. The value of ϵ^{MC} in Equation 4.14 is given by:

$$\epsilon^{\text{MC}}(i) = \frac{N_{e^\pm}^{\text{CFele}}(i)}{N_{e^\pm}^{\text{Total}}(i)}, \tag{4.15}$$

obtained by counting the number of the electrons identified at truth-level as CF (see Section 4.3.1) with respect to all electrons with $p_{\text{T}} \geq 25$ GeV in every di-electron event of all the MC backgrounds considered (mainly Z+jets and $t\bar{t}$).

The method used, based on Equation 4.14, allows to estimate the CF rates with relatively high statistical precision, by means the cancellation of all the possible sources of experimental systematic (Section 4.4.1) uncertainties which equally affect the numerator and the denominator of Equation 4.15.

In the Wh-SS analysis, CF rates are measured for both signal electrons and Loose-Not-Tight electrons (Section 4.2.1). Having a data-driven estimation of the CF background in events with Loose-Not-Tight electrons has been necessary in the procedure used for the estimation of the FNP background, which is explained in detail in Section 4.3.5. The measured values of the CF rates for every p_{T} and $|\eta|$ bins are shown in Figure 4.14.

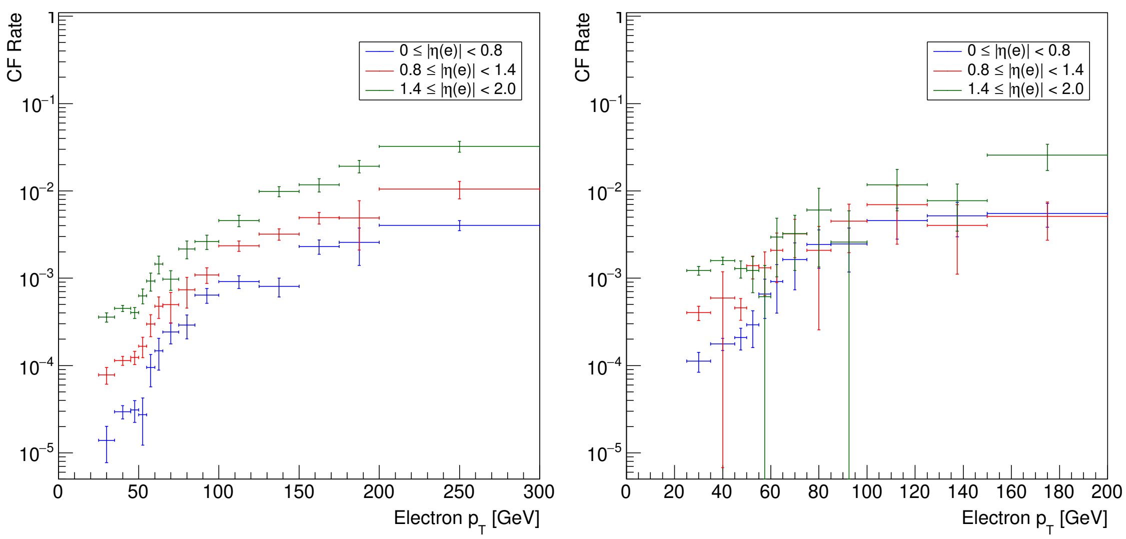

(a) Signal electrons (b) Loose-Not-Tight electrons

Figure 4.14: Measured values of the CF rate for (a) signal and (b) Loose-Not-Tight electrons in all the adopted p_{T} and $|\eta|$ bins. The last p_{T} bin is inclusive of $p_{\text{T}} \geq 200$ GeV ($p_{\text{T}} \geq 150$ GeV) for signal (Loose-Not-Tight) electrons. The error bars represent the statistical uncertainties propagated from MC.

The bin sizes have been chosen to minimise the impact of the statistical uncertainties propagated from MC, and represented by the error bars in Figure 4.14. As expected, the measured CF rate values rapidly increase with the p_{T} of the electron, reflecting the fact that for straighter tracks the probability for mis-reconstructing the charge increases. At the same time, an even steeper increase is observed as a function of $|\eta|$, consistently with the electron traversing more of the detector material which enhances the likelihood of bremsstrahlung emission (Figure 3.6b).

The CF rates for Loose-Not-Tight electrons in general have larger statistical uncertainties than those for signal electrons. This is a direct consequence of the fact that the contribution of the CF background for events with Loose-Not-Tight electrons, which are instead dominated by the FNP lepton background, is significantly smaller than in events with signal leptons.

Systematic uncertainties

Three different sources of systematic uncertainties are taken into consideration for the data-driven estimation of the CF background:

- **MCstat**: The propagated uncertainty from the statistical error from MC on the measured CF rates (shown in the error bars of Figure 4.14);
- **SFstat**: the propagated uncertainty from the statistical error on $\mathrm{SF}_{\mathrm{CF}}$ (provided in Reference [121]);
- **SFsys**: the propagated uncertainty from the systematic error on $\mathrm{SF}_{\mathrm{CF}}$ (provided in Reference [121]).

The impact of each of these sources of systematic uncertainty on the final CF estimation is evaluated by recomputing the CF weight in Equation 4.13 after changing the input CF rates according to their corresponding systematic variation, so that:

$$w_{\mathrm{CF}} = w_{\mathrm{CF}}(\epsilon_1, \epsilon_2) \quad \rightarrow \quad w_{\mathrm{CF}} + \delta w_{\mathrm{CF}}^{Sys} = w_{\mathrm{CF}}(\epsilon_1 + \delta\epsilon_1^{Sys}, \epsilon_2 + \delta\epsilon_2^{Sys}) \tag{4.16}$$

where $\delta\epsilon_i^{Sys}$ represents the systematic variation of the CF rate of the i-th electron. This recomputed CF weight is then used in Equation 4.12 to obtain the estimation of the CF background changed due to original systematic variation. The impact of each uncertainty source in each region is finally obtained by considering the relative difference with respect to the nominal, estimated CF background. For instance, in the $e^{\pm}e^{\pm}$ channel of the Wh-SS pre-selection (Table 4.5): MCstat corresponds to a ~20% variation, SFstat to ~8% and SFsys to a ~16% variation.

Since the measurements of $\mathrm{SF}_{\mathrm{CF}}$ for Loose-Not-Tight electrons were not available at the time that the Wh-SS analysis was performed, discrepancies in the final CF background estimation with respect to data have been observed. Through dedicate studies, which I have not personally contributed to, it has been possible to establish that such discrepancies can be covered by assigning in this case a conservative 25% flat systematic uncertainty on the estimated CF background, which has been taken into account in the rest of the analysis.

Closure test

In order to assess the validity of the data-driven CF estimation discussed above, a closure test has been performed considering Z+jets MC events. This is done by comparing the MC events in Z+jets which fall into the “ChargeFlip” truth-event category (defined in Section 4.3.1) to the corresponding data-driven CF estimation obtained by applying the procedure described in this Section to MC Z+jets events instead of data. If the procedure for the data-driven estimation is correct, these two yields should coincide.

The results of the closure test for events passing the Wh-SS preselection (Table 4.5) but with a complementary $E_{\mathrm{T}}^{\mathrm{miss}}$ cut (i. e. $E_{\mathrm{T}}^{\mathrm{miss}} < 50$ GeV to enhance the Z+jets and, therefore, the CF contribution) are shown in Figure 4.15.

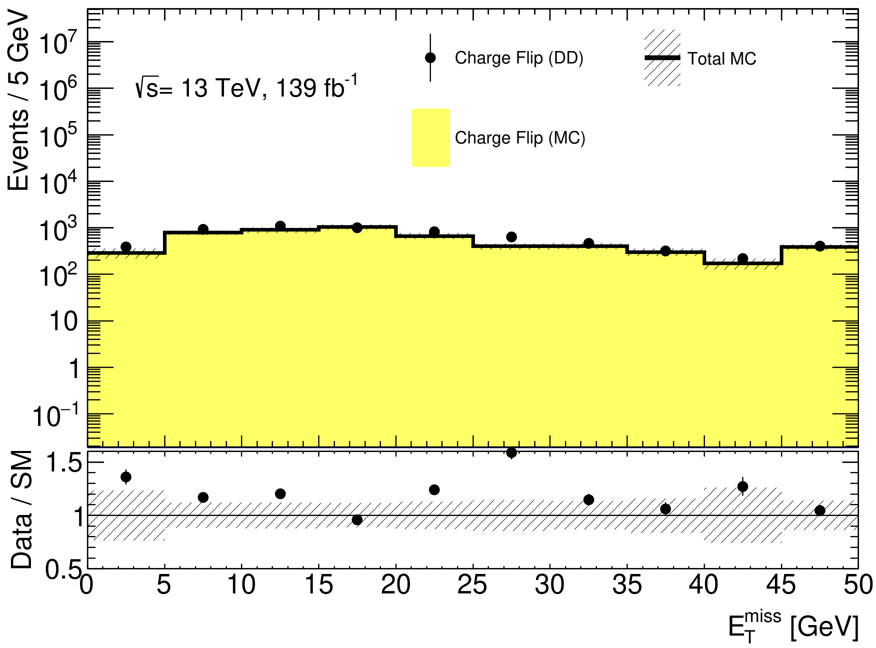

Figure 4.15: Result of the closure test CF events from Z+jets comparing MC prediction (shaded yellow area) with the corresponding estimated CF contribution (“DD” in the plots and indicated with black dots) for the $E_{\mathrm{T}}^{\mathrm{miss}}$ distribution. The test is performed for signal electrons in events passing the Wh-SS preselection (Table 4.5) with an inverted $E_{\mathrm{T}}^{\mathrm{miss}}$ cut ($E_{\mathrm{T}}^{\mathrm{miss}} < 50$ GeV). The lower panel shows the agreement between MC and the estimated CF background. Only statistical uncertainties on MC are shown.

In general, the results of the closure test show a satisfactory agreement with the CF events from MC, thus proving the validity of the CF estimation for the phase-space targeted by the Wh-SS SRs. Although, localised discrepancies are still observed for specific values of $E_{\mathrm{T}}^{\mathrm{miss}}$ (e. g. for $E_{\mathrm{T}}^{\mathrm{miss}} \in [25, 30]$ GeV), these are associated with statistical underestimations of the background from MC and are covered by each of the three systematic uncertainties sources, described above, which are not shown in Figure 4.15.

4.3.4 The Fake Factor method

The Fake Factor (FF) is a data-driven method which allows to estimate the number of events with FNP leptons in given regions of interest, such as the SRs. It relies on the Loose-Not-Tight, Loose and Tight lepton selection criteria defined in Section 4.2.1.

In the FF method, the number of events with FNP leptons in a region with only Tight leptons is correlated to an orthogonal control sample obtained by requiring one or more lepton in the same regions to be Loose-Not-Tight. The FNP estimate in the region in question is then obtained by reweighting events in the control sample multiplying them by a "transfer factor", called the *Fake Factor*.

The following quantities are essential for the formulation of the method:

- the *real lepton efficiency* (r), defined as the probability that a real/prompt lepton passing the Loose criteria also passes the Tight criteria;
- *fake lepton efficiency* (f), or *fake rate*, defined as the probability that a FNP lepton passing the Loose criteria also passes the Tight criteria;

The probability that a Loose real lepton fails the Tight criteria, thus passing the Loose-Not-Tight selection, is then $(1-r)$. Similarly, the probability for a Loose FNP lepton to be Loose-Not-Tight is $(1-f)$.

One can illustrate the method considering the simplified case with only one lepton in the event, when it is possible to write:

$$\begin{pmatrix} N_T \\ N_{\overline{T}} \end{pmatrix} = \begin{pmatrix} r & f \\ (1-r) & (1-f) \end{pmatrix} \begin{pmatrix} N_L^R \\ N_L^F \end{pmatrix}, \tag{4.17}$$

where N_T ($N_{\overline{T}}$) is the number of events with one Tight (Loose-Not-Tight) lepton, and N_L^R (N_L^F) is the number of events with one real (FNP) lepton passing the Loose criteria.

Using a frequentist interpretation of probability [148], it is possible to compute:

$$(1-r) = \frac{N_{\overline{T}}^R}{N_L^R} \quad \text{and} \quad f = \frac{N_T^F}{N_L^F}, \tag{4.18}$$

where $N_{\overline{T}}^R$ is the number of events with one real lepton passing the Loose-Not-Tight criteria, and N_T^F is the number of events with one FNP lepton passing the Tight criteria, namely the FNP contribution to be estimated.

By inverting the matrix in Equation 4.17 and applying the relations in Equation 4.18, it is possible to obtain:

$$N_T^F = \frac{f}{r-f} \left\{ r \cdot N_{\overline{T}} - \frac{r-f}{1-f} \left[N_{\overline{T}}^R + \frac{f(1-r)}{r-f} N_{\overline{T}} \right] \right\}. \tag{4.19}$$

This can be simplified by making the approximation $r \simeq 1$, which is valid in the regime in which the efficiencies for the reconstruction, identification and isolation of leptons (see Section 3.3.2) approach 100%, which is generally true in the phase-space targeted by the Wh-SS analysis, given the adopted lepton definitions, the OvR procedure and event selections. Equation 4.19 then reduces to:

$$N^{FNP} = N^F_T = \frac{f}{1-f}\left(N_{\overline{T}} - N^R_{\overline{T}}\right) = FF\left(N_{\overline{T}} - N^R_{\overline{T}}\right). \tag{4.20}$$

Equation 4.20 is at the core of the FF method. This relation shows that it is possible to estimate the FNP contribution in a region with one Tight lepton by counting the number of events with one Loose-Not-Tight (usually measured from data) in the corresponding control sample after subtracting the contribution from prompt/real leptons in the same sample (typically taken from MC). The formulation of the same method which however takes into account measured values of $r < 1$ is known as the *Matrix method*.

The transfer factor "FF" in Equation 4.20 is what is often called the Fake Factor. Using Equation 4.18, it is possible to write:

$$FF = \frac{f}{1-f} = \frac{N^F_T}{N^F_L - N^F_T} = \frac{N^F_T}{N^F_{\overline{T}}}. \tag{4.21}$$

The ratio in Equation 4.21 can be measured from a combination data and MC simulations (Section 5.3.2).

Having established the formulation of the FF method in the simplest possible case, it is necessary to generalise for events with higher lepton multiplicity. For this purpose, Equation 4.17 needs to implement a matrix of dimensions 2^{n_ℓ}, where n_ℓ is the desired lepton multiplicity, and which considers all possible permutations of Tight and Loose-Not-Tight leptons (corresponding to real and FNP leptons, respectively). For events with two leptons in the final state, the matrix becomes 4×4 and Equation 4.20 takes the form:

$$N^{FNP} = FF_1\left(N_{\overline{T}T} - N^{RR}_{\overline{T}T}\right) + FF_2\left(N_{T\overline{T}} - N^{RR}_{T\overline{T}}\right) - FF_1 \cdot FF_2\left(N_{\overline{T}\overline{T}} - N^{RR}_{\overline{T}\overline{T}}\right). \tag{4.22}$$

Here FF_i refers to the FF associated to the i-th lepton (typically ordered in decreasing p_{T} values). The multiple subscripts and superscripts refer to each of the leptons separately, i. e. $N_{\overline{T}T}$ indicates the number of events in which the leading lepton is Loose-Not-Tight and the sub-leading lepton is Tight. The minus sign in Equation 4.22 is needed to remove double-counting arising from events in which both leptons are FNP.

Similarly, in the three-lepton case (which is relevant in the analysis described in Chapter 5), a 8×8 matrix needs to be considered and the final expression for the estimated N^{FNP} becomes:

$$\begin{aligned} N^{FNP} = {} & FF_1\left(N_{\overline{T}TT} - N^{RRR}_{\overline{T}TT}\right) + FF_2\left(N_{T\overline{T}T} - N^{RRR}_{T\overline{T}T}\right) + FF_3\left(N_{TT\overline{T}} - N^{RRR}_{TT\overline{T}}\right) \\ & - FF_1 \cdot FF_2\left(N_{\overline{T}\overline{T}T} - N^{RRR}_{\overline{T}\overline{T}T}\right) - FF_2 \cdot FF_3\left(N_{T\overline{T}\overline{T}} - N^{RRR}_{T\overline{T}\overline{T}}\right) \\ & - FF_1 \cdot FF_3\left(N_{\overline{T}T\overline{T}} - N^{RRR}_{\overline{T}T\overline{T}}\right) + FF_1 \cdot FF_2 \cdot FF_3\left(N_{\overline{T}\overline{T}\overline{T}} - N^{RRR}_{\overline{T}\overline{T}\overline{T}}\right). \end{aligned} \tag{4.23}$$

In practice, the FNP estimation procedure requires to subtract from data the contribution from events with prompt leptons and then reweighting this yield by a *FF weight*, w_{FF}. Depending on which term of Equation 4.22 (or Equation 4.23 for the three-lepton case) each event belongs to, w_{FF} can be generally viewed as a function of the FFs of every lepton in the event, namely $w_{FF} = w_{FF}(FF_i)$ with $i = 1, ..., n_\ell$. For instance, in the two-lepton case, for events in which the leading lepton is Loose-Not-Tight $w_{FF} = FF_1$, whereas if both leptons are Loose-Not-Tight then $w_{FF} = -FF_1 \cdot FF_2$.

Similarly to the CF estimation (Equation 4.16), the impact in the final FNP estimation of any source of systematic uncertainty is then evaluated by re-computing the FF weight after applying the corresponding systematic variation each lepton FF, namely:

$$w_{FF} = w_{FF}\left(FF_i\right) \quad \rightarrow \quad w_{FF} + \delta w_{FF}^{Sys} = w_{FF}\left(FF_i + \delta FF_i^{Sys}\right), \tag{4.24}$$

where i runs from 1 to n_ℓ and δFF_i^{Sys} is the systematic variation of each FF. The relative difference of the FNP thus obtained with respect to the the nominal FNP background estimation gives the impact of the source of systematic uncertainty considered in a given region.

4.3.5 Results of the Fake Factor method in the Wh-SS analysis

Having provided the general mathematical formulation of the FF method in Section 4.3.4, this Section is devoted to the description of all the aspects of the data-driven estimation of FNP lepton background specifically concerning the Wh-SS analysis.

The procedure employed is fundamentally linked to the definition of the Loose-Not-Tight leptons, given in Section 4.2.1. As Loose-Not-Tight leptons are supposed to be related to the FNP lepton composition in the SRs, the Loose-Not-Tight criteria must reflect the types of FNP leptons that contribute in the SRs (Section 4.3.1). For FNP muons in the Wh-SS regions, which are almost always from HF decays, this is achieved by requiring Loose-Not-Tight muons to fail only the signal isolation. On the other hand, since both LF and HF sources contribute to the FNP background with electrons, Loose-Not-Tight electrons are required to fail the signal identification, isolation or both. Hence, these definition of the Loose-Not-Tight criteria makes the employed data-driven estimation of the FNP background via the FF method specifically tailored to the Wh-SS analysis.

Electron and muon Fake Factors measurements

In order to measure the FFs the Tag-and-Probe technique, firstly introduced in Section 2.4.3, is used. First, events are requested to pass the selection in specifically designed CRs which are enriched in FNP events. In these, the presence of a same-sign lepton pair is required. The enhancement of the FNP contribution is achieved by considering an inclusive b-jet multiplicity and $E_T^{miss} < 50$ GeV, which also guarantee the orthogonality with the SRs of the Wh-SS analysis. Furthermore, events are selected requiring the presence of one of the leptons in the same-sign pair – i. e. the *Tag* or ℓ_{Tag} – to satisfy requirements which are as stringent or even more stringent compared to the signal lepton definition. The FFs are then measured with respect to the remaining lepton – i. e. the *Probe* or ℓ_{Probe} – which is required to be either Loose-Not-Tight or Tight. The Tag-and-Probe technique guarantees an unbiased measurement of the FFs from events in which the Tag is prompt whilst the probe is FNP. Similarly to the CF rates, the FFs are also measured as functions of the Probe lepton p_{T} and $|\eta|$.

In the muon FF measurement, the Tag muon in $\mu^{\pm}\mu^{\pm}$ events is required to be signal and also to pass the `Tight` isolation WP, which is more stringent than the signal isolation. If both muons pass such requirement, the leading muon is chosen as the Tag. The validity of this choice is confirmed by the consideration that in the MC $t\bar{t}$ process (the main source of FNP muons) 85% of the FNP events have a leading, prompt muon (Figure 4.9). The measurement of the muon FFs, in the CR here called $\text{CR}FF_{\mu}^{Wh}$, follows directly from the application of Equation 4.21 which uses data after subtracting from numerator and denominator the contribution from MC of all events with two prompt muons, namely:

$$FF_{\mu}(i) = \frac{N^{\text{Data}}_{\mu_{\text{Tag}}\mu_{\text{Probe}},\,\text{CR}FF_{\mu}^{Wh}}(i) - N^{\text{prompt MC}}_{\mu_{\text{Tag}}\mu_{\text{Probe}},\,\text{CR}FF_{\mu}^{Wh}}(i)}{N^{\text{Data}}_{\mu_{\text{Tag}}\overline{\mu_{\text{Probe}}},\,\text{CR}FF_{\mu}^{Wh}}(i) - N^{\text{prompt MC}}_{\mu_{\text{Tag}}\overline{\mu_{\text{Probe}}},\,\text{CR}FF_{\mu}^{Wh}}(i)}, \tag{4.25}$$

where the discrete index i runs over every p_{T} and $|\eta|$ bin for which the FF is measured and the overline notation indicates the cases in which the Probe is required to be Loose-Not-Tight.

For the electrons, the measurement of the FFs is more challenging due to the additional presence of LF FNP sources and the CF background. The Tag electron in $e^{\pm}e^{\pm}$ events is selected to be signal and also to satisfy the `Tight` identification WP, which is more stringent compared to the signal criteria. If both electrons pass such requirement, the leading electron is chosen as Tag. As in the muon case, this allows to increase the available statistics for the calculation of the electron FF, while also introducing the least amount of biases as possible in the event selection. Moreover, if both electrons pass the `Tight` identification, the leading, Tag electron is also required to be central ($|\eta_{e_{\text{Tag},1}}| < 1.0$), in order to suppress the CF background. The choice of such requirement is justified by the fact that the CF rates significantly increase for increasing electron p_{T} and $|\eta|$ (Figure 4.14). The level of suppression of the CF contribution from Tag electron with this choice has been found to be about 60%. Due to large statistical fluctuations the electron FFs are extracted in different p_{T} bins and a single, inclusive $|\eta|$ bin ($|\eta(e_{\text{probe}})| < 2.0$). Similarly to the muon FFs (Equation 4.25), the electron FFs are measured, in a CR here called $\text{CR}FF_{e}^{Wh}$, from data after subtracting from numerator and denominator the contribution from MC of all events with two prompt electrons and the corresponding estimated contributions of the CF background (Section 4.3.3), specifically:

$$FF_{e}(i) = \frac{N^{\text{Data}}_{e_{\text{Tag}}e_{\text{Probe}},\,\text{CR}FF_{e}^{Wh}}(i) - N^{\text{prompt MC}}_{e_{\text{Tag}}e_{\text{Probe}},\,\text{CR}FF_{e}^{Wh}}(i) - N^{\text{CF DD}}_{e_{\text{Tag}}e_{\text{Probe}},\,\text{CR}FF_{e}^{Wh}}(i)}{N^{\text{Data}}_{e_{\text{Tag}}\overline{e_{\text{Probe}}},\,\text{CR}FF_{e}^{Wh}}(i) - N^{\text{prompt MC}}_{e_{\text{Tag}}\overline{e_{\text{Probe}}},\,\text{CR}FF_{e}^{Wh}}(i) - N^{\text{CF DD}}_{e_{\text{Tag}}\overline{e_{\text{Probe}}},\,\text{CR}FF_{e}^{Wh}}(i)} \tag{4.26}$$

where, once again, the discrete index i runs over every p_{T} bin for which the FF is measured and the overline notation indicates the cases in which the Probe is required to be Loose-Not-Tight.

Once the electron and muon FFs have been measured, the data-driven estimation of the FNP background in any same-sign region follows from the application of Equation 4.22 independently for each flavour channel, and after subtracting the prompt lepton contribution from MC and the estimated CF background, namely for the $e^{\pm}e^{\pm}$ channel:

$$\begin{aligned}N^{FNP}_{e_1e_2} =& FF_{e_1} \times \left(N^{\text{Data}}_{\overline{e_1}e_2} - N^{\text{prompt MC}}_{\overline{e_1}e_2} - N^{\text{CF DD}}_{\overline{e_1}e_2}\right) + FF_{e_2} \times \left(N^{\text{Data}}_{e_1\overline{e_2}} - N^{\text{prompt MC}}_{e_1\overline{e_2}} - N^{\text{CF DD}}_{e_1\overline{e_2}}\right) \\ &- FF_{e_1} \times FF_{e_2} \times \left(N^{\text{Data}}_{\overline{e_1}\,\overline{e_2}} - N^{\text{prompt MC}}_{\overline{e_1}\,\overline{e_2}} - N^{\text{CF DD}}_{\overline{e_1}\,\overline{e_2}}\right)\end{aligned} \tag{4.27}$$

for the $e^{\pm}\mu^{\pm}$ channel:

$$\begin{aligned}N^{FNP}_{e\mu} =& FF_{e} \times \left(N^{\text{Data}}_{\overline{e}\mu} - N^{\text{prompt MC}}_{\overline{e}\mu} - N^{\text{CF DD}}_{\overline{e}\mu}\right) + FF_{\mu} \times \left(N^{\text{Data}}_{e\overline{\mu}} - N^{\text{prompt MC}}_{e\overline{\mu}} - N^{\text{CF DD}}_{e\overline{\mu}}\right) \\ &- FF_{e} \times FF_{\mu} \times \left(N^{\text{Data}}_{\overline{e}\,\overline{\mu}} - N^{\text{prompt MC}}_{\overline{e}\,\overline{\mu}} - N^{\text{CF DD}}_{\overline{e}\,\overline{\mu}}\right)\end{aligned} \tag{4.28}$$

and for the $\mu^{\pm}\mu^{\pm}$ channel:

$$\begin{aligned}N^{FNP}_{\mu_1\mu_2} =& FF_{\mu_1} \times \left(N^{\text{Data}}_{\overline{\mu_1}\mu_2} - N^{\text{prompt MC}}_{\overline{\mu_1}\mu_2}\right) + FF_{\mu_2} \times \left(N^{\text{Data}}_{\mu_1\overline{\mu_2}} - N^{\text{prompt MC}}_{\mu_1\overline{\mu_2}}\right) \\ &- FF_{\mu_1} \times FF_{\mu_2} \times \left(N^{\text{Data}}_{\overline{\mu_1}\,\overline{\mu_2}} - N^{\text{prompt MC}}_{\overline{\mu_1}\,\overline{\mu_2}}\right)\end{aligned} \tag{4.29}$$

The definitions of the cuts used to define CRFF^{Wh}_{e} and CRFF^{Wh}_{μ} are summarised in Table 4.10.

Figure 4.16 shows the Probe muon p_{T} distributions of data and total SM background from MC in the two $|\eta|$ bins considered. The fact that all distributions are dominated by $t\bar{t}$ events indicates that indeed in CRFF^{Wh}_{μ} the FNP muon contribution is enhanced. The bin-by-bin ratio of these distribution, after subtracting the corresponding prompt background contribution, gives the final value of the muon FFs, which is shown in Figure 4.17.

Table 4.10: Summary of the selection criteria of CRFF^{Wh}_{e} and CRFF^{Wh}_{μ} used in the Wh-SS analysis for the measurement of the FFs.

Variable	CRFF^{Wh}_{e}	CRFF^{Wh}_{μ}
n^{BL}_{ℓ}	$= 2$	
n^{Signal}_{ℓ}	≥ 1	
$p_{\text{T}}^{\ell_{\text{Tag}}}$, $p_{\text{T}}^{\ell_{\text{Probe}}}$ [GeV]	$> 25, 25$	
Charge(ℓ_{Tag},ℓ_{Probe})	++ or −−	
n_{jets}	≥ 1	
$m_{\ell\ell}$ [GeV]	≥ 20	
Flavour	$e^{\pm}e^{\pm}$	$\mu^{\pm}\mu^{\pm}$
$E_{\text{T}}^{\text{miss}}$ [GeV]	$\in [30, 50]$	< 50
$n_{b-\text{jets}}$	-	$= 1$
$\lvert m_{\ell\ell} - m_{Z}\rvert$ [GeV]	≥ 15	-
ℓ_{Tag} Collection	Signal	
ℓ_{Tag} Identification WP	`Tight`	-
ℓ_{Tag} Isolation WP	-	`Tight`
ℓ_{Tag} Acceptance	$\lvert\eta_{e_{\text{Tag},1}}\rvert < 1.0$	-
ℓ_{Probe} Collection	Loose-Not-Tight or Tight	

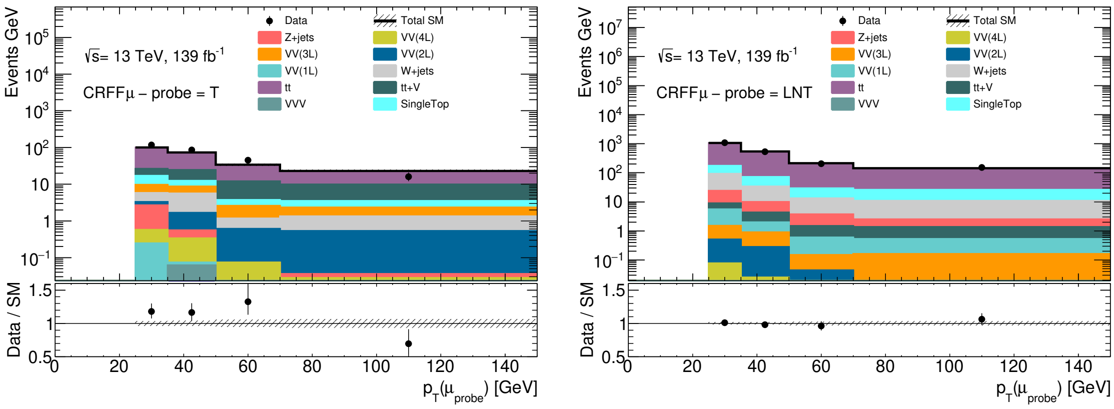

(a) $\mathrm{CR}FF_{\mu}^{Wh}$, $|\eta(\mu_{\mathrm{probe}})| < 1.25$

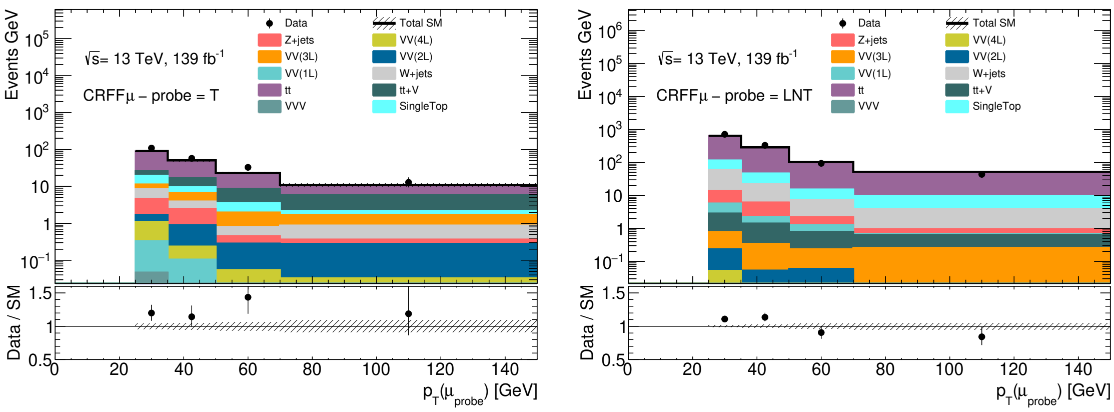

(b) $\mathrm{CR}FF_{\mu}^{Wh}$, $1.25 \leq |\eta(\mu_{\mathrm{probe}})| < 2.5$

Figure 4.16: Distributions of the p_{T} of the Probe muons in $\mathrm{CR}FF_{\mu}^{Wh}$ used for the measurement of the FFs for the different Probe muon $|\eta|$ bins. The plots on the left (right) are obtained by requiring the probe muon to be Tight (Loose-Not-Tight or "LNT" as indicated in the plot labels), thus representing the numerator (denominator) of the FF calculation before the subtraction of prompt MC backgrounds. The last bins of the histograms include the overflow. Statistical uncertainties on the MC are shown.

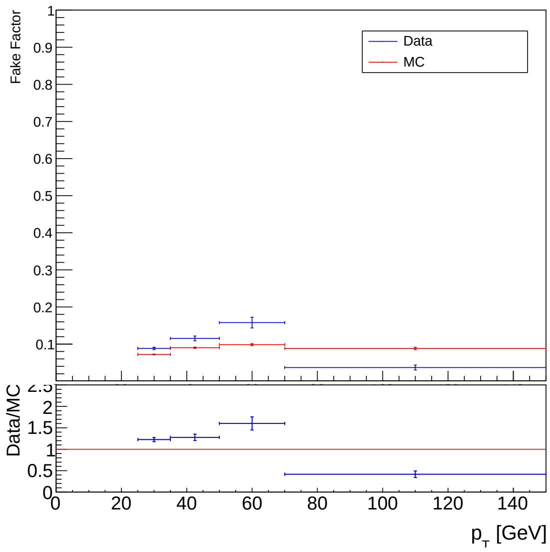

(a) Muon FFs, $|\eta(\mu_{\mathrm{probe}})| < 1.25$

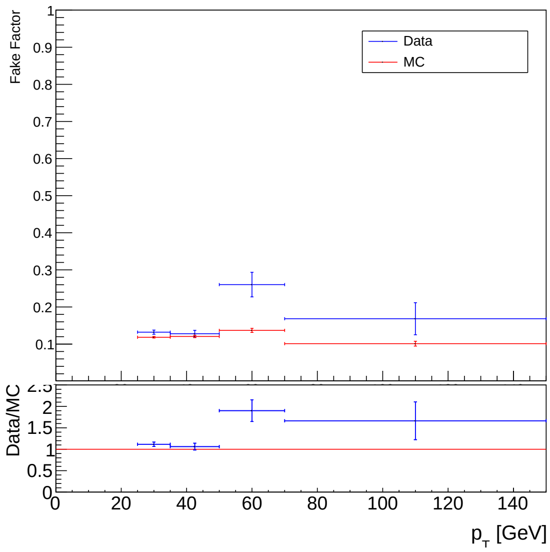

(b) Muon FFs, $1.25 \leq |\eta(\mu_{\mathrm{probe}})| < 2.5$

Figure 4.17: Measured values of the muon FFs in data and for all the adopted p_{T} and $|\eta|$ bins. Measurements from data are compared to those obtained using only MC. The last bin represents the inclusive measurement for muons with $p_{\mathrm{T}} \geq 70$ GeV . The bottom panels show the agreement between the results of the measurement from data and MC-only. Only statistical uncertainties are shown.

Similarly, in the electron case, the distributions onto which the FF measurement are based are shown in Figure 4.18. The enhanced contribution of W+jets and $t\bar{t}$ events, especially for Loose-Not-Tight Probe electrons, ultimately validates the choice of the event selection used in CRFF_e^{Wh}. The measured values of the electron FFs are shown in Figure 4.19.

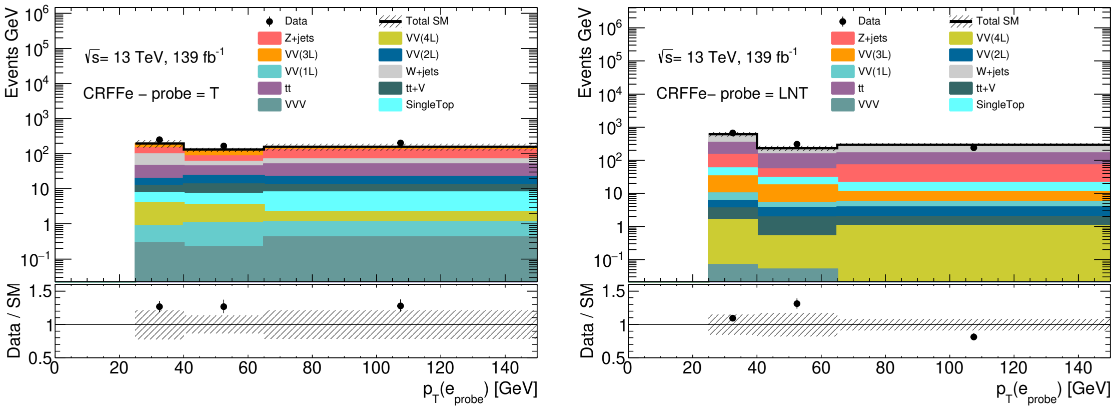

(a) CRFF_e^{Wh}, $|\eta(e_{\text{probe}})| < 2.0$

Figure 4.18: Distributions of the p_{T} of the Probe electrons in CRFF_e^{Wh} used for the measurement of the FFs. The plots on the left (right) are obtained by requiring the probe electron to be Tight (Loose-Not-Tight or "LNT" as indicated in the plot labels), thus representing the numerator (denominator) of the FF calculation before the subtraction of prompt MC and data-driven-estimated CF backgrounds. The last bins of the histograms include the overflow. Statistical uncertainties on the MC are shown.

Both Figures 4.17 and 4.19 show the comparison of the FFs measured from data with respect to those extracted using MC events only. The discrepancy between these testifies the level of mis-modelling of the FNP lepton background in MC, thus the need for a data-driven estimation of this background.

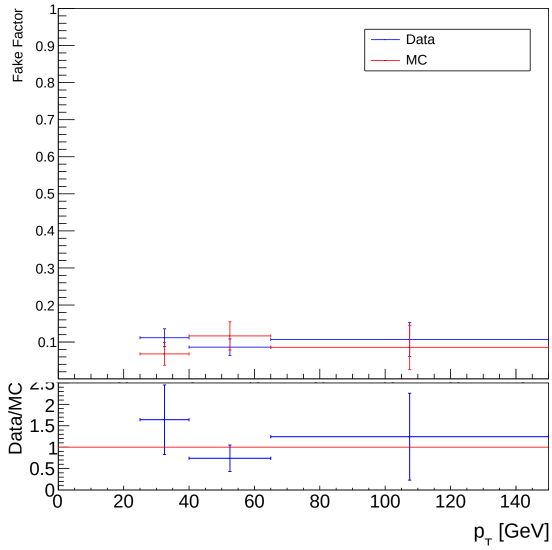

(a) Electron FFs, $|\eta(e_{\text{probe}})| < 2.0$

Figure 4.19: Measured values of the electron FFs in data and for all the adopted p_{T} bins. Measurements from data are compared to those obtained using only MC. The last bin represents the inclusive measurement for electrons with $p_{\text{T}} \geq 65$ GeV . The bottom panels show the agreement between the results of the measurement from data and MC-only. Only statistical uncertainties are shown.

Systematic uncertainties

The impact of each systematic sources for the FNP data-driven background is extracted by propagating the uncertainties of the FF measurements according to the prescription in Equation 4.24. Different sources of systematic uncertainties are taken into account for the data-driven estimation of the FNPs background:

- **FFstat**: arising from the propagated statistical uncertainty form the data and MC used in the FFs measurement, and shown in the error bars of Figures 4.17 and 4.19;
- **PromptSub**: from the subtraction of the prompt background from MC;
- **CFsub**: associated to the subtraction of the data-driven CF background;
- **CR→SRextr**: accounting for possible differences in the estimation of the FNP contribution when moving from the FF measurement CRs (CRFF_e^{Wh} and CRFF_μ^{Wh}) to a SR-like region.

The PromptSub systematic uncertainty is assigned by varying the normalization of the prompt MC backgrounds being subtracted by an amount corresponding to the theoretical uncertainty (see Section 4.4.2) on the total fiducial cross-section of the dominant prompt SM process. Figures 4.16 and 4.18 show that these processes are mainly $t\bar{t}+V$ for the muon FFs and WZ for the electron FFs. Typical values of such uncertainties are extensively documented in the available literature [137, 140]. Therefore, the envelope values taken into account are 5% for muons and 13% for electrons.

Similarly, the CFsub systematic uncertainty in the electron FF measurement is obtained by varying at the same time the estimated CF background being subtracted in the numerator and in the denominator of Equation 4.26 by the overall CF uncertainties propagated from the three different sources of data-driven CF systematics discussed in Section 4.3.3. These affect differently the numerator and the denominator of Equation 4.26 and correspond to 27% for Tight Probe electrons (numerator) and 61% for Loose-Not-Tight Probe electrons (denominator).

Finally, the CR→SRextr uncertainty is extracted by performing a closure test in CRFF_e^{Wh} and CRFF_μ^{Wh} and in the $e^\pm e^\pm$ and $\mu^\pm\mu^\pm$ flavour channels of the Wh-SS preselection. The closure test is performed by comparing the FNP events in all SM backgrounds from MC to their estimation obtained by applying the data-driven procedure to these MC backgrounds instead of data. The results of the closure test, reported in Figure 4.20, show in general a satisfactory agreement between the events with FNP leptons in MC and the same background estimated with the FF method. Any residual discrepancies, or non-closures, are taken as the systematic uncertainty. Given the nature of the closure test, these uncertainties accounts for all sources of mis-modelling of the FF procedure that can lead to a non-perfect estimation. These include the difference in the FNP lepton composition between the CRs for the FF measurements and a SR-like region, and the contamination from residual events in which the Tag lepton is not prompt.

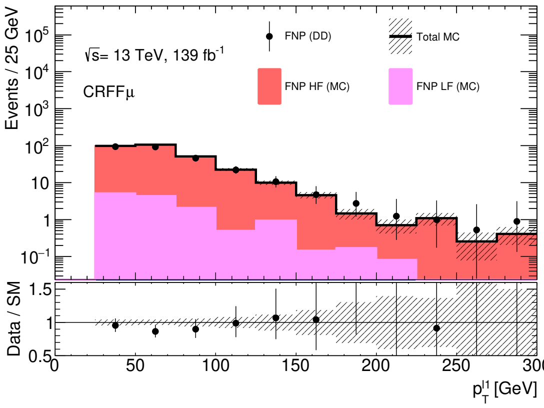

(a) CRFF_{μ}^{Wh}

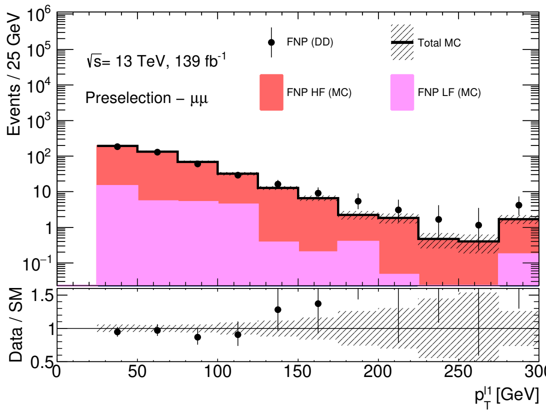

(b) Preselection - $\mu^{\pm}\mu^{\pm}$

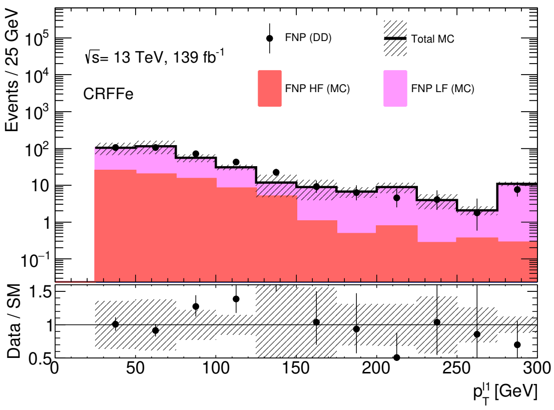

(c) CRFF_{e}^{Wh}

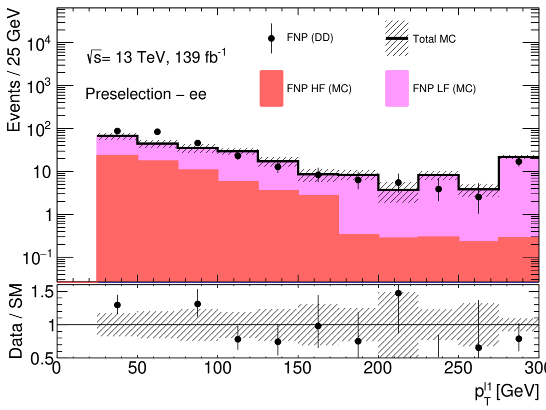

(d) Preselection - $e^{\pm}e^{\pm}$

Figure 4.20: Distributions of the leading lepton p_{T} showing the results of the closure tests between the data-driven-estimated FNP background and its MC prediction for LF and HF FNP lepton sources.

The results of the closure test show a satisfactory agreement between the predicted and estimated FNP contributions, which ultimately validates the data-driven procedure used. Moreover, the fact that similar FNP lepton composition is found between the CRs and the preselection makes the choice of the event selection of CRFF_{e}^{Wh} and CRFF_{μ}^{Wh} specifically suitable for the Wh-SS analysis. The final values of for the CR→SRextr uncertainty are taken to be 20% for electron FFs and 7% for muon FFs.

4.3.6 Fake/Non-Prompt and Charge-Flip backgrounds validation

The data-driven estimations of the CF and FNP backgrounds in the Wh-SS analysis are validated in dedicated VRs defined to be kinematically as close as possible to the SRs. Analogous cuts to those defining the SRs are considered, with the exception of the $m_{\mathrm{T}}^{\mathrm{min}} < 100$ GeV and Sig($E_{\mathrm{T}}^{\mathrm{miss}}$) < 5 requirements, which invert the selection used in the SRs thus ensuring the orthogonality. A summary of the selection criteria for the VRs of the FNP (VRFNP^{Wh}) and CF (VRCF^{Wh}) backgrounds is reported in Table 4.11.

VRFNP^{Wh} is divided into the three flavour channels: $e^{\pm}e^{\pm}$, $e^{\pm}\mu^{\pm}$ and $\mu^{\pm}\mu^{\pm}$. On the other hand, VRCF^{Wh} is simply "extracted" from VRFNP^{Wh}-ee by taking the portion whose di-electron invariant mass, m_{ee}, is compatible with the mass of the Z boson. The comparison between data and the estimated SM background in VRFNP^{Wh} and VRCF^{Wh} before the background-only fit is shown in Figure 4.21.

Table 4.11: Summary of the selection criteria for the VRs for the FNP and CF backgrounds in the Wh-SS search. Preselection criteria (Table 4.5) are applied to all regions. VRFNP^{Wh} is split into three orthogonal regions according to the flavours of the leptons: VRFNP^{Wh}-ee, VRFNP^{Wh}-$e\mu$, and VRFNP^{Wh}-$\mu\mu$.

Variable	VRFNP^{Wh}			VRCF^{Wh}
	-ee	-$e\mu$	-$\mu\mu$	
Wh-SS preselection	Applied			
m_{jj} [GeV]	< 350			
m_{T2} [GeV]	< 80			
$m_{\mathrm{T}}^{\mathrm{min}}$ [GeV]	< 100			
$E_{\mathrm{T}}^{\mathrm{miss}}$ significance	< 5			
Flavour	$e^{\pm}e^{\pm}$	$e^{\pm}\mu^{\pm}$	$\mu^{\pm}\mu^{\pm}$	$e^{\pm}e^{\pm}$
$\lvert m_{ee} - m_{Z}\rvert$ [GeV]	≥ 15	-	-	< 15

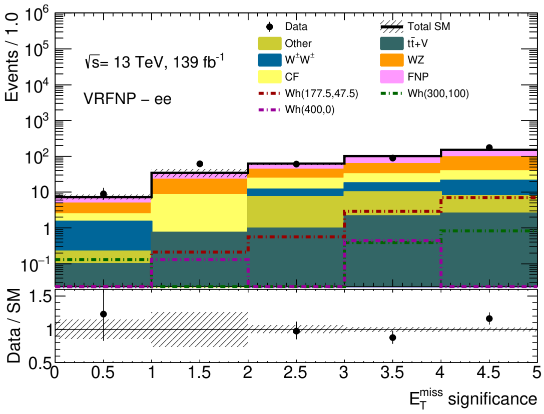

(a) VRFNP^{Wh}-ee

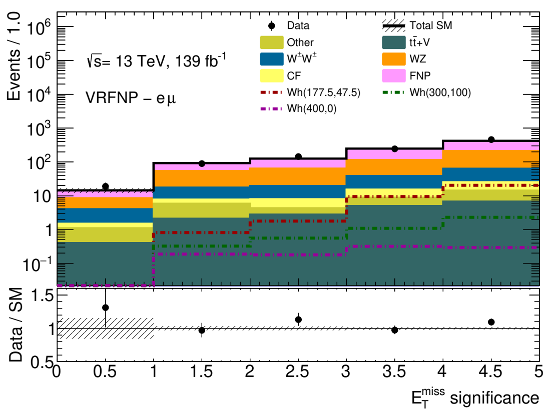

(b) VRFNP^{Wh}-$e\mu$

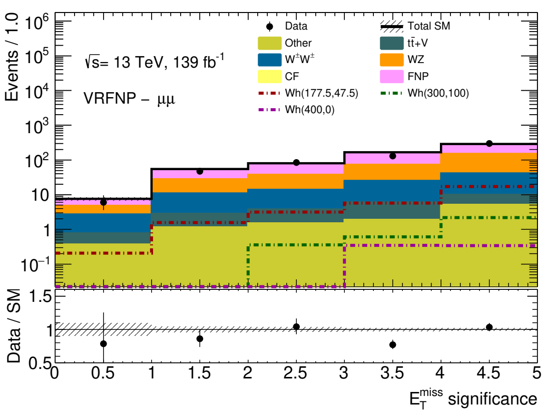

(c) VRFNP^{Wh}-$\mu\mu$

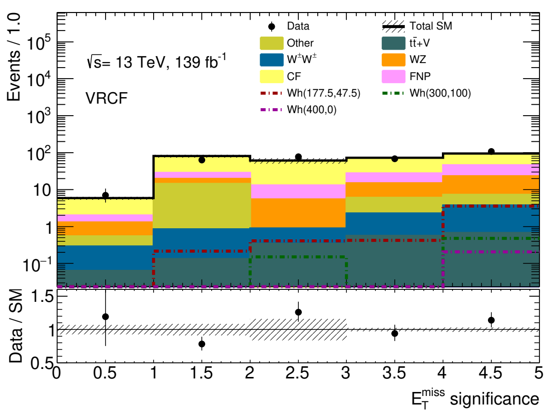

(d) VRCF^{Wh}

Figure 4.21: Distributions of $E_{\mathrm{T}}^{\mathrm{miss}}$ significance for observed data and expected SM background before the background-only fit, in the three flavour channels of VRFNP^{Wh} and in VRCF^{Wh}. MC backgrounds and data-driven-estimated contributions for CF and FNP are shown. The MC $W^{\pm}W^{\pm}$ contribution has been scaled by the corresponding k-factor (see Section 4.3.2). The lower panel shows the ratio between data and SM background. Only statistical uncertainties are shown.

Given the observed satisfactory agreement with data, it can be concluded that the entire procedure for the estimation of the data-driven backgrounds here described is to be considered validated.

4.4 Systematic uncertainties

In this Section, the different sources of systematic uncertainties affecting the Wh-SS analysis are described. Apart from the systematic uncertainties affecting the data-driven CF and FNP backgrounds, outlined in Sections 4.3.3 and 4.3.5, and the statistical uncertainties of the MC simulations, the remaining uncertainty sources that have been considered in this analysis can be grouped into two categories. To the first category, referred to as *experimental systematics* (Section 4.4.1), belong all uncertainty sources related to the detection of particles and associated with the reconstruction, energy calibration and the resolution of physics objects. The second category, called *theoretical systematics* (Section 4.4.2), groups all uncertainty sources directly associated with the generation of MC simulations of the different processes and, consequently, related to the accuracy with which the theoretical modelling of such processes is understood.

4.4.1 Experimental systematics

The various sources of detector-related systematics that have been considered for this analysis are associated with:

Luminosity The relative uncertainty on the integrated luminosity of the combined Run 2 dataset, corresponding to 139 fb^{-1}, after applying the necessary data-quality selections, has been measured to be $\pm 1.7\%$ [73]. This uncertainty is considered for all MC samples.

Pile-up Simulated samples are generated with the pile-up profile corresponding to the data campaign they refer to (Figure 2.3). This is applied in MC samples by means of an event-by-event *pile-up re-weighting* procedure. The systematic uncertainty on the pile-up is obtained varying the original distribution of the average number of interaction per bunch crossing, $\langle\mu\rangle$, corresponding to specifically varied event-by-event pile-up weights for MC.

Trigger efficiency The difference of the measured trigger efficiency between data and MC is accounted for with the application of appropriate SF, which are varied by the corresponding measured uncertainties to assess the impact of this systematic source.

Electrons The uncertainties related to electrons come from the electron energy scale, resolution, reconstruction, identification, isolation and charge identification. Specifically, electron energy scale and resolution uncertainties are measured as a function of the electron E_{T} and η

from $Z \to ee$ in data [121], whereas the reconstruction, identification and isolation systematic sources arise from the measured uncertainties on the corresponding efficiencies, i. e. represented by the error bars in Figures 3.4 and 3.5.

Muons Similarly to the electrons, muon energy scale, resolution, reconstruction, identification and isolation uncertainties are considered. Additionally, uncertainties on combined muon tracks reflected in sagitta distortions caused by small detector mis-alignment [149], and to the track-to-vertex association [125] are also taken into account.

Jets Jet Energy Scale (JES) uncertainties originate from the calibration process consisting of a combination of MC-based methods and in-situ measurements [150]. On the other hand, Jet Energy Resolution (JER) arise from the smearing procedure applied to MC events in order to match the energy resolution measured in data [151]. Systematic uncertainties which account for the residual contamination from pile-up jets after the pile-up suppression from the usage of the JVT algrithm [129] are also considered.

Flavour-tagging Uncertainties to the flavour-tagging procedure illustrated in Section 3.3.2 are also considered. These arise from the difference in the relative fraction of jets originating from b, c and light quarks between data and MC simulations [131].

Missing transverse momentum Given the method to reconstruct the $E_{\mathrm{T}}^{\mathrm{miss}}$ summarised in Equation 3.2, the energy scale and resolution effects of all the objects mentioned above, all affect its measurement. Additionally, systematics specific to the tracks making up the soft-term of the $E_{\mathrm{T}}^{\mathrm{miss}}$ have been taken into account [135].

4.4.2 Theoretical systematics

Theoretical systematics have been estimated for the main irreducible backgrounds, WZ and $W^{\pm}W^{\pm}$, following the recommendations of the ATLAS Collaboration. The different sources of theoretical uncertainties considered for each background are described as follows:

QCD scales The uncertainties associated with the different choices of renormalisation scale, μ_{R}, and factorisation scale, μ_{F}, described in Section 1.1.2, are estimated from the MC simulations used in the analysis by changing the generator weights corresponding to the cross-section calculation of each process. These variations of the generator weights have been obtained by scaling each of the nominal μ_{R} and μ_{F} parameters by a multiplicative factor of 1/2 and 2. Additionally, another uncertainty obtained with the coherent variation of both μ_{R} and μ_{F} simultaneously, indicated as "$\mu_{\mathrm{R}} + \mu_{\mathrm{F}}$", has been considered. The impact of each of these scale uncertainties with respect to the nominal yield in each CR, VR and SR of the Wh-SS analysis are reported in the form of up and down relative variations.

PDF and α_S The systematics associated with the uncertainty on the PDF, has been estimated, in an analogous fashion as the QCD scale uncertainties, by taking into account a set of varied generator weights each corresponding to the different choices of the PDF set. The final envelope for each region is takes by considering the standard deviation of each of relative deviation from the nominal yield. Similarly, the two variations of the generator weights arising from the up and down scaling of the strong coupling constant, α_S, by amounts equal to its uncertainty have been used to assess its impact in the acceptance of every region. Symmetrised envelopes have been taken as the final uncertainty value. PDF and α_S variations have been considered as a single uncertainty by taking into account the squared sum of the two.

Merging scale, re-summation scale and PS recoil scheme The systematics corresponding to uncertainties on choice of the CKKW merging scale, the re-summation scale (QSF) – i. e. upper cut-off of the perturbative calculations for the PS evolution – and the impact of using different recoil schemes for single particle emission in the PS (CSSKIN) have all been evaluated at truth-level using specifically-produced alternative MC samples. Specifically, the the CKKW systematic is estimated from the impact of changing the nominal CKKW merging scale of 20 GeV to the alternative values of 15 GeV and 30 GeV and the nominal QSF value of 2 GeV is varied of a factor 1/4 and 4. For MC $t\bar{t}$ simulations, inclusive PS-related uncertainties are estimated by comparing the yields in every region obtained with the nominal `POWHEG+PYTHYA8` generator to `POWHEG+HERWIG7`.

Radiation ISR and FSR uncertainties are extracted by adjusting the parameters corresponding to the different PS tuning variations available in the `PYTHYA8` generator an by comparing with the nominal yield in each region.

Matrix-element The impact of choosing a different matrix-element (ME) generator, `aMC@NLO`, compared to the nominal choice, `POWHEG`, for MC $t\bar{t}$ has also been taken into account.

The evaluation of the impact of the different theoretical sources of uncertainties involves comparing nominal MC yields in each region with the corresponding yield obtained after applying a dedicated systematic variation. However, this makes the process sensitive to the statistical fluctuations of the different processes. This holds especially true for regions in which such contributions are small or negligible. In order to ultimately reduce the probability of double-counting the statistical uncertainties, which are considered separately in the Wh-SS analysis, when necessary theoretical systematics have been estimated in inclusive regions (e. g. by merging SRs together), thus reducing the impact of statistical fluctuations in their estimation. The estimated envelopes relative to the theoretical uncertainties of the WZ and $W^{\pm}W^{\pm}$ backgrounds for all the regions of the Wh-SS analysis have been reported in Tables 4.12-4.13 and Tables 4.14-4.15, respectively.

Table 4.12: Breakdown of theoretical uncertainties concerning the QCD scales, PDF and α_S estimated for the WZ background in the SRs, CRs and VRs of the Wh-SS analysis.

Region	μ_R [%]	μ_F [%]	$\mu_R + \mu_F$ [%]	PDF [%]	α_S [%]	PDF+α_S [%]
$SR^{Wh}_{high\text{-}m_{T2}}$-1-$ee/e\mu/\mu\mu$	+1.49/-1.43	+0.41/-0.40	+1.23/-0.94	±0.26	±0.22	±0.34
$SR^{Wh}_{high\text{-}m_{T2}}$-2-$ee/e\mu/\mu\mu$	+3.26/-2.91	+1.26/-1.43	+1.94/-1.60	±0.47	±0.22	±0.52
$SR^{Wh}_{high\text{-}m_{T2}}$-3-$ee/e\mu/\mu\mu$	+3.56/-4.10	+1.65/-2.69	+1.04/-2.00	±1.24	±0.27	±1.26
$SR^{Wh}_{low\text{-}m_{T2}}$-$ee/e\mu/\mu\mu$	+2.61/-2.47	+0.77/-0.93	+1.84/-1.55	±0.21	±0.27	±0.35
$CRWZ^{Wh}$	+6.06/-5.54	+1.64/-1.94	+4.45/-3.67	±0.39	±1.43	±1.48
$CRWW^{Wh}$	+18.15/-14.39	+3.32/-3.64	+14.23/-11.34	±1.20	±1.43	±1.87
$VRWZ^{Wh}$	+4.92/-4.58	+1.52/-1.77	+3.40/-2.89	±0.38	±0.43	±0.57
$VRWW^{Wh}$	+16.90/-13.46	+3.35/-3.70	+12.87/-10.46	±1.24	±0.43	±1.32
$VRFNP^{Wh}$-$ee/e\mu/\mu\mu$	+5.01/-4.50	+1.33/-1.59	+3.66/-3.01	±0.26	±0.24	±0.36
$VRCF^{Wh}$	+3.30/-3.13	+0.70/-0.85	+2.76/-2.26	±0.40	±0.24	±0.47

Table 4.13: Breakdown of theoretical uncertainties concerning the merging scale (CKKW), re-summation scale (QSF) and PS recoil scheme (CSSKIN) estimated at truth-level for the WZ background in the SRs, CRs and VRs of the Wh-SS analysis.

Region	QSF [%]	CKKW [%]	CSSKIN [%]
$SR^{Wh}_{high\text{-}m_{T2}}$-1/2/3-$ee/e\mu/\mu\mu$	+15.51/-2.06	-18.67	-16.92
$SR^{Wh}_{low\text{-}m_{T2}}$-$ee/e\mu/\mu\mu$	-11.71	-11.25	+19.64
$CRWZ^{Wh}$	+1.83/-2.45	+4.90	-4.07
$CRWW^{Wh}$	+1.89/-3.09	-7.02	-1.54
$VRWZ^{Wh}$	+10.34/-4.72	+2.94/-3.35	+2.54
$VRWW^{Wh}$	+3.35/-3.36	+3.95/-14.94	-3.32
$VRFNP^{Wh}$-$ee/e\mu/\mu\mu$	+1.87/-1.77	+1.33/-2.54	+0.47
$VRCF^{Wh}$	+37.31/-11.86	+1.05/-13.95	-4.18

Table 4.14: Breakdown of theoretical uncertainties concerning the QCD scales, PDF and α_S estimated for the $W^{\pm}W^{\pm}$ background in the SRs, CRs and VRs of the Wh-SS analysis.

Region	μ_R [%]	μ_F [%]	$\mu_R + \mu_F$ [%]	PDF [%]	α_S [%]	PDF+α_S [%]
$SR^{Wh}_{high\text{-}m_{T2}}$-1-$ee/e\mu/\mu\mu$	+8.02/-8.35	+0.06/-0.03	+8.07/-8.40	±0.29	±0.74	±0.79
$SR^{Wh}_{high\text{-}m_{T2}}$-2-$ee/e\mu/\mu\mu$	+8.35/-8.53	+0.53/-0.41	+7.88/-8.09	±0.45	±0.74	±0.87
$SR^{Wh}_{high\text{-}m_{T2}}$-3-$ee/e\mu/\mu\mu$	+6.36/-6.79	+1.53/-1.34	+4.93/-5.38	±0.56	±0.81	±0.98
$SR^{Wh}_{low\text{-}m_{T2}}$-$ee/e\mu/\mu\mu$	+7.98/-8.20	+0.33/-0.25	+7.72/-7.89	±0.45	±0.81	±0.92
$CRWZ^{Wh}$	+8.46/-8.43	+0.66/-0.65	+9.25/-8.96	±2.55	±0.68	±2.64
$CRWW^{Wh}$	+7.17/-7.22	+0.46/-0.40	+6.73/-6.81	±0.49	±0.68	±0.83
$VRWZ^{Wh}$	+4.32/-4.28	+0.79/-0.87	+5.03/-5.23	±3.03	±0.78	±3.13
$VRWW^{Wh}$	+7.10/-7.16	+0.46/-0.41	+6.65/-6.75	±0.17	±0.78	±0.80
$VRFNP^{Wh}$-$ee/e\mu/\mu\mu$	+8.04/-8.35	+0.79/-0.64	+7.33/-7.64	±0.33	±0.75	±0.82
$VRCF^{Wh}$	+8.83/-9.30	+0.85/-0.66	+8.10/-8.55	±0.36	±0.75	±0.83

Table 4.15: Breakdown of theoretical uncertainties concerning the merging scale (CKKW), re-summation scale (QSF) and PS recoil scheme (CSSKIN) estimated at truth-level for the $W^{\pm}W^{\pm}$ background in the SRs, CRs and VRs of the Wh-SS analysis.

Region	QSF [%]	CKKW [%]	CSSKIN [%]
$\mathrm{SR}^{Wh}_{\text{high-}m_{\mathrm{T2}}}$-1/2/3-$ee/e\mu/\mu\mu$	+5.07/-4.32	+3.07/-1.06	+5.17
$\mathrm{SR}^{Wh}_{\text{low-}m_{\mathrm{T2}}}$-$ee/e\mu/\mu\mu$	+4.45/-3.29	+2.33/-4.33	+2.11
$\mathrm{CR}WZ^{Wh}$	-	-	-
$\mathrm{CR}WW^{Wh}$	+8.23/-2.86	+1.25/-0.69	-1.33
$\mathrm{VR}WZ^{Wh}$	-	-	-
$\mathrm{VR}WW^{Wh}$	+6.56/-3.16	+1.37/-2.23	+0.68
$\mathrm{VR}FNP^{Wh}$-$ee/e\mu/\mu\mu$	+4.49/-3.47	+1.31/-2.40	-1.08
$\mathrm{VR}CF^{Wh}$	+6.68/-0.61	+4.66	+2.16

For what concerns the $t\bar{t}+V$ background, given its large statistical fluctuations in the SRs which could not be decoupled from the systematic uncertainties by simply considering inclusive bins, flat envelopes have been taken into account and applied to all regions. These uncertainties, relative to QCD scales, PDF and α_{S}, are available in literature [152] and have been estimated considering inclusive phase-spaces. Their values are shown in Table 4.16. As opposed to the WZ and $W^{\pm}W^{\pm}$ case, in which systematics have been evaluated, the used values of the uncertainties for PDF and α_{S} taken from literature are considered separately.

Table 4.16: Breakdown of the theoretical uncertainties for the $t\bar{t}+V$ process including QCD scale or $\mu_{R,F}$, PDF, α_{S}. These flat uncertainties are applied to every region of the Wh-SS analysis.

Process	$\mu_{R,F}$ [%]	PDF [%]	α_{S} [%]
$t\bar{t}+V$	+12.9/-11.5	±2.8	±2.8

For all other less dominant SM backgrounds with prompt leptons and estimated from MC, which most notably include VVV and $ZZ \to 4\ell$ events, an analogous strategy have been employed: a conservative flat ±20% envelope, encompassing the largest total uncertainty on the inclusive cross-section measurements for these processes (also available in [152]), has been considered.

Finally, theoretical systematics relative to the modelling of the MC simulations of the Wh-SS signals have also been estimated. Three different sources of uncertainties have been considered, concerning QCD scale, merging scale and radiation. These have been estimated at truth-level separately for each point of the Wh-SS signal grid (Figure 4.2). Since no significant change in the estimated values of the signal theory systematics have been observed moving from one mass point to another within their respective statistical fluctuation, single values have been obtained by averaging the these values across the signal grid (Table 4.17). This allowed to suppress the impact of the statistical uncertainties themselves.

Table 4.17: Breakdown of theoretical uncertainties concerning the merging scale QCD scale ($\mu_{R,F}$), merging scale and radiation estimated at truth-level for the Wh-SS signal processes in the SRs of the Wh-SS analysis.

Region	$\mu_{R,F}$ [%]	Merging Scale [%]	Radiation [%]
$\mathrm{SR}^{Wh}_{\text{high-}m_{\mathrm{T2}}}$-1/2/3-$ee/e\mu/\mu\mu$	+11.05/-13.86	+11.68/-14.75	+20.18/-14.77
$\mathrm{SR}^{Wh}_{\text{low-}m_{\mathrm{T2}}}$-$ee/e\mu/\mu\mu$	+16.53/-22.42	+13.96/-21.68	+23.05/-28.56

4.5 Results of the Wh-SS search

4.5.1 Statistical analysis

This section outlines the technical procedure used to achieve a statistical interpretation of the results of a search for BSM physics phenomena. The tools here described are relevant not only for the Wh-SS analysis, but also for the other analyses included in this thesis (Chapters 5 and 6).

In a particle physics search the view is usually to evaluate the statistical significance that the observed data either are compatible with a previously established physics scenario, i. e. the SM, or indicate the presence of processes that have been predicted but not yet observed, i. e. BSM phenomena such as SUSY. This is usually assessed in a procedure called *hypothesis testing*, in which the compatibility of the observed data in the *background-only hypothesis* (B) is tested against the *signal+background hypothesis* ($S+B$) [148]. In the specific case of high-energy particle physics experiments this is achieved by performing a fit simultaneously in all CRs and SRs. The functional form which data, background and signal yields are fitted against is the *Likelihood* [153, 154], which in the context of ATLAS SUSY analyses is defined as:

$$
\begin{aligned}
L\left(\mu_{\mathrm{S}},\vec{\theta}\right) = \prod_{i\in\mathrm{SR}} P_i\left(n_i^{\mathrm{Obs}}\middle|\, b_i(\vec{\mu}_{\mathrm{B}},\vec{\theta}) + \mu_{\mathrm{S}}\cdot s_i(\vec{\theta})\right) \times \\
\prod_{j\in\mathrm{CR}} P_j\left(n_j^{\mathrm{Obs}}\middle|\, b_j(\vec{\mu}_{\mathrm{B}},\vec{\theta}) + \mu_{\mathrm{S}}\cdot s_j(\vec{\theta})\right) \times \prod_{k\in\mathrm{NP}} G_k\left(\theta_k^0-\theta_k\right)
\end{aligned}
\tag{4.30}
$$

where the first two terms represent the Poisson distributions of observing $n_{i(j)}^{\mathrm{Obs}}$ in each SR and CR, respectively, given the corresponding expectations of the signal+background yields, $b_{i(j)}+\mu_{\mathrm{S}}\cdot s_{i(j)}$. The parameter μ_{S} is called *signal strength*. It scales the signal yields in the SRs to match the corresponding observations and is, thus, a free-floating parameter set in the fit. Other free, unconstrained parameters are $\vec{\mu}_{\mathrm{B}}$, which represent the NFs for the backgrounds that are being normalised in their specific CRs. The impact of each of the different sources of systematic uncertainties (Section 5.4) is assessed by means of the corresponding *Nuisance Parameter* (NP), θ_k. Each NP changes the yields of both the background and the signal expectation values and it is constrained in the fit with Gaussian functions, shown in the third term of Equation 4.30. In these Gaussian terms, the parameters θ_k^0 are their central values which are taken from the systematic uncertainty envelopes that are given as inputs to the fit along with $n_{i(j)}^{\mathrm{Obs}}$. For backgrounds that are normalised in dedicated CRs, the impact of the NPs of their systematic uncertainties in the SRs can be further constrained by extrapolating their effect to the transfer factors from the CRs to the SRs (calculated as $N_{\mathrm{SR}}/N_{\mathrm{CR}}$, where N_{SR} and N_{CR} are the yields in the SRs to the CRs, respectively), and taking that variation as the NP, instead.

From the Neyman-Pearson lemma, the most powerful discriminant to probe the $S+B$ hypothesis against the B hypothesis, namely the so-called *test statistic*, is given by the *likelihood ratio* between the two hypotheses [148]. A common choice in hypothesis testing is as follows:

$$q_{\mu_{\mathrm{S}}} = -2\ln\left(\frac{L(\mu_{\mathrm{S}}, \hat{\hat{\theta}})}{L(\hat{\mu}_{\mathrm{S}}, \hat{\theta})}\right) \tag{4.31}$$

where $\hat{\mu}_{\mathrm{S}}$ and $\hat{\theta}$ globally maximise the likelihood function (Equation 4.30), and $\hat{\hat{\theta}}$ maximises the likelihood as a function of every fixed value of μ_{S}. In order to compute the statistical significance of the compatibility of the observations with the background-only hypothesis, obtained by setting $\mu_{\mathrm{S}} = 0$, and the $S+B$ hypothesis, for $\mu_{\mathrm{S}} = 1$, it is necessary to consider the *probability density function* (pdf), $f(q_{\mu_{\mathrm{S}}}\,|\,\mu_{\mathrm{S}}, \hat{\hat{\theta}})$, of the test statistic of Equation 4.31. This is, in general, sampled with pseudo-experiments, or "toys", which mostly rely on MC techniques [148]. However, in the limit of sufficiently high statistics the pdf can be accurately approximated using analytic, asymptotic formulae [153]. This approach is the one that has been used in the Wh-SS analysis. The compatibility with each hypothesis can then be measured considering the value of the test statistic corresponding to the observation, $q_{\mu_{\mathrm{S}}}^{\mathrm{Obs}}$, and the following p-values:

$$\begin{aligned} p_{S+B} &= \int_{q^{\mathrm{Obs}}_{\mu_{\mathrm{S}}=1}}^{+\infty} f(q_{\mu_{\mathrm{S}}}\,|\,\mu_{\mathrm{S}}=1, \hat{\hat{\theta}})\,\mathrm{d}q_{\mu_{\mathrm{S}}} = CL_{S+B} \\ p_B &= \int_{-\infty}^{q^{\mathrm{Obs}}_{\mu_{\mathrm{S}}=0}} f(q_{\mu_{\mathrm{S}}}\,|\,\mu_{\mathrm{S}}=0, \hat{\hat{\theta}})\,\mathrm{d}q_{\mu_{\mathrm{S}}} = 1 - CL_B \end{aligned} \tag{4.32}$$

which have been graphically represented in Figure 4.22.

As it can also be seen in Figure 4.22, the quantities CL_{S+B} and $(1-CL_B)$ measure the degree of incompatibility of the observations with the signal+background and background-only hypotheses, respectively.

Confidence intervals, commonly parametrised by the quantity called Confidence Level (CL), can be defined by convention to accept or reject the hypothesis in question. In particular, 95% CL intervals around the median[2] define the $\pm 1\sigma$ band. Conventionally, in high-energy physics experiments, observations with a p_B corresponding to upward deviations of 3σ from the background expectation are commonly associated with the observation of an *excess*, whereas 5σ deviations are acknowledged as the *discovery* of a new signal. On the other hand, in case the observations are found to be compatible with the background prediction, the signal+background hypothesis can be rejected by means of the CL_S *prescription* [155], which is based on the quantity:

$$CL_S = \frac{CL_{S+B}}{CL_B} \tag{4.33}$$

A signal model is said to be excluded at 95% CL if $CL_S < 0.05 = 1 - 0.95$. CL_S values can be estimated by taking in Equation 4.30 the data in the SRs as the observation. These correspond

[2] The median is defined as the quantile of a pdf corresponding to 50% of the probability.

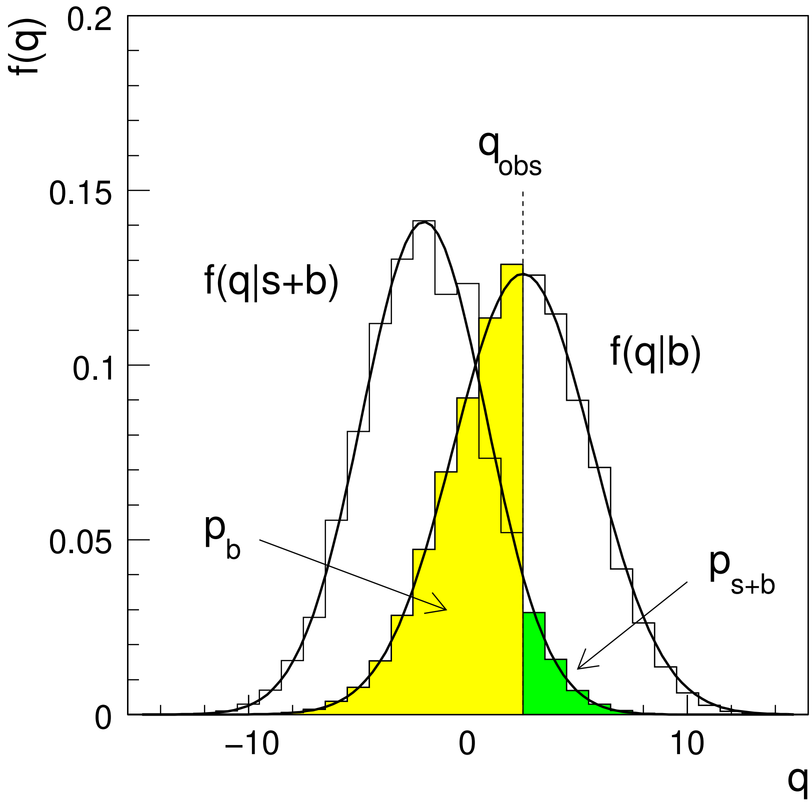

Figure 4.22: Graphical representations of p_{S+B} and p_B as well as the pdfs of the $S+B$ and B hypotheses, taken from [153].

to the so-called *observed* CL_S values. On the other hand, *expected* CL_S values are obtained by taking e. g. $b+s$ in the SRs as the observation. Finally, 95% CL *upper limits* on the signal cross-sections can also be computed by repeating the fit for different values of the signal strength, μ_S, and by finding the largest one admissible that is still compatible with the background-only hypothesis [153].

For SUSY searches in the ATLAS experiment, all the fit functionalities described in this Section are implemented in the `HistFitter` framework [154], which has also been employed in the Wh-SS search. Three different types of fit are possible in the `HistFitter` framework and have been considered for the statistical interpretation of the results of the Wh-SS analysis:

- **Background-only fit**, which is performed considering the absence of any BSM signal in the SRs, therefore testing the compatibility with the background-only hypothesis;

- **Model-independent or discovery fit**, in which a dummy signal for a generic BSM process (usually $s=1$) in the SRs is considered along with a scan for the 95% CL upper limit on μ_S, which can equivalently be expressed as a limit on the visible cross-section for such process;

- **Model-dependent or exclusion fit**, which takes into account the SUSY signals in question and, if the observations are compatible with the SM background prediction, determines whether such signal is excluded at 95% CL.

The stability of each of these types of fits are assessed by evaluating the so-called *pulls* of every constrained NP which are defined as:

$$\mathcal{P}(\theta) = \frac{\theta - \hat{\theta}}{\Delta\theta} \tag{4.34}$$

where θ is the observed value of the NP, $\hat{\theta}$ is the value which maximises the Likelihood (Equation 4.31), and $\Delta\theta$ is the value of the uncertainty of the NP as assigned in the fit. If $\Delta\theta$ is smaller than the uncertainty used as an input in the fit, that uncertainty is said to be "over-constrained", otherwise it is "under-constrained". Moreover, in cases in which the value of $\mathcal{P}(\theta)$ is approximately zero, the fit is said not to introduce a pull. On the other hand, large observed pulls usually can cause the fit not to converge to the global extremum of the Likelihood function, thus making the fit itself unstable. Pulls are typically reported with respect to the number of standard deviations, σ, they are found to be away from the input uncertainty on each NP, so that e. g. $\sigma \geq 1$ indicates an under-constrained uncertainty.

Large pulls and/or under-constrained NPs can be a consequence of possible discrepancies between data and the SM background in a CR/SR. In this case, a shift in the relevant NPs compared to the original value of the considered uncertainty must be introduced in order to stabilise the fit. Pulls not larger than 2-3σ are not considered significant. The absence of significant pulls represents a satisfactory agreement between data observations and the model being tested, thus validating quality of the fit.

4.5.2 Background-only fit results of the Wh-SS analysis

In the Wh-SS analysis a background-only fit is performed by fitting the overall SM background simultaneously all CRs, thus extracting the final estimate of the SM backgrounds. In this context, all NPs, corresponding to the experimental, theoretical and data-driven systematics outlined in the previous Sections, are considered correlated across the different regions of the Wh-SS search. This allows to constrain the variability of such systematics. Additional constraints arise from the normalisation of the WZ and $W^{\pm}W^{\pm}$ in the respective CRs. The extracted NFs in these CRs have been measured to be $\mu_{WZ} = 1.06^{+0.14}_{-0.08}$ and $\mu_{W^{\pm}W^{\pm}} = 1.00^{+0.25}_{-0.28}$. Given the satisfactory agreement with data before the fit in observed in the CRs (Figures 4.11a and 4.13a), the NFs are compatible with one within their respective uncertainties.

Figure 4.23 shows the comparison between data and the estimated yields of the SM backgrounds after the background-only fit in the CRs and VRs of the Wh-SS analysis. Data are been found compatible with the final background prediction in the VR (within 1σ), which ultimately demonstrate the validity of the overall background estimation procedure.

The comparison between the observed data and the final estimate of the SM backgrounds have been reported in Table 4.18 and shown in Figure 4.24.

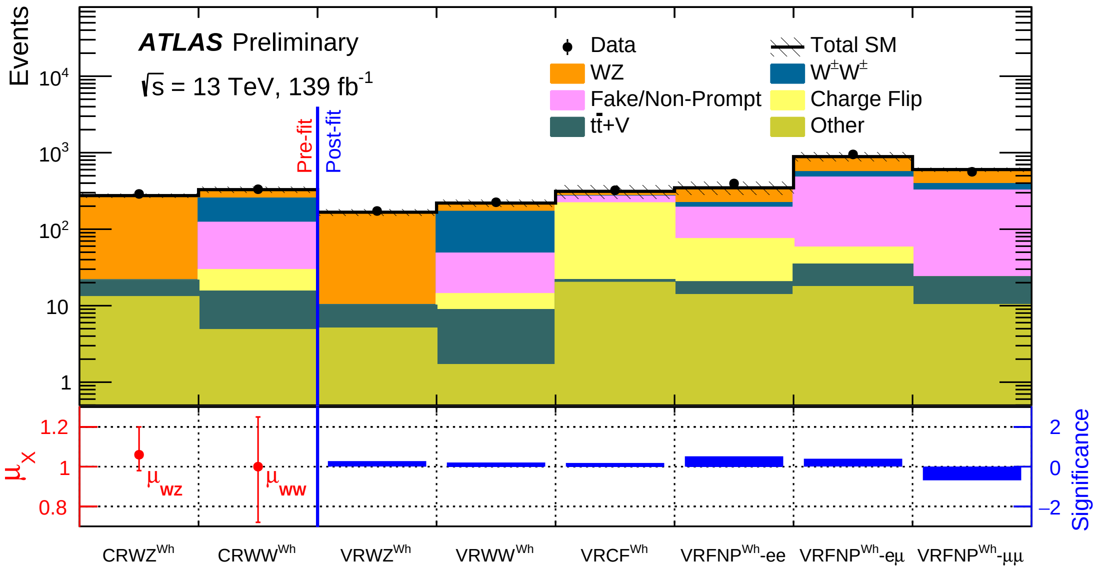

Figure 4.23: Data and SM background predictions in all the CRs and VRs of the Wh-SS analysis. Data and SM background yields in the CRs (VRs) are taken before (after) the background-only fit. The lower panel shows the measured values of the NPs of the WZ and $W^{\pm}W^{\pm}$ processes (μ_{WZ} and $\mu_{W^{\pm}W^{\pm}}$) in the CRs, and the comparison between data and SM prediction in the VRs expressed as the significance (number of σ from the background expectation), after the background-only fit. Statistical and systematic uncertainties are shown. [136]

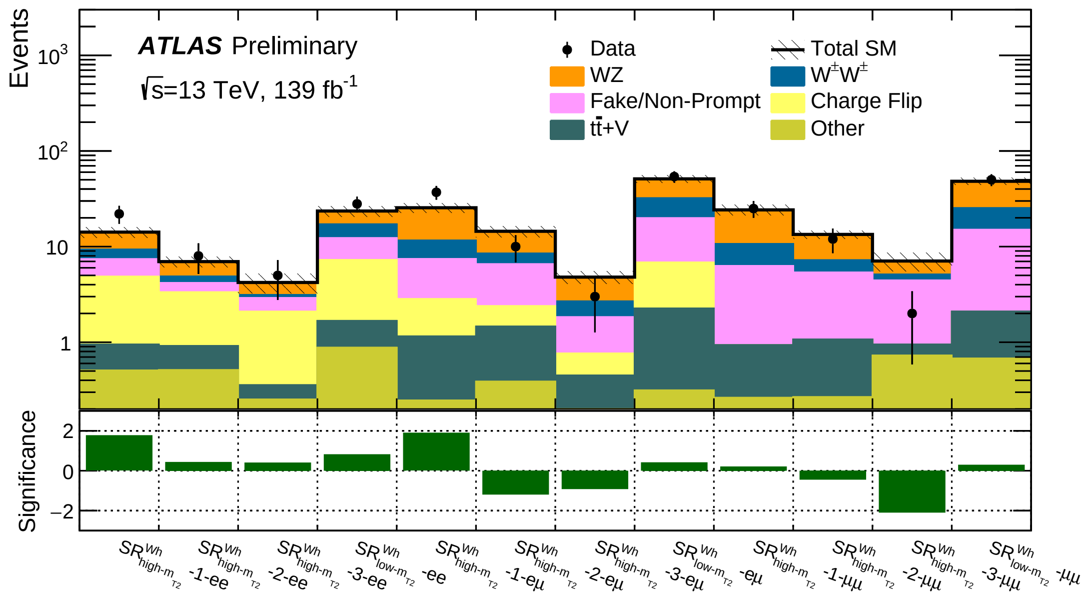

Figure 4.24: Data and SM background predictions in all the SRs of the Wh-SS analysis. In the lower panel, the comparison between data and SM prediction is expressed as the significance (number of σ from the background expectation), after the background-only fit. Statistical and systematic uncertainties are shown. [136]

Table 4.18: Observed sata and SM background yields in all the SRs of the Wh-SS analysis. Statistical and systematic uncertainties are shown.

Regions	$\mathrm{SR}^{Wh}_{\text{high-}m_{\mathrm{T2}}}$-1-$ee$	$\mathrm{SR}^{Wh}_{\text{high-}m_{\mathrm{T2}}}$-2-$ee$	$\mathrm{SR}^{Wh}_{\text{high-}m_{\mathrm{T2}}}$-3-$ee$	$\mathrm{SR}^{Wh}_{\text{low-}m_{\mathrm{T2}}}$-$ee$
Data	22	8	5	28
Total SM	14.17 ± 1.82	6.97 ± 0.87	4.22 ± 0.97	23.56 ± 3.01
WZ	4.85 ± 0.87	2.08 ± 0.40	1.08 ± 0.23	6.42 ± 0.99
$W^{\pm}W^{\pm}$	1.92 ± 0.55	0.71 ± 0.23	0.23 ± 0.11	4.86 ± 1.37
CF	3.91 ± 1.06	2.42 ± 0.64	1.73 ± 0.48	5.58 ± 1.52
FNP	2.54 ± 1.47	0.84 ± 0.43	$0.81^{+0.84}_{-0.81}$	5.02 ± 3.18
$t\bar{t}+V$	0.44 ± 0.09	0.40 ± 0.09	0.10 ± 0.04	0.80 ± 0.13
Other	0.51 ± 0.16	0.51 ± 0.12	0.25 ± 0.07	0.88 ± 0.34
Regions	$\mathrm{SR}^{Wh}_{\text{high-}m_{\mathrm{T2}}}$-1-$e\mu$	$\mathrm{SR}^{Wh}_{\text{high-}m_{\mathrm{T2}}}$-2-$e\mu$	$\mathrm{SR}^{Wh}_{\text{high-}m_{\mathrm{T2}}}$-3-$e\mu$	$\mathrm{SR}^{Wh}_{\text{low-}m_{\mathrm{T2}}}$-$e\mu$
Data	37	10	3	54
Total SM	25.49 ± 2.84	14.46 ± 1.95	4.80 ± 0.73	51.09 ± 4.32
WZ	13.90 ± 2.45	5.98 ± 1.03	2.11 ± 0.42	18.99 ± 2.81
$W^{\pm}W^{\pm}$	4.17 ± 1.34	1.92 ± 0.55	0.85 ± 0.28	12.25 ± 3.32
CF	1.67 ± 0.46	0.93 ± 0.25	0.31 ± 0.08	4.57 ± 1.23
FNP	4.60 ± 1.57	4.17 ± 1.95	1.07 ± 0.68	13.02 ± 4.67
$t\bar{t}+V$	0.91 ± 0.17	1.07 ± 0.17	0.34 ± 0.07	1.95 ± 0.29
Other	0.25 ± 0.10	0.39 ± 0.08	0.11 ± 0.03	0.31 ± 0.09
Regions	$\mathrm{SR}^{Wh}_{\text{high-}m_{\mathrm{T2}}}$-1-$\mu\mu$	$\mathrm{SR}^{Wh}_{\text{high-}m_{\mathrm{T2}}}$-2-$\mu\mu$	$\mathrm{SR}^{Wh}_{\text{high-}m_{\mathrm{T2}}}$-3-$\mu\mu$	$\mathrm{SR}^{Wh}_{\text{low-}m_{\mathrm{T2}}}$-$\mu\mu$
Data	25	12	2	50
Total SM	24.21 ± 3.03	13.41 ± 1.27	7.07 ± 1.56	48.20 ± 4.01
WZ	13.51 ± 2.61	6.19 ± 1.09	1.95 ± 0.43	22.93 ± 3.40
$W^{\pm}W^{\pm}$	4.40 ± 1.36	1.84 ± 0.53	0.67 ± 0.22	10.25 ± 2.77
CF	0.00 ± 0.00	0.00 ± 0.00	0.00 ± 0.00	0.00 ± 0.00
FNP	5.36 ± 0.56	4.30 ± 0.60	3.50 ± 0.80	12.93 ± 1.49
$t\bar{t}+V$	0.67 ± 0.14	0.81 ± 0.14	0.22 ± 0.05	1.42 ± 0.22
Other	0.26 ± 0.14	0.27 ± 0.08	$0.73^{+1.23}_{-0.73}$	0.68 ± 0.16

No significant deviation from the SM expectation is found. Mild excesses are observed in $\mathrm{SR}^{Wh}_{\text{high-}m_{\mathrm{T2}}}$-1-$ee$ ($+1.70\sigma$) and $\mathrm{SR}^{Wh}_{\text{high-}m_{\mathrm{T2}}}$-1-$e\mu$ ($+1.83\sigma$). In $\mathrm{SR}^{Wh}_{\text{high-}m_{\mathrm{T2}}}$-3-$\mu\mu$ data show a deficit compared to the SM background prediction (-2.02σ). This behaviour is associated with the statistical under-fluctuation of data for $\mu^{\pm}\mu^{\pm}$ events with relatively high $E_{\mathrm{T}}^{\mathrm{miss}}$, as shown in Figure 4.25, where only one event from data has been observed for $E_{\mathrm{T}}^{\mathrm{miss}} \geq 200$ GeV . Nevertheless, since these deviations from the background expectation have been found to be well below the 3σ threshold, they are not sufficient to claim the observation of a significant excess compared the SM prediction.

The impact of each source of systematic uncertainty on the background in each SR after the background-only fit has also been evaluated, as shown in Figure 4.26.

Other than the total relative uncertainty, systematic uncertainties are grouped into five categories: “Experimental” for the detector-related uncertainties, “Theoretical” for the theoretical systematics, “Normalisation” which represent the errors on the extracted NFs, “MC stats” which is the statistical uncertainty associated with the backgrounds from MC, “Fake/Non-

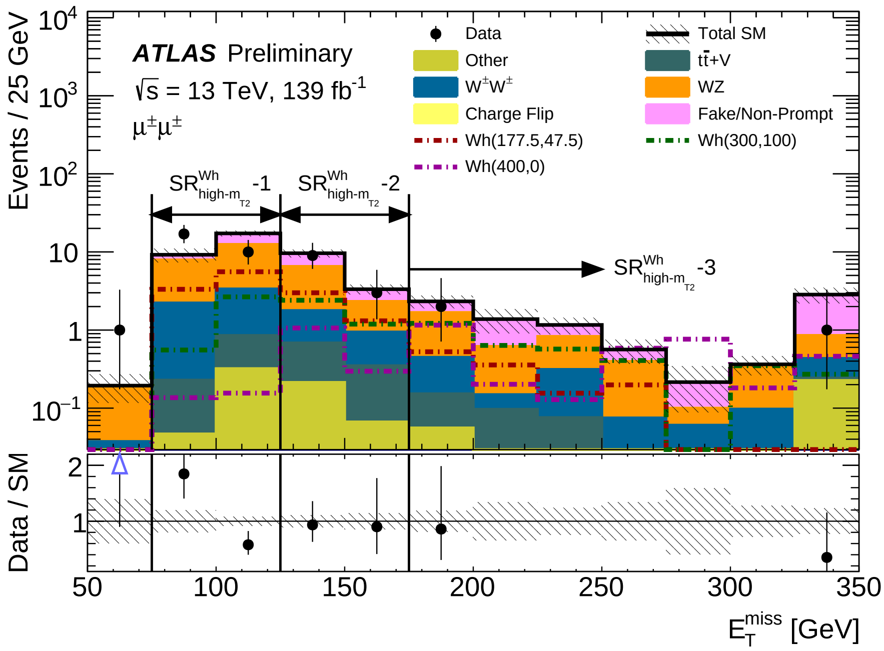

Figure 4.25: $E_{\mathrm{T}}^{\mathrm{miss}}$ distribution after the background-only fit showing the data and the post-fit expected background in the three $E_{\mathrm{T}}^{\mathrm{miss}}$ bins of the $\mu^{\pm}\mu^{\pm}$ channel of $\mathrm{SR}^{Wh}_{\text{high-}m_{\mathrm{T2}}}$. The bottom panel shows the ratio of the observed data to the predicted yields. Statistical and systematic uncertainties are shown. [136]

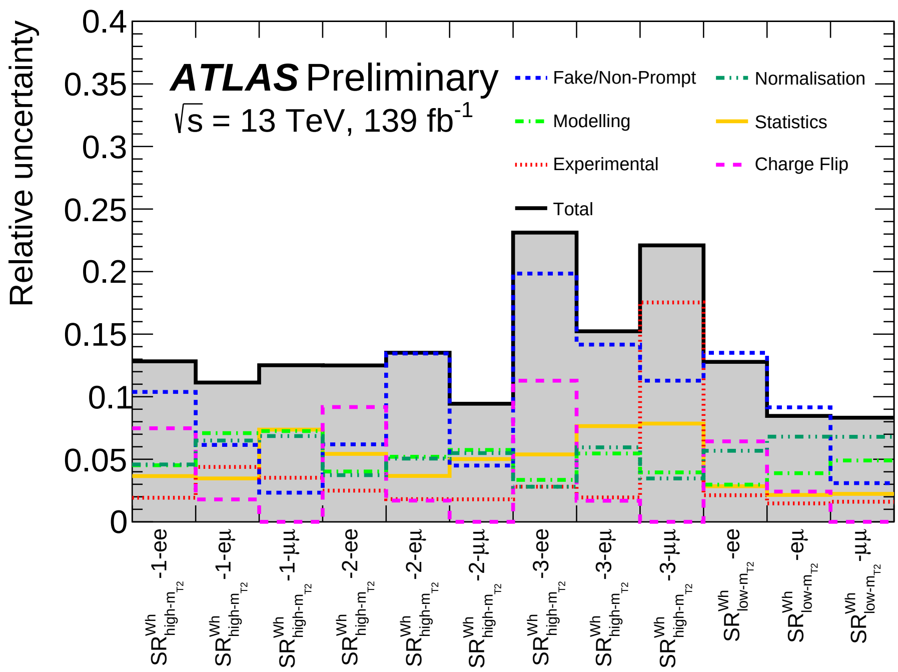

Figure 4.26: Breakdown of the relative uncertainties in the SRs of the Wh-SS analysis for all the sources of the statistical and systematic uncertainties considered. [136]

Prompt" and "Charge-Flip" which are the total uncertainties associated with the data-driven estimation of the FNP and CF backgrounds, respectively. The FNP background-related uncertainties have been found to be in general the dominant sources of uncertainties in the SRs of the Wh-SS analysis. CF-related uncertainties become relevant only in SRs with a $e^{\pm}e^{\pm}$ lepton pair. In $\mathrm{SR}^{Wh}_{\text{high-}m_{\mathrm{T2}}}$-3-$\mu\mu$ experimental systematics arising from the reconstruction of muons are the most dominant source. Due to the fact that the purity of the CR in which the $W^{\pm}W^{\pm}$ process is normalised is only ∼ 45%, with non-negligible contributions from the WZ and FNP backgrounds (Figure 4.13a), the fit introduces non-negligible anti-correlations between the NPs associated with the normalisations of $W^{\pm}W^{\pm}$ and WZ, and between the NPs associated with the normalisation of $W^{\pm}W^{\pm}$ and the uncertainties of the FNPs background. As a consequence, e. g. the impact of the total uncertainty in $\mathrm{SR}^{Wh}_{\text{low-}m_{\mathrm{T2}}}$-$ee$ and $\mathrm{SR}^{Wh}_{\text{low-}m_{\mathrm{T2}}}$-$e\mu$ is smaller compared to the impact of the FNPs uncertainty alone.

4.5.3 Model-independent fit results of the Wh-SS analysis

A model-independent fit has been performed, using the procedure outlined in Section 4.5.1, in the so-called *discovery regions*. The definition of the discovery regions, referred to as $\mathrm{SR}^{Wh}_{\text{high-}m_{\mathrm{T2}}}$-Disc and $\mathrm{SR}^{Wh}_{\text{low-}m_{\mathrm{T2}}}$-Disc, is inspired by the search for the Wh-SS model and is obtained by merging together the flavour and $E_{\mathrm{T}}^{\mathrm{miss}}$ bins of the SRs of the Wh-SS analysis, as shown in Table 4.19.

Table 4.19: Summary of the selection criteria for the inclusive SRs. The final selections are obtained by merging the flavour and $E_{\mathrm{T}}^{\mathrm{miss}}$ bins of the SRs targeting the Wh-SS model (Table 4.6).

Variable	$\mathrm{SR}^{Wh}_{\text{high-}m_{\mathrm{T2}}}$-Disc	$\mathrm{SR}^{Wh}_{\text{low-}m_{\mathrm{T2}}}$-Disc
Wh-SS preselection	Applied	
m_{T2} [GeV]	≥ 80	< 80
$m_{\mathrm{T}}^{\mathrm{min}}$ [GeV]	-	≥ 100
$E_{\mathrm{T}}^{\mathrm{miss}}$ significance	≥ 7	≥ 6
$E_{\mathrm{T}}^{\mathrm{miss}}$ [GeV]	≥ 75	≥ 50

The rationale behind such choice is based on the fact that, for instance, bins with increasing $E_{\mathrm{T}}^{\mathrm{miss}}$ have higher sensitivity for progressively higher Δm_{Sig} (see Section 4.2.5). Thus, taking into account inclusive SRs as discovery regions removes the dependency on the Wh-SS search whilst making the regions sensitive simultaneously to different Δm_{Sig} values. Since this holds true in general for a variety of BSM models other than Wh-SS, it can be stated that these inclusive regions maximise the overall discovery potential for BSM physics in the phase-space targeted by the Wh-SS analysis.

The results of the model-independent fit, performed separately in the two discovery regions, are shown in Table 4.20.

Table 4.20: Results of the model-independent fit in the discovery SRs of the Wh-SS analysis. The number of observed and expected yields, N_{Obs} and N_{Exp}, are obtained from a background-only fit in the same regions. Upper limits at 95% CL on the visible signal cross-section, σ^{95}_{Vis}, and the corresponding observed and expected number of signal events, S^{95}_{Obs} and S^{95}_{Exp} are shown as well as the CL_B of the discovery fit and the corresponding p-value (p_B for no signal), which is also reported as the number of σ deviations, Z, from the background expectation.

Region	N_{Obs}	N_{Exp}	σ^{95}_{Vis} [fb]	S^{95}_{Obs}	S^{95}_{Exp}	CL_B	$p_B(s=0)$ (Z)
$\text{SR}^{Wh}_{\text{high-}m_{\text{T2}}}$-Disc	124	115.77 ± 10.48	0.28	39.3	$33.9^{+14.3}_{-10.0}$	0.66	0.34 (0.41)
$\text{SR}^{Wh}_{\text{low-}m_{\text{T2}}}$-Disc	132	123.84 ± 8.37	0.24	33.0	$29.5^{+11.7}_{-8.8}$	0.63	0.33 (0.43)

The observed data have been once again found to be compatible with the SM prediction in both discovery regions. This is further represented by the computed discovery p-values, for which the highest discrepancy with the background prediction is only 0.43σ.

4.5.4 Model-dependent fit results of the Wh-SS analysis

The absence of any significant excess observed with data in any of the SRs of the Wh-SS analysis after the background-only fit, allows to interpret the result by setting 95% exclusion limits on the masses of the charginos and neutralinos considered in the context of the Wh-SS model. This was achieved by performing an exclusion fit (see Section 4.5.1) in all SRs. The stability of the exclusion fit has been assessed by evaluating pulls (Figure 4.27) for each mass point of the Wh-SS signal grid. A description of all the NPs constrained by the fit and shown in Figure 4.27 is reported in Table 4.21.

Table 4.21: Description of the set of NPs constrained by the fit.

NP name	Description
`staterror_*`	Statistical error in each region
`sys_CF_{Stat,Sys,MCstat}`	Systematic uncertainties on the CF (Section 4.3.3).
`sys_FF_{Stat,Psub,CFsub,CRSRextr}`	Systematic uncertainties on the FF (Section 4.3.5).
`sys_kWWSS_{stat,sys}`	Statistical and systematic error on the K-factor applied to the MC $W^{\pm}W^{\pm}$ process (Section 4.3.2).
`sys_theory_*`	Theoretical systematic errors on MC processes (Section 4.4.2).
`SigXsec_*`	Theoretical uncertainty on the signal cross-sections.
`sys_{JET,JVT,FT}*`	Experimental systematic errors concerning jets.
`sys_{MUON,mu}*`	Experimental systematic errors concerning muons.
`sys_{EG,el,ECIDS}*`	Experimental systematic errors concerning electrons.
`sys_MET_*`	Experimental systematic errors concerning $E_{\text{T}}^{\text{miss}}$.
`sys_PU`, `lumi`	Experimental systematic errors concerning pile-up and luminosity.

The most relevant pulls are due to the mild excesses between data and SM background in $\text{SR}^{Wh}_{\text{high-}m_{\text{T2}}}$-1-$ee$ and $\text{SR}^{Wh}_{\text{high-}m_{\text{T2}}}$-1-$e\mu$, and to the deficit in $\text{SR}^{Wh}_{\text{high-}m_{\text{T2}}}$-3-$\mu\mu$. In particular, the mild excess in the ee and $e\mu$ channels of $\text{SR}^{Wh}_{\text{high-}m_{\text{T2}}}$-1 are responsible for the $\gtrsim 1\sigma$ pull of `sys_FF_CFsub`, associated with the CF background subtraction in the measurement of the FF for electrons, which becomes particularly relevant in these regions. However, all the pulls have been found to be compatible with the original prediction of the systematic uncertainties within 2σ. Since analogous results have been obtained for every point of the signal grid, the results of the exclusion fit are thus validated.

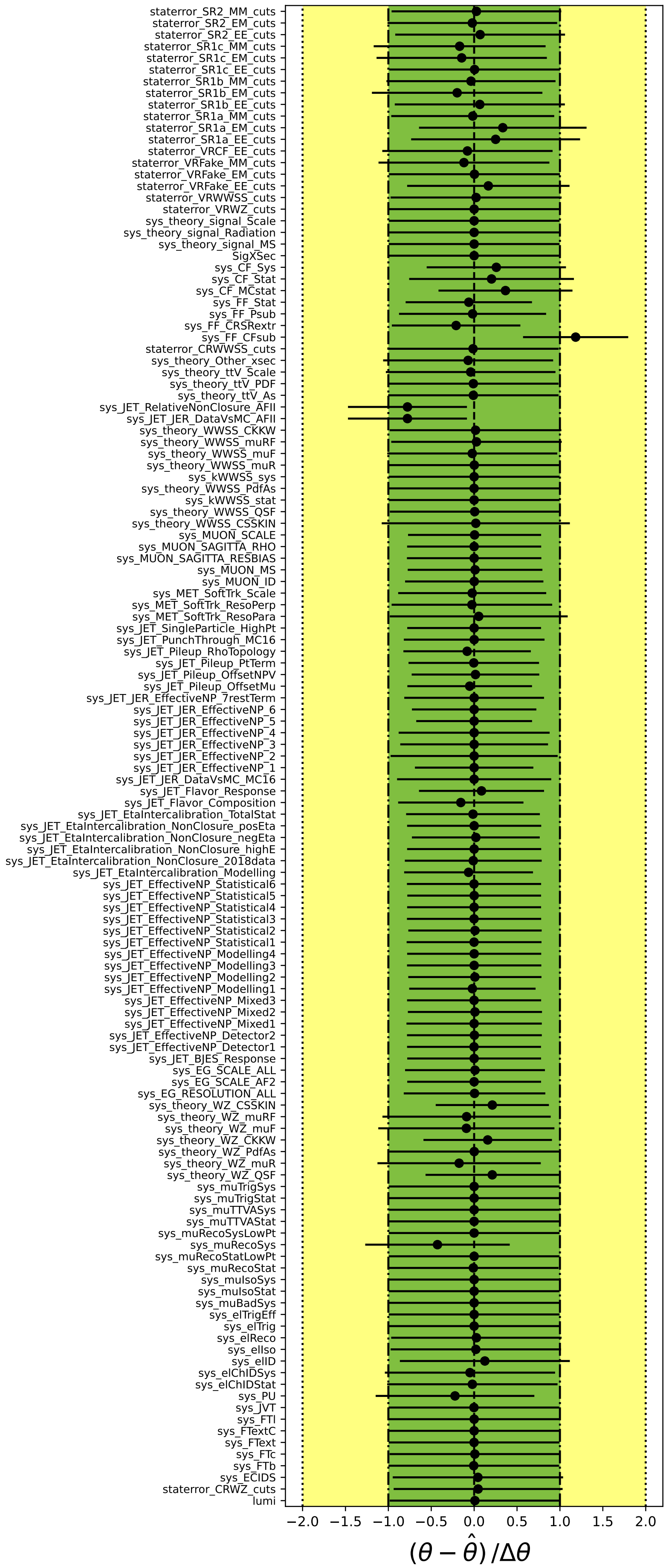

Figure 4.27: Pulls for every NP obtained by carrying out an exclusion fit in the Wh (300,0) mass point of the Wh-SS signal grid. A description of each of the shown NPs is reported in Table 4.21.

The observed and expected 95% exclusion limits for the Wh-SS model are shown in Figure 4.28. The observed limit excludes a larger area of the signal mass plane compared to the expected limit as a consequence of the deficit observed in $\mathrm{SR}^{Wh}_{\mathrm{high}\text{-}m_{\mathrm{T2}}}$-3-$\mu\mu$. Values as $m_{\tilde{\chi}_1^\pm,\tilde{\chi}_2^0}$ are excluded up to 520 GeV for massless LSPs, whereas $m_{\tilde{\chi}_1^0}$ are excluded up to about 175 GeV for $m_{\tilde{\chi}_1^\pm,\tilde{\chi}_2^0} \simeq 400$ GeV. Moreover, mass points are excluded for Δm_{Sig} down to the kinematic limit for $m_{\tilde{\chi}_1^\pm,\tilde{\chi}_2^0}$ up to 225 GeV.

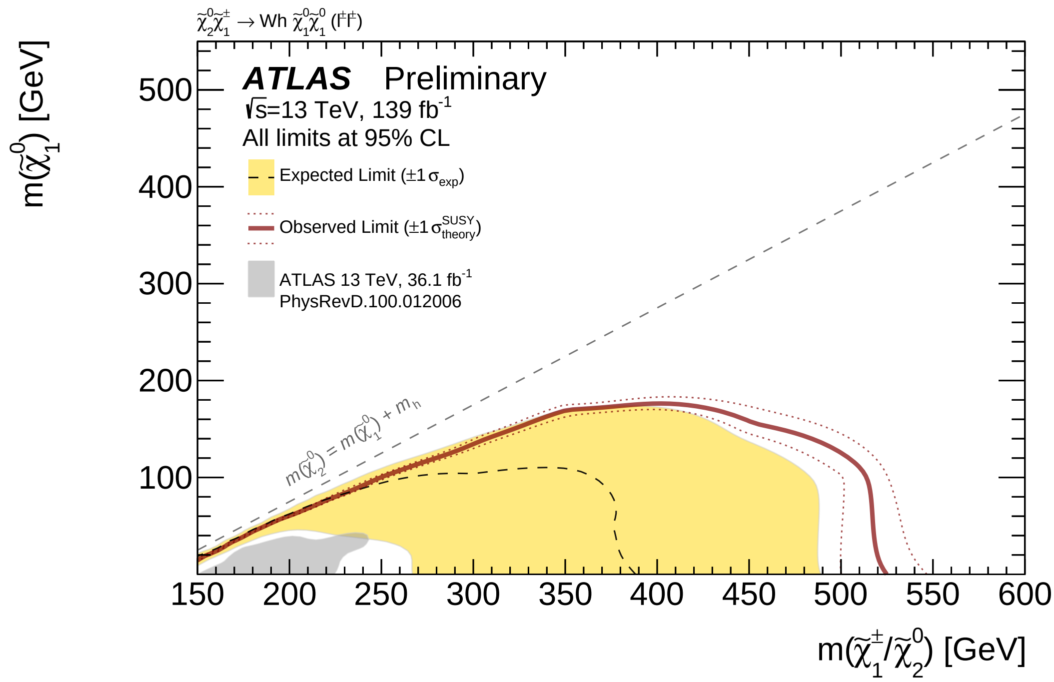

Figure 4.28: Observed (red solid line) and expected (dashed black line) exclusion limits at 95% CL on $m_{\tilde{\chi}_1^\pm,\tilde{\chi}_2^0}$ and $m_{\tilde{\chi}_1^0}$ for the Wh-SS model [136]. The yellow band represents $\pm 1\sigma$ total uncertainty on the expected result, whereas the dotted red lines represent $\pm 1\sigma$ on the signal cross-section. The grey area represents the exclusion limits of the previous ATLAS searches in the same model using the early Run 2 dataset with 36.1 fb^{-1} [57].

This analysis allows to improve the sensitivity for the search in the Wh-SS model compared to an analogous analysis targeting the same model obtained in the ATLAS experiment with the early Run 2 dataset with 36.1 fb^{-1} [57]. This can be appreciated by comparing the grey-shaded area in Figure 4.28, representing the previous observed exclusion limit of the Wh-SS model obtained by the ATLAS Collaboration with the limit obtained in this search.

Outlook of the Wh-SS analysis

The substantial increase in the bounds on $m_{\tilde{\chi}_1^\pm,\tilde{\chi}_2^0}$ and $m_{\tilde{\chi}_1^0}$ compared to what was possible using early Run 2 data allows to better probe the phase-space targeted by the Wh-SS model. Together with the results of other searches based on simplified models with the same theoretical assumptions but different final states, due to the different decay of the intermediate bosons, this allows to set limits on the parameters of mSUGRA models and, in general, on the possible mass hierarchies of the MSSM. Additional informations can be extracted by statistically combining the results of these searches. An effort targeting the combination of the Wh-SS model with similar models in currently ongoing in the ATLAS Collaboration. An overview about such task will be given in Chapter 6.

Search for $\tilde{\chi}_1^{\pm}\,\tilde{\chi}_2^0$ decaying to three leptons via intermediate WZ and Wh bosons

5

This Chapter presents the analysis searching for the EWK $\tilde{\chi}_1^{\pm}\,\tilde{\chi}_2^0$ production through their R-Parity-conserving decays to final states with three light leptons ($\ell = e, \mu$) and $E_{\mathrm{T}}^{\mathrm{miss}}$. The analysis uses the full Run 2 dataset (with 139 fb^{-1}) collected with the ATLAS detector. Two intermediate states involving the on-shell production of W and Z bosons (*WZ-3ℓ model*) or W and Higgs bosons (*Wh-3ℓ model*) are considered for a range of relevant parameters. These two searches are also collectively referred to as the *3ℓ-onShell analysis*. Results from the 3ℓ-onShell analysis have been published in a paper, found in Reference [156]. This paper also includes details about other EWK SUSY searches in three-lepton final states, focusing instead on intermediate decays to off-shell W and Z bosons.

I have contributed to the 3ℓ-onShell analysis since the start of my PhD until its publication. In particular, I have contributed to the development and maintenance of the analysis framework used for processing and analysis data and MC samples. I have personally developed the techniques to estimate detector-level systematic uncertainties and I have also been responsible for the estimation of theoretical systematic uncertainties on the main SM backgrounds of the search. Finally, I have provided assistance in the production of the final result plots, also included in the publication of Reference [156].

In the following Sections an overview of the 3ℓ-onShell analysis strategy is given. Results presented in this Chapter which I have personally produced will be highlighted specifically, with additional material taken from Reference [156], also shown for completeness. The results of the 3ℓ-onShell analysis will be combined with the Wh-SS search (Chapter 4) and other EWK SUSY searches with intermediate states of W and Z/h bosons. Preliminary results of their combination, to which I have made key contributions for my PhD, will be discussed in detail in Chapter 6.

5.1 Targeted SUSY scenarios

The simplified models addressed in the WZ-3ℓ and Wh-3ℓ searches are shown in the diagrams of Figure 5.1.

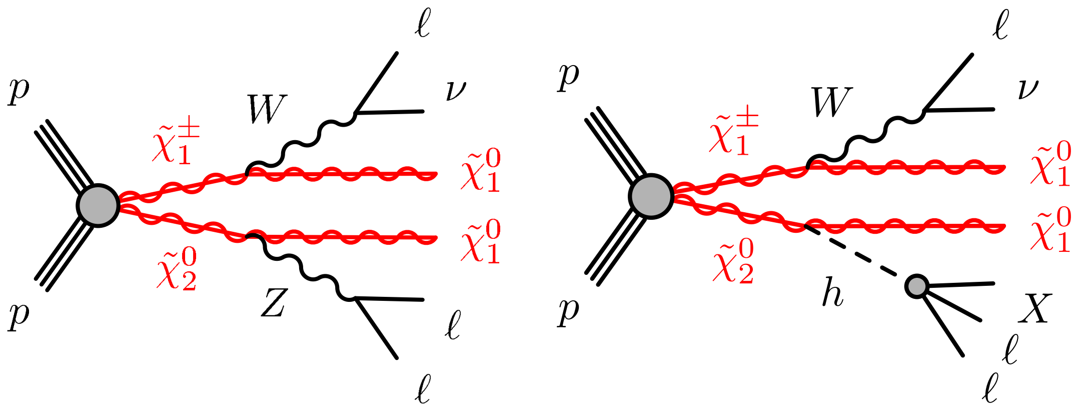

(a) WZ-3ℓ model

(b) Wh-3ℓ model

Figure 5.1: Diagrams for the production of chargino and neutralino, decaying to three-lepton final states via (a) WZ and (b) Wh bosons.

The $\tilde{\chi}_1^{\pm}$ and $\tilde{\chi}_2^0$ are assumed to be mostly Wino-like and mass-degenerate ($m_{\tilde{\chi}_1^{\pm},\tilde{\chi}_2^0} = m_{\tilde{\chi}_1^{\pm}} = m_{\tilde{\chi}_2^0}$). In both the models, the $\tilde{\chi}_1^{\pm}$ is assumed to decay with a 100% BR to an on-shell W boson and a stable $\tilde{\chi}_1^0$ ($\tilde{\chi}_1^{\pm} \to W^{\pm}\tilde{\chi}_1^0$). In the WZ-3ℓ (Wh-3ℓ) model $\tilde{\chi}_2^0$ decays with a 100% BR to a $\tilde{\chi}_1^0$ and an on-shell Z (Higgs) boson, namely $\tilde{\chi}_2^0 \to Z\tilde{\chi}_1^0$ ($\tilde{\chi}_2^0 \to h\tilde{\chi}_1^0$). The $\tilde{\chi}_1^0$ in the final state is in turn assumed to be mostly Bino-like and the stable LSP. Three-lepton final states arise from fully leptonic decays of the gauge bosons. In the Wh-3ℓ model, all possible decays of the Higgs boson are considered if they result in two opposite-sign leptons, in particular W^+W^-, ZZ and $\tau^+\tau^-$.

Similar to the Wh-SS analysis described in Chapter 4, the WZ-3ℓ and Wh-3ℓ models are studied by taking into account two dedicated signal grids. A similar nomenclature is employed to indicate the mass point of each search: WZ ($m_{\tilde{\chi}_1^{\pm},\tilde{\chi}_2^0}, m_{\tilde{\chi}_1^0}$) for the WZ-3ℓ model and Wh ($m_{\tilde{\chi}_1^{\pm},\tilde{\chi}_2^0}, m_{\tilde{\chi}_1^0}$) for the Wh-3ℓ model. As only on-shell intermediate particles are considered in the 3ℓ-onShell analysis, two different kinematic limits are considered. These are $\Delta m_{\mathrm{Sig}} \gtrsim m_Z$ for the WZ-3ℓ signal grid and $\Delta m_{\mathrm{Sig}} \gtrsim m_h$ in the Wh-3ℓ signal grid.

MC samples for each mass point of both signal grids have been generated from LO matrix-elements with up to additional partons using the `MadGraph` generator interfaced with `PYTHIA8` for PS modelling. In order to ensure the signal MC samples to have sufficiently high statistics, dedicated three-lepton filters are applied at generation-level. For the WZ-3ℓ model events are generated requiring the presence of at least two truth-level leptons with $p_{\mathrm{T}} > 7$ GeV. In the Wh-3ℓ model all three truth-level leptons must pass $p_{\mathrm{T}} > 7$ GeV.

5.2 Analysis strategy

5.2.1 Object definitions and trigger selection

The targeted final states requires events with reconstructed electrons, muons, jets ad $E_{\mathrm{T}}^{\mathrm{miss}}$ passing the OvR procedure (Section 3.3.3). Signal electrons and signal muons criteria are applied on top of the corresponding baseline selection. The full list of cuts used in the 3ℓ-onShell analysis is reported in Table 5.1.

Table 5.1: Summary of the electron and muon selection criteria used in the WZ-3ℓ and Wh-3ℓ analyses. The signal criteria are applied on top of the baseline criteria.

	Baseline electrons	Baseline muons
Acceptance	$p_{\mathrm{T}} \geq 10$ GeV , $\lvert\eta\rvert < 2.47$	$p_{\mathrm{T}} \geq 10$ GeV , $\lvert\eta\rvert < 2.5$
Identification WP	`LooseAndBLayer`	`Medium`
Impact parameter	$\lvert d_0/\sigma(d_0)\rvert < 5.0$, $\lvert z_0 \cdot \sin(\theta)\rvert < 0.5$ mm	$\lvert z_0 \cdot \sin(\theta)\rvert < 0.5$ mm
	Signal electrons	**Signal muons**
Identification WP	`Medium`	-
Isolation WP	`Tight`	`Tight`
Impact parameter	-	$\lvert d_0/\sigma(d_0)\rvert < 3.0$

The selection criteria chosen for jets and b-jets in the WZ-3ℓ and Wh-3ℓ analyses are summarised in Table 5.2. In this analysis, EMTopo jets are used. The highest efficiency b-tagging WP, 85%, has been chosen, in order to maximise the rejection of b-jets in the SRs.

Table 5.2: Summary of the jet selection criteria used in the WZ-3ℓ and Wh-3ℓ analyses.

	Baseline jets
Collection	EMTopo
Acceptance	$p_{\mathrm{T}} \geq 20$ GeV , $\lvert\eta\rvert < 4.5$
	Signal jets
Acceptance	$p_{\mathrm{T}} \geq 20$ GeV , $\lvert\eta\rvert < 2.8$
JVT	`Medium` WP for $p_{\mathrm{T}} < 120$ GeV , $\lvert\eta\rvert < 2.5$
	Signal b-jets
Acceptance	$p_{\mathrm{T}} \geq 20$ GeV , $\lvert\eta\rvert < 2.5$
b-tagger	`MV2c10`, 85% efficiency WP

The 3ℓ-onShell analysis adopts a trigger selection based on the logical `OR` of the same di-lepton trigger chains used in the Wh-SS analysis (Table 4.4).

5.2.2 Standard Model background processes

Sources of SM backgrounds are once again classified *irreducible* and *reducible*. The fundamental difference with the Wh-SS analysis (Chapter 4) is that reducible backgrounds from CF are not expected to contribute to three-lepton final states.

The contribution in the 3ℓ-onShell analysis of the different SM processes has been studied initially by relying on MC simulation, generated with NLO accuracy according to the details given in Section 3.2.2. Below, the main sources of SM background to the 3ℓ-onShell analysis are listed along with the MC generator used to simulate them.

Multi-boson (VV, VVV) These are events from the SM production of two or three vector bosons, $V = W, Z$ [137]. When considering fully leptonic decays of the vector bosons, e. g. for $WZ \to \ell\ell\ell\nu$ or $WWW \to 3\ell + 3\nu$, the multi-boson production is the main expected source of irreducible SM background for the WZ-3ℓ and Wh-3ℓ analyses. MC samples are generated using `SHERPA`.

Higgs These are processes involving the production of a Higgs boson from gluon-gluon fusion, or via Vector Boson Fusion (VBF), or in association with another vector boson or with a top–anti-top pair [157]. Given the possible decay modes of the Higgs boson, Vh and $t\bar{t}+h$ processes can contribute as irreducible backgrounds of the 3ℓ-onShell analysis. MC samples are generated with `POWHEG` interfaced with `PYTHYA8`, for PS modelling, and `EvtGen`, to improve the simulation of the hadronisation.

t$\bar{\text{t}}$+V Another source of irreducible background comes from the production of $t\bar{t}$ in association with a vector boson, $V = W, Z$ [140]. These events are generated with the `aMC@NLO` extension of `MadGraph`, interfaced with `PYTHYA8` and `EvtGen`.

Z+jets The main source of reducible background both in the WZ-3ℓ and the Wh-3ℓ searches comes from the SM production of a leptonically-decaying Z boson accompanied by jets in the final state [141]. The three-lepton final state mainly arises from the mis-identification of a jet as a lepton. `SHERPA` is used to generate this process.

Other top processes (t$\bar{\text{t}}$, single-top) These processes involve the di-leptonic-decaying $t\bar{t}$ [142] and single-top production [143], which also contribute to the final state through FNP leptons coming from the HF hadron decay or light jet mis-identification. These backgrounds are simulated with `POWHEG` interfaced with `PYTHYA8` and `EvtGen`.

5.2.3 Discriminant variables used in the 3ℓ-onShell analysis

A set of different kinematic variables is used to discriminate SUSY signal events from the SM background. $E_{\mathrm{T}}^{\mathrm{miss}}$ (Equation 3.2) and Sig($E_{\mathrm{T}}^{\mathrm{miss}}$), already introduced in Section 4.2.4 for the Wh-SS analysis still provide an effective discrimination of the the SUSY signals expected in the WZ-3ℓ and the Wh-3ℓ models. Other relevant variables used in the 3ℓ-onShell analysis are introduced below.

Invariant mass of the SFOS lepton pair Events of the WZ-3ℓ model are characterised by the presence of a SFOS lepton pair from the leptonic decay of the Z boson. The same situation occurs in the Wh-3ℓ depending of the different decay modes of the Higgs boson. The invariant mass (Equation 4.1) of the SFOS pair, called $m_{\ell\ell}^{\mathrm{SFOS}}$, is considered. If in a three-lepton event more than one SFOS lepton pair is found ($n_{\ell\ell}^{\mathrm{SFOS}} \geq 1$), the pair whose $m_{\ell\ell}^{\mathrm{SFOS}}$ is closer to m_Z (i. e. with the minimum $|m_{\ell\ell}^{\mathrm{SFOS}} - m_Z|$ value) is chosen. Such pair is associated with the decay of the Z (or Higgs) boson, whereas the remaining lepton, indicated as ℓ_W, is assigned to the W boson.

Transverse mass of $\ell_{\mathbf{W}}$ and $\mathbf{E}_{\mathbf{T}}^{\mathbf{miss}}$ The transverse mass, defined in Equation 4.5, computed with the $E_{\mathrm{T}}^{\mathrm{miss}}$ and the lepton out of three in the event which is associated with the decay of the W boson (ℓ_W), called m_{T}^{W}, is taken into account in the 3ℓ-onShell analysis. Since the $E_{\mathrm{T}}^{\mathrm{miss}}$ in every event of the WZ-3ℓ and Wh-3ℓ models arise from the undetected, massive LSPs, the corresponding m_{T}^{W} distribution is expected to reach high values, depending on Δm_{Sig}. Also, in the vast majority of the SM backgrounds with a leptonically-decaying W boson, most events have $m_{\mathrm{T}}^{W} \lesssim m_W$, instead. Hence, m_{T}^{W} provides a good discrimination of the targeted SUSY signal against the SM background.

Hadronic and leptonic activity Further discrimination is achieved by considering the *hadronic activity*, H_{T}, and the *leptonic activity*, H_{T}^{ℓ}, of a three-lepton event. These are defined as the scalar sum of the p_{T} of all the jets and leptons in the event, as indicated as follows:

$$H_{\mathrm{T}} = \sum_{i=1}^{n_{\mathrm{jets}}} p_{\mathrm{T}}^{\mathrm{jet}_i}, \tag{5.1}$$

$$H_{\mathrm{T}}^{\ell} = \sum_{i=1}^{3} p_{\mathrm{T}}^{\ell_i}. \tag{5.2}$$

5.2.4 WZ-3ℓ and the Wh-3ℓ event selections

This Section presents an overview of the event selections used to define the SRs targeting the WZ-3ℓ and Wh-3ℓ models, which is based on the cut-and-count approach, as in the Wh-SS analysis (Chapter 4). As I have not been directly involved in this aspect of the 3ℓ-onShell analysis, details about the SR optimisation procedure are omitted here and can be found in Reference [156].

An initial event preselection is achieved by requiring the cuts summarised in Table 5.3.

Table 5.3: Summary of the preselection cuts used in the WZ-3ℓ and Wh-3ℓ analyses.

Variable	Preselection cut
n_{ℓ}^{BL}, $n_{\ell}^{\mathrm{Signal}}$	$= 3$
$p_{\mathrm{T}}^{\ell_1}$, $p_{\mathrm{T}}^{\ell_2}$, $p_{\mathrm{T}}^{\ell_3}$ [GeV]	$\geq 25, 20, 10$
$E_{\mathrm{T}}^{\mathrm{miss}}$ [GeV]	≥ 50
$n_{b-\mathrm{jets}}$	$= 0$

The requirement of events with exactly three light leptons is applied for both baseline, n_ℓ^{BL}, and signal, n_ℓ^{Signal}, leptons [1] (see Table 5.1), thus suppressing the contribution from FNP leptons. The $p_{\mathrm{T}} > 25, 20, 10$ GeV thresholds ensure to select events with high trigger efficiencies for the di-lepton trigger chains used (Table 4.4). Events are also required to have $E_{\mathrm{T}}^{\mathrm{miss}} > 50$ GeV to effectively reject backgrounds from Z+jets and Drell-Yan [147] processes. Finally, a veto is applied for events with b-tagged jets ($n_{b-\mathrm{jets}} \geq 1$), to reject the top-related SM backgrounds.

The main event classification is performed by counting the number of SFOS leptons in the event, $n_{\ell\ell}^{\mathrm{SFOS}}$. As explained in Section 5.2.3, the SFOS lepton pair, associated with the decay of a Z or Higgs boson, and ℓ_W, assigned to the W boson, are identified for all events with $n_{\ell\ell}^{\mathrm{SFOS}} \geq 1$. If $m_{\ell\ell}^{\mathrm{SFOS}}$ is found to be compatible with m_Z (i. e. $m_{\ell\ell}^{\mathrm{SFOS}} \in [75, 105]$) events are assigned to the WZ-3ℓ, otherwise if $m_{\ell\ell}^{\mathrm{SFOS}}$ is not compatible with m_Z (i. e. $m_{\ell\ell}^{\mathrm{SFOS}} \notin [75, 105]$) events are to the Wh-3ℓ model. This provides a first categorisation of the SRs of the 3ℓ-onShell analysis, which henceforth are referred to as SR^{WZ} and $\mathrm{SR}^{Wh}_{\mathrm{SFOS}}$, respectively. Furthermore, since lepton pairs arising from the Higgs boson decay are not necessarily of the same flavour, an additional SR category with $n_{\ell\ell}^{\mathrm{SFOS}} = 0$ has been taken into account to target the Wh-3ℓ model. Events in this region are characterised by the presence of a Different-Flavour Opposite-Sign (DFOS) lepton pair, consistent with the Higgs boson decay, and an third lepton forming a Same-Flavour Same-Sign (SFSS) pair with one of the other two leptons. This additional SR category is called $\mathrm{SR}^{Wh}_{\mathrm{DFOS}}$. The details of separation between the three SR categories thus defined are summarised in Table 5.4.

Table 5.4: Main distinction between the SRs targeting the WZ-3ℓ model and those targeting Wh-3ℓ model.

$n_{\ell\ell}^{\mathrm{SFOS}}$	$m_{\ell\ell}^{\mathrm{SFOS}}$ [GeV]	Targeted model	SR name
≥ 1	$\in [75, 105]$	WZ-3ℓ	SR^{WZ}
	$\notin [75, 105]$	Wh-3ℓ	$\mathrm{SR}^{Wh}_{\mathrm{SFOS}}$
$= 0$	-	Wh-3ℓ	$\mathrm{SR}^{Wh}_{\mathrm{DFOS}}$

In order to improve the sensitivity of the search in events with at least a SFOS lepton pair, the corresponding SRs are further binned in different intervals of the $E_{\mathrm{T}}^{\mathrm{miss}}$ and m_{T}^{W}. The binning allows to optimise the sensitivity for WZ-3ℓ and Wh-3ℓ signals with different Δm_{Sig}. This follows from the fact that regions with higher $E_{\mathrm{T}}^{\mathrm{miss}}$ and m_{T}^{W} values are expected to be more sensitive to signals with progressively larger Δm_{Sig} values. Moreover, the sensitivity of scenarios with ISR jets is exploited by taking into account $n_{\mathrm{jets}} = 0$ and $n_{\mathrm{jets}} \geq 1$ events with dedicated cuts on H_{T} (Equation 5.1) and H_{T}^{ℓ} (Equation 5.2). Finally, events are rejected if they contain a SFOS lepton pair with $m_{\ell\ell} < 12$ GeV (Equation 4.2), in order to reduce the contribution from SM processes with low-mass di-lepton resonances (e. g. J/ψ), and if the three-lepton invariant mass, $m_{\ell\ell\ell}$ (Equation 4.3), is compatible with m_Z (i. e. $|m_{\ell\ell\ell} - m_Z| \geq 15$ GeV), to suppress the photon conversion backgrounds from Z+jets.

[1] As both the WZ-3ℓ and Wh-3ℓ models are also included in the EWK combination (Chapter 6), the orthogonality with other participating is obtained by requiring all three-lepton regions to satisfy the $n_\ell^{\mathrm{Comb}} = 3$ (Table 6.2), as well.

In summary, all the cuts defining the SRs targeting the WZ-3ℓ and Wh-3ℓ models with at least a SFOS lepton pair are reported in Tables 5.5 and 5.6, respectively.

Table 5.5: Summary of the selection criteria for the SRs targeting the WZ-3ℓ model. Regions selections are binned in m_{T} (rows) and $E_{\mathrm{T}}^{\mathrm{miss}}$ (columns) for three different sets of regions. Each set has different requirement on n_{jets}, H_{T} and H_{T}^{ℓ}. Preselection criteria (Table 5.3) as well as the resonance veto and the $m_{\ell\ell\ell}$ requirement (last row) are applied to all regions.

Selection requirements for the SRs targeting the WZ-3ℓ model				
$m_{\ell\ell}^{\mathrm{SFOS}} \in [75,105]$ GeV , $n_{\mathrm{jets}}=0$				
m_{T}^{W} [GeV]	$E_{\mathrm{T}}^{\mathrm{miss}}$ [GeV]			
$\in[100,160]$	SR^{WZ}-1: $\in[50,100]$	SR^{WZ}-2: $\in[100,150]$	SR^{WZ}-3: $\in[150,200]$	SR^{WZ}-4: ≥ 200
≥ 160	SR^{WZ}-5: $\in[50,150]$	SR^{WZ}-6: $\in[150,200]$	SR^{WZ}-7: $\in[200,350]$	SR^{WZ}-8: ≥ 350
$m_{\ell\ell}^{\mathrm{SFOS}} \in [75,105]$ GeV , $n_{\mathrm{jets}}\geq 1$, $H_{\mathrm{T}}<200$ GeV				
m_{T}^{W} [GeV]	$E_{\mathrm{T}}^{\mathrm{miss}}$ [GeV]			
$\in[100,160]$	SR^{WZ}-9: $\in[100,150]$	SR^{WZ}-10: $\in[150,250]$	SR^{WZ}-11: $\in[250,300]$	SR^{WZ}-12: ≥ 300
≥ 160	SR^{WZ}-13: $\in[50,150]$	SR^{WZ}-14: $\in[150,250]$	SR^{WZ}-15: $\in[250,400]$	SR^{WZ}-16: ≥ 400
$m_{\ell\ell}^{\mathrm{SFOS}} \in [75,105]$ GeV , $n_{\mathrm{jets}}\geq 1$, $H_{\mathrm{T}}\geq 200$ GeV , $H_{\mathrm{T}}^{\ell}<350$ GeV				
m_{T}^{W} [GeV]	$E_{\mathrm{T}}^{\mathrm{miss}}$ [GeV]			
≥ 100	SR^{WZ}-17: $\in[150,200]$	SR^{WZ}-18: $\in[200,300]$	SR^{WZ}-19: $\in[300,400]$	SR^{WZ}-20: ≥ 400
All SR^{WZ}: Resonance veto ($m_{\ell\ell}\geq 12$ GeV), $\lvert m_{\ell\ell\ell}-m_Z\rvert\geq 15$ GeV				

Table 5.6: Summary of the selection criteria for the SRs targeting events with at least one SFOS lepton pair, for the Wh-3ℓ model. Regions selections are binned in m_{T} (rows) and $E_{\mathrm{T}}^{\mathrm{miss}}$ (columns) for three different sets of regions. Each set has different requirement on $m_{\ell\ell}^{\mathrm{SFOS}}$, n_{jets} and H_{T}. Preselection criteria (Table 5.3) as well as the resonance veto and the $m_{\ell\ell\ell}$ requirement (last row) are applied to all regions.

Selection requirements for the SFOS SRs targeting the Wh-3ℓ model			
$m_{\ell\ell}^{\mathrm{SFOS}}<75$ GeV , $n_{\mathrm{jets}}=0$			
m_{T}^{W} [GeV]	$E_{\mathrm{T}}^{\mathrm{miss}}$ [GeV]		
$\in[0,100]$	SR$^{Wh}_{\mathrm{SFOS}}$-1: $\in[50,100]$	SR$^{Wh}_{\mathrm{SFOS}}$-2: $\in[100,150]$	SR$^{Wh}_{\mathrm{SFOS}}$-3 ≥ 150
$\in[100,160]$	SR$^{Wh}_{\mathrm{SFOS}}$-4: $\in[50,100]$		SR$^{Wh}_{\mathrm{SFOS}}$-5: ≥ 100
≥ 160	SR$^{Wh}_{\mathrm{SFOS}}$-6: $\in[50,100]$		SR$^{Wh}_{\mathrm{SFOS}}$-7: ≥ 100
$m_{\ell\ell}^{\mathrm{SFOS}}<75$ GeV , $n_{\mathrm{jets}}\geq 1$, $H_{\mathrm{T}}<200$ GeV			
m_{T}^{W} [GeV]	$E_{\mathrm{T}}^{\mathrm{miss}}$ [GeV]		
$\in[0,50]$		SR$^{Wh}_{\mathrm{SFOS}}$-8: $\in[50,100]$	
$\in[50,100]$		SR$^{Wh}_{\mathrm{SFOS}}$-9: $\in[50,100]$	
$\in[0,100]$	SR$^{Wh}_{\mathrm{SFOS}}$-10: $\in[100,150]$		SR$^{Wh}_{\mathrm{SFOS}}$-11: ≥ 150
$\in[100,160]$	SR$^{Wh}_{\mathrm{SFOS}}$-12: $\in[50,100]$	SR$^{Wh}_{\mathrm{SFOS}}$-13: $\in[100,150]$	SR$^{Wh}_{\mathrm{SFOS}}$-14: ≥ 150
≥ 160	SR$^{Wh}_{\mathrm{SFOS}}$-15: $\in[50,150]$		SR$^{Wh}_{\mathrm{SFOS}}$-16: ≥ 150
$m_{\ell\ell}^{\mathrm{SFOS}}\geq 150$ GeV , $n_{\mathrm{jets}}=0$			
m_{T}^{W} [GeV]	$E_{\mathrm{T}}^{\mathrm{miss}}$ [GeV]		
≥ 100	SR$^{Wh}_{\mathrm{SFOS}}$-17: $\in[50,100]$	SR$^{Wh}_{\mathrm{SFOS}}$-18: $\in[100,200]$	SR$^{Wh}_{\mathrm{SFOS}}$-19: ≥ 200
All SR$^{Wh}_{\mathrm{SFOS}}$: Resonance veto ($m_{\ell\ell}\geq 12$ GeV), $\lvert m_{\ell\ell\ell}-m_Z\rvert\geq 15$ GeV			

For what concerns the DFOS regions, also targeting the Wh-3ℓ model, the SRs are once again divided considering two categories based on the jet multiplicity: events without any jet (SR$^{Wh}_{\mathrm{DFOS}}$-1), and with one or two light jets (SR$^{Wh}_{\mathrm{DFOS}}$-2). In order to reject the background from

$t\bar{t}$ production, events with $n_{\text{jets}} \geq 3$ are excluded. This background is further suppressed by increasing the lower threshold of the p_{T} of the third-leading lepton (considering an ordering with decreasing values of the p_{T}), which is the likeliest to be FNP in $t\bar{t}$ events, especially in the lower p_{T} range, given the fact that at most only two prompt leptons are expected in the final state for this SM process. Higher sensitivity is also achieved by requesting a lower threshold on Sig($E_{\text{T}}^{\text{miss}}$). Finally, the main discrimination between signal and SM background in the DFOS regions is obtained by requiring the angular proximity between the leptons coming from the Higgs decay. This is achieved by considering the $\Delta R_{\text{OS,near}}$ variable, which is the ΔR between the only DFOS lepton in the event and the SFSS lepton closest to it in ϕ. As for the lower threshold on $p_{\text{T}}^{\ell_3}$, the value of the upper threshold on $\Delta R_{\text{OS,near}}$ has been optimised separately in each of the two SR categories considered, in the view of achieving the highest possible sensitivity. A summary of the cuts of the DFOS SRs targeting the Wh-3ℓ model has been reported in Table 5.7.

Table 5.7: Summary of the selection criteria for the SRs targeting events with at a DFOS lepton pair, for the Wh-3ℓ model. Preselection criteria (Table 5.3) are applied to all regions.

Selection requirements for the DFOS SRs targeting the Wh-3ℓ model		
Variable	$\text{SR}_{\text{DFOS}}^{Wh}$-1	$\text{SR}_{\text{DFOS}}^{Wh}$-2
n_{jets}	$= 0$	$\in [1,2]$
$E_{\text{T}}^{\text{miss}}$ significance	≥ 8	≥ 8
$p_{\text{T}}^{\ell_3}$ [GeV]	≥ 15	≥ 20
$\Delta R_{\text{OS,near}}$	< 1.2	< 1.0

5.3 SM background estimation

This Section provides a summary of the estimation of the SM background in the 3ℓ-onShell analysis. As I have not directly contributed to this task, the reader is referred to Reference [156] for further details on this aspect of the analysis.

5.3.1 Strategy for Standard Model background estimation

The bulk of the background contributing to the SRs with $n_{\ell\ell}^{\text{SFOS}} \geq 1$ targeting both the WZ-3ℓ and Wh-3ℓ models comes from the SM production of fully leptonically decaying WZ. The prediction of this background in the 3ℓ-onShell analysis relies on MC simulations which are normalised to data in dedicated CRs, whose details are reported in Section 5.3.3. On the other hand, in the two DFOS SRs targeting the Wh-3ℓ model SM processes such as triboson (VVV), Higgs, and especially $t\bar{t}$ and Z+jets dominate. In particular, $t\bar{t}$ and Z+jets are the main sources of the FNP lepton background in all the SRs. In the 3ℓ-onShell analysis, the Z+jets background is estimated by means of the FF method (Section 4.3.4), while the MC simulation of $t\bar{t}$ is validated in a dedicated VR (Section 5.3.3). A summary of the strategy used for the background estimation is reported in Table 5.8.

Table 5.8: Overview of the background estimation techniques used to estimate the various SM background processes of the 3ℓ-onShell search. The "Other" category includes: WW, ZZ, VVV, $t\bar{t}+V$ and other top- and Higgs-related processes.

Process	Estimation method
WZ	MC, normalised in CR
FNP (Z+jets)	Data-driven, FF method
$t\bar{t}$	MC, validated in VR
Other	MC

5.3.2 The Fake Factor method in the 3ℓ-onShell analysis

In the 3ℓ-onShell analysis, for the application of the FF method, the Tight and Loose-Not-Tight criteria are defined in the following way: electrons and muons which satisfy the signal selections listed in Table 5.1 are taken to be Tight, whereas they are considered Loose-Not-Tight if they satisfy the chosen baseline criteria whilst failing the signal selection. Such Loose-Not-Tight definition allows to define a control sample with an enriched contribution of FNP leptons, mainly as a consequence of the requirement to fail the signal lepton identification and isolation criteria. The FFs are measured separately for electrons and muons as functions of the lepton p_{T} in a dedicated CR, called CRFF^{WZ}.

The cuts in this regions are designed to enhance the FNP contribution, in order to have greater available statistics for the measurement of the FFs. In particular, since the targeted FNP events for the data-driven estimation are those arising from the SM Z+jets background (as explained in Table 5.8), the leading and sub-leading leptons are required to be "Z-tagged" and, therefore, both satisfying the signal lepton criteria and belonging the main SFOS lepton pair. These leptons are indicated as ℓ_1^Z and ℓ_2^Z. The FF is then extracted with respect to the remaining lepton, which is assumed to be FNP, hence, allowed to be Loose-Not-Tight. The final measurement, which relies on the formula of Equation 4.21, is performed in data after subtracting all the MC contributions (e. g. WZ, $t\bar{t}$, etc.) except of course Z+jets:

$$FF(i) = \frac{N^{\mathrm{Data}}_{\ell_1^Z\ell_2^Z\ell_3,\mathrm{CR}FF^{WZ}}(i) - N^{\mathrm{other\,MC}}_{\ell_1^Z\ell_2^Z\ell_3,\mathrm{CR}FF^{WZ}}(i)}{N^{\mathrm{Data}}_{\ell_1^Z\ell_2^Z\overline{\ell_3},\mathrm{CR}FF^{WZ}}(i) - N^{\mathrm{other\,MC}}_{\ell_1^Z\ell_2^Z\overline{\ell_3},\mathrm{CR}FF^{WZ}}(i)} \tag{5.3}$$

where the discrete index i runs over every p_{T} bins for which the FF is measured. The overline notation indicates the cases in which ℓ_3 is required to be Loose-Not-Tight. The FNP estimation can then proceed for any given region of the 3ℓ-onShell analysis by following the guidelines outlined in Section 4.3.4 and specifically from the application of the formula in Equation 4.23.

Two different sources of systematic uncertainties are considered for the data-driven estimation of the FNP lepton background:

- **Statistical uncertainties on the FFs**: arising from the propagation of the statistical errors associated with the event counts considered in the FF calculation;
- **Closure test**: a closure test is performed similarly to the one used in the Wh-SS analysis

(Section 4.3.5). Possible discrepancies from the residual non-closure of the test are taken as a source of systematic uncertainty on the FNP background estimation.

A dedicated VR, called VRFF^{WZ} and orthogonal to any other region of the analysis, is defined to assess the agreement of the estimated FNP background with data. The event selections used to define CRFF^{WZ} and VRFF^{WZ} are summarised in Table 5.9.

Table 5.9: Summary of the selection criteria of CRFF^{WZ} and VRFF^{WZ} of the 3ℓ-onShell search.

Variable	CRFF^{WZ}	VRFF^{WZ}
n_{ℓ}^{BL}	$=3$	
$n_{\ell}^{\mathrm{Signal}}$	≥ 2	$=3$
$n_{b\text{-jets}}$	$=0$	
$p_{\mathrm{T}}^{\ell_1^Z}, p_{\mathrm{T}}^{\ell_2^Z}, p_{\mathrm{T}}^{\ell_3}$ [GeV]	$>25, 20, 10$	
$n_{\ell\ell}^{\mathrm{SFOS}}$	≥ 1	
$m_{\ell\ell}^{\mathrm{SFOS}}$ [GeV]	<15	
ℓ_1^Z, ℓ_2^Z	SFOS & Z-tagged & signal	
m_{T} [GeV]	<20	
$E_{\mathrm{T}}^{\mathrm{miss}}$ [GeV]	$\in [20, 50]$	$\in [50, 100]$
$m_{\ell\ell\ell}$ [GeV]	-	$\in [105, 160]$

5.3.3 Background normalisation and validation

The predicted yields from MC of the irreducible WZ background are normalised to data observed in a dedicated CR, called CRWZ^{WZ}, scaling them by the corresponding NF. This procedure is carried when performing the background-only fit (Section 4.5.1). The definition of CRWZ^{WZ} relies on events with at least a SFOS lepton pair with $m_{\ell\ell}^{\mathrm{SFOS}} \in [75, 105]$ GeV consistently with the decay of a Z boson. The requirement $|m_{\ell\ell\ell} - m_Z| \geq 15$ GeV guarantees that the third lepton would not arise from photon conversion and would be instead much likelier to be produced from the decay of the W boson. The WZ purity is further improved with the $E_{\mathrm{T}}^{\mathrm{miss}} \in [50, 100]$ GeV and $m_{\mathrm{T}} \in [20, 100]$ GeV requirements, the latter of which also ensures the orthogonality with all the SFOS SRs, especially SR^{WZ}-1-20 (Table 5.5). To address any possible mis-modelling of WZ for different jet multiplicities, CRWZ^{WZ} is binned using the same jet multiplicity and H_{T} categories as the SFOS SRs namely: CR$WZ_{0\mathrm{j}}^{WZ}$, CR$WZ_{\text{low-}H_{\mathrm{T}}}^{WZ}$ and CR$WZ_{\text{high-}H_{\mathrm{T}}}^{WZ}$. The NFs are the extracted separately in each of these CRs and applied accordingly in the corresponding SR categories. Finally, the estimation of the WZ background is validated in corresponding VRs (VR$WZ_{0\mathrm{j}}^{WZ}$, VR$WZ_{\text{low-}H_{\mathrm{T}}}^{WZ}$ and VR$WZ_{\text{high-}H_{\mathrm{T}}}^{WZ}$) with the same definitions as the CRs except for $E_{\mathrm{T}}^{\mathrm{miss}} \geq 100$ GeV, which makes them orthogonal. The cuts defining the CRs and VRs of the WZ process are summarised in Table 5.10. The WZ purity has been found to be more than 80% in the CRs and VRs, whereas the SUSY signal contamination is very small.

For what concerns the $t\bar{t}$ process, which is the second-leading source of FNP leptons in the 3ℓ-onShell analysis and, also, one of the main backgrounds in the DFOS SRs, its modelling from MC is validated in two VRs, called VR$t\bar{t}^{WZ}$ and VR$t\bar{t}_{\mathrm{incl}}^{WZ}$. Both VRs target events with $n_{\ell\ell}^{\mathrm{SFOS}} = 0$

Table 5.10: Summary of the selection criteria for the CRs and VRs of the SM WZ background in 3ℓ-onShell search.

Variable	CRWZ^{WZ}			VRWZ^{WZ}		
	0j	low-H_T	high-H_T	0j	low-H_T	high-H_T
n_ℓ^{BL}, n_ℓ^{Signal}	$= 3$			$= 3$		
$p_T^{\ell_1}$, $p_T^{\ell_2}$, $p_T^{\ell_3}$ [GeV]	$> 25, 20, 10$			$> 25, 20, 10$		
$n_{b\text{-jets}}$	$= 0$			$= 0$		
$n_{\ell\ell}^{\mathrm{SFOS}}$	≥ 1			≥ 1		
$m_{\ell\ell}^{\mathrm{SFOS}}$ [GeV]	$\in [75, 105]$			$\in [75, 105]$		
m_T [GeV]	$\in [20, 100]$			$\in [20, 100]$		
$\lvert m_{\ell\ell\ell} - m_Z\rvert$ [GeV]	≥ 15			≥ 15		
E_T^{miss} [GeV]	$\in [50, 100]$			> 100		
n_{jets}	$= 0$	≥ 1	≥ 1	$= 0$	≥ 1	≥ 1
H_T [GeV]	-	< 200	≥ 200	-	< 200	≥ 200

(thus being orthogonal to the SFOS SRs) and $E_T^{\mathrm{miss}} \geq 50$ GeV. In VR$t\bar{t}^{WZ}$ the presence of one or two b-tagged jets is required, whereas in VR$t\bar{t}_{\mathrm{incl}}^{WZ}$ an inclusive-b jet selection is considered to assess the modelling for events with $n_{\mathrm{jets}} = 0$, as well. Here, the orthogonality with the DFOS SRs is achieved by virtue of the Sig(E_T^{miss}) < 8 cut. A summary of the event selection of the VRs or the $t\bar{t}$ background is shown in Table 5.11.

Table 5.11: Summary of the selection criteria for the VRs of the SM $t\bar{t}$ background in 3ℓ-onShell search.

Variable	VR$t\bar{t}^{WZ}$	VR$t\bar{t}_{\mathrm{incl}}^{WZ}$
n_ℓ^{BL}, n_ℓ^{Signal}	$= 3$	
$p_T^{\ell_1}$, $p_T^{\ell_2}$, $p_T^{\ell_3}$ [GeV]	$> 25, 20, 10$	
$n_{\ell\ell}^{\mathrm{SFOS}}$	$= 0$	
E_T^{miss} [GeV]	≥ 50	
$n_{b\text{-jets}}$	$\in [1, 2]$	-
E_T^{miss} significance	-	< 8

5.4 Systematic uncertainties

As explained in the introduction of this Chapter, the estimation of the systematic uncertainties is my main contribution to the 3ℓ-onShell analysis. I have implemented the software-based functionalities used for the evaluation of the experimental uncertainties. Moreover, I was responsible for the extraction of the impact of all the theoretical uncertainties affecting the CRs, VRs and SRs of the 3ℓ-onShell analysis.

Similar sets of experimental and theoretical sources of systematics as those considered in the Wh-SS analysis, described in Sections 4.4.1 and 4.4.2 respectively, have been taken into account in the case of the 3ℓ-onShell analysis as well.

5.4.1 Experimental systematics

The estimation of the impact of detector-level uncertainties is of crucial importance for the 3ℓ-onShell analysis, especially considering its reliance on MC to estimate some of the most relevant sources of SM backgrounds, e. g. ZZ and $t\bar{t}$ production.

The types of the sources of experimental systematics, which are expected to most significantly affect the background prediction, had to be carefully chosen and properly implemented in the framework to process MC samples. Apart from the detector-level systematics related to pile-up, luminosity, and trigger efficiency, which are the same as those considered in the Wh-SS analysis (Section 4.4.1), the choice for the other sources had to be tailored to the objects selections used in the 3ℓ-onShell search (Section 5.2.1). Most notably, due to the absence of the CF background, uncertainties related to the electron charge identification are not expected to yield a significant impact and are, thus, not considered. Furthermore, although analogous uncertainties have been taken into account for jets in the Wh-SS and 3ℓ-onShell analysis, their impact in the latter is different compared to that in the former, due to the different jet reconstruction (PFlow for the Wh-SS search and EMTopo for the 3ℓ-onShell search) and b-tagging (`DL1r` for the Wh-SS search and `MV2c10` for the 3ℓ-onShell search) algorithms employed. This also affects the experimental uncertainties on the $E_{\mathrm{T}}^{\mathrm{miss}}$. The impact of each of these systematic uncertainties is discussed in more details in Section 5.5.

5.4.2 Theoretical systematics

Theoretical systematics have been estimated for the main irreducible background, WZ, and the reducible $t\bar{t}$ background in every region of the 3ℓ-onShell analysis. A similar procedure as that employed for the Wh-SS analysis (Section 4.4.2) has been used. This once again implies comparing the nominal yield from MC in every region to that obtained after applying the systematic variation. Depending on the MC sample, this is obtained by considering either alternative generator weights (e. g. for QCD scales, PDF and α_S) or alternative samples at both truth-level (e. g. for CKKW, QSF and CSSKIN) and reconstruction-level (e. g. regarding matrix element, PS and radiation uncertainties). The value of a theoretical systematic uncertainty in a region is then taken from the relative variation of each one from the nominal yield and it is assigned as a flat envelope on the latter.

In the 3ℓ-onShell analysis, the likelihood of double-counting the statistical fluctuations in the determination of the theoretical uncertainties is exacerbated due to the very fine binning adopted in the definition of the SRs (Section 5.2.4). Hence, the same approach used in the Wh-SS analysis, namely to evaluate the uncertainties in inclusive bins, thus minimising the impact of the statistical errors, has been followed. Only SR bins that share similar kinematic properties are merged together for this purpose. For example, SR^{WZ}-9 to SR^{WZ}-20 which all require $n_{\text{jets}} \geq 1$ and $m_{\mathrm{T}}^{W} \geq 100$ GeV , and SR$^{Wh}_{\text{SFOS}}$-17 to SR$^{Wh}_{\text{SFOS}}$-19 with $m_{\ell\ell}^{\text{SFOS}} \geq 150$ GeV and $n_{\text{jets}} = 0$. The estimated envelopes relative to the theoretical uncertainties of WZ and $t\bar{t}$ in the SRs of the 3ℓ-onShell analysis have been reported in Tables 5.12-5.14 and 5.15, respectively.

Table 5.12: Breakdown of theoretical uncertainties concerning the QCD scales, PDF and α_S estimated for the WZ background in SR^{WZ}-1–20.

Region	μ_R [%]	μ_F [%]	$\mu_R + \mu_F$ [%]	PDF [%]	α_S [%]	PDF+α_S [%]
SR^{WZ}-1	-3.07/+4.79	-1.04/+0.90	-3.07/+4.79	±0.51	±0.01	±0.51
SR^{WZ}-2	-1.88/+0.70	-0.54/+0.55	-2.63/+1.00	±0.42	±0.01	±0.42
SR^{WZ}-3–4	-1.76/+2.96	-0.56/+0.86	-1.76/+2.96	±1.09	±0.05	±1.09
SR^{WZ}-5	-3.15/+5.30	-0.32/+0.43	-3.20/+5.30	±0.54	±0.00	±0.54
SR^{WZ}-6	-1.88/+2.80	-2.73/+2.45	-2.73/+2.80	±0.91	±0.10	±0.92
SR^{WZ}-7–8	-4.93/+8.78	-1.11/+1.50	-4.93/+8.78	±1.08	±0.05	±1.08
SR^{WZ}-9	-2.16/+2.74	-0.20/+0.04	-2.38/+2.74	±0.18	±0.01	±0.18
SR^{WZ}-10–11	-0.85/+0.54	-0.01/+0.44	-1.19/+0.54	±0.44	±0.06	±0.44
SR^{WZ}-12	-3.17/+2.32	-2.86/+1.23	-4.34/+2.75	±8.89	±0.55	±8.91
SR^{WZ}-13	-1.34/+1.17	-0.46/+0.61	-2.00/+1.65	±0.30	±0.07	±0.31
SR^{WZ}-14–16	-2.32/+0.74	-0.04/+0.35	-2.73/+0.74	±0.55	±0.03	±0.55
SR^{WZ}-17	-0.21/+0.10	-0.14/+0.08	-0.22/+0.10	±0.80	±0.02	±0.80
SR^{WZ}-18	-1.61/+1.40	-0.03/+0.26	-1.93/+1.40	±0.98	±0.05	±0.98
SR^{WZ}-19	-0.65/+1.01	-0.10/+0.82	-0.75/+1.01	±0.70	±0.01	±0.70
SR^{WZ}-20	-1.94/+2.27	-0.85/+1.07	-1.94/+2.27	±1.18	±0.02	±1.18

Table 5.13: Breakdown of theoretical uncertainties concerning the QCD scales, PDF and α_S estimated for the WZ background in SR$^{Wh}_{\mathrm{SFOS}}$-1–19 and SR$^{Wh}_{\mathrm{DFOS}}$-1–2.

Region	μ_R [%]	μ_F [%]	$\mu_R + \mu_F$ [%]	PDF [%]	α_S [%]	PDF+α_S [%]
SR$^{Wh}_{\mathrm{SFOS}}$-1	-1.84/+3.19	-1.23/+0.82	-1.84/+3.19	±0.31	±0.02	±0.32
SR$^{Wh}_{\mathrm{SFOS}}$-2	-4.76/+2.30	-2.95/+3.26	-9.10/+4.70	±0.76	±0.18	±0.78
SR$^{Wh}_{\mathrm{SFOS}}$-3	-0.91/+1.73	-1.73/+0.73	-2.65/+1.73	±14.86	±0.04	±14.86
SR$^{Wh}_{\mathrm{SFOS}}$-4	-1.83/+3.32	-0.87/+0.71	-1.83/+3.32	±0.30	±0.00	±0.30
SR$^{Wh}_{\mathrm{SFOS}}$-5	-2.24/+3.99	-1.74/+1.40	-2.24/+3.99	±0.38	±0.12	±0.40
SR$^{Wh}_{\mathrm{SFOS}}$-6	-2.33/+1.27	-0.10/+0.61	-2.33/+1.27	±0.48	±0.00	±0.48
SR$^{Wh}_{\mathrm{SFOS}}$-7	-0.47/+0.69	-1.14/+0.85	-2.07/+0.85	±6.35	±0.32	±6.35
SR$^{Wh}_{\mathrm{SFOS}}$-8	-2.05/+2.59	-0.15/+0.18	-2.20/+2.69	±0.16	±0.02	±0.16
SR$^{Wh}_{\mathrm{SFOS}}$-9	-1.59/+0.89	-2.05/+1.83	-2.05/+1.83	±0.16	±0.00	±0.16
SR$^{Wh}_{\mathrm{SFOS}}$-10	-1.43/+1.72	-0.01/+0.25	-1.61/+1.72	±0.25	±0.04	±0.25
SR$^{Wh}_{\mathrm{SFOS}}$-11	-0.67/+0.37	-0.11/+0.45	-1.21/+0.45	±0.45	±0.02	±0.45
SR$^{Wh}_{\mathrm{SFOS}}$-12	-4.28/+2.58	-6.16/+6.09	-6.16/+6.09	±0.20	±0.06	±0.21
SR$^{Wh}_{\mathrm{SFOS}}$-13	-1.50/+1.92	-0.33/+0.28	-1.50/+1.92	±0.24	±0.02	±0.25
SR$^{Wh}_{\mathrm{SFOS}}$-14	-0.22/+0.34	-0.74/+1.23	-1.55/+1.23	±0.38	±0.02	±0.38
SR$^{Wh}_{\mathrm{SFOS}}$-15	-1.00/+0.66	-0.44/+0.89	-2.09/+1.06	±0.36	±0.03	±0.36
SR$^{Wh}_{\mathrm{SFOS}}$-16	-4.91/+1.69	-0.70/+0.07	-6.13/+1.69	±0.87	±0.04	±0.87
SR$^{Wh}_{\mathrm{SFOS}}$-17	-5.46/+5.71	-0.69/+4.87	-5.84/+5.71	±5.36	±1.37	±5.53
SR$^{Wh}_{\mathrm{SFOS}}$-18	-1.70/+3.02	-1.06/+1.50	-1.70/+3.02	±0.71	±0.25	±0.75
SR$^{Wh}_{\mathrm{SFOS}}$-19	-4.12/+1.99	-2.04/+2.74	-9.33/+2.79	±2.99	±0.96	±3.14
SR$^{Wh}_{\mathrm{DFOS}}$-1–2	-5.66/+1.89	-3.77/+1.89	-9.43/+3.77	±1.56	±0.94	±1.82

As explained in Section 4.4.2, regarding the QCD scale uncertainties three separate sources have been considered and are obtained by varying μ_R and μ_F simultaneously (“$\mu_R + \mu_F$”) and each independently. Given the large statistical fluctuations, e. g. for SR$^{Wh}_{\mathrm{SFOS}}$-1 in Table 5.13, one of these scales dominates, resulting in the envelope for the $\mu_R + \mu_F$ being the same as e. g. μ_R.

Table 5.14: Breakdown of theoretical uncertainties concerning the merging scale (CKKW), re-summation scale (QSF) and PS recoil scheme (CSSKIN) estimated at truth-level for the WZ background in all SRs of the 3ℓ-onShell analysis.

Region	CKKW [%]	QSF [%]	CSSKIN [%]
SR^{WZ}-1–8	±2.07	±2.88	±2.05
SR^{WZ}-9–20	±3.46	±6.02	±0.65
$\mathrm{SR}^{Wh}_{\mathrm{SFOS}}$-1–7	±4.33	±4.66	±9.03
$\mathrm{SR}^{Wh}_{\mathrm{SFOS}}$-8–16	±4.77	± 8.35	± 1.78
$\mathrm{SR}^{Wh}_{\mathrm{SFOS}}$-17–19	±2.49	±3.56	±10.44
$\mathrm{SR}^{Wh}_{\mathrm{DFOS}}$-1–2	±5.51	±8.86	±1.19

Table 5.15: A breakdown of theoretical uncertainties concerning the matrix-element (ME), PS, ISR, FSR, PDF and α_S estimated for the $t\bar{t}$ background in all the SRs of the 3ℓ-onShell analysis.

Region	ME [%]	PS [%]	ISR [%]	FSR [%]	PDF+α_S [%]
SR^{WZ}-1–4	+26.98	-7.04	+47.21/-7.92	+3.81/-20.53	±1.23
SR^{WZ}-5–8	-25.30	-21.08	+15.06/-14.46	-6.02/+31.93	±1.26
SR^{WZ}-9–12	+19.26	-8.15	+13.09/-12.59	+1.98/-11.36	±1.30
SR^{WZ}-13–16	-36.30	-31.23	+11.51/-10.00	+9.73/-25.75	±1.23
SR^{WZ}-17	+16.67	-21.79	+29.49/-20.51	+19.23/-64.10	±1.06
SR^{WZ}-18–20	+27.27	-24.24	+10.61/-19.70	+30.30/-48.48	±1.60
$\mathrm{SR}^{Wh}_{\mathrm{SFOS}}$-1–4	+4.54	-20.97	+2.27/-9.73	+3.78/-12.76	±1.24
$\mathrm{SR}^{Wh}_{\mathrm{SFOS}}$-5–7	-23.65	-35.81	+6.98/-10.59	+3.83/-13.74	±1.16
$\mathrm{SR}^{Wh}_{\mathrm{SFOS}}$-8	-1.14	-26.34	+13.07/-10.53	+2.17/-0.23	±1.32
$\mathrm{SR}^{Wh}_{\mathrm{SFOS}}$-9	+13.11	-23.71	+3.98/-12.92	+0.92/+9.29	±1.25
$\mathrm{SR}^{Wh}_{\mathrm{SFOS}}$-10–11	+15.33	-16.82	+3.20/-14.14	+6.85/-1.93	±1.41
$\mathrm{SR}^{Wh}_{\mathrm{SFOS}}$-12	+11.08	-23.60	+1.17/-11.36	+4.83/-3.92	±1.21
$\mathrm{SR}^{Wh}_{\mathrm{SFOS}}$-13–16	-0.57	-21.45	+7.53/-12.96	+1.91/-14.30	±1.33
$\mathrm{SR}^{Wh}_{\mathrm{SFOS}}$-17–19	+30.60	-29.85	+14.93/-8.96	+13.43/-1.49	±1.51
$\mathrm{SR}^{Wh}_{\mathrm{DFOS}}$-1	-25.22	-44.35	+0.00/-10.43	+0.87/-25.22	±1.35
$\mathrm{SR}^{Wh}_{\mathrm{DFOS}}$-2	-18.97	-53.33	+21.03/-12.31	+4.10/-17.95	±1.07

Due to its the small impact of the α_S uncertainty has not been considered separately, but rather together with the PDF-related one.

For the $t\bar{t}$ process, given its expected high hadronic activity, the uncertainties corresponding to the different choice of matrix element, PS and radiation (ISR and FSR) schemes, compared to the simple variation of the QCD scales. These are either represented by one-sided or two-sided envelopes as shown in Table 5.15.

Finally, due to the small contribution in the regions of the 3ℓ-onShell analysis of all the remaining SM background processes (e. g. WW, ZZ, Higgs, tri-boson, $t\bar{t}+X$ processes) estimated from MC, flat cross-section uncertainties are taken into account [152]. These flat uncertainties have been computed considering inclusive phase-spaces. Indeed, the estimation of these uncertainties performed in a similar fashion as to the WZ and $t\bar{t}$ processes, given their small yield in the SRs, would unavoidably lead to a significant double-counting of the statistical errors.

Theoretical uncertainties of the modelling of the WZ-3ℓ and Wh-3ℓ MC signals have also been evaluated. Studies have shown that regardless of the mass point these uncertainties account at most for a ±10% of the signal yields. Therefore, a flat cross-section uncertainty of ±10% on the expected yields is considered for all the signal points of the WZ-3ℓ and Wh-3ℓ models. All of these uncertainties are reported in Table 5.16.

Table 5.16: Inclusive cross-section uncertainties considered for the MC samples of the 3ℓ-onShell analysis.

SM process	Cross-section uncertainty [%]
WW, ZZ	±6
Higgs	±7
VVV	±20
$t\bar{t}+Z$	±13
$t\bar{t}+W$	±12
$t\bar{t}+H$	±10
Other	±50
WZ-3ℓ/Wh-3ℓ signals	±10

As the experimental systematics, the impact of the theoretical sources of uncertainties in the 3ℓ-onShell search is also further discussed in the following Section.

5.5 Results of the 3ℓ-onShell search

The techniques used to carry out the statistical analyses of the results of the 3ℓ-onShell analysis are the same as those described in Section 4.5.1 for the Wh-SS analysis. In the following Sections an overview of the results of the background-only, discovery and exclusion fits is given for completeness and, also, in view of the statistical combination described in Chapter 6. None of the results discussed in this Section would have been possible without a proper estimation of the impact of the experimental and theoretical sources of systematic uncertainties, which I have performed and that has been outlined in Section 5.4. My personal contribution to the 3ℓ-onShell analysis also includes to the production of all the plots shown in Section 5.5.1.

5.5.1 Background-only fit results

The final estimate of all the SM background contributions is extracted by performing a background-only fit to data simultaneously in all the CRs. In this context the NF for the SM WZ process are also estimated in the dedicated CRs and applied accordingly to all other regions. All sources of systematic uncertainties have been taken into account, including the experimental and theoretical errors on the MC SM backgrounds and signals discussed in Section 5.4. The constraints imposed in the fit, especially for the normalised backgrounds, allow to reduce the impact of the systematic uncertainties affecting the SRs.

Figure 5.2 shows the comparison between the final estimate of the SM background with data in each VR of the 3ℓ-onShell search. The extracted values of the NFs of the WZ process

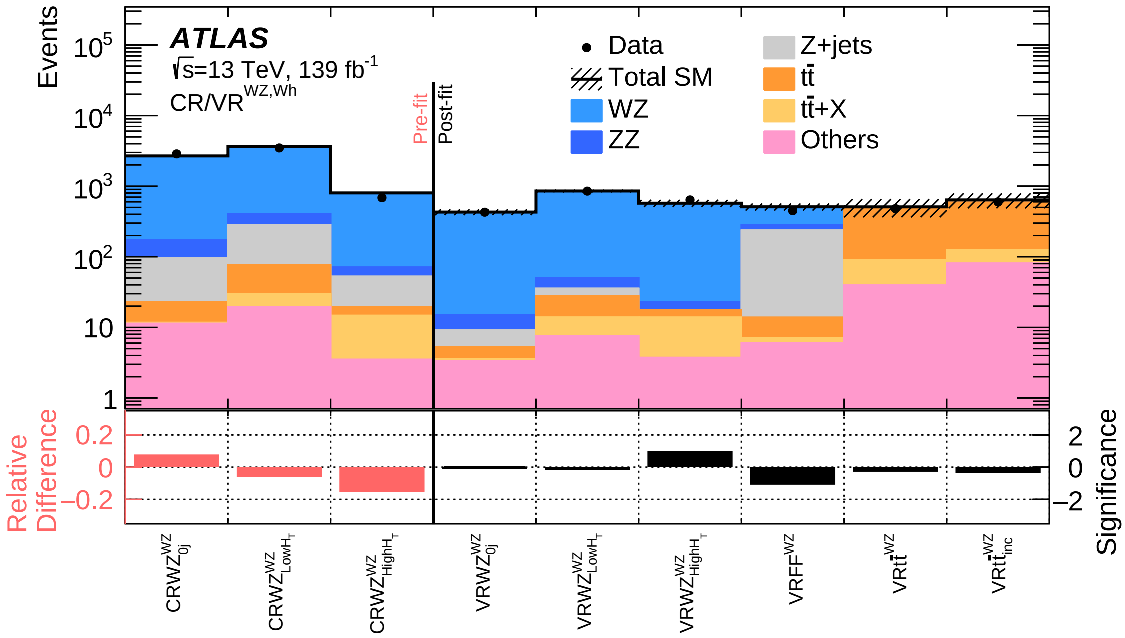

Figure 5.2: Data and SM predictions in all the CRs and VRs of the 3ℓ-onShell search. In the lower panel, the comparison between data and SM prediction is expressed as the relative difference (in red) for the CRs before the background-only fit, and as the significance for the VRs (in black), after the background-only fit. Statistical and systematic uncertainties (which I have estimated) are shown. [156]

in CRWZ$^{WZ}_{0j}$, CRWZ$^{WZ}_{\text{low-}H_T}$ and CRWZ$^{WZ}_{\text{high-}H_T}$ are $\mu^{0j}_{WZ} = 1.07 \pm 0.02$, $\mu^{\text{low-}H_T}_{WZ} = 0.94 \pm 0.03$ and $\mu^{\text{high-}H_T}_{WZ} = 0.85 \pm 0.05$, respectively. The relative difference between data and MC shown in the bottom panel of Figure 5.2 for the WZ CRs, represents the level of disagreement prior to the fit which is corrected with these NFs. The results of the background-only fit demonstrate the satisfactory agreement with data as observed in the VRs.

The final estimate of the SM background with data in the SRs targeting the WZ-3ℓ and the Wh-3ℓ models are shown in Figure 5.3.

These results are overlayed with the prediction of two benchmark signal points in each scenario. No significant deviation in the observed data with the SM background prediction is found within the total uncertainty bands (which include the systematic uncertainties that I have estimated). A mild $+2\sigma$ deviation from the SM expectation is observed in SR$^{Wh}_{\text{DFOS}}$-1 (Figure 5.3b). However, since such deviation is $< 3\sigma$ it it considered not significant and, therefore, not sufficient to claim the observation of an excess.

The impact of each source of systematic uncertainty on the background in each SR is shown in Figure 5.4.

Other than the total relative uncertainty in each region, systematic uncertainties are grouped into five categories: "Experimental" for the detector-related uncertainties, "Modelling" for the theoretical systematics, "Normalisation" which represent the errors on the extracted NFs, "MC stats" which is the statistical uncertainty associated with the backgrounds from MC, and "FNP" associated with the data-driven estimation of the FNP lepton background. Experimental systematics and MC statistical uncertainties are found to be the dominant ones in almost all the

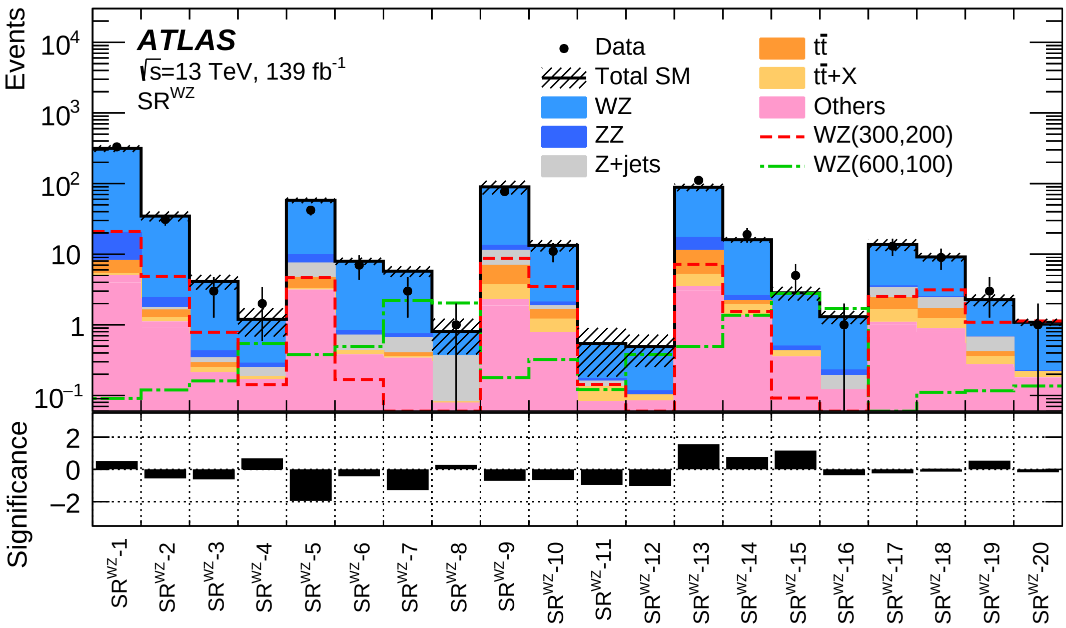

(a) SR^{WZ}

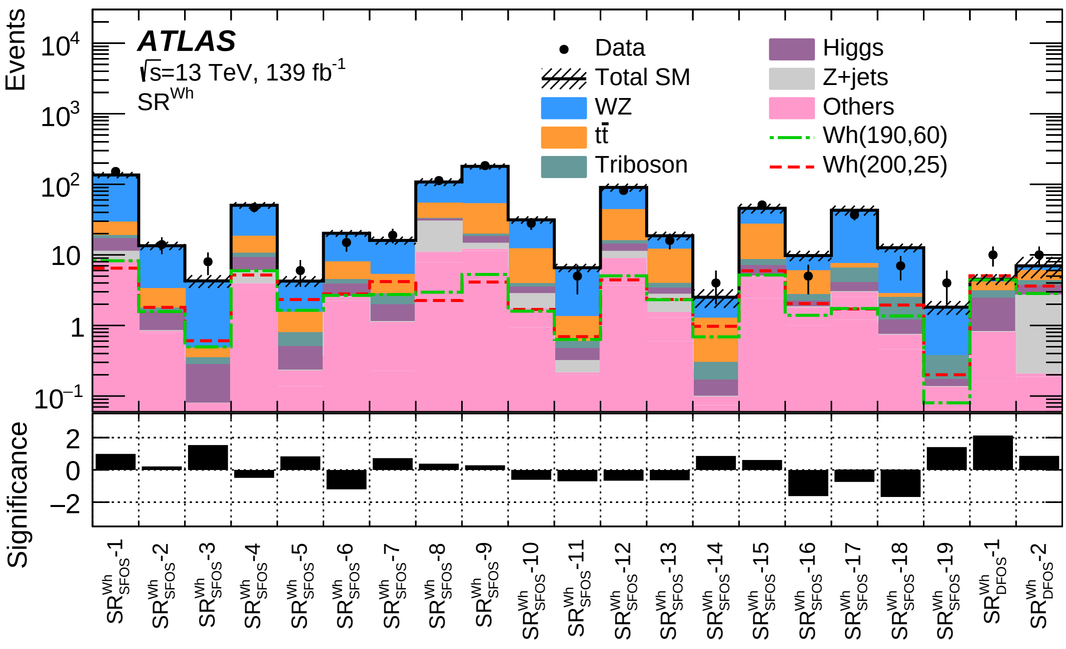

(b) SR^{Wh}

Figure 5.3: Data and SM predictions in the SRs targeting (a) the WZ-3ℓ model and (b) the Wh-3ℓ model. The lower panel shows the significance of data compared to the SM expectations. Statistical and systematic uncertainties (which I have estimated) are shown. [156]

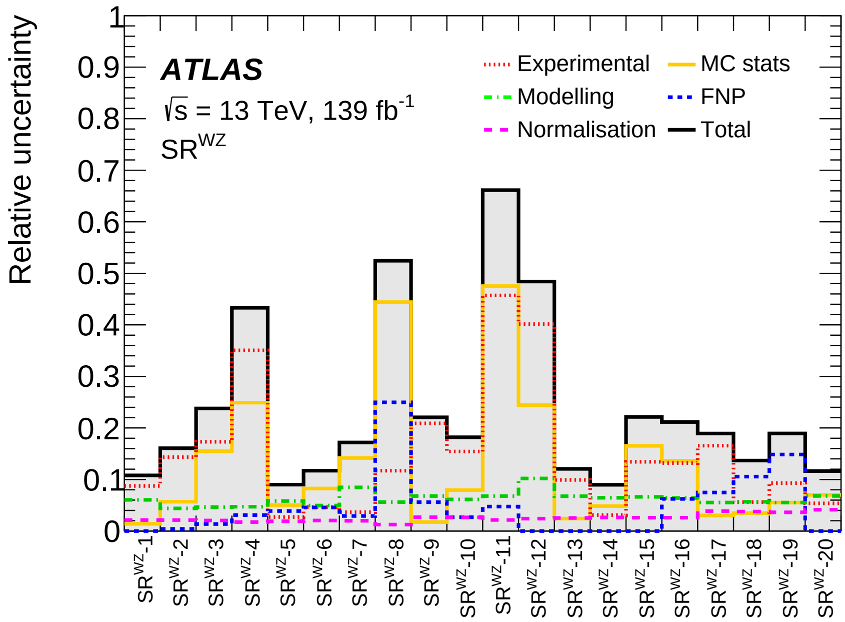

(a) SR^{WZ}

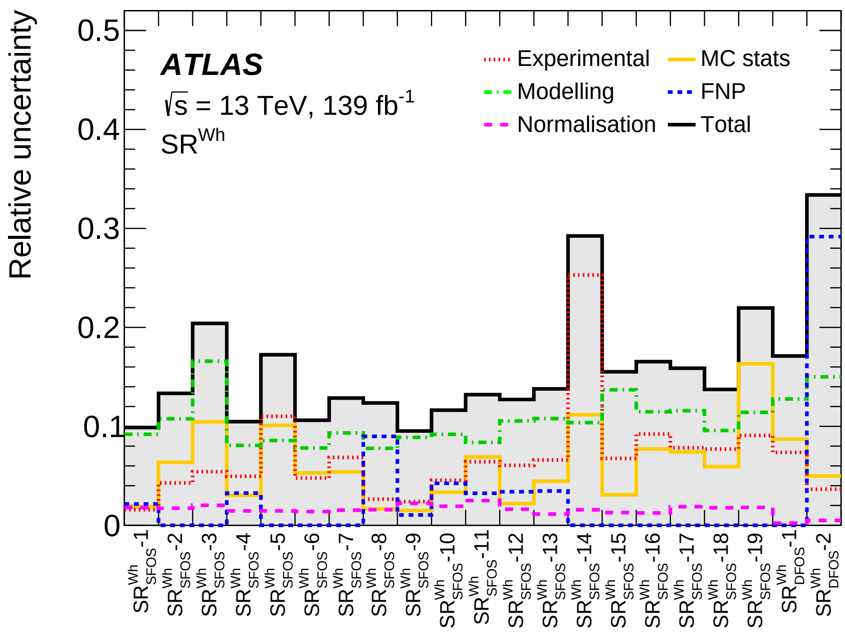

(b) SR^{Wh}

Figure 5.4: Breakdown of the relative uncertainties in the SRs targeting (a) the WZ-3ℓ model and (b) the Wh-3ℓ model for all the sources of the statistical and systematic uncertainties considered. [156]

SRs targeting the WZ-3ℓ model (Figure 5.3a). The fact that the theoretical systematic uncertainties never exceed 10% in any SR, despite the very high impact of the statistical errors (which reaches values up to $\sim 50\%$), is a reflection of the procedure used to estimate the theory systematics. Indeed, estimating them in inclusive SRs demonstrate the fact that they have been successfully de-coupled from the high statical fluctuation, thus validating the approach used. On the other hand, the theoretical sources of uncertainties are dominant in the SRs of the Wh-3ℓ model, except for $\mathrm{SR}^{Wh}_{\mathrm{DFOS}}$, in which the FNP background from Z+jets dominate and consequently its uncertainties are the most significant. This is due to the relatively greater contribution in these regions of events with FNP leptons. Therefore, having a precise estimate of the uncertainties on the $t\bar{t}$ process (Table 5.15) in these regions has been found to be especially important for the overall determination of the total SM background.

5.5.2 Model-independent fit results

A model-independent fit has been performed in dedicated discovery regions driven by the search for the WZ-3ℓ and Wh-3ℓ models. These have been defined by merging some of the bins of the SRs of the 3ℓ-onShell analysis, as shown in Table 5.17. This exploits the fact that bins at high $E_{\mathrm{T}}^{\mathrm{miss}}$ values have higher sensitivity for progressively higher Δm_{Sig}. Hence, merging these together makes the regions sensitive simultaneously to different Δm_{Sig} values.

Table 5.17: Summary of the selection criteria for the inclusive SRs: incSR^{WZ}, $\mathrm{incSR}^{Wh}_{\mathrm{SFOS}}$ and $\mathrm{incSR}^{Wh}_{\mathrm{DFOS}}$. The final selections are obtained by merging the bins of SR^{WZ}, $\mathrm{SR}^{Wh}_{\mathrm{SFOS}}$ and $\mathrm{SR}^{Wh}_{\mathrm{DFOS}}$(Tables 5.5-5.7).

Selection requirements for the inclusive SRs for the discovery fit		
incSR^{WZ} ($m_{\ell\ell}^{\mathrm{SFOS}} \in [75, 105]$ GeV)		
m_{T} [GeV]	$n_{\mathrm{jets}} = 0$	$n_{\mathrm{jets}} \geq 1$
	$E_{\mathrm{T}}^{\mathrm{miss}}$ [GeV]	
$[100, 160]$	incSR^{WZ}-1: $[100, 200]$ incSR^{WZ}-2: > 200	incSR^{WZ}-3: $[150, 250]$ incSR^{WZ}-4: > 250
≥ 160	incSR^{WZ}-5: > 200	incSR^{WZ}-6: > 200
$\mathrm{incSR}^{Wh}_{\mathrm{SFOS}}$ ($m_{\ell\ell}^{\mathrm{SFOS}} < 75$ GeV)		
m_{T} [GeV]	$n_{\mathrm{jets}} = 0$	$n_{\mathrm{jets}} \geq 1$
	$E_{\mathrm{T}}^{\mathrm{miss}}$ [GeV]	
$[0, 100]$	$\mathrm{incSR}^{Wh}_{\mathrm{SFOS}}$-7: > 50	-
$[100, 160]$	$\mathrm{incSR}^{Wh}_{\mathrm{SFOS}}$-8: > 50	$\mathrm{incSR}^{Wh}_{\mathrm{SFOS}}$-9: > 75
≥ 160	$\mathrm{incSR}^{Wh}_{\mathrm{SFOS}}$-10: > 50	$\mathrm{incSR}^{Wh}_{\mathrm{SFOS}}$-11: > 75
$\mathrm{incSR}^{Wh}_{\mathrm{DFOS}}$		
$\mathrm{incSR}^{Wh}_{\mathrm{DFOS}}$-12: $n_{\mathrm{jets}} \in [0, 2]$, $\Delta R_{\mathrm{OS,near}} < 1.2$, $p_{\mathrm{T}}^{\ell_3} \geq 20$ GeV		

Upper limits at 95% CL on the visible cross-section for BSM physics signals have been computed separately for every inclusive SR and are reported in Table 5.18.

The observed data have been once again found to be compatible with the SM prediction in every discovery SR. This is confirmed by the computed discovery p-values, giving a discrepancy with the background predictions of at most 1.48σ (in incSR^{WZ}-6 and $\mathrm{incSR}^{Wh}_{\mathrm{DFOS}}$-12).

Table 5.18: Results of the model-independent fit in the inclusive SRs. The number of observed and expected yields, N_{Obs} and N_{Exp}, are obtained from a background-only fit in the same regions. Upper limits at 95% CL on the visible signal cross-section, σ^{95}_{Vis}, and the corresponding observed and expected number of signal events, S^{95}_{Obs} and S^{95}_{Exp} are shown as well as the CL_B of the discovery fit and the corresponding p-value (p_B for no signal), which is also reported as the number of σ deviations, Z, from the background expectation. As only one-sided p-values are considered, those corresponding to $CL_B < 0.50$ ($p_B > 50\%$) are manually set to $p_B = 0.50$ ($Z = 0.00$). [156]

Region	N_{Obs}	N_{Exp}	σ^{95}_{Vis} [fb]	S^{95}_{Obs}	S^{95}_{Exp}	CL_B	$p_B(s=0)$ (Z)
incSR^{WZ}-1	34	38 ± 5	0.10	14	16^{+7}_{-4}	0.32	0.50 (0.00)
incSR^{WZ}-2	2	1.2 ± 0.5	0.04	5.0	$4.0^{+1.6}_{-0.7}$	0.76	0.23 (0.73)
incSR^{WZ}-3	4	6.5 ± 1.1	0.03	4.8	$6.5^{+2.6}_{-1.8}$	0.19	0.50 (0.00)
incSR^{WZ}-4	25	31 ± 6	0.09	12	15^{+6}_{-4}	0.25	0.50 (0.00)
incSR^{WZ}-5	1	5.2 ± 1.1	0.03	3.9	$5.8^{+2.2}_{-1.4}$	0.03	0.50 (0.00)
incSR^{WZ}-6	23	16.4 ± 1.4	0.12	17.0	$10.3^{+3.9}_{-3.0}$	0.93	0.07 (1.48)
incSR$^{Wh}_{\text{SFOS}}$-7	174	150 ± 14	0.41	58	38^{+15}_{-11}	0.90	0.10 (1.27)
incSR$^{Wh}_{\text{SFOS}}$-8	53	55 ± 5	0.12	17	18^{+7}_{-5}	0.42	0.50 (0.00)
incSR$^{Wh}_{\text{SFOS}}$-9	34	36 ± 4	0.10	14	15^{+6}_{-4}	0.40	0.50 (0.00)
incSR$^{Wh}_{\text{SFOS}}$-10	56	55 ± 7	0.16	22	21^{+8}_{-6}	0.55	0.41 (0.22)
incSR$^{Wh}_{\text{SFOS}}$-11	41	45 ± 6	0.11	16	18^{+7}_{-5}	0.34	0.50 (0.00)
incSR$^{Wh}_{\text{DFOS}}$-12	18	11.5 ± 4.1	0.12	17.0	$10.5^{+4.2}_{-2.7}$	0.92	0.07 (1.48)

5.5.3 Model-dependent fit results

Given the absence of any significant discrepancy between data and expectations in any of the 3ℓ-onShell SRs after the background-only fit, is is possible to interpret the results by setting 95% exclusion limits on the masses of the charginos and neutralinos considered in the WZ-3ℓ and Wh-3ℓ models. This was achieved by performing an exclusion fit (see Section 4.5.1) separately on the WZ-3ℓ and Wh-3ℓ SRs.

The stability of the exclusion fits across the two signal grids is assessed by checking the observed value of the pulls for every NP of the fit. The results of the pulls for the WZ-3ℓ model are shown in Figure 5.5 whilst a description of all the NPs is summarised in Table 5.19. The fact that no significant pulls are observed, along with the absence of any under-constrained systematics, is a further confirmation of the agreement between data and SM prediction. It also demonstrates the validity of the followed background estimation procedure, especially for what concerns the precise determination of the different systematic uncertainty sources.

Table 5.19: Description of the set of NPs constrained by the fit.

NP name	Description
`staterror_*`	Statistical error in each region
`sys_FFstat_*`	Propagated statistical errors on the computation of the FFs (Section 5.3.2).
`sys_FakeClosure_*`	Systematic errors on the FNP background computed from the closure test (Section 5.3.2).
`sys_Theory_*`	Theoretical systematic errors on MC processes (Section 5.4.2).
`sys_xSec_*_flat`	Flat cross-section uncertainties on MC processes (Table 5.16).
`SigXsec_*`	Theoretical uncertainty on the signal cross-sections.
`JET_*,syst_{jes,jvt,eta,PU,FT,flav}*`	Experimental systematic errors concerning jets.
`Muon_*`	Experimental systematic errors concerning muons.
`syst_{elec}*, EG_*`	Experimental systematic errors concerning electrons.
`MET_*`	Experimental systematic errors concerning $E_{\text{T}}^{\text{miss}}$.
`lumi`	Experimental systematic errors concerning luminosity.

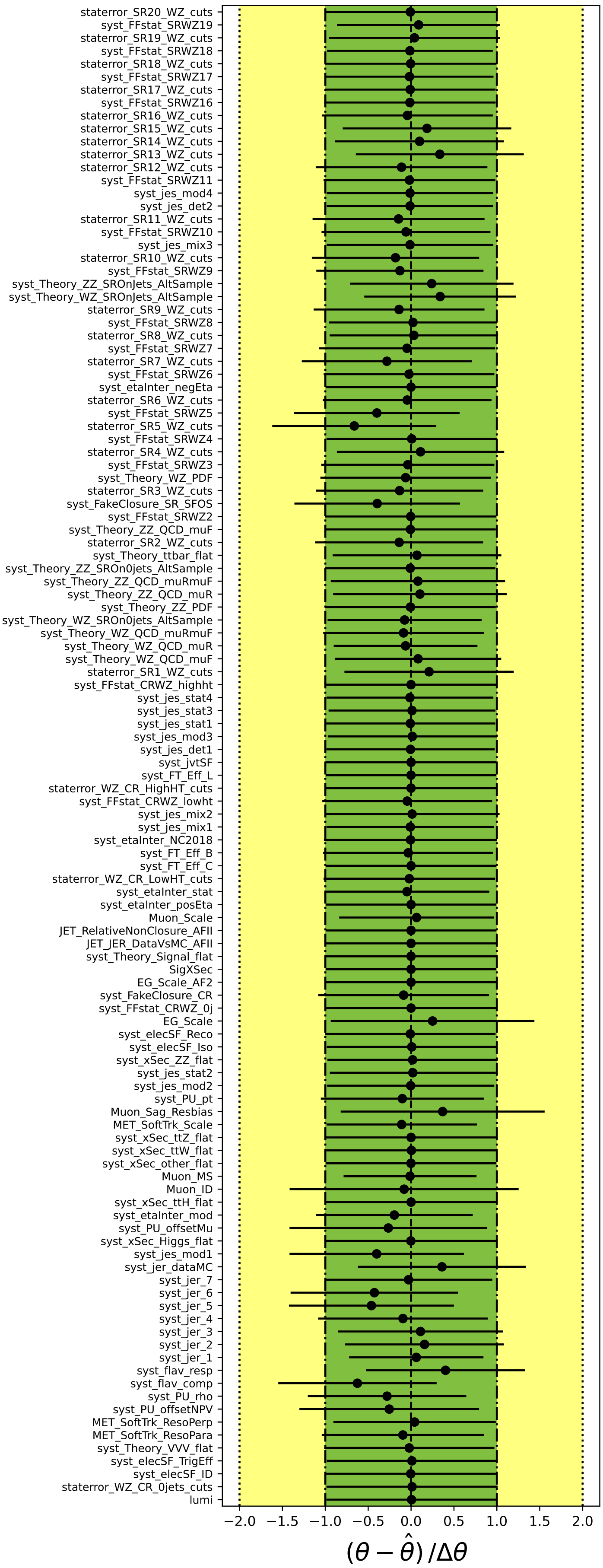

Figure 5.5: Pulls for every NP obtained by performing an exclusion fit in the WZ (600,300) mass point of the WZ-3ℓ signal grid. A description of each of the shown NPs is reported in Table 5.19.

The observed and expected 95% CL exclusion limits for the two models are shown in Figures 5.6 and 5.7.

Regarding the WZ-3ℓ model, the results have been reported in the area of Figure 5.6 with $\Delta m_{\text{Sig}} > m_{\text{Z}}$. The limits for $\Delta m_{\text{Sig}} < m_{\text{Z}}$ (the off-shell region for WZ-mediated models) are taken from the combination (see Chapter 6) with two other analyses, referred to as the 3ℓ-offShell [156] and the "Compressed" [158] searches. More details about these analyses are given in Section 6.1. The obtained results and the sensitivity of the search in the WZ-mediated scenarios are greatly improved compared to the previous equivalent ATLAS search which uses the Run 1, 8 TeV dataset [58]. In particular, in the context of the WZ-3ℓ model, $m_{\tilde{\chi}_1^\pm,\tilde{\chi}_2^0}$ are excluded up to 640 GeV for massless $\tilde{\chi}_1^0$, and up to 300 GeV for $\Delta m_{\text{Sig}} \simeq m_{\text{Z}}$ (Figure 5.6).

For the Wh-3ℓ exclusion limit, reported in Figure 5.7, since most of the sensitivity is driven by the DFOS SRs, the mild 2σ excess found in $\text{SR}^{Wh}_{\text{DFOS}}$-1 causes the observed limit to be less stringent than the expected limit. However, the limits have been found to be compatible with each other within 2σ. In this analysis, the sensitivity for the Wh-3ℓ model is significantly improved compared to the previous ATLAS obtained with the Run 1 dataset [58]. In particular, $m_{\tilde{\chi}_1^\pm,\tilde{\chi}_2^0}$ are excluded up to 190 GeV for massless $\tilde{\chi}_1^0$.

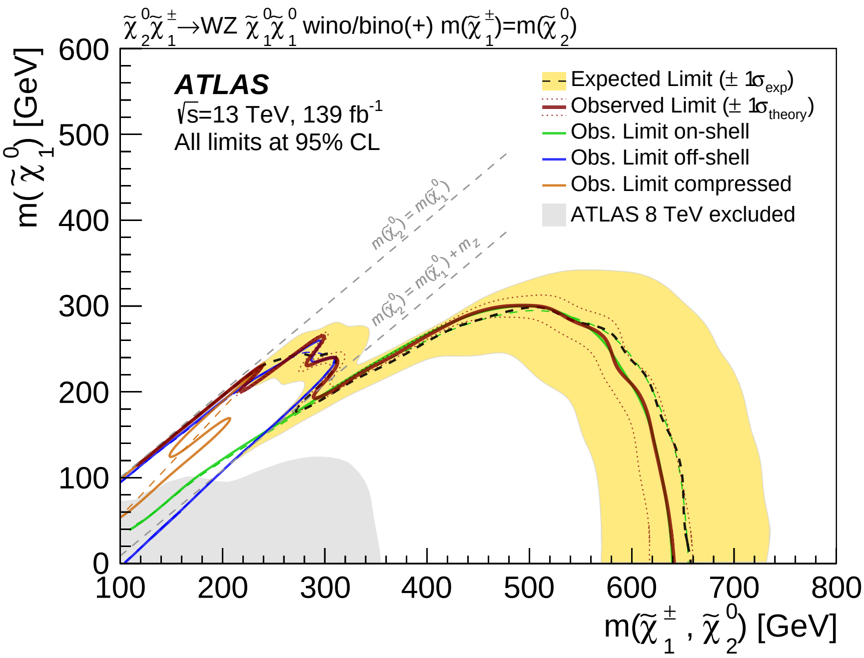

Figure 5.6: Observed (red solid line) and expected (dashed black line) exclusion limits at 95% CL on $m_{\tilde{\chi}_1^\pm,\tilde{\chi}_2^0}$ and $m_{\tilde{\chi}_1^0}$ for the WZ-mediated $\tilde{\chi}_1^\pm\ \tilde{\chi}_2^0$ production models in three-leptons and $E_{\text{T}}^{\text{miss}}$ final states [156]. The yellow band represents $\pm 1\sigma$ total uncertainty on the expected result, whereas the dotted red lines represent $\pm 1\sigma$ on the signal cross-section. The observed limit of the 3ℓ-onShell search (solid green line) is overlayed with that of the 3ℓ-offShell search [156] (solid blue line) and the "Compressed" search [158] (solid orange line). The final exclusion limit is given by the combination of the three analyses. The grey area represents the exclusion limits of the previous ATLAS searches in the same models using the 8 TeV 20.3 fb^{-1} dataset [58].

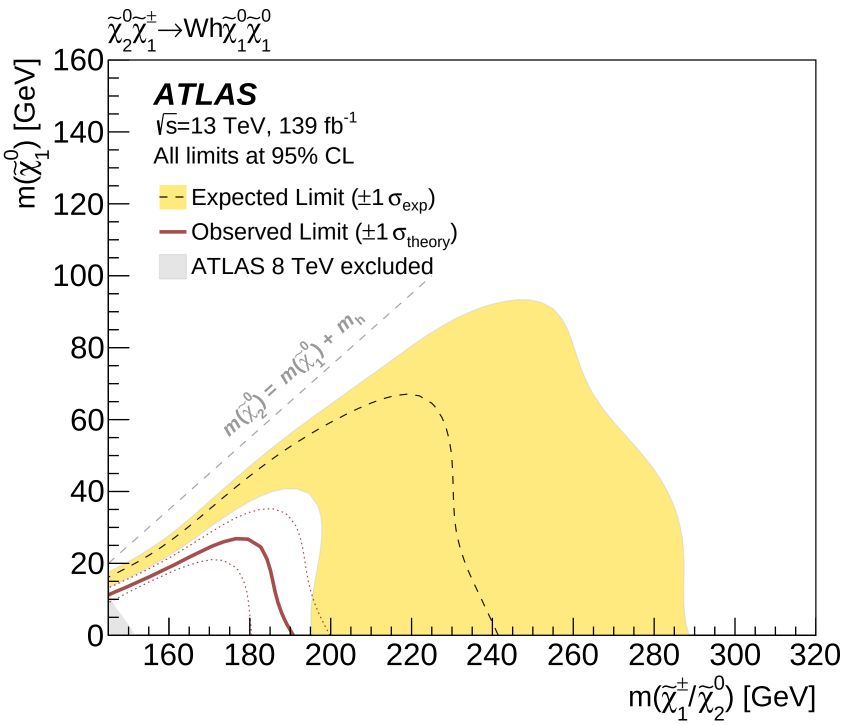

Figure 5.7: Observed (red solid line) and expected (dashed black line) exclusion limits at 95% CL on $m_{\tilde{\chi}_1^\pm,\tilde{\chi}_2^0}$ and $m_{\tilde{\chi}_1^0}$ for the Wh-3ℓ model [156]. The yellow band represents $\pm 1\sigma$ total uncertainty on the expected result, whereas the dotted red lines represent $\pm 1\sigma$ on the signal cross-section. The grey area represents the exclusion limits of the previous ATLAS search in the same model using the 8 TeV 20.3 fb^{-1} dataset [58].

Outlook of the 3ℓ-onShell analysis

The results of the exclusion limits for the search in both the WZ-3ℓ and Wh-3ℓ models show a substantial increase in the sensitivity for these scenario compared to what was achievable using early Run 2 data.

In particular, for the WZ-3ℓ the covered phase-space is further increased to the off-shell region by means of the combination with other searches (Figure 5.6), as done in the context of the paper in which this analysis was published [156]. Further combining these results, with other searches in different final states and targeting different phase-spaces, not only can help to cover a larger excluded area, it can also allow to exclude mass points which it not possible to exclude through the individual searches. An overview about such task, which I have also undertaken over the course of my PhD, is given Chapter 6.

The area excluded by the Wh-3ℓ search (Figure 5.7) is also covered by the Wh-SS analysis (Figure 4.28). The statistical combination of these two searches, which at the time of writing is ongoing, can still provide additional information by improving the level of the exclusion (i. e. smaller CL_S values) of the relevant sparticles masses. This can help to set more stringent bounds on the parameters of mSUGRA and other SUSY models.

Statistical combination of Run 2 $\tilde{\chi}_1^{\pm}\,\tilde{\chi}_2^0$ searches

6

At the time of writing, the ATLAS Collaboration has produced many analyses using the full Run 2 dataset and targeting SUSY simplified models, including the Wh-SS (Chapter 4) and the 3ℓ-onShell (Chapter 5) analyses. To date, no significant deviation from the SM predictions has been discovered for any of these searches. Therefore, given that these analyses typically show unique sensitivities to the targeted models, different constraints on the sparticle mass values are extracted. Exploiting the fact that some of these analyses target the same SUSY production mechanism but with different final states, a statistical combination of their results is possible. Such combination provides a way to extend the constraints on the explored SUSY parameters and, particularly, on the bounds of the sparticles masses.

This Chapter presents a description of the effort within the ATLAS Collaboration to statistically combine the results of analyses targeting the EWK production of $\tilde{\chi}_1^{\pm}\,\tilde{\chi}_2^0$ with R-Parity-conserving decays. The main focus is given to searches in simplified models with intermediate states with a W and a Z boson. Amongst the analyses taken into account is the search targeting the WZ-3ℓ model, described in Chapter 5, which in this Chapter will be just referred to as the 3ℓ-onShell analysis. The combination of results from searches exploring $\tilde{\chi}_1^{\pm}\tilde{\chi}_2^0 \to Wh\tilde{\chi}_1^0\tilde{\chi}_1^0$ decays (*Wh combination*), which include the Wh-SS (Chapter 4) and the Wh-3ℓ (Chapter 5) searches, is ongoing and will not be discussed in this Chapter.

The EWK SUSY combination is a task that I have undertaken in the final eighteen months of my PhD. I have been personally in charge of virtually all the aspects of the combination of $\tilde{\chi}_1^{\pm}\tilde{\chi}_2^0 \to WZ\tilde{\chi}_1^0\tilde{\chi}_1^0$ models. This effort will be henceforth referred to as *WZ combination*. Unless specifically stated, all the results presented in this Chapter have been produced by me.

6.1 Analyses included in the WZ combination

The WZ combination takes into account the results of five different searches. As stated earlier, these searches all target the same SUSY simplified model, namely $\tilde{\chi}_1^{\pm}\,\tilde{\chi}_2^0$ with R-Parity-conserving decays to $WZ\tilde{\chi}_1^0\tilde{\chi}_1^0$ with 100% BR. Each analysis targets different decay modes of the W and Z bosons leading to different final states, notably with different lepton multiplicity. The five input analyses for the WZ combination are:

- *3ℓ-onShell analysis*, to which I have contributed and whose details have been reported in Chapter 5;

- *3ℓ-offShell analysis*, considering an analogous model with respect to that of the 3ℓ-onShell analysis but with off-shell W and Z boson, leading to a final state with three "soft" leptons, i. e. a "compressed" scenario (with $\Delta m_{\text{Sig}} < m_Z$); this analysis has been published together with the 3ℓ-onShell search in the paper in Reference [156];

- *Compressed analysis* [158], which, as the name suggests, also targets a compressed scenario but with two opposite sign leptons in the final state from the Z decay whilst the W decays hadronically;

- *$2\ell 2j$ analysis* [159], targeting a similar model than that of the compressed analysis but also considering on-shell W and Z bosons;

- *AllHad analysis* [55], in which the W and Z bosons are assumed to decay only hadronically leading to a final state with light-jets and/or b-jets and without any lepton.

The diagrams representing the SUSY production models of each of the five analyses are shown in Figure 6.1.

The 95% CL exclusion limits obtained in each of these searches are reported in Figure 6.2.

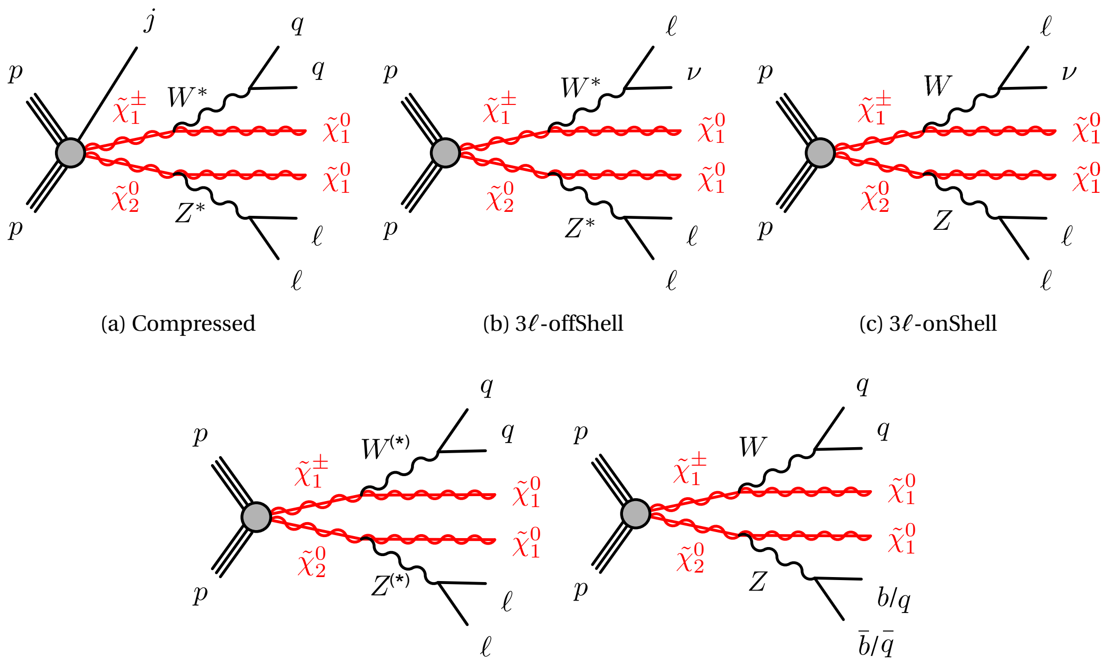

(a) Compressed (b) 3ℓ-offShell (c) 3ℓ-onShell

(d) $2\ell 2j$ (e) AllHad

Figure 6.1: Feynman diagrams representing the simplified models considered in the WZ combination.

These results show how unique the sensitivity for each targeted model is. Each of these five searches excludes a different portion of the relevant sparticle mass plane. Only in some cases, e. g. between the 3ℓ-offShell and Compressed analyses, or between the 3ℓ-onShell and

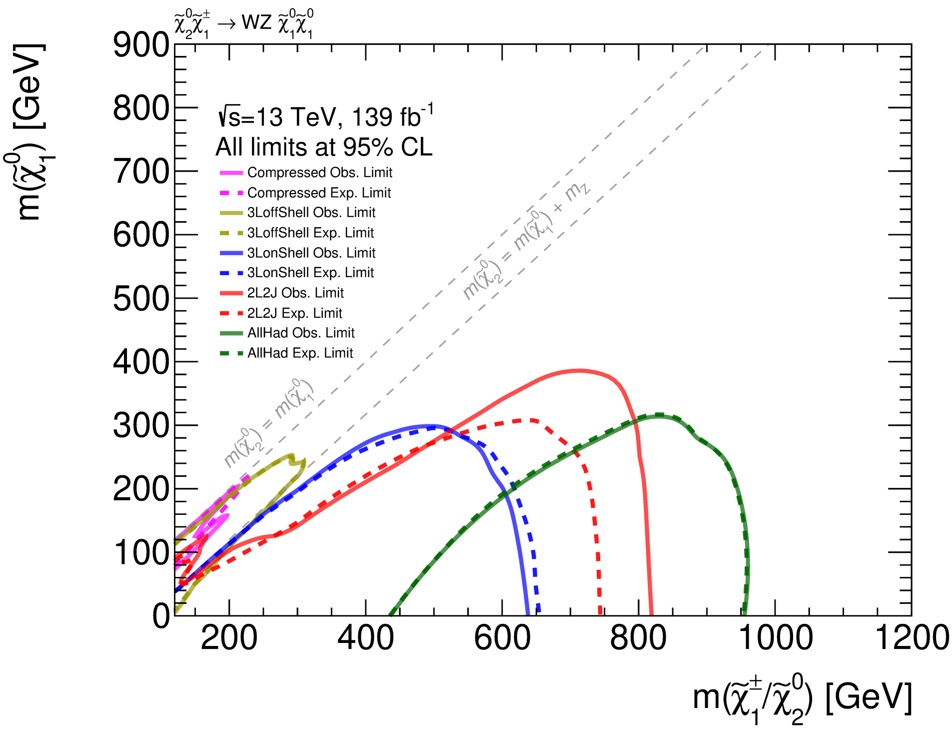

(a)

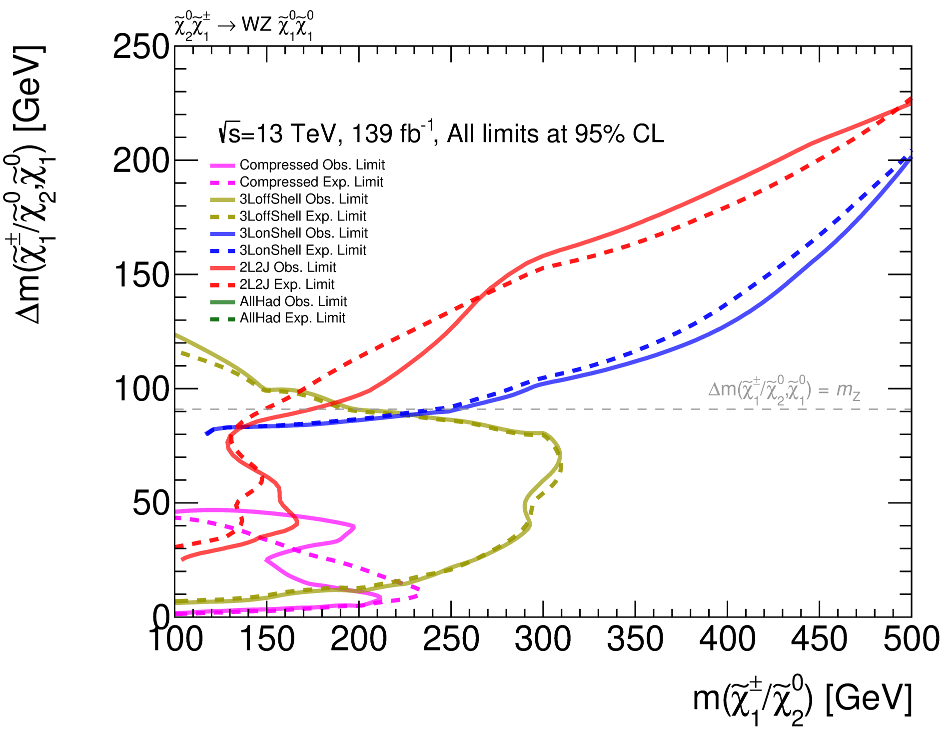

(b)

Figure 6.2: Observed (solid lines) and expected (dashed lines) exclusion limits at 95% CL on $m_{\tilde{\chi}_1^\pm,\tilde{\chi}_2^0}$ and $m_{\tilde{\chi}_1^0}$ for each model of the WZ combination. Exclusion limits are shown in (a) the $m_{\tilde{\chi}_1^\pm,\tilde{\chi}_2^0}$-vs-$m_{\tilde{\chi}_1^0}$ plane and (b) the Δm_{Sig}-vs-$m_{\tilde{\chi}_1^0}$ plane.

$2\ell 2j$ analyses, these searches share a common part of the excluded mass ranges. The Compressed and 3ℓ-offShell analyses are most sensitive for very small Δm_{Sig} values, given their assumption on the off-shell production of the intermediate W and Z bosons. In this area, the $2\ell 2j$ search also contributes (Figure 6.2b). Moving to progressively grater Δm_{Sig} values, thus allowing on-shell decays of the W and Z bosons, the sensitivity is dominated by the 3ℓ-onShell, $2\ell 2j$ and AllHad analyses, respectively. This is an expected behaviour considering the higher BRs of the hadronic decays of the W and Z bosons compared to their leptonic decays. For higher Δm_{Sig} values, decays to hadrons are preferred leading to a higher sensitivity for the corresponding models. Conversely, moving closer to the kinematic limit for on-shell models ($\Delta m_{\mathrm{Sig}} \lesssim m_Z$), decays to hadrons may not be kinematically allowed, favouring instead decays to lighter particles, such as to electrons or muons.

Together, these searches are able to exclude a portion of the values of the sparticle masses, which is greater than what is possible to exclude by each analysis individually. These exclusion limits can be further expanded by exploiting the common sensitive areas between the analyses and by performing the statistical combination there. This is a result of the fact that in the SRs targeting those areas a larger signal sample is generally expected from the combined effect of "adding" together the signal yields of each relevant model. Concurrently, the corresponding SM background prediction and data observations remain unchanged, leading to a much improved sensitivity. Given that no significant discrepancy exists between SM expectation and data, mass points which were not excluded prior to the combination, and that are sensitive and common to different analyses, can therefore be excluded, i. e. their CL_S value drops below 0.05.

The statistical combination of the Compressed, 3ℓ-offShell and 3ℓ-onShell analyses has already been performed by the ATLAS Collaboration in the context of the publication of Reference [156], as also shown in Figure 5.6. The effort outlined in this Chapter, extends and supersedes those results by means of the inclusion of the $2\ell 2j$ and AllHad searches.

As described previously for the Wh-SS (Section 4.1) and 3ℓ-onShell (Section 5.1) searches, each analysis relies on a discrete signal grid, in which MC signal samples of each mass points are generated depending on the area of the mass plane where most of the sensitivity is expected. For instance, mass points of the off-shell analysis are generally only produced with $\Delta m_{\mathrm{Sig}} < m_Z$. In the most ideal scenario, searches taking part in a statistical combination effort should share the same signal grid, since only combinations of different analyses for the same mass point can be performed. This would allow to evaluate the impact of the combination for every mass point. However, as shown in Figure 6.3, the signal grids used by each analysis do not necessarily overlap.

Although most overlaps between the grids are still present in regions which are generally sensitive to two or more analyses, this precludes the possibility to assess the possible improvements in the exclusion limits given by the combination. Therefore, although it was unnecessary for the individual analyses, MC samples for some new signal mass points had to be generated specifically for the WZ combination. It is the case, for example, of the points of the $2\ell 2j$ and AllHad analyses with $m_{\tilde{\chi}_1^0} = 450$ GeV (Figure 6.3a). These five points are not excluded by any analysis, but, given that their are sensitive to both these searches, being able to perform the combination in them is beneficial in extending the area excluded at 95% CL. More details about the points of the various signal grids that have been taken into account for the WZ combination are given in Section 6.2.1.

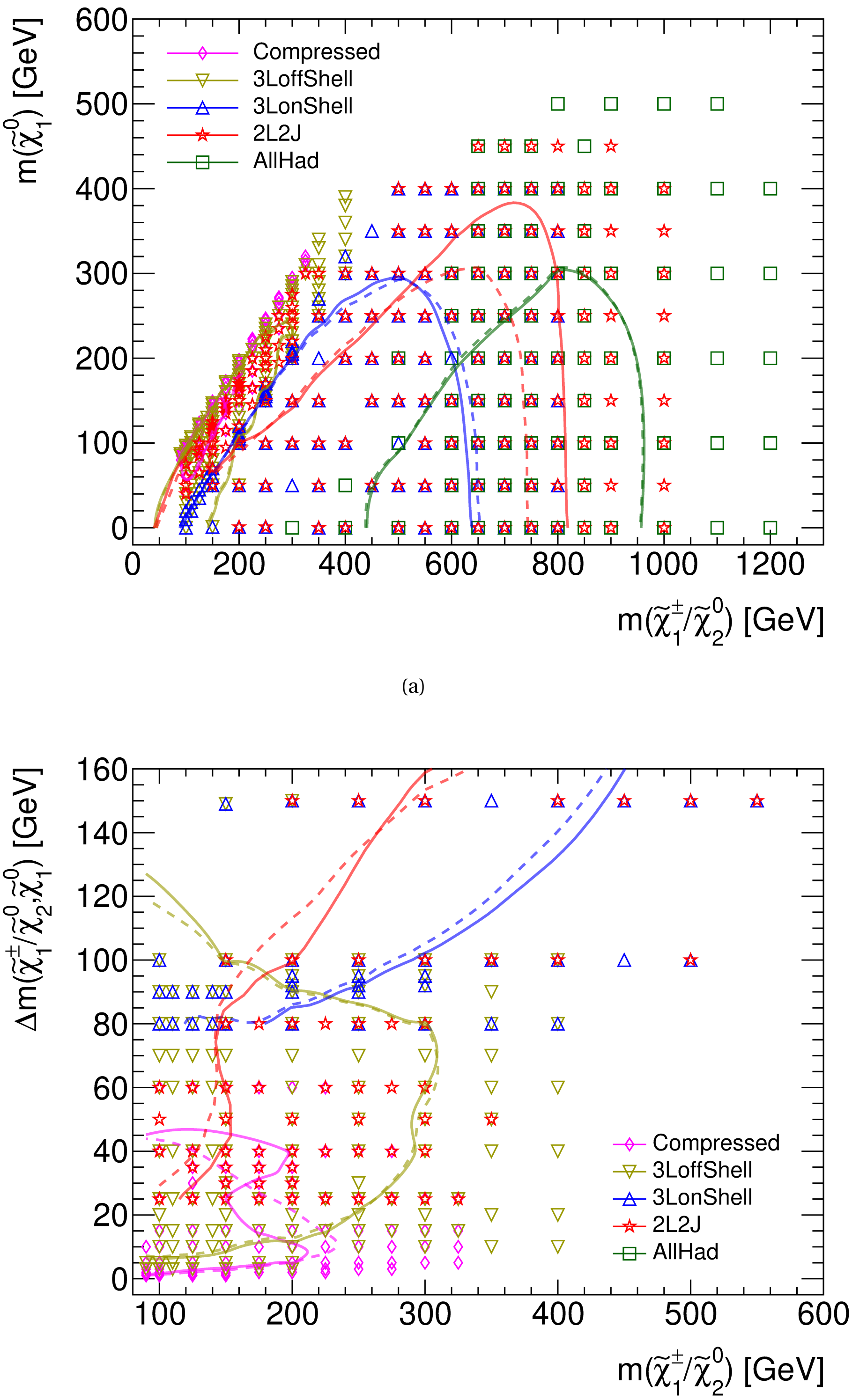

(a)

(b)

Figure 6.3: Signal grids for each analysis included in the WZ combination, overlayed with the corresponding observed (solid lines) and expected (dashed lines) exclusion limits at 95% CL. The signal grids and the exclusion limits are shown (a) in the $m_{\tilde{\chi}_1^\pm,\tilde{\chi}_2^0}$-vs-$m_{\tilde{\chi}_1^0}$ plane and (b) the Δm_{Sig}-vs-$m_{\tilde{\chi}_1^0}$ plane.

6.2 WZ combination strategy

6.2.1 Composition scheme and systematic uncertainties

Considering that not all signal grids are overlapping with each other and that specific analyses have sensitivity in different parts of the parameters space (Figure 6.3), a choice needs to be made about which analysis to include in the WZ combination for each of the available points. Such choice is henceforth referred to as the *composition scheme*.

As stated in Section 6.1 the expected effect of the combination is to improve the degree with which a point is to be considered excluded at 95% CL by virtue of a smaller CL_S value compared to what is obtained in the individual searches. Therefore, an area of the sparticle mass plane to which two or more analyses are sensitive would definitely benefit from the combination. However, if some points in that area are not available for one of the relevant analyses, for those points the combination would not be possible. Then, if those points from the other analyses were to be considered, they would likely have a higher CL_S value compared to that of neighbouring points in which, instead, the combination is possible. This would result in unphysical discontinuities in the CL_S values across the signal grid of the combination, which must be avoided. In this case, a typical choice for the composition scheme is to remove these points, thus avoiding the occurrence of the mentioned discontinuities.

Another motivation for the definition of the composition scheme, based on the availability of the input grids, stems from purely technical reasons. Performing a combination implies repeating the exclusion fit (Section 4.5.1) considering simultaneously the information of several analyses (see Section 6.3). Compared to the individual analyses, this can dramatically increase the CPU time required to compute the results of such fits. Therefore, a combination should be avoided if it is not beneficial beyond any reasonable doubt. This circumstance is met for mass points for which an analysis is sensitive (i. e. expected $CL_S < 0.15$) and another is not (i. e. expected $CL_S \gg 0.15$). Combining these two analyses would not necessarily result in the minimum possible CL_S value but it can, in fact, lead to values greater than the ones prior to the combination. In these cases, only the analyses which have a good sensitivity are kept whilst others are removed from the combination.

Given these considerations, the grids availabilities and the configurations resulting in the best expected CL_S possible, the chosen composition scheme for the WZ combination is shown in Figure 6.4.

These plots are very similar to those showing the various signal grids and reported in Figure 6.3. However, instead of showing the availabilities of those grids, they show for each mass point the analyses which have been ultimately chosen to take part in the WZ combination, thus defining the composition scheme. Amongst the most notable choices is the non-inclusion of mass points with $m_{\tilde{\chi}_1^\pm,\tilde{\chi}_2^0} \in [800, 1000]$ GeV which belong to the $2\ell 2j$ analysis but not to the AllHad analysis (Figure 6.4a). Indeed, this area is expected to significantly benefit from their combination, so the inclusion of these points would result in unphysical discontinuit-

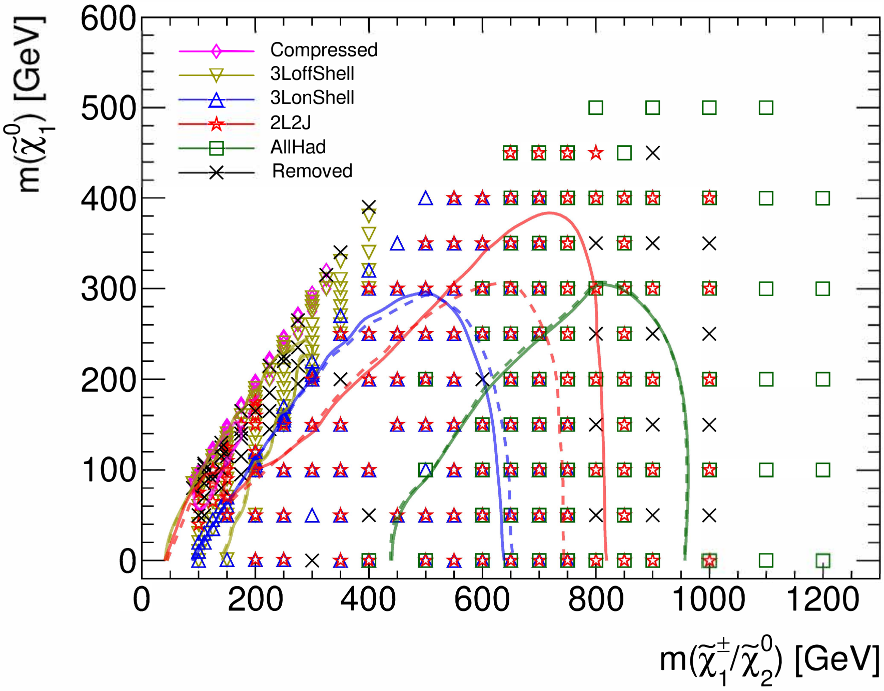

(a)

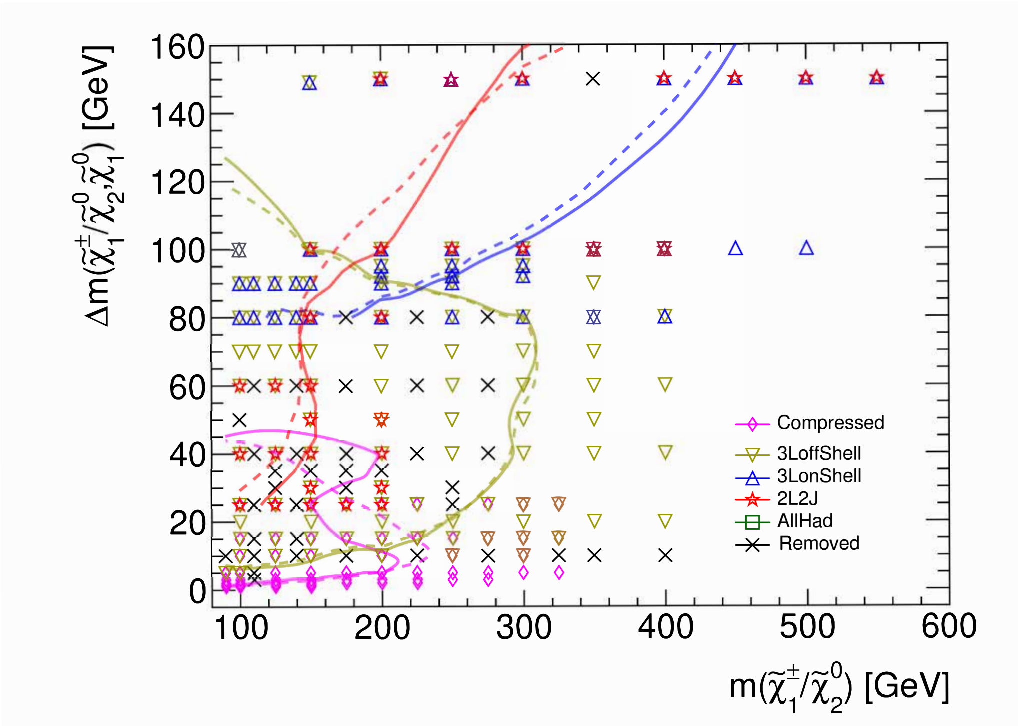

(b)

Figure 6.4: Composition scheme of the WZ combination, overlayed with the corresponding observed (solid lines) and expected (dashed lines) exclusion limits at 95% CL. Signal points and the exclusion limits are shown (a) in the $m_{\tilde{\chi}_1^\pm,\tilde{\chi}_2^0}$-vs-$m_{\tilde{\chi}_1^0}$ plane and (b) in the Δm_{Sig}-vs-$m_{\tilde{\chi}_1^0}$ plane (bottom). For each point only the analyses ultimately taking part in the combination are shown. The points indicated with a "×" symbol are removed from the combination.

ies in the CL_S values. Furthermore, in the area of Figure 6.4b with $m_{\tilde{\chi}_1^\pm,\tilde{\chi}_2^0} > 220$ GeV and $\Delta m_{\mathrm{Sig}} \in [40, 70]$ GeV the sensitivity is entirely dominated by the 3ℓ-offShell analysis. The combination with any other search (i. e. $2\ell 2j$ and Compressed analyses which there present expected $CL_S \gg 0.15$) would unnecessarily increase the computational time required to extract the result, and also would likely not improve from the one of the 3ℓ-offShell analysis. Hence, in this area points not belonging to the 3ℓ-offShell analysis are removed.

In general for the WZ composition scheme, points with $\Delta m_{\mathrm{Sig}} < 10$ GeV are only available for the Compressed analysis; for $\Delta m_{\mathrm{Sig}} \in [10,30]$ GeV, points are taken from the Compressed+3ℓ-offShell combination whereas for $\Delta m_{\mathrm{Sig}} \in [30,70]$ GeV, points are generally taken exclusively from the 3ℓ-offShell analysis and combined with those of the $2\ell 2j$ search for $\Delta m_{\mathrm{Sig}} \in [25,60]$ GeV and $m_{\tilde{\chi}_1^\pm,\tilde{\chi}_2^0} < 200$ GeV. For $\Delta m_{\mathrm{Sig}} \in [70,91]$ GeV, the 3ℓ-offShell+3ℓ-onShell combination is considered. In the on-shell region ($\Delta m_{\mathrm{Sig}} \geq m_Z$), points are generally combined between the 3ℓ-onShell and $2\ell 2j$ analyses for $m_{\tilde{\chi}_1^\pm,\tilde{\chi}_2^0} < 600$ GeV. The points with $m_{\tilde{\chi}_1^\pm,\tilde{\chi}_2^0} \in [600,800]$ GeV are dominated by the 3ℓ-onShell+$2\ell 2j$+AllHad combination, whereas for $m_{\tilde{\chi}_1^\pm,\tilde{\chi}_2^0} \geq 800$ GeV the $2\ell 2j$+AllHad combination is considered if points are available, otherwise only the AllHad analysis is taken into account. These choices are summarised in Table 6.1.

Table 6.1: General criteria employed to define the composition scheme for the WZ combination

Δm_{Sig} [GeV]	$m_{\tilde{\chi}_1^\pm,\tilde{\chi}_2^0}$ [GeV]	Composition scheme
< 10	-	Compressed
$\in [10,30]$	-	Compressed+3ℓ-offShell
$\in [30,70]$	≤ 200	3ℓ-offShell+$2\ell 2j$
	> 200	3ℓ-offShell
$\in [70, m_Z]$	-	3ℓ-offShell+3ℓ-onShell
$\geq m_Z$	< 600	3ℓ-onShell+$2\ell 2j$
	$\in [600,800]$	3ℓ-onShell+$2\ell 2j$+AllHad
	$\in [800,1000]$	$2\ell 2j$+AllHad
	> 1000	AllHad

6.2.2 Statistical independence of combined analyses

A key point and a prerequisite of the statistical procedure followed in the WZ combination is based on the assumption that all input analyses are statistically independent. This implies that no kinematic overlap must exist between SRs and CRs belonging to different analyses. In this case, the situation explained in Section 6.1 occurs, i. e. the data and SM predictions in these regions remain unchanged, whereas the signal yields of different models add up to increase the overall sensitivity of the combination. On the other hand, should any overlap exist, e. g. a MC event of a SM background process can contribute simultaneously to CRs of different analyses. This necessarily introduces a degree of correlation between the parameters of the exclusion fit, e. g. in the final value of the NFs of certain background, to account for the corresponding data observation. In the worst-case scenario, the contamination of signals from an analysis in a CR of a different search may hamper the overall SM background estimation.

Although the overlaps in a statistical combination can be accounted for by introducing dedicated correlations between the NPs, requiring each analysis to be maximally orthogonal to each other dramatically simplifies the execution of the combined exclusion and, in general, prevents unwanted effects such as the changing of the background prediction for different mass points. Therefore, the orthogonality is here considered a strict requirement.

In the WZ combination the statistical orthogonality is achieved by requiring a lepton multiplicity cut on every CR and SR of each participating analysis. The lepton selection criteria used in this case are reported in Table 6.2.

Table 6.2: Electron and muon selection criteria used to impose the orthogonality between the analyses taking part in the EWK combination.

	Combination electrons	Combination muons
Acceptance	$p_T \geq 4.5$ GeV , $\|\eta\| < 2.47$	$p_T \geq 3$ GeV , $\|\eta\| < 2.7$
Identification WP	`LooseAndBLayer`	`Medium`
Impact parameter	$\|z_0 \cdot \sin(\theta)\| < 0.5\,\text{mm}$	

These criteria represent the loosest requirement amongst the baseline lepton collections used in the input analyses. Leptons satisfying such criteria are counted before they pass the OvR procedure (Section 3.3.3), n_ℓ^{Comb}. Then, for example, in a region with three leptons the orthogonality can be achieved by requiring events to also satisfy $n_\ell^{\text{Comb}} = 3$.

Any residual overlap between the various analyses, arising e. g. from the adoption of different OvR strategies, is evaluated by counting the data selected by the CRs and SRs of each search, as shown in Figure 6.5. This is possible because an event number identifier is assigned to each recorded datum. Hence, counting the data events which pass simultaneously the selections of two regions is a measure of the overlap between them. No overlap in data has been found between any of the regions of the analyses taking part in the WZ combination.

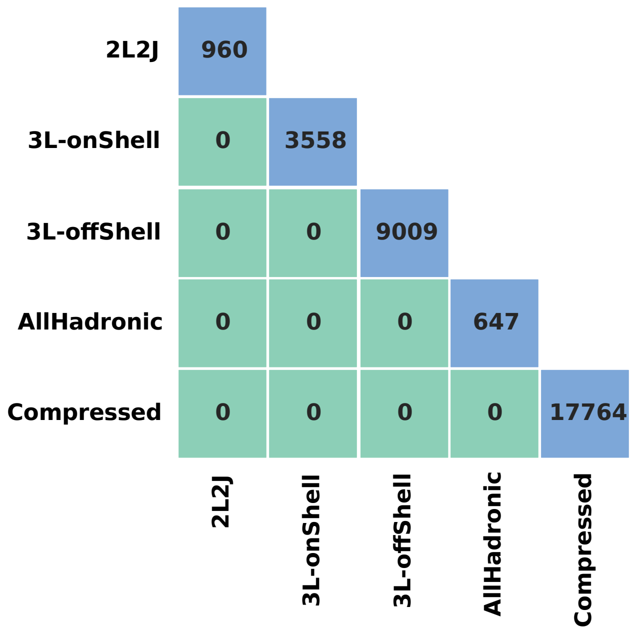

Figure 6.5: The number of overlapping events in data selected by each analysis of the WZ combination.

Overlaps are also checked by considering a sample composed by MC simulations of benchmark signal points of every SUSY model. These studies, which were performed by a collaborator, also highlighted the absence of any overlap regarding the SUSY signal. Therefore, the analyses taking part in the WZ combination are indeed maximally orthogonal with each other.

6.2.3 Systematic uncertainties

Even though the different analyses in the WZ combination are kinematically orthogonal to one another, they still share similar criteria for their object selections and they may rely on the same simulations of SM background processes. For example, the effect of a systematic fluctuation in the CR targeting a specific background process of an analysis can impact similar sources of systematic uncertainties for the same process in certain regions of other analyses. This can be all taken into account in the final exclusion fit of the WZ combination by considering specific correlations between the NPs across the different analyses. Requiring such correlations typically results in the further constraining of relevant systematic uncertainties after the combined exclusion fit compared to what had been obtained in the individual analyses.

Introducing such correlations across different analyses is not straightforward. Pre-fit, only NPs (e. g. theoretical systematics) affecting the same MC samples and the detector-level uncertainties associated with the same type of objects (i. e. with the same object definition criteria) can be considered fully correlated across the various analyses. Only in a few cases do the analyses in the WZ combination share the same object definitions or the same MC background samples. Therefore, it is necessary to consider the corresponding NPs as uncorrelated prior to the fit.

Considering the NPs of different analyses uncorrelated is, in general, a more conservative approach. This happens because, as stated previously, the most noticeable impact expected from such correlations is the further constraining of the systematic uncertainties as a consequence of the combination. Without any correlation, the squared sum of each (statistically independent) source of uncertainty is taken. This conservative approach suits the purpose of the WZ combination and it is thus adopted in what follows.

6.3 Statistical combination: technical procedure

In order to perform a statistical combination of the considered analyses, it is necessary to repeat the exclusion fit allowing it to fit simultaneously the data in all CRs and SRs of each analysis. This task poses some technical challenges mainly related to the need to "extract" the necessary information from the fits performed for each individual analyses and then to "re-use" them for a combined fit.

In general, the first step of statistical analysis procedure followed for SUSY searches (described in Section 4.5.1) is the definition of the *fit configuration*. This includes information about: all the SRs and CRs, the data observations, the yields from every SM background and signal process, and a set of parameters. Amongst these parameters are: any NFs, along with the instructions on which CR and for which processes they are extracted for; the constrained and unconstrained NPs representing the impact of systematic and statistical uncertainties; and the *parameters of interest* for the fit. In an exclusion fit, the only parameter of interest is usually the signal strength, μ_S [160]. The full set of samples, regions and parameters thus defined, along with their interaction in the fit, constitute the basic ingredients to construct the Likelihood (Equation 4.30). In the ROOT-based HistFitter framework used for the statistical interpretation of the SUSY analyses in the ATLAS experiment, the information about such fit configurations is included and saved in objects referred to as *workspaces* [161].

Therefore, in order to perform a statistical combination of N analyses it is necessary to first extract each of the corresponding workspaces, and then to combine them to create a new *combined workspace*. The exclusion fit performed on the latter provides the results of the combination. This workflow is schematically illustrated in Figure 6.6.

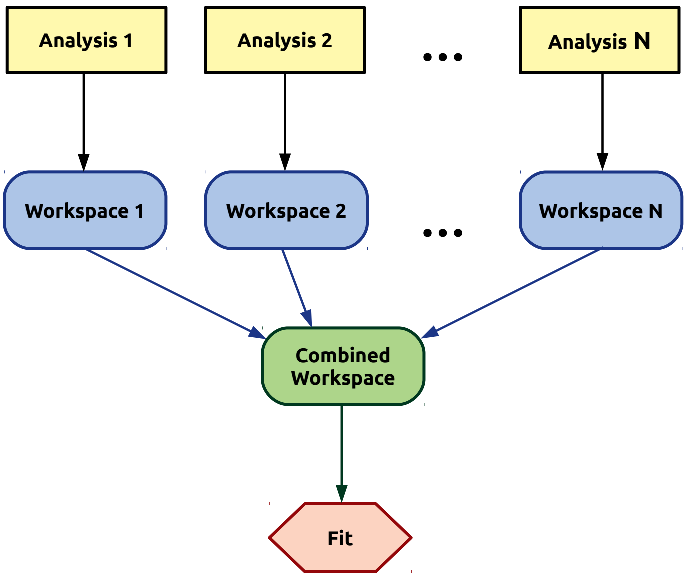

Figure 6.6: Schematic representation of the workflow used to combine SUSY analyses.

A fundamental aspect that differentiates the original workspaces from the combined workspace is that in the latter the exclusion fit is carried out by considering a single μ_S, applied equally to all the SUSY models taken into account. This is justified by the fact that these signals all share the same SUSY production simplified model. Having a single μ_S, applied indiscriminately to all signals in every SR, is what ultimately allows to overall increase the sensitivity for these scenarios and, thus, to extract new bounds on the relevant SUSY mass parameters thanks to the combination.

In the ATLAS experiment the technical procedure to combine and fit workspaces is simplified by using the PyHF framework [162]. Unlike the HistFitter framework, in which the workspace creation is strongly dependent on the specific version of the ROOT toolkit used, PyHF is entirely based on the human-readable text files written in JSON (JavaScript Object Notation) format [163] for reading workspaces and then configuring the fit. The workspaces of the input analyses are, thus, converted to JSON format and then fitted separately through PyHF.

Editing these human-readable text files specifying the fit configurations allows to dramatically simplify the creation of combined workspaces compared to interacting with ROOT-based data formats. Moreover, the input JSON workspaces can be also easily *harmonised*, e. g. to introduce correlations across the different analyses. This is simply done by assigning the same name to the NP that one wishes to correlate. This procedure is also schematically represented in Figure 6.7.

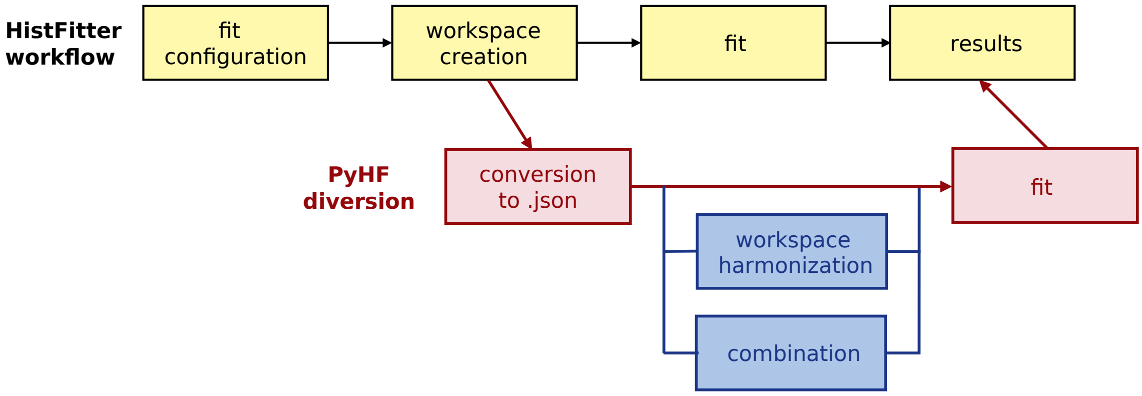

Figure 6.7: Schematic representation of the HistFitter workflow used to extract results of each separate analysis and the interaction with PyHF which enables the combination of workspaces. The diagram is taken from [164].

In the PyHF framework the performance of the fitting procedure is dependent on the implementation of different tensor algebra *back-ends*, among which: JAX [165], PyTorch [166], TensorFlow [167] and NumPy [168]. Moreover, maximisation and minimisation procedures, onto which the fit is based, are implemented in PyHF via the Minuit [169] and SciPy [170] libraries. For the WZ combination the usage of PyHF is validated against the original results of each analysis, obtained with HistFitter. Studies have shown that the results obtained with PyHF are compatible to the original ones, thus justifying the usage of this tool for the combination effort.

6.4 WZ combination results

6.4.1 Fit stability

As the combined fit may introduce additional correlations across the different analyses, other than the intrinsic ones that can be defined a priori, it is necessary to make sure that the combined fit remains stable moving from one mass point to another in the signal grid. This is verified by checking the pull plots (see Section 4.5.1) before and after the combination.

For illustration purposes, the value of the pulls for every NP for the exclusion fit in the WZ (600,300) point performed separately for the 3ℓ-onShell, $2\ell 2j$, and AllHad analyses and their combinations are shown in this Section. The values of the pulls for this point in the 3ℓ-onShell analysis have already been shown in Chapter 5 (Figure 5.5), whilst the pulls for the

$2\ell 2j$ and AllHad analyses for the exclusion fit in the same mass point are shown in Figures 6.8 and 6.9, respectively. The description of each NPs is summarised in Tables 6.3 and 6.4.

Table 6.3: Description of the set of NPs constrained by the fit of the $2\ell 2j$ analysis. Further information can be found in Reference [159].

NP name	Description
`staterror_*`	Statistical error in each region
`fake_wgt`	Systematic uncertainty of the data-driven FNP background.
`diboson_*,ttbar_*,topOther_*,` `Zjets_*,triboson_*,higgs_*`	Theoretical systematic errors on backgroundMC processes.
`C1N2_WZ_*_2L2J_acc`	Theoretical uncertainty on the signal.
`jet_*,jes_*,jer_*,ft_*`	Experimental systematic errors concerning jets.
`muon_*`	Experimental systematic errors concerning muons.
`el_*,eg_*`	Experimental systematic errors concerning electrons.
`met_*`	Experimental systematic errors concerning $E_{\mathrm{T}}^{\mathrm{miss}}$.
`lumi`	Experimental systematic errors concerning luminosity.

Table 6.4: Description of the set of NPs constrained by the fit of the AllHad analysis. Further information can be found in Reference [55].

NP name	Description
`staterror_*`	Statistical error in each region
`diboson_*,ttbar_*,ttbarX_*,` `tX_*,Zjets_*,Wjets_*`	Theoretical systematic errors on backgroundMC processes.
`SigTheory`	Theoretical uncertainty on the signal.
`JET_*,bTag_*`	Experimental systematic errors concerning jets.
`MET_*`	Experimental systematic errors concerning $E_{\mathrm{T}}^{\mathrm{miss}}$.
`pileup*,lumi`	Experimental systematic errors concerning pile-up and luminosity.

The pulls of the individual fits performed separately in each analysis are compatible with zero with no significant over- or under-constraints, which demonstrate that the individual fits are stable. In the $2\ell 2j$ analysis a NP, called `Zjets_alt`, associated with the uncertainties on the SM Z+jets process, has been found to have a larger pull (Figure 6.8). However, this pull does not exceed 2σ from the original expectation and does not negatively impact the overall stability of the fit [159].

Having established the stability of the individual fits, it is necessary to assess whether the combination would introduce unwanted pulls with respect to the original ones, which might make the result unreliable. Given that the fitting procedure implements a computationally iterative approach to search for the extrema [169, 170] and the increased complexity of the combined fit, this situation can occur, for instance, when the fit converges to a local extremum of the Likelihood instead of a global extremum, which would correspond to the wrong CL_S value and, therefore, to an unreliable final result. The values of the pulls after performing the combination are reported in Figures 6.10-6.12.

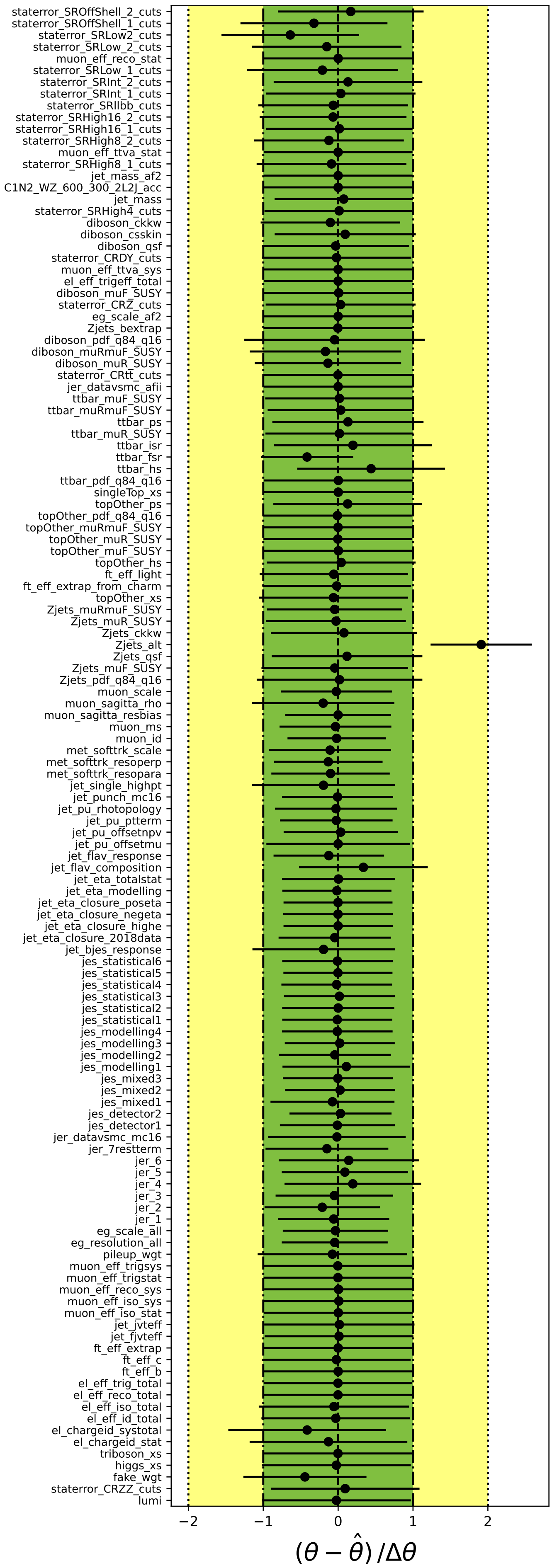

Figure 6.8: Pulls for every NP obtained by carrying out an exclusion fit in the WZ (600,300) point for the $2\ell 2j$ analysis. A description of each of the shown NPs is reported in Table 6.3.

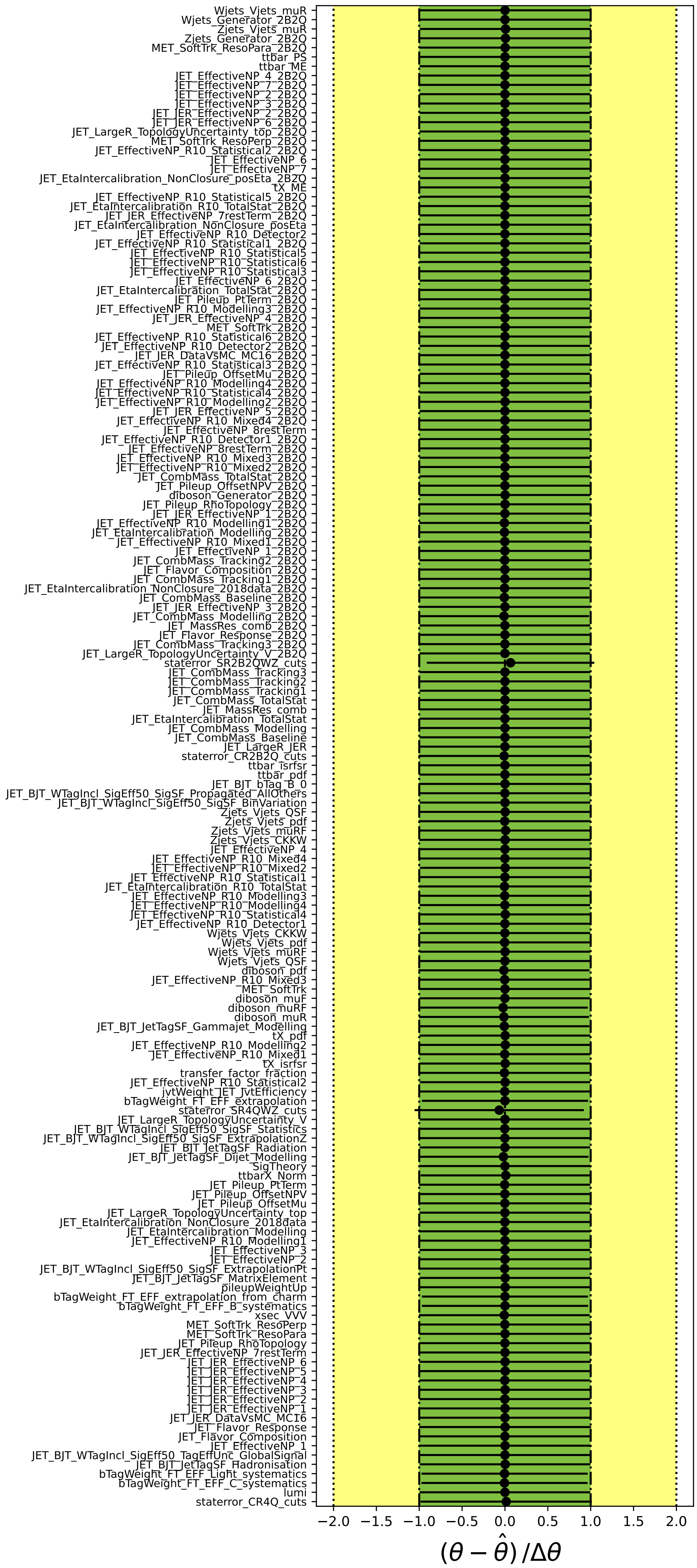

Figure 6.9: Pulls for every NP obtained by carrying out an exclusion fit in the WZ (600,300) point for the AllHad analysis. A description of each of the shown NPs is reported in Table 6.4.

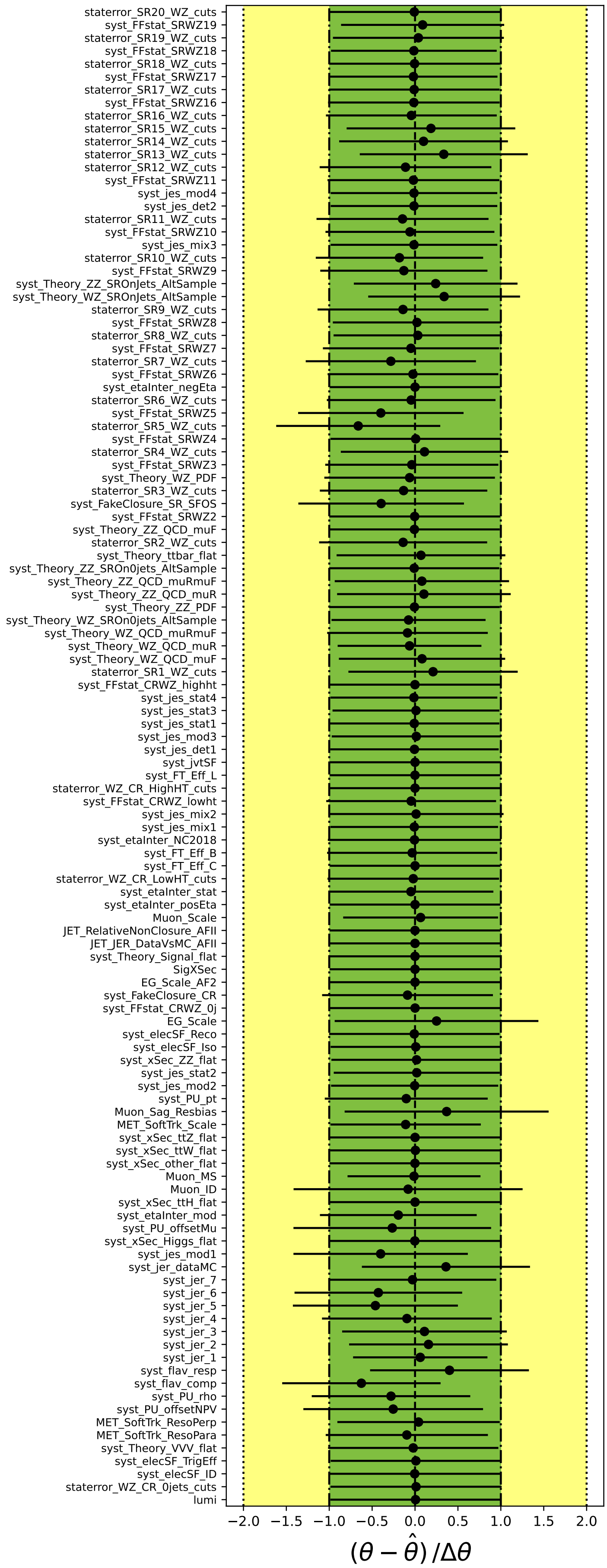

Figure 6.10: Pulls for every NP, originally belonging to the 3ℓ-onShell search, obtained by performing the exclusion fit after the WZ combination in the WZ (600,300) mass point. A description of each of the shown NPs is reported in Table 5.19.

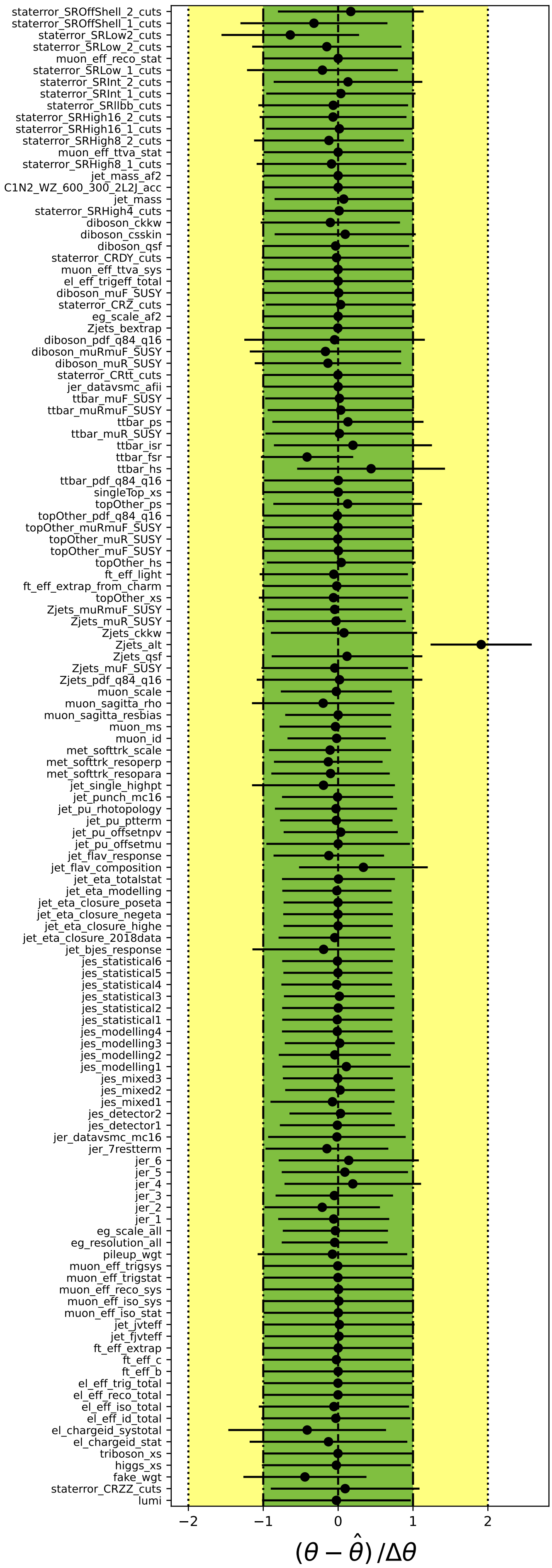

Figure 6.11: Pulls for every NP, originally belonging to the $2\ell 2j$ search, obtained by performing the exclusion fit after the WZ combination in the WZ (600,300) mass point. A description of each of the shown NPs is reported in Table 6.3.

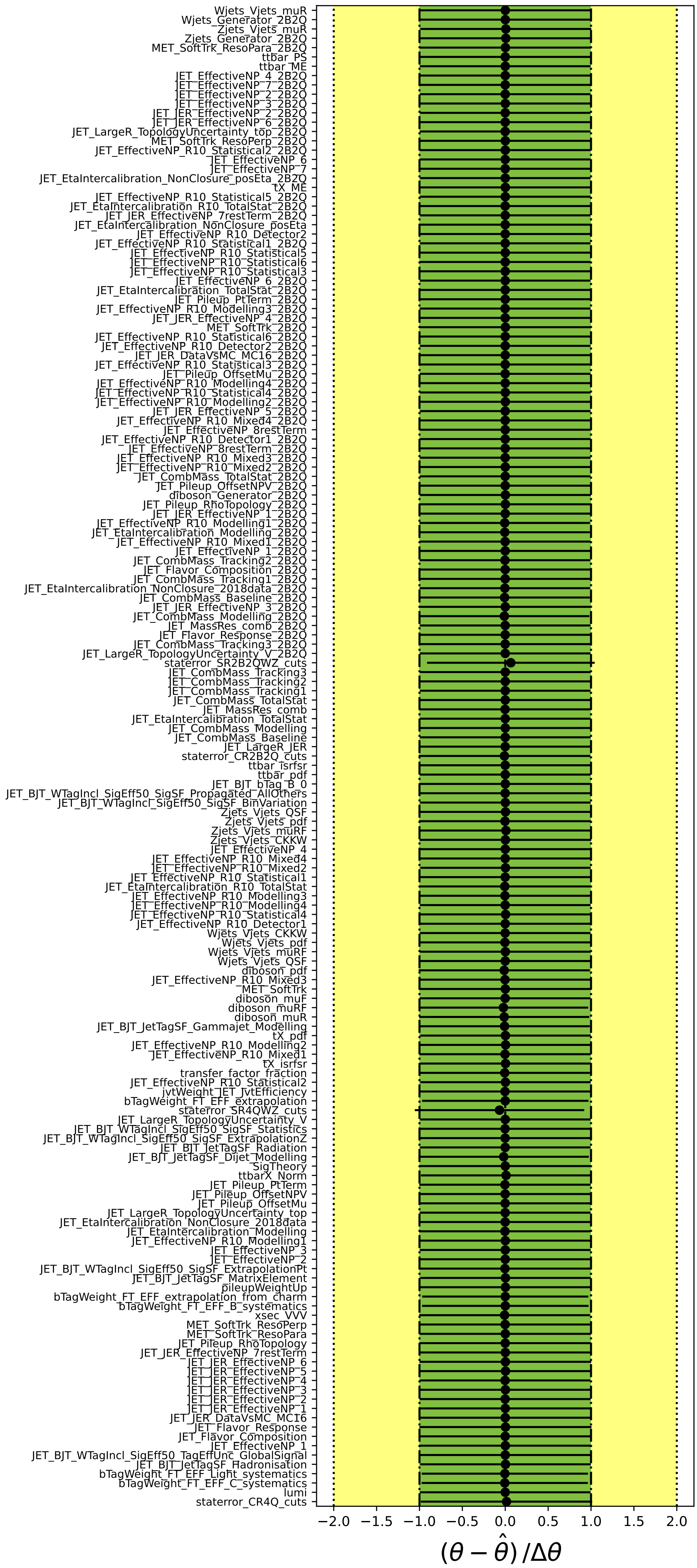

Figure 6.12: Pulls for every NP, originally belonging to the AllHad search, obtained by performing the exclusion fit after the WZ combination in the WZ (600,300) mass point. A description of each of the shown NPs is reported in Table 6.4.

First of all, the complexity of the combined fit is evident by simply considering the sheer number of constrained NPs which are reported in Figures 6.10-6.12. Such situation is exacerbated by the fact that, since no a priori correlation is introduced in these instance, none of the NPs is “shared” between two or more analyses and it is instead applied exclusively to the original search. Therefore, the number of the constrained NPs in the WZ combination is essentially given by the sum of those of the original analyses.

The results of the combination show that all the pulls are again compatible with zero within their respective uncertainties. Since the same situation occurs for all of the other points of the signal grid, regardless of the composition scheme used for them (Section 6.2.1), the combined fit can be considered stable. More importantly, from a one-to-one comparison with the pull values of the individual analyses (Figure 5.5 and 6.10; Figure 6.8 and 6.11; Figure 6.9 and 6.12), it is possible to assess that the change of each pull and its uncertainty after the combination is indeed small. From this it is legitimate to conclude that the combination itself does not introduce significant correlations between the NPs, which would instead appear as a significant shift in the pulls. Once again, this is a desired effect of having required each analysis to be statistically independent through the orthogonality criteria. This confirms the reliability of the WZ combination fits.

6.4.2 WZ combination exclusion limits

This Section illustrates the final results of the WZ combination, having established the composition scheme and the reliability of the results of the fits for every considered mass point.

The procedure used to extract exclusion limits at 95% CL on $m_{\tilde{\chi}_1^\pm,\tilde{\chi}_2^0}$ and $m_{\tilde{\chi}_1^0}$ from the results of the fit in a discrete signal grid relies on interpolating the observed and expected CL_S values in the sparticle mass plane. The algorithm used for this purpose is based on the RBF (Radial Basis Function) interpolation [171], implemented in the `SciPy` library [170]. Having interpolated the mass plane, the expected and observed limits are extracted from the contour of this surface which satisfies $CL_S = 0.05$, i. e. the 95% CL. The same procedure has been also followed to extract the exclusion limits for the Wh-SS (Figure 4.28 in Chapter 4) and 3ℓ-onShell analyses (Figures 5.6-5.7 in Chapter 5). Since the signal grid used for the WZ combination (Figure 6.4) has not been specifically designed for this purpose, but rather is given by the composition of pre-existing signal grids (Figure 6.3), its granularity changes significantly depending on the area of the mass spectrum considered. This introduces inefficiencies in the interpolation algorithm, which thus fails to extract reliable contours. To avoid such inefficiencies, which would instead result in a physically unreliable exclusion limit, in the WZ combination it has been decided to interpolate the $\log_{10}(\Delta m_{\mathrm{Sig}})$-vs-$m_{\tilde{\chi}_1^\pm,\tilde{\chi}_2^0}$ plane, instead. This allows to interpolate a grid in which the points are roughly equally-spaced, thus removing any possible effects due to the inefficiencies of the interpolation algorithm. The exclusion limits are finally obtained by performing a change of coordinates to the Δm_{Sig}-vs-$m_{\tilde{\chi}_1^\pm,\tilde{\chi}_2^0}$ and $m_{\tilde{\chi}_1^0}$-vs-$m_{\tilde{\chi}_1^\pm,\tilde{\chi}_2^0}$ planes, respectively. The obtained result is shown in Figure 6.13.

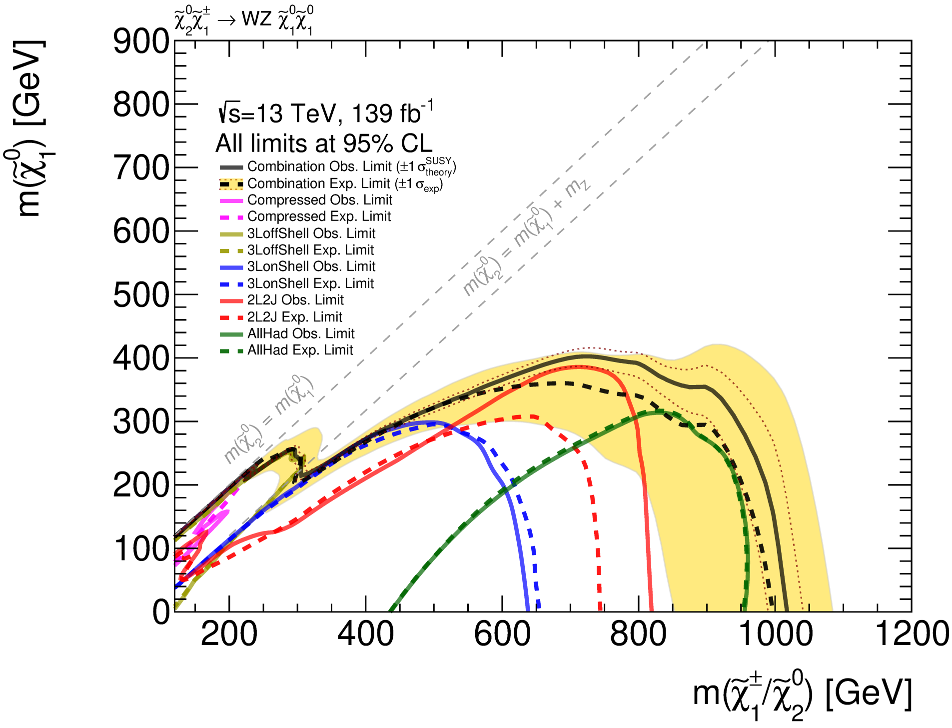

(a)

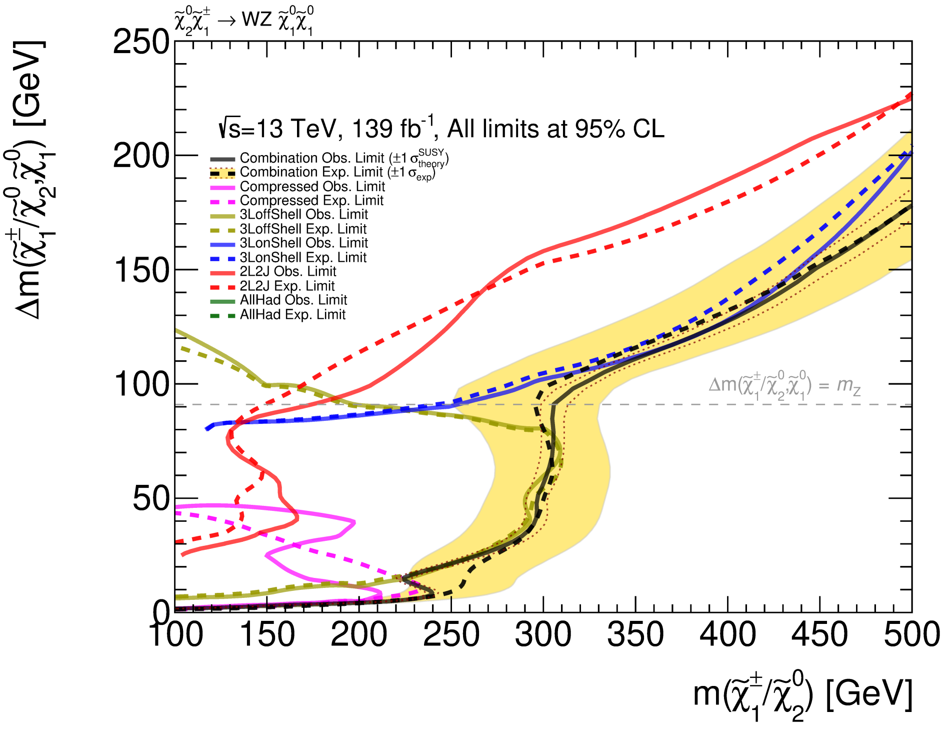

(b)

Figure 6.13: Observed (solid black lines) and expected (dashed black lines) exclusion limits at 95% CL on $m_{\tilde{\chi}_1^\pm,\tilde{\chi}_2^0}$ and $m_{\tilde{\chi}_1^0}$ for the WZ combination. The yellow band represents $\pm1\sigma$ total uncertainty on the expected result, whereas the dotted red lines represent $\pm1\sigma$ on the signal cross-section. The WZ combination exclusion limits are overlayed with those of the input analyses. The exclusion limits are shown (a) in the $m_{\tilde{\chi}_1^\pm,\tilde{\chi}_2^0}$-vs-$m_{\tilde{\chi}_1^0}$ plane and (b) in the Δm_{Sig}-vs-$m_{\tilde{\chi}_1^0}$ plane (bottom).

The results of the WZ combination show that the new exclusion limits fully cover the areas previously excluded by each analysis individually. The off-shell region (Figure 6.13b) is almost entirely dominated by the sensitivity of the Compressed and 3ℓ-offShell analyses. The combination of the results of these two searches, which has been considered for $\Delta m_{\text{Sig}} \in [10, 30]$ GeV, allows to extend the excluded $m_{\tilde{\chi}_1^\pm, \tilde{\chi}_2^0}$ values to about 240 GeV (for $\Delta m_{\text{Sig}} \simeq 10$ GeV). In this area the slight disagreement between the expected and observed line reflects the same behaviour observed in the Compressed search, due to mild discrepancies between data and SM predictions in some of its SRs [158]. The results of the WZ combination in the off-shell region are also consistent with those published in Reference [156] and shown in Figure 5.6. Moreover, the combination between the 3ℓ-offShell and $2\ell 2j$ analyses, considered for $\Delta m_{\text{Sig}} \in [30, 70]$ GeV and $m_{\tilde{\chi}_1^\pm, \tilde{\chi}_2^0} \leq 200$ GeV, allows to further increase the level of the exclusion in that area, due to the reduction of the corresponding CL_S values. Finally, in the boundary between the off- and on-shell region ($\Delta m_{\text{Sig}} = m_Z$), the combination between the 3ℓ-offShell and 3ℓ-onShell analyses allows to improve the exclusion limit from $m_{\tilde{\chi}_1^\pm, \tilde{\chi}_2^0} \simeq 250$ GeV to $m_{\tilde{\chi}_1^\pm, \tilde{\chi}_2^0} \simeq 300$ GeV.

In the on-shell region (Figure 6.13a), not only the area being excluded covers the corresponding ones of the three relevant searches – namely 3ℓ-onShell, $2\ell 2j$ and AllHad analyses – but their combination further extends the areas excluded at 95% CL. In particular, for $m_{\tilde{\chi}_1^\pm, \tilde{\chi}_2^0} \simeq 525$ GeV the excluded limit is improved from $m_{\tilde{\chi}_1^0} \simeq 290$ GeV to $m_{\tilde{\chi}_1^0} \simeq 340$ GeV, thanks to the 3ℓ-onShell+$2\ell 2j$ combination. Concurrently, the 3ℓ-onShell+$2\ell 2j$+AllHad combination generally improves the exclusion in the $m_{\tilde{\chi}_1^\pm, \tilde{\chi}_2^0} \in [600, 800]$ GeV range by about 20 GeV in the $\tilde{\chi}_1^0$ mass. Finally, the $2\ell 2j$+AllHad combination is particularly beneficial in improving the excluded area from $m_{\tilde{\chi}_1^0} \simeq 260$ GeV to $m_{\tilde{\chi}_1^0} \simeq 360$ GeV for $m_{\tilde{\chi}_1^\pm, \tilde{\chi}_2^0} \simeq 900$ GeV, and from $m_{\tilde{\chi}_1^\pm, \tilde{\chi}_2^0} \simeq 950$ GeV to $m_{\tilde{\chi}_1^\pm, \tilde{\chi}_2^0} \simeq 1025$ GeV for massless $\tilde{\chi}_1^0$.

Outlook of the EWK combination

The results illustrated in this Chapter have clearly shown the validity of carrying out the statistical combination of separate EWK SUSY searches targeting the same production simplified model but with different final states. Having demonstrated the advantage, the techniques that have been employed in the WZ combination are currently being used as a cornerstone to perform statistical combinations in other scenarios.

In general, through the combination it is possible to exclude a larger area of the plane of the relevant sparticle masses. This further helps to set more stringent bounds on the parameters of mSUGRA and other SUSY models. More importantly, from the combinations it is possible to extract more general phenomenological considerations by virtue of the different decay modes of the intermediate bosons taken into account, through which is possible to explore a much larger phase space.

In conclusion, the work on the statistical combination of the results of several EWK SUSY searches continues and a publication is expected in the near future which will summarise the results.

7 Conclusions and Outlook

This thesis presents the work that I have carried out over the course of my PhD, which concerns the ATLAS experiment at the LHC and searches for SUSY scenarios in multileptonic final states using $\sqrt{s} = 13$ TeV p-p collisions.

The possibility of observing any evidence for BSM physics in the ATLAS experiment is undeniably linked to the ability to select and record events from p-p collisions of physical interest even in the challenging pile-up conditions of Run 2. The ATLAS trigger system plays a key role in this context. As any evidence for new physics may present itself in events with charged leptons in the final state, it is essential to ensure the reliability of trigger decisions based on the tracks reconstructed in the ID. For this reason, it is crucial to measure the performance of the ID trigger in Run 2 in the most unbiased and precise way possible. In this context, the Tag-and-Probe technique, which I implemented in the official software of the ATLAS Collaboration, allows to drastically improve the statistical precision for the determination of the ID trigger tracking efficiency compared to the previously-used approach. These findings have been published as part of the official paper reporting the latest measurements for the performance of the ATLAS ID trigger in Run 2 [85].

Over the course of my PhD, my main involvement in the ATLAS Collaboration has focused on searches for SUSY using simplified models which concern the EWK production of a $\tilde{\chi}_1^{\pm}\,\tilde{\chi}_2^0$ pair which decay with 100% BR to intermediate states with WZ or Wh bosons, conserving R-Parity. The conservation of R-Parity is responsible for the presence in the final state of a pair of stable $\tilde{\chi}_1^0$, assumed to be the LSP and resulting in $E_{\mathrm{T}}^{\mathrm{miss}}$ in the event.

Final states with electrons and muons coming from the decay of the on-shell intermediate bosons are considered. Specifically, in the Wh-SS analysis which employs the full Run 2 dataset with 139 fb^{-1}, final states with same-sign light-leptons from the decay of W and Higgs bosons are targeted. I have been the leading analyser for this search, having developed and carried out the vast majority of the parts of the analysis, from the SRs optimisation to the statistical interpretation of the results, going through the estimation of SM backgrounds and their associated systematic uncertainties. No significant deviation between data and the SM prediction was observed and the obtained 95% CL exclusion limits on $m_{\tilde{\chi}_1^{\pm}} = m_{\tilde{\chi}_2^0} = m_{\tilde{\chi}_1^{\pm},\tilde{\chi}_2^0}$ and $m_{\tilde{\chi}_1^0}$ remarkably extend the known bounds on these masses for this model, compared to the previous early Run 2 ATLAS search which had used the 36.1 fb^{-1} dataset at $\sqrt{s} = 13$ TeV. An increment of about 300 GeV in the exclusion of $m_{\tilde{\chi}_1^\pm,\tilde{\chi}_2^0}$ for massless LSP is obtained with the new analysis I performed. At the same time, for $m_{\tilde{\chi}_1^\pm,\tilde{\chi}_2^0} \lesssim 230$ GeV the 95% CL exclusion reaches the kinematic limit, $\Delta m_{\text{Sig}} = m_h$, which provides a unique sensitivity for the search in the considered simplified model. The results of this analysis have been published and can be found in Reference [136].

Since the beginning of my PhD I have also contributed to another search for chargino and neutralino production in decays with intermediate WZ or Wh, on-shell bosons, yielding three-lepton final states. My involvements in this analysis were primarily related to the estimation of experimental and theoretical systematic uncertainties, which were of crucial importance for obtaining the final results and derive the statistical interpretation. Also in this case, no significant deviation in data from the SM predictions was observed. The obtained exclusion limits in both the WZ-3ℓ and Wh-3ℓ scenarios once again extend the known constraints on $m_{\tilde{\chi}_1^\pm,\tilde{\chi}_2^0}$ and $m_{\tilde{\chi}_1^0}$ compared to previous searches by the ATLAS Collaboration with the Run 1, $\sqrt{s} = 8$ TeV dataset. In the WZ-3ℓ search, for massless LSP the upper limit on $m_{\tilde{\chi}_1^\pm,\tilde{\chi}_2^0}$ is increased by about 300 GeV, whilst for $\Delta m_{\text{Sig}} = m_Z$ the exclusion is improved by approximately 100 GeV. Similarly, for the Wh-3ℓ model, a ~ 40 GeV increase in the exclusion of $m_{\tilde{\chi}_1^\pm,\tilde{\chi}_2^0}$ for massless $m_{\tilde{\chi}_1^0}$ with respect to the Run 1 analysis. The results of both these searches have been published in the paper reported in Reference [156].

The reliance on simplified models to search for SUSY in the ATLAS experiment offers a unique opportunity to scan and probe the most remote regions of the phase-space in a systematic and orderly fashion for the search for BSM physics. Although none of the searches for SUSY up to the time of writing have reported any significant excess from the SM prediction, the unique sensitivity provided by each analysis gives different constraints on the relevant MSSM parameters, particularly on the sparticles masses. The statistical combination of the results of searches which share the same assumptions on the SUSY production mechanism and that have overlapping excluded areas of the parameters space can be used to further extend the overall constraints. The combination of EWK SUSY searches represents the final major task that I have undertaken during my PhD. In the case of the combination of analyses targeting the $\tilde{\chi}_1^\pm \tilde{\chi}_2^0$ production with a WZ intermediate state, for which I have been personally responsible, the overall exclusion limits show large improvements in extending the bounds by $\sim 50-100$ GeV compared to the constraints from each analysis individually. This ultimately deepens the knowledge about the available phase-space in which SUSY can be discovered.

Looking ahead, the information provided by all of the analyses described in this thesis can be used to further investigate the possible values of the free parameters of the MSSM. Specifically, these results can be used to perform global fits on the MSSM [172], to extract constraints on generic SUSY models, such as mSUGRA. This can in turn be exploited to provide additional insights on the nature of DM. Furthermore, the results of these analyses can also be reinterpreted to extract constraints on other SUSY models, such as the *phenomenological MSSM* (pMSSM) [173], in which only 19 free parameters are predicted. Finally, global fits simultaneous to all searches can also be employed to gain constraints on generic BSM models [174].

Throughout this thesis it has been highlighted how the search in multileptonic final states can provide an extremely powerful tool to search for new evidence of physics BSM and, particularly, SUSY, both independently and in combination with other searches. A vast range of scenarios can be explored, including those with very compressed predicted mass hierarchies between new particle states. Moreover, the tools and techniques developed to carry out these searches using Run 2 data provide increasingly advanced methods to probe the phase-space for new physics. Multileptonic searches can definitely benefit from having larger datasets also through the employment of advanced techniques, e. g. those based on MVA approaches. For this reason these searches will continue to be relevant and play a crucial role in the upcoming Run 3 and, more importantly, in the High-Luminosity LHC phase [175].

In conclusion, the work and the results outlined in this thesis provide novel and stringent constraints on key models for BSM physics explored in the ATLAS experiment. The obtained results will also form an important basis for future searches which will allow to gain greater insight into the fundamental laws of Nature.

GLOSSARY

ALICE A Large Ion Collider Experiment

AFII ATLFastII

AOD Analysis Objects Data

ATLAS A Toroidal LHC ApparatuS

BDT Boosted Decisions Tree

BEH Brout-Englert-Higgs

BR Branching Ratio

BSM Beyond Standard Model

CERN European Organization for Nuclear Research

CF Charge-Flip

CKKW Catani, Krauss, Kuhn and Webber

CL Confidence Level

CMS Compact Muon Solenoid

CP Cluster Processor

CPU Central Processing Unit

CR Control Region

CSC Cathode Strip Chamber

CTP Central Trigger Processor

DAOD Derived AOD

DFOS Different-Flavour Opposite-Sign

DIS Deep Inelastic Scattering

DM Dark Matter

FCal Forward Calorimeter

ECIDS ElectronChargeIDSelector

EM Electromagnetic

EMB Electromagnetic Barrel

EMEC Electromagnetic End-Cap

EWK Electroweak

ECal Electromagnetic Calorimeter

FE Front-End

FF Fake Factor

FNP Fake/Non-Prompt

FSR Final State Radiation

FTF Fast Track Finder

GUT Grand Unification Theory

GSF Gaussian Sum Filter

GWS Glashow-Weinberg-Salam

HCal Hadronic Calorimeter

HEC Hadronic End-Cap

HF Heavy-Flavour

HLT High-Level Trigger

IBL Insertable B-Layer

ID Inner Detector

ISR Initial State Radiation

JEP Jet/Energy-sum Processor

JES Jet Energy Scale

JER Jet Energy Resolution

JSON JavaScript Object Notation

JVT Jet Vertex Tagger

L1 Level-1

L1Calo L1 Calorimeter

L1Muon L1 Muon

L1Topo L1 Topological

LAr Liquid Argon

LEP Large Electron-Positron collider

LF Light-Flavour

LH Likelihood

LHC Large Hadron Collider

LHCb LHC beauty

LHCf LHC forward

LINAC2 Linear Accelerator 2

LO Leading Order

LS Long Shutdown

LS1 Long Shutdown 1

LS2 Long Shutdown 2

LSP Lightest Supersymmetric Particle

MC Monte Carlo

MDT Monitored Drift Tube

MoEDAL Monopole & Exotics Detector At the LHC

MS Muon Spectrometer

MSSM Minimal Supersymmetric Standard Model

MUCTPI L1Muon Central Trigger Processor Interface

MVA Multi-Variate Analysis

NF Normalisation Factor

NN Neural Network

NP Nuisance Parameter

NLO Next-to-Leading Order

OvR Overlap Removal

PDF Parton Distribution Function

pdf probability density function

PS Parton Shower

PSB Proton Synchrotron Booster

QCD Quantum Chromodynamics

QED Quantum Electrodynamics

QFT Quantum Field Theory

RDO Raw Data Object

RF Radio-Frequency

ROB Read-Out Buffer

ROD Read-Out Driver

RoI Region of Interest

ROS Read-Out System

RPC Resistive-Plate Chamber

SCT SemiConductor Tracker

SF Scale Factor

SFSS Same-Flavour Same-Sign

SFOS Same-Flavour Opposite-Sign

SM Standard Model

SPS Super Proton Synchrotron

SR Signal Region

SSB Spontaneous Symmetry Breaking

SUSY Supersymmetry

TDAQ Trigger and Data Acquisition

TGC Thin-Gap Chamber

TOTEM TOTal cross section, Elastic scattering and diffraction dissociation Measurement at the LHC

TRT Transition Radiation Tracker

VBF Vector Boson Fusion

VBS Vector Boson Scattering

VEV Vacuum Expectation Value

VR Validation Region

WP Working Point

LIST OF FIGURES

LIST OF TABLES

BIBLIOGRAPHY

[1] M. Thomson, *Modern particle physics.* Cambridge University Press, New York, 2013.

[2] A. Einstein, *The Foundation of the General Theory of Relativity*, Annalen Phys. **49** no. 7, (1916) 769–822.

[3] M. E. Peskin, D. V. Schroeder, *An Introduction to Quantum Field Theory.* Westview Press, 1995.

[4] A. Arbuzov, *Quantum Field Theory and the Electroweak Standard Model*, `arXiv:1801.05670`. `https://cds.cern.ch/record/2315477`. 35 pages.

[5] Particle Data Group Collaboration, R. L. Workman and Others, *Review of Particle Physics*, PTEP **2022** (2022) 083C01.

[6] S. Weinberg, *The quantum theory of fields. Vol. 2: Modern applications.* Cambridge University Press, 2013.

[7] R. P. Feynman, *Space-Time Approach to Quantum Electrodynamics*, Phys. Rev. **76** (1949) 769–789. `https://link.aps.org/doi/10.1103/PhysRev.76.769`.

[8] D. Hanneke, S. Fogwell, and G. Gabrielse, *New Measurement of the Electron Magnetic Moment and the Fine Structure Constant*, Physical Review Letters **100** no. 12, (2008). `https://doi.org/10.1103%2Fphysrevlett.100.120801`.

[9] Muon g-2 Collaboration, G. W. Bennett et al., *Final Report of the Muon E821 Anomalous Magnetic Moment Measurement at BNL*, Phys. Rev. D **73** (2006) 072003, `arXiv:hep-ex/0602035`.

[10] M. Gell-Mann, *The interpretation of the new particles as displaced charge multiplets*, Nuovo Cim. **4** no. S2, (1956) 848–866.

[11] K. Nishijima, *Charge Independence Theory of V Particles*, Prog. Theor. Phys. **13** no. 3, (1955) 285–304.

[12] S. L. Glashow, *Partial Symmetries of Weak Interactions*, Nucl. Phys. **22** (1961) 579–588.

[13] S. Weinberg, *A Model of Leptons*, Phys. Rev. Lett. **19** (1967) 1264–1266. https://link.aps.org/doi/10.1103/PhysRevLett.19.1264.

[14] A. Salam and J. Ward, *Electromagnetic and weak interactions*, Physics Letters **13** no. 2, (1964) 168 – 171. http://www.sciencedirect.com/science/article/pii/0031916364907115.

[15] P. W. Higgs, *Broken Symmetries and the Masses of Gauge Bosons*, Phys. Rev. Lett. **13** (1964) 508–509.

[16] F. Englert and R. Brout, *Broken Symmetry and the Mass of Gauge Vector Bosons*, Phys. Rev. Lett. **13** (1964) 321–323.

[17] T. W. B. Kibble, *Symmetry Breaking in Non-Abelian Gauge Theories*, Phys. Rev. **155** (1967) 1554–1561. http://link.aps.org/doi/10.1103/PhysRev.155.1554.

[18] J. Goldstone, *Field Theories with Superconductor Solutions*, Nuovo Cim. **19** (1961) 154–164.

[19] J. Goldstone, A. Salam and S. Weinberg, *Broken Symmetries*, Phys. Rev. **127** (1962) 965–970.

[20] N. Cabibbo, *Unitary Symmetry and Leptonic Decays*, Phys. Rev. Lett. **10** (1963) 531–533.

[21] M. Kobayashi and T. Maskawa, *CP-Violation in the Renormalizable Theory of Weak Interaction*, Progress of Theoretical Physics **49** no. 2, (1973) 652–657, https://academic.oup.com/ptp/article-pdf/49/2/652/5257692/49-2-652.pdf. https://doi.org/10.1143/PTP.49.652.

[22] B. Pontecorvo, *Inverse beta processes and nonconservation of lepton charge*, Zh. Eksp. Teor. Fiz. **34** (1957) 247.

[23] Z. Maki, M. Nakagawa, and S. Sakata, *Remarks on the unified model of elementary particles*, Prog. Theor. Phys. **28** (1962) 870–880.

[24] Super-Kamiokande Collaboration, Y. Fukuda et al., *Evidence for oscillation of atmospheric neutrinos*, Phys. Rev. Lett. **81** (1998) 1562–1567, arXiv:hep-ex/9807003 [hep-ex].

[25] ATLAS Collaboration, *Observation of a New Particle in the Search for the Standard Model Higgs Boson with the ATLAS Detector at the LHC*, Phys.Lett. **B716** (2012), arXiv:1207.7214 [hep-ex].

[26] CMS Collaboration, *Observation of a new boson at a mass of 125 GeV with the CMS experiment at the LHC*, Phys.Lett. **B716** (2012), arXiv:1207.7235 [hep-ex].

[27] ATLAS and CMS Collaborations, *Combined Measurement of the Higgs Boson Mass in pp Collisions at $\sqrt{s}$ = 7 and 8 TeV with the ATLAS and CMS Experiments*, Phys. Rev. Lett. **114** (2015), arXiv:1503.07589 [hep-ex].

[28] S. P. Martin, *A Supersymmetry primer*, arXiv:hep-ph/9709356 [hep-ph]. [Adv. Ser. Direct. High Energy Phys.18,1(1998)].

[29] H. Georgi and S. L. Glashow, *Unity of All Elementary Particle Forces*, Phys. Rev. Lett. **32** (1974) 438–441.

[30] A. V. Zasov, A. S. Saburova, A. V. Khoperskov, and S. A. Khoperskov, *Dark matter in galaxies*, Physics, Uspekhi. **60** no. 1, (2017-01-31).

[31] M. Markevitch, A. H. Gonzalez, D. Clowe, A. Vikhlinin, L. David, W. Forman, C. Jones, S. Murray, and W. Tucker, *Direct constraints on the dark matter self-interaction cross-section from the merging galaxy cluster 1E0657-56*, Astrophys. J. **606** (2004) 819–824, arXiv:astro-ph/0309303.

[32] M. Bartelmann, *Gravitational Lensing*, Class. Quant. Grav. **27** (2010) 233001, arXiv:1010.3829 [astro-ph.CO].

[33] Planck Collaboration, N. Aghanim et al., *Planck 2018 results. VI. Cosmological parameters*, Astron. Astrophys. **641** (2020) A6, arXiv:1807.06209 [astro-ph.CO]. [Erratum: Astron.Astrophys. 652, C4 (2021)].

[34] J. Wess and B. Zumino, *Supergauge Transformations in Four-Dimensions*, Nucl. Phys. B **70** (1974) 39–50.

[35] J. Wess and J. Bagger, *Supersymmetry and supergravity*. Princeton University Press, Princeton, NJ, USA, 1992.

[36] M. Dine and A. E. Nelson, *Dynamical supersymmetry breaking at low-energies*, Phys. Rev. D **48** (1993) 1277–1287, arXiv:hep-ph/9303230.

[37] L. Randall and R. Sundrum, *A Large mass hierarchy from a small extra dimension*, Phys. Rev. Lett. **83** (1999) 3370–3373, arXiv:hep-ph/9905221.

[38] A. H. Chamseddine, R. Arnowitt, and P. Nath, *Locally Supersymmetric Grand Unification*, Phys. Rev. Lett. **49** (1982) 970–974. https://link.aps.org/doi/10.1103/PhysRevLett.49.970.

[39] L. J. Hall, J. D. Lykken and S. Weinberg, *Supergravity as the Messenger of Supersymmetry Breaking*, Phys. Rev. **D27** (1983) 2359–2378.

[40] Super-Kamiokande Collaboration, M. Tanaka et al., *Search for proton decay into three charged leptons in 0.37 megaton-years exposure of the Super-Kamiokande*, Phys. Rev. D **101** no. 5, (2020) 052011, arXiv:2001.08011 [hep-ex].

[41] G. R. Farrar and P. Fayet, *Phenomenology of the Production, Decay, and Detection of New Hadronic States Associated with Supersymmetry*, Phys. Lett. B **76** (1978) 575–579.

[42] G. A. Blair, W. Porod, and P. M. Zerwas, *The Reconstruction of supersymmetric theories at high-energy scales*, Eur. Phys. J. C **27** (2003) 263–281, arXiv:hep-ph/0210058.

[43] ATLAS Collaboration, "SUSY cross sections for $\sqrt{s} = 13$ TeV pp collisions." https://twiki.cern.ch/twiki/bin/view/LHCPhysics/SUSYCrossSections.

[44] J. Alwall, P. Schuster, and N. Toro, *Simplified models for a first characterization of new physics at the LHC*, Phys. Rev. D **79** (2009) 075020, arXiv:0810.3921 [hep-ph].

[45] LHC New Physics Working Group Collaboration, D. Alves, *Simplified models for LHC new physics searches*, J. Phys. G **39** (2012) 105005, arXiv:1105.2838 [hep-ph].

[46] ATLAS Collaboration, G. Aad et al., *Search for squarks and gluinos in final states with one isolated lepton, jets, and missing transverse momentum at $\sqrt{s} = 13$ with the ATLAS detector*, Eur. Phys. J. C **81** no. 7, (2021) 600, arXiv:2101.01629 [hep-ex]. [Erratum: Eur.Phys.J.C 81, 956 (2021)].

[47] CMS Collaboration, A. M. Sirunyan et al., *Search for supersymmetry in proton-proton collisions at 13 TeV in final states with jets and missing transverse momentum*, JHEP **10** (2019) 244, arXiv:1908.04722 [hep-ex].

[48] ATLAS Collaboration, G. Aad et al., *Search for a scalar partner of the top quark in the all-hadronic $t\bar{t}$ plus missing transverse momentum final state at $\sqrt{s} = 13$ TeV with the ATLAS detector*, Eur. Phys. J. C **80** no. 8, (2020) 737, arXiv:2004.14060 [hep-ex].

[49] ATLAS Collaboration, G. Aad et al., *Search for new phenomena with top quark pairs in final states with one lepton, jets, and missing transverse momentum in pp collisions at $\sqrt{s} = 13$ TeV with the ATLAS detector*, JHEP **04** (2021) 174, arXiv:2012.03799 [hep-ex].

[50] CMS Collaboration, A. M. Sirunyan et al., *Search for direct top squark pair production in events with one lepton, jets, and missing transverse momentum at 13 TeV with the CMS experiment*, JHEP **05** (2020) 032, arXiv:1912.08887 [hep-ex].

[51] CMS Collaboration, A. M. Sirunyan et al., *Search for top squark pair production in a final state with two tau leptons in proton-proton collisions at $\sqrt{s} = 13$ TeV*, JHEP **02** (2020) 015, arXiv:1910.12932 [hep-ex].

[52] ATLAS Collaboration, *SUSY Summary Plots March 2022*,. https://atlas.web.cern.ch/Atlas/GROUPS/PHYSICS/PUBNOTES/ATL-PHYS-PUB-2022-013/.

[53] ATLAS Collaboration, G. Aad et al., *Search for electroweak production of charginos and sleptons decaying into final states with two leptons and missing transverse momentum in $\sqrt{s} = 13$ TeV pp collisions using the ATLAS detector*, Eur. Phys. J. C **80** no. 2, (2020) 123, arXiv:1908.08215 [hep-ex].

[54] CMS Collaboration, A. M. Sirunyan et al., *Search for supersymmetric partners of electrons and muons in proton-proton collisions at $\sqrt{s} = 13$ TeV*, Phys. Lett. B **790** (2019) 140–166, arXiv:1806.05264 [hep-ex].

[55] ATLAS Collaboration, *Search for charginos and neutralinos in final states with two boosted hadronically decaying bosons and missing transverse momentum in pp collisions at $\sqrt{s}$ = 13 TeV with the ATLAS detector*, Phys. Rev. D **104** no. 11, (2021) 112010, arXiv:2108.07586 [hep-ex].

[56] CMS Collaboration, A. M. Sirunyan et al., *Combined search for electroweak production of charginos and neutralinos in proton-proton collisions at $\sqrt{s}$ = 13 TeV*, JHEP **03** (2018) 160, arXiv:1801.03957 [hep-ex].

[57] ATLAS Collaboration, M. Aaboud et al., *Search for chargino and neutralino production in final states with a Higgs boson and missing transverse momentum at $\sqrt{s} = 13$ TeV with the ATLAS detector*, Phys. Rev. D **100** no. 1, (2019) 012006, arXiv:1812.09432 [hep-ex].

[58] ATLAS Collaboration, G. Aad et al., *Search for direct production of charginos and neutralinos in events with three leptons and missing transverse momentum in $\sqrt{s}$ = 8TeV pp collisions with the ATLAS detector*, JHEP **04** (2014) 169, arXiv:1402.7029 [hep-ex].

[59] L. Evans and P. Bryant, *LHC Machine*,. https://doi.org/10.1088/1748-0221/3/08/s08001.

[60] *LEP Design Report: Vol.2. The LEP Main Ring*, CERN-LEP-84-01 (1984).

[61] ATLAS Collaboration, *The ATLAS experiment at the CERN Large Hadron Collider*, Journal of Instrumentation **3** no. 08, (2008) S08003. http://stacks.iop.org/1748-0221/3/i=08/a=S08003.

[62] CMS Collaboration, *The CMS experiment at the CERN LHC*, Journal of Instrumentation **3** no. 08, (2008) S08004. http://stacks.iop.org/1748-0221/3/i=08/a=S08004.

[63] LHCb Collaboration, *The LHCb Detector at the LHC*,. https://doi.org/10.1088/1748-0221/3/08/s08005.

[64] ALICE Collaboration, *The ALICE experiment at the CERN LHC*, Journal of Instrumentation **3** no. 08, (2008) S08002. http://stacks.iop.org/1748-0221/3/i=08/a=S08002.

[65] TOTEM Collaboration, *The TOTEM Experiment at the CERN Large Hadron Collider*, Journal of Instrumentation **3** no. 08, (2008) S08007. http://stacks.iop.org/1748-0221/3/i=08/a=S08007.

[66] J. Pinfold, *The MoEDAL experiment at the LHC*, EPJ Web Conf. **145** (2017) 12002.

[67] LHCf Collaboration, O. Adriani et al., *Technical design report of the LHCf experiment: Measurement of photons and neutral pions in the very forward region of LHC*,.

[68] S. Fartoukh et al., *LHC Configuration and Operational Scenario for Run 3*, tech. rep., CERN, Geneva, Nov, 2021. https://cds.cern.ch/record/2790409.

[69] E. Mobs, *The CERN accelerator complex - August 2018. Complexe des accélérateurs du CERN - Août 2018*,. https://cds.cern.ch/record/2636343. General Photo.

[70] J. Wenninger, *Operation and Configuration of the LHC in Run 2*,. https://cds.cern.ch/record/2668326.

[71] W. Herr and B. Muratori, *Concept of luminosity*,. https://cds.cern.ch/record/941318.

[72] G. Avoni et al., *The new LUCID-2 detector for luminosity measurement and monitoring in ATLAS*,. https://doi.org/10.1088/1748-0221/13/07/p07017.

[73] ATLAS Collaboration, *Luminosity determination in pp collisions at $\sqrt{s} = 13$ TeV using the ATLAS detector at the LHC*, ATLAS-CONF-2019-021 (2019).

[74] ATLAS Collaboration, "ATLAS luminosity measurements." https://twiki.cern.ch/twiki/bin/view/AtlasPublic/LuminosityPublicResultsRun2.

[75] J. T. Boyd, *LHC Run-2 and Future Prospects*, in *2019 European School of High-Energy Physics*. 1, 2020. arXiv:2001.04370 [hep-ex].

[76] F. Kuger, *Signal Formation Processes in Micromegas Detectors and Quality Control for large size Detector Construction for the ATLAS New Small Wheel*,.

[77] J. Goodson, "ATLAS magnet systems." http://www.jetgoodson.com/images/thesisImages/magnetSystems.png.

[78] K. Potamianos, *The upgraded Pixel detector and the commissioning of the Inner Detector tracking of the ATLAS experiment for Run-2 at the Large Hadron Collider*, PoS **EPS-HEP2015** (2015) 261, arXiv:1608.07850 [physics.ins-det].

[79] ATLAS Collaboration, *ATLAS Insertable B-Layer Technical Design Report*,. https://cds.cern.ch/record/1291633.

[80] ATLAS Collaboration, G. Aad et al., *Operation of the ATLAS trigger system in Run 2*, JINST **15** no. 10, (2020) P10004, arXiv:2007.12539 [physics.ins-det].

[81] ATLAS Collaboration, *The ATLAS Level-1 Calorimeter Trigger*, Journal of Instrumentation **3** no. 03, (2008) P03001. http://stacks.iop.org/1748-0221/3/i=03/a=P03001.

[82] E. Simoni, *The Topological Processor for the future ATLAS Level-1 Trigger: from design to commissioning*, arXiv:1406.4316.

[83] ATLAS Collaboration, *Athena*, Apr., 2019. https://doi.org/10.5281/zenodo.2641997.

[84] G. Barrand et al., *GAUDI - A software architecture and framework for building HEP data processing applications*, Comput. Phys. Commun. **140** (2001) 45–55.

[85] ATLAS Collaboration, G. Aad et al., *The ATLAS Inner Detector Trigger performance in pp collisions at 13 TeV during LHC Run 2*, arXiv:2107.02485 [hep-ex].

[86] ATLAS Collaboration, *Electron efficiency measurements with the ATLAS detector using 2012 LHC proton–proton collision data*, Eur. Phys. J. C **77** no. 3, (2017) 195, arXiv:1612.01456 [hep-ex].

[87] V. N. Gribov and L. N. Lipatov, *Deep inelastic e p scattering in perturbation theory*, Sov. J. Nucl. Phys. **15** (1972) 438–450. [Yad. Fiz.15,781(1972)].

[88] H1 Collaboration, I. A. et al., *The H1 detector at HERA*, Nuclear Instruments and Methods in Physics Research Section A: Accelerators, Spectrometers, Detectors and Associated Equipment **386** no. 2, (1997) 310–347. https://www.sciencedirect.com/science/article/pii/S0168900296008935.

[89] ZEUS Collaboration, B. Lohr, *The ZEUS experiment at HERA*, in *1st German-Polish Symposium on Particles and Fields*. 4, 1992.

[90] ATLAS Collaboration, *Determination of the parton distribution functions of the proton from ATLAS measurements of differential W and Z/γ^* and $t\bar{t}$ cross sections*, tech. rep., CERN, Geneva, Aug, 2018. https://cds.cern.ch/record/2633819.

[91] R. K. Ellis, W. J. Stirling, and B. R. Webber, *QCD and collider physics*. Cambridge monographs on particle physics, nuclear physics, and cosmology. Cambridge University Press, Cambridge, 2003. https://cds.cern.ch/record/318585. Photography by S. Vascotto.

[92] A. Buckley, J. Butterworth, S. Gieseke, D. Grellscheid, S. Hoche, et al., *General-purpose event generators for LHC physics*, Phys.Rept. **504** (2011). http://arXiv.org/abs/1101.2599.

[93] S. Höche, *Introduction to parton-shower event generators*, arXiv:1411.4085 [hep-ph].

[94] ATLAS Collaboration, *Properties of Jets and Inputs to Jet Reconstruction and Calibration with the ATLAS Detector Using Proton-Proton Collisions at $\sqrt{s}$ = 7 TeV*,. http://cds.cern.ch/record/1281310/files/ATLAS-CONF-2010-053.pdf.

[95] M. R. Whalley, D. Bourilkov, and R. C. Group, *The Les Houches accord PDFs (LHAPDF) and LHAGLUE*, arXiv:hep-ph/0508110.

[96] NNPDF Collaboration, R. D. Ball et al., *Parton distributions for the LHC Run II*, JHEP **04** (2015) 040, arXiv:1410.8849 [hep-ph].

[97] L. Lönnblad and S. Prestel, *Merging multi-leg NLO matrix elements with parton showers*, JHEP **03** (2013) 166, arXiv:1211.7278 [hep-ph].

[98] B. Andersson, S. Mohanty and F. Soderberg, *Recent Developments in the Lund Model*, arXiv:hep-ph/0212122 [hep-ph].

[99] A. Kupco , *Cluster Hadronization in HERWIG 5.9*, arXiv:hep-ph/9906412 [hep-ph].

[100] ATLAS Collaboration, Z. Marshall, *Simulation of Pile-up in the ATLAS Experiment*, J. Phys. Conf. Ser. **513** (2014) 022024.

[101] M. Bahr, S. Gieseke, M. Gigg, D. Grellscheid, K. Hamilton, et al., *Herwig++ Physics and Manual*, Eur.Phys.J **C58** (2008).

[102] T. Sjöstrand, S. Mrenna, and P. Z. Skands, *A brief introduction to PYTHIA 8.1*, Comput. Phys. Commun. **178** (2008) 852–867, arXiv:0710.3820 [hep-ph].

[103] F. Maltoni and T. Stelzer, *MadEvent: Automatic event generation with MadGraph*, JHEP **02** (2003) 027, arXiv:hep-ph/0208156.

[104] Sherpa Collaboration, E. Bothmann et al., *Event Generation with Sherpa 2.2*, SciPost Phys. **7** no. 3, (2019) 034, arXiv:1905.09127 [hep-ph].

[105] S. Frixione and B. R. Webber, *Matching NLO QCD computations and parton shower simulations*, JHEP **06** (2002) 029, arXiv:hep-ph/0204244 [hep-ph].

[106] S. Alioli, P. Nason, C. Oleari, and E. Re, *A general framework for implementing NLO calculations in shower Monte Carlo programs: the POWHEG BOX*, JHEP **06** (2010) 043, arXiv:1002.2581 [hep-ph].

[107] S. Frixione, and P. Nason, and C. Oleari, *Matching NLO QCD computations with Parton Shower simulations: the POWHEG method*, JHEP **11** (2007) 070.

[108] D. J. Lange, *The EvtGen particle decay simulation package*, Nucl. Instrum. Meth. **462** no. 1–2, (2001) 152 – 155.

[109] GEANT4 Collaboration, *Geant4 a simulation toolkit*, Nucl. Instrum. Meth. A **506** (2003).

[110] ATLAS Collaboration, *The simulation principle and performance of the ATLAS fast calorimeter simulation FastCaloSim*,. https://cds.cern.ch/record/1300517.

[111] W. Lukas, *Fast Simulation for ATLAS: Atlfast-II and ISF*, J. Phys.: Conf. Ser **396** no. 022031, (2012).

[112] M. Bandieramonte, R. M. Bianchi, and J. Boudreau, *FullSimLight: ATLAS standalone Geant4 simulation*, EPJ Web Conf. **245** (2020) 02029.

[113] M. Dobbs and J. B. Hansen, *The HepMC C++ Monte Carlo event record for High Energy Physics*, Computer Physics Communications **134** no. 1, (2001) 41 – 46. http://www.sciencedirect.com/science/article/pii/S0010465500001892.

[114] W. Bhimji, J. Cranshaw, P. van Gemmeren, D. Malon, R. D. Schaffer, and I. Vukotic, *The ATLAS ROOT-based data formats: recent improvements and performance measurements*, ATL-SOFT-PROC-2012-020, ATL-COM-SOFT-2012-054 (2012).

[115] R. Brun and F. Rademakers, *ROOT: An object oriented data analysis framework*, Nucl. Instrum. Meth. **A389** (1997) 81–86.

[116] T. Cornelissen, M. Elsing, I. Gavrilenko, W. Liebig, E. Moyse, and A. Salzburger, *The new ATLAS track reconstruction (NEWT)*,. https://doi.org/10.1088/1742-6596/119/3/032014.

[117] ATLAS Collaboration, M. Aaboud et al., *Performance of the ATLAS Track Reconstruction Algorithms in Dense Environments in LHC Run 2*, Eur. Phys. J. C **77** no. 10, (2017) 673, arXiv:1704.07983 [hep-ex].

[118] R. Frühwirth, *Application of Kalman filtering to track and vertex filtering*, Nucl.Instrum.Meth. **A262** (1987).

[119] ATLAS Collaboration, G. Aad et al., *A neural network clustering algorithm for the ATLAS silicon pixel detector*, JINST **9** (2014) P09009, arXiv:1406.7690 [hep-ex].

[120] ATLAS Collaboration, M. Aaboud et al., *Electron reconstruction and identification in the ATLAS experiment using the 2015 and 2016 LHC proton-proton collision data at $\sqrt{s}$ = 13 TeV*, Eur. Phys. J. C **79** no. 8, (2019) 639, arXiv:1902.04655 [physics.ins-det].

[121] ATLAS Collaboration, G. Aad et al., *Electron and photon performance measurements with the ATLAS detector using the 2015–2017 LHC proton-proton collision data*, JINST **14** no. 12, (2019) P12006, arXiv:1908.00005 [hep-ex].

[122] ATLAS Collaboration, *Improved electron reconstruction in ATLAS using the Gaussian Sum Filter-based model for bremsstrahlung*, ATLAS-CONF-2012-047, ATLAS-CONF-2012-047 (2012).

[123] ATLAS Collaboration, *ElectronChargeIDSelector tool*, 2018. https://twiki.cern.ch/twiki/bin/view/AtlasProtected/IsolationSelectionTool.

[124] J. Illingworth and J. Kittler, *A survey of the hough transform*, Computer Vision, Graphics, and Image Processing **44** no. 1, (1988) 87–116. https://www.sciencedirect.com/science/article/pii/S0734189X88800331.

[125] ATLAS Collaboration, G. Aad et al., *Muon reconstruction and identification efficiency in ATLAS using the full Run 2 pp collision data set at $\sqrt{s} = 13$ TeV*, Eur. Phys. J. C **81** no. 7, (2021) 578, arXiv:2012.00578 [hep-ex].

[126] ATLAS Collaboration, *Topological cell clustering in the ATLAS calorimeters and its performance in LHC Run 1*, Eur. Phys. J. **C77** (2017) 490, arXiv:1603.02934 [hep-ex].

[127] G. S. M. Cacciari, G. P. Salam, *The Anti-k(t) jet clustering algorithm*, JHEP **0804** (2008), arXiv:0802.1189 [hep-ph].

[128] ATLAS Collaboration, M. Aaboud et al., *Jet reconstruction and performance using particle flow with the ATLAS Detector*, Eur. Phys. J. C **77** no. 7, (2017) 466, arXiv:1703.10485 [hep-ex].

[129] ATLAS Collaboration, *Tagging and suppression of pileup jets with the ATLAS detector*, Tech. Rep. ATLAS-CONF-2014-018, CERN, Geneva, May, 2014. https://cds.cern.ch/record/1700870.

[130] ATLAS Collaboration, "Pile-up jet recommendations." https://twiki.cern.ch/twiki/bin/view/AtlasProtected/PileupJetRecommendations.

[131] ATLAS Collaboration, G. Aad et al., *ATLAS b-jet identification performance and efficiency measurement with $t\bar{t}$ events in pp collisions at $\sqrt{s} = 13$ TeV*, Eur. Phys. J. C **79** no. 11, (2019) 970, arXiv:1907.05120 [hep-ex].

[132] ATLAS Collaboration, M. Aaboud et al., *Measurements of b-jet tagging efficiency with the ATLAS detector using $t\bar{t}$ events at $\sqrt{s} = 13$ TeV*, JHEP **08** (2018) 089, arXiv:1805.01845 [hep-ex].

[133] ATLAS Collaboration, *Monte Carlo to Monte Carlo scale factors for flavour tagging efficiency calibration*, ATL-PHYS-PUB-2020-009 (2020).

[134] ATLAS Collaboration, *Performance of the Reconstruction and Identification of Hadronic Tau Decays with ATLAS*,. https://cds.cern.ch/record/1398195.

[135] ATLAS Collaboration, M. Aaboud et al., *Performance of missing transverse momentum reconstruction with the ATLAS detector using proton-proton collisions at $\sqrt{s}$ = 13 TeV*, Eur. Phys. J. C **78** no. 11, (2018) 903, arXiv:1802.08168 [hep-ex].

[136] ATLAS Collaboration, *Search for direct production of winos and higgsinos in events with two same-sign or three leptons in pp collision data at $\sqrt{s} = 13$ TeV with the ATLAS detector*, tech. rep., CERN, Geneva, 2022. https://cds.cern.ch/record/2826603.

[137] ATLAS Collaboration, *Multi-Boson Simulation for 13 TeV ATLAS Analyses*, Tech. Rep. ATL-PHYS-PUB-2017-005, CERN, Geneva, May, 2017. https://cds.cern.ch/record/2261933.

[138] ATLAS Collaboration, M. Aaboud et al., *Observation of electroweak production of a same-sign W boson pair in association with two jets in pp collisions at $\sqrt{s} = 13$ TeV with the ATLAS detector*, Phys. Rev. Lett. **123** no. 16, (2019) 161801, arXiv:1906.03203 [hep-ex].

[139] CMS Collaboration, A. M. Sirunyan et al., *Observation of electroweak production of same-sign W boson pairs in the two jet and two same-sign lepton final state in*

proton-proton collisions at $\sqrt{s}$ = 13 TeV, Phys. Rev. Lett. **120** no. 8, (2018) 081801, arXiv:1709.05822 [hep-ex].

[140] ATLAS Collaboration, *Modelling of the $t\bar{t}H$ and $t\bar{t}V$ $(V = W, Z)$ processes for $\sqrt{s} = 13$ TeV ATLAS analyses*, Tech. Rep. ATL-PHYS-PUB-2016-005, CERN, Geneva, Jan, 2016. https://cds.cern.ch/record/2120826.

[141] ATLAS Collaboration, *Monte Carlo Generators for the Production of a W or Z/γ^* Boson in Association with Jets at ATLAS in Run 2*, Tech. Rep. ATL-PHYS-PUB-2016-003, CERN, Geneva, Jan, 2016. https://cds.cern.ch/record/2120133.

[142] ATLAS Collaboration, *Simulation of top quark production for the ATLAS experiment at sqrt(s) = 13 TeV*, Tech. Rep. ATL-PHYS-PUB-2016-004, CERN, Geneva, Jan, 2016. https://cds.cern.ch/record/2120417.

[143] S. Alioli, P. Nason, C. Oleari, and E. Re, *NLO single-top production matched with shower in POWHEG: s- and t-channel contributions*, JHEP **09** (2009) 111, arXiv:0907.4076 [hep-ph]. [Erratum: JHEP 02, 011 (2010)].

[144] ATLAS Collaboration, *Object-based missing transverse momentum significance in the ATLAS detector*, Tech. Rep. ATLAS-CONF-2018-038, CERN, Geneva, Jul, 2018. https://cds.cern.ch/record/2630948.

[145] C. G. Lester and D. J. Summers, *Measuring masses of semiinvisibly decaying particles pair produced at hadron colliders*, Phys. Lett. B **463** (1999) 99–103, arXiv:hep-ph/9906349.

[146] R. D. Cousins, J. T. Linnemann, and J. Tucker, *Evaluation of three methods for calculating statistical significance when incorporating a systematic uncertainty into a test of the background-only hypothesis for a Poisson process*, Nuclear Instruments and Methods in Physics Research Section A: Accelerators, Spectrometers, Detectors and Associated Equipment **595** no. 2, (2008) 480 – 501. http://www.sciencedirect.com/science/article/pii/S0168900208010255.

[147] The ATLAS Collaboration, *Measurement of the low-mass Drell-Yan differential cross section at $\sqrt{s}$ = 7 TeV using the ATLAS detector*, JHEP **06** (2014).

[148] G. Cowan, *Statistical Data Analysis*. Clarendon Press, 1998.

[149] ATLAS Collaboration, G. Aad et al., *Alignment of the ATLAS Inner Detector in Run-2*, Eur. Phys. J. C **80** no. 12, (2020) 1194, arXiv:2007.07624 [hep-ex].

[150] ATLAS Collaboration, *Jet energy scale measurements and their systematic uncertainties in proton-proton collisions at $\sqrt{s} = 13$ TeV with the ATLAS detector*, Phys. Rev. **D96** no. 7, (2017) 072002, arXiv:1703.09665 [hep-ex].

[151] ATLAS Collaboration, *Jet energy resolution and selection efficiency relative to track jets from in-situ techniques with the ATLAS Detector Using Proton-Proton Collisions at a*

Center of Mass Energy sqrts = 7 TeV, Tech. Rep. ATLAS-CONF-2010-054, CERN, Geneva, Jul, 2010. https://cds.cern.ch/record/1281311.

[152] LHC Higgs Cross Section Working Group Collaboration, D. de Florian et al., *Handbook of LHC Higgs Cross Sections: 4. Deciphering the Nature of the Higgs Sector*, arXiv:1610.07922 [hep-ph].

[153] G. Cowan, K. Cranmer, E. Gross, and O. Vitells, *Asymptotic formulae for likelihood-based tests of new physics*, Eur. Phys. J. **C71** (2011) 1554, arXiv:1007.1727 [physics.data-an]. [Erratum: Eur. Phys. J.C73,2501(2013)].

[154] M. Baak, G. J. Besjes, D. Côte, A. Koutsman, J. Lorenz, and D. Short, *HistFitter software framework for statistical data analysis*, Eur. Phys. J. **C75** (2015) 153, arXiv:1410.1280 [hep-ex].

[155] A. L. Read, *Presentation of search results: the CL s technique*, Journal of Physics G: Nuclear and Particle Physics **28** no. 10, (2002) 2693. http://stacks.iop.org/0954-3899/28/i=10/a=313.

[156] ATLAS Collaboration, G. Aad et al., *Search for chargino–neutralino pair production in final states with three leptons and missing transverse momentum in* $\sqrt{s} = 13$ *TeV pp collisions with the ATLAS detector*, Eur. Phys. J. C **81** no. 12, (2021) 1118, arXiv:2106.01676 [hep-ex].

[157] ATLAS Collaboration, *Studies of Monte Carlo generators in Higgs boson production for ATLAS Run 2*, Tech. Rep. ATL-PHYS-PUB-2014-022, CERN, Geneva, Dec, 2014. https://cds.cern.ch/record/1978192.

[158] ATLAS Collaboration, G. Aad et al., *Searches for electroweak production of supersymmetric particles with compressed mass spectra in* $\sqrt{s}$ *= 13 TeV* pp *collisions with the ATLAS detector*, Phys. Rev. D **101** no. 5, (2020) 052005, arXiv:1911.12606 [hep-ex].

[159] ATLAS Collaboration, *Searches for new phenomena in events with two leptons, jets, and missing transverse momentum in* 139 fb^{-1} *of* $\sqrt{s} = 13$ *TeV* pp *collisions with the ATLAS detector*, arXiv:2204.13072 [hep-ex].

[160] ATLAS Collaboration, *Reproducing searches for new physics with the ATLAS experiment through publication of full statistical likelihoods*, tech. rep., CERN, Geneva, Aug, 2019. https://cds.cern.ch/record/2684863.

[161] L. Moneta, K. Cranmer, G. Schott, and W. Verkerke, *The RooStats project*, arXiv:1009.1003 [physics.data-an].

[162] L. Heinrich, M. Feickert, and G. Stark, *scikit-hep/pyhf: v0.4.4*, July, 2020. https://doi.org/10.5281/zenodo.3928663.

[163] F. Pezoa, J. L. Reutter, F. Suarez, M. Ugarte, and D. Vrgoč, *Foundations of JSON schema*. 2016.

[164] C. A. Gottardo, L. Pedraza Diaz, G. H. Stark, J. R. Dandoy, and S. C. Alderweireldt, *Statistical combinations of Electroweak SUSY searches in two and three lepton final states*, tech. rep., CERN, Geneva, Jun, 2020. https://cds.cern.ch/record/2722093.

[165] J. Bradbury et al., *JAX: composable transformations of Python+NumPy programs*, 2018. http://github.com/google/jax.

[166] A. Paszke et al., *PyTorch: An Imperative Style, High-Performance Deep Learning Library*. Curran Associates, Inc., 2019. http://papers.neurips.cc/paper/9015-pytorch-an-imperative-style-high-performance-deep-learning-library.pdf.

[167] M. Abadi et al., *TensorFlow: Large-Scale Machine Learning on Heterogeneous Systems*, 2015. https://www.tensorflow.org/. Software available from tensorflow.org.

[168] C. R. Harris et al., *Array programming with NumPy*, Nature **585** no. 7825, (2020) 357–362. https://doi.org/10.1038/s41586-020-2649-2.

[169] F. James et al., *MINUIT: Function Minimization and Error Analysis Reference Manual*,. https://cds.cern.ch/record/2296388. CERN Program Library Long Writeups.

[170] P. Virtanen et al., *SciPy 1.0: Fundamental Algorithms for Scientific Computing in Python*, Nature Methods **17** (2020) 261–272.

[171] G. Wright, *Radial Basis Function Interpolation: Numerical and Analytical Developments*. University of Colorado, 2003. https://books.google.co.uk/books?id=T9f_NwAACAAJ.

[172] GAMBIT Collaboration, P. Athron et al., *A global fit of the MSSM with GAMBIT*, Eur. Phys. J. C **77** no. 12, (2017) 879, arXiv:1705.07917 [hep-ph].

[173] ATLAS Collaboration, G. Aad et al., *Summary of the ATLAS experiment's sensitivity to supersymmetry after LHC Run 1 — interpreted in the phenomenological MSSM*, JHEP **10** (2015) 134, arXiv:1508.06608 [hep-ex].

[174] S. Kraml, S. Kulkarni, U. Laa, A. Lessa, W. Magerl, D. Proschofsky-Spindler, and W. Waltenberger, *SModelS: a tool for interpreting simplified-model results from the LHC and its application to supersymmetry*, Eur. Phys. J. C **74** (2014) 2868, arXiv:1312.4175 [hep-ph].

[175] ATLAS Collaboration, *Prospects for searches for staus, charginos and neutralinos at the high luminosity LHC with the ATLAS Detector*, tech. rep., CERN, Geneva, Dec, 2018. http://cds.cern.ch/record/2651927.

Acknowledgements

My PhD and especially my PhD thesis have been by far the most difficult and trying tasks of my entire life so far. There are some wonderful people that have been on my side helping me during this time, and without whom none of this would have been remotely thinkable, let alone possible. To these people I am now and forever sincerely grateful.

First and foremost I would like to thank my supervisor Antonella for her constant, patient and unshakable guidance. During my PhD I can confidently say that I have grown up much faster that I have ever done before, not only as a researcher but as a person, as well. And this is mostly thanks to her, for her help and advices which have not only gotten me through some of my toughest moments, but have allowed me to spring back up on my feet and dash forward more confidently that I would have imagined.

I would also like to really thank the whole group at Sussex, PhD students, postdocs and professors. Fab T., Fabio, Meirin, Mario G., Mario S., Ioannis, Ondra, Zoe, Harry, Tom, Mark, Batool, Kerim, Fab S., Iacopo, Alex, Kate, Lily… so many to mention (so sorry if I forgot some). I am so appreciative to each and every one of these people for making these last few years so exciting and fun. Amongst the group at Sussex, I must especially thank Dani, with whom I have shared almost all of my PhD adventures, and who has also been a true friend to me through this whole ordeal.

I am so grateful to all the other awesome people that I have met over these past few years, and that are now my dear friends. Ash, Chinmay, Giada, Rhiannon and Miro, thank you for having made my experiences and my life in Brighton so much richer and colourful than I thought possible. Nico and Emily, thank you for being such good friends and for making one of the most strange, bleak and difficult times in the life of us all in this generation – when the covid pandemic first broke out – so fun and enjoyable. I will always cherish those memories.

Passando all’italiano, ci tengo tantissimo a ringraziare Piero per il suo supporto, per la sua comprensione e per le sue immancabili iniezioni di fiducia che sono state fondamentali per me, specie di recente.

Voglio inoltre ringraziare mio fratello Daniele e mia (futura) sorella Francesca per essermi sempre stati vicino, anche quando eravamo lontani. In loro ho sempre trovato un sostegno incondizionato, che per me è una fonte di forza inesauribile.

Infine, il mio ringraziamento più sentito e più grande è senza ombra di dubbio alcuno dovuto ai miei genitori. Mamma e Papà, voi siete sempre stati i miei più grandi sostenitori e la mia roccia. È principalmente grazie alla vostra fiducia in me e al vostro supporto, che non hanno mai vacillato, che sono riuscito a raggiungere tutti i miei obiettivi fino ad ora. Questa tesi, che rappresenta l’apice dei miei sforzi fino ad oggi, è dedicata a voi.

Grazie!

Marco

This thesis was typeset using the LaTeX typesetting system created by Leslie Lamport.
The body text size is set to 11 pt with *Utopia Regular* with *Fourier* font, part of TeX Live.
The bibliography was typeset using the ATLAS-paper style.